BNL-211405-2019-INRE

Self-Healing, Re-adhering, and Corrosion-Mitigating Inorganic Cement Composites for Geothermal Wells at 270-300C

T. Sugama, T. Pyatina

February 2019

Sustainable Energy Technologies Department

Brookhaven National Laboratory

U.S. Department of Energy

USDOE Office of Energy Efficiency and Renewable Energy (EERE), Geothermal Technologies Office (EE-4G)

DISCLAIMER

Self-healing, Re-adhering, and Corrosion-mitigating Inorganic Cement Composites for Geothermal Wells at 270º-300ºC

Final Report

BNL-211405-2019-INRE

June 2019

Prepared for

The U.S. Department of Energy
Energy Efficiency and Renewable Energy
Geothermal Technologies Program
1000 Independence Avenue SW
Washington, D.C. 20585

Prepared by

Toshifumi Sugama and Tatiana Pyatina
Sustainable Energy Technologies Department
Brookhaven National Laboratory
Upton, NY 11973-5000

TABLE OF CONTENTNTS

Pages

Summary 5
1. Introduction 12
2. Experimental Procedure 17
2.1. Starting Materials 17
2.2. Formula of various types of cements 20
2.3. Samples preparation 23
2.4. Measurements 24
3. Results and Discussion 26
3.1. Screening of candidates for self-healing cements 26
3.1.1. Fracture toughness 26
3.1.2. Brittleness and softness of cements in three different environments 27
3.1.3. Compressive strength and strength recovery of various cements before and after self-healing in three different environments 29
3.1.4. Acid resistance 31
3.1.5. Thermal shock resistance 32
3.2. Self-healing capability of repeatedly cracked cements 34
3.3. Study of self-healing and re-adhering mechanisms for TSRC 41
3.3.1. 3D micro-image analysis 41
3.3.2. XRD study 46
3.3.3. SEM-EDX study 49
3.4. Study of self-healing and re-adhering mechanisms for CAP-B 50
3.4.1. Compressive strength and its recovery 51
3.4.2. Surface analyses -3D micro-imaging, Raman spectroscopy, and SEM-EDX 51
3.4.3. Matrix analyses – XRD, FTIR, and SEM-EDX 55
3.5. Evaluation of pozzolan additives as self-healing aides 60
3.5.1. Clays in natural pozzolans 60
3.5.2. Zeolites in natural pozzolans 62
3.5.2.1. Clinoptilolite (Clin) 62
3.5.2.2. Ferrierite (FER) 64
3.5.2.2.1. Mechanical properties and microscope study of fractures' sealing 64
3.5.2.2.2. Analyses of degraded samples – crystalline phases, XRD patterns 67
3.5.2.2.3. Derivative thermogravimetry (DTG) measurements 73
3.5.2.2.4. ATR-FTIR measurements 75
3.5.2.2.5. Morphologies of silica-modified and unmodified samples cured in water or alkali carbonate 78
3.5.2.2.6. Acid resistance and acid strength recoveries 78
3.5.3. E-type micro-glass fibers as artificial pozzolan 80
3.5.4. 30-day-long autoclaved MGF-modified TSRC composites in plain 89

water
3.5.4.1. Unmodified TSRC after 15- or 30-day initial curing time: 3D micro-image analyses of crack's sealing 91
3.5.4.2. MGF-modified TSRC after 1-, 15-, or 30-day initial curing time: 3D micro-image analyses crack's sealing 93
3.5.4.3. Phase analyses of MGF-modified and unmodified TSRC in plain water 94
3.5.4.4. Raman analyses of crack areas for long-term cured MGF-modified and unmodified TSRC samples 105
3.5.4.5. Phase analyses of MGF-modified and unmodified TSRC in carbonate and brine 109
3.6. Re-adhering behaviors of debonded composite sheath cement to CS casing surfaces 111
3.6.1. Sheath-shear bond strength and its recovery 111
3.6.2. Re-adhering properties of 30-day-long autoclaved composites 113
3.6.3. Bond durability of composites adhered to CS under cyclic thermal shock stresses 114
3.7. Corrosion protection of CS by re-adhered cements 115
3.7.1. Lap-shear bond strength 116
3.7.2. Bond durability in acid 119
3.7.2.1. pH 0.6 H_2SO_4/brine environment 120
3.7.2.1.1. Crystalline phase identification-XRD 121
3.7.2.1.2. Elemental mapping-μEDX 123
3.7.2.1.3. ATR-FTIR analyses 126
3.7.2.1.4. Raman imaging 128
3.7.2.2. pH 5.5 $scCO_2$-laden brine environment 129
3.7.3. Corrosion mitigation 129
3.8. Bond strength between composites and granite rock before and after re-adhering 138
3.9. Placement technology of self-healing TSRC composite: Set control and properties of retarded composite 139
3.9.1. MGF-free TSRC 140
3.9.1.1.Compressive strength and its recovery 141
3.9.1.2. Crack sealing, optical microscope and μEDX elemental analyses 142
3.9.1.3. XRD study 145
3.9.1.4. DTG study 148
3.9.1.5. ATR-FTIR study 149
3.9.1.6. Microstructural characterization 152
3.9.1.7. Discussion 153
3.9.2. MGF-modified TSRC 155
3.9.2.1. Micro-calorimetry and HPHT Consistometer studies 155
3.9.2.2. Compressive strength and its recovery 159
3.9.2.3. Sheath-shear bond strength and its recovery 160
3.9.2.4. Corrosion mitigation of CS by composite adhering to CS 161
4. Conclusions 162
5. Impact of work 176

6. Publications and Awards 177
7. Acknowledgements 178
8. References 178

Summary

Under the DOE EERE Geothermal Technologies Office (GTO)-funding project in FY 2016-2018, the scope of work at Brookhaven National Laboratory (BNL) aimed 1) to conduct the screening of qualified candidates for self-healing cement composites reinforced with micro-carbon fiber (MCF), 2) to obtain the fundamental understanding of self-healing mechanism, to develop self-healing aides, 3) to evaluate re-adhering performance of debonded self-healing composites to carbon steel (CS) casing or granite rock formation, 4) to evaluate bond durability of composite/CS joint in acid and thermal shock environments, 5) to assess the corrosion mitigation of CS by composites adhering and re-adhering to CS surfaces, and 6) to investigate the maintenance of pumpability at 85^{o} and 100^{o}C of optimized composite slurry as well as to evaluate self-healing and re-adhering ability of pumpable composite formulation at hydrothermal temperatures, ranging from 270^{o} to 300^{o}C. In this work, three different cementitious material groups, 1) Ordinary Portland Cement (OPC)-based cements, 2) alkali (sodium metasilicate, SMS)-activated cements, and 3) phosphate (sodium hexametaphosphate, SHMP)-bonded cements, were evaluated to meet the following ten material criteria suitable for inorganic cement composites in six different environments, the plain water, alkali carbonate, geo-brine, thermal shock, pH 0.6 H_2SO_4/brine, and pH 5.5 scCO_2/brine:

1) Maintenance of pumpability for >3 hours at 85° and 100^{o}C;
2) Thermal and hydrothermal stability >300°C;
3) Compressive strength >1000 psi, Young's modulus <400 x 10^3 psi, and flexure toughness >0.006 MN/m$^{3/2}$ for cement matrix after 300°C- 24-hr-autoclaving;
4) Sheath-shear bond strength to CS casing and granite rock >100 psi based upon non-confined cement sheath samples surrounding CS tube and granite column cylinder;
5) For defected cements, compressive strength recovery >80% of original strength after self-healing treatments for 5 days;
6) For debonded cements, sheath-shear bond strength recovery >40% of original strength after re-adhering treatments for 5 days;
7) ≥30% higher sheath-shear bond strength than that of OPC/SiO_2 after 6 cycles thermal shock (one cycle, 350°C heating and 25°C water cooling by passing water through inner CS casing);
8) ≥30% higher lap-shear bond strength than that of OPC/SiO_2 after exposure for 30 days in pH 0.6 H_2SO_4/brine at 90°C as well as in pH 5.5 scCO_2/brine at 90°C;
9) ≥50% lower corrosion rate of CS by cement adhered and re-adhered cement to CS than that of OPC/SiO_2 after autoclaving for up to 30 days at 300°C;
10) Cost not to exceed 30 cents/lb (≤5× OPC cost).

In the first OPC material group, there were two composite systems made with Class G/silica flour (SiO_2) and Type I/II clinker with and without SiO_2. The second SMC-activated group encompassed three composite systems, calcium aluminate cement (#80CAC)/Fly ash F (FAF) blend known as thermal shock resistant-cement (TSRC), Fly ash C (FAC)/FAF blend, and granulated blast furnace slag (GBFS)/SiO_2 blend. The third SHMP-bonded calcium aluminate phosphate (CAP) group included two composite systems, #51CAC with low Fe_2O_3 /FAF (denoted as CAP-A) and Fondu CAC with high Fe_2O_3/FAF (marked as CAP-B) blends. TSRC was developed at BNL in FY 2013-2015 GTO-funded project. Since one key factor to an

effective self-healing performance is the control of micro-crack formation, MCF was incorporated into these cementitious groups to create the narrow and shallow cracks.

Two potential cost-effective self-healing technical strategies suitable for high-temperature geothermal well cements were utilized in this work: One was the autogenous-healing technology with the defected cements remedied by the hydration of residual partially- and non-hydrated cement particles and the carbonation of pre-hydrated products; the other one was the autonomic-healing technology due to the reactions of incorporated pozzolan-latent cementitious materials into the composites. In the latter technology, three different pozzolanic groups, 1) natural (zeolites, silica, and clays), 2) industrial by-products (FAC, FAF, and GBFS), and 3) artificial (E-type micro-glass fiber), were employed. The FAF possessed a highly pozzolanic nature, and preferentially reacted with Ca- and Na-based alkaline activators, while, both FAC and GBFS not only displayed pozzolanic nature, but also were capable of self-assembling the cementitious structure in aqueous medium. Thus, like OPC and CAC, the FAC and GBFS also belonged to the former self-healing technology. All composite systems evaluated in this work were designed to have the combination of these two self-healing pathways.

Screening of candidates for self-healing composites

The screening was performed based upon the data of the Young's modulus (YM), compressive strength, and flexure toughness for various composites made in a short-term 1-day curing in plain water, alkali carbonate, and geo-brine environments at 300ºC, the recovery of compressive strength after 5-day self-healing treatment in the same environments, the acid resistance after exposure for 28 days in pH 0.2 H_2SO_4 solution at 90ºC, and 5-cycle thermal shock resistance (one cycle; 350°C-24-hr-healing and quenching in 25°C water). To define the brittleness and softness of composites in a quantitative way, YM was measured and the fracture nature after YM test was categorized in four modes, very brittle (>500 x10^3 psi), brittle (>300-500 x 10^3 psi), moderate (>100-300 x 10^3 psi), and soft (≤100 x 10^3 psi).

Of these composites, the four, OPC, TSRC, CAP-A, and CAP-B, met the mechanical-related material criteria as YM <400 x 10^3 psi, compressive strength >1000 psi, and flexure toughness >0.006 MN/$m^{3/2}$. Although the ranking of compressive strength developed in plain water was in the following order: GBFS/SiO_2 (7060 psi) > FAC/FAF (4450 psi) > OPC/SiO_2 (3130 psi) > CAP-A (2920 psi) > CAP-B (2730 psi) > TSRC (1740 psi), TSRC revealed the highest average strength recovery rate of 94% and only this composite met the material criterion of the recovery rate >80%. In the acid resistance evaluation, three composites, TSRC, CAP-B, and FAC/FAF, as acid-erosion types, displayed the strength recovery rates, ranging from 39 to 48%. In contrast, OPC/SiO_2 and GBFS/SiO_2 as acid-scale corrosion types completely disintegrated. After thermal shock testing, TSRC exhibited the lowest strength reduction of 21%. Consequently, the qualified candidates for self-healing composites were ranked as follows: TSRC > CAP-B> GBFS/SiO_2 and FAC/FAF >OPC/SiO_2.

Self-healing performance for repeatedly cracked composites and fundamental understanding of healing mechanisms

It is possible to assume that when self-healed composites suffered once more from the mechanical stress failure, the failed composites not only develop newly generated cracks in the cement bodies, but also may bring about a reopening of the cracks once closed by self-healing.

To respond to such important concerns, our investigation was centered on whether the self-healed composites still are capable of re-self-healing and reclosing the reopened cracks after repeated stress loadings. As a result, TSRC exhibited an excellent recovery >85% for all 2nd and 3rd cracked composites, initially cured for 1 day, and 78% for 3rd time cracked 10-day-aged composite. More importantly, the average recovery of re-self-healed 3rd time cracked TSRC for 1-, 5-, and 10-day-aged composite was 87%, corresponding to 50% higher than that of OPC/SiO_2. Compared with a plain water environment, the susceptibility of both OPC/SiO_2 and TSRC composites to carbonation obviously assisted in promoting the re-self-healing. The visual observations confirmed the disappearance or partial sealing of cracks in the carbonate environment, clearly verifying that carbonation served as the autogenous healer for both composites.

There are two major factors contributing to strength recovery after healing treatment: One is an adequate sealing and plugging of cracks by reaction and precipitation products; the other is the formation of crystalline and amorphous reaction products and their phase transitions in composite matrix during the treatment period. As for crack generation, the moderate brittle nature of composites had controlled sizes of cracks, ranging from 0.1 to 0.3 mm in width and from 0.1 to 0.7 mm in depth. TSRC showed a great sealing performance of these cracks in 10-day healing treatments in plain water and carbonate. In plain water, the contributors to sealing effect were identified as silica, analcime [$Na_8Al_8Si_{16}O_{48}(H_2O)_8$] and cancrinite [$Na_8(AlSiO_4)_6(CO_2)(H_2O)_2$] as the major crystalline compounds and boehmite (Υ-AlOOH) as the minor one. The cancrinite phase formed through the carbonation of analcime as the original sealing contributor. In a carbonate environment, the major sealing compounds were cancrinite, boehmite, and silica. Unlike in water and carbonate environments, the crack-sealing effect by brine environment was very poor because of the lack of analcime, silica, and boehmite precipitation in cracks. In a composite matrix, two major phases, hydrogrossular [$Ca_3Al_2(SiO_4)_2(OH)_4$] and dmisteinbergite/anorthite feldspar [$Ca(Al_2Si_2)O_8$], were responsible for improving the compressive strength in both water and carbonate environments.

Pozzolan additives as self-healing aides for further improvement of healing ability

Among the pozzolans including two naturals, Clays and zeolites, and one artificial E-type micro-glass fiber (MGF), MGF-modified TSRC composite possessed a great self-reattaching capability of broken fragments to mother composite. There were two potential reasons for this: One was a specific chemistry of modified TSRC to promote the interactions between the fragments and its mother composite; the other was associated with a ductile failure mode; namely, both the fractured piece and defected mother composite sides had a rough surface texture along with high surface contact area, leading to a strong interfacial bonding. Whereas very brittle GBFS/SiO_2 composite disclosed undesirable fractures' surfaces, which were smooth and sharp, thereby resulting in a weak interfacial bonding. On the other hand, ferrierite and clinoptilolite additives as natural zeolite minerals offered the improved self-healing ability of OPC/SiO_2 composites. The outstanding effectiveness of these specific pozzolan additives in further improving the crack sealing and strength recovery were due to the liberation of reactive ionic species by thermo-chemical *in-situ decomposition* of these additives, which resulted in autonomic healing. Similar effect also was observed from an industrial pozzolan, FAF.

Self-healing and crack-sealing ability of 30-day-long cured MGF-modified TSRC composites and in-situ phase transitions

A major character of MGF-modified TSRC composite after 300°C-30-day curing age in plain water was a considerably (nearly 3-fold) increased YM and compressive strength increased by 1.6 times compared with that of 1-day-aged composites, leading to the alterations in mechanical behavior from moderate brittleness to true brittle nature resulting in generation of wider cracks. Correspondingly, the recovery of compressive strength was only 61% compared with 86% recovery of unmodified TSRC at the same curing age. However, MGF conferred a short-term crack sealing efficacy on 30-day-aged composites, compared with that of 1-day-aged one. This fact strongly suggested that the disintegration of MGF in TSRC composite was very slow, thereby ensuring the sealing feasibility at later times. The combination of MGF and FAF pozzolans as autonomic-healing chemical compounds led to the formation of amorphous (CaO, Na_2O)-Al_2O_3-SiO_2-H_2O phase and crystalline cancrinite, carbonated sodalite**,** silica, aegirine [$NaFe^{3+}(Si_2O_6)$], sodium aluminum silicate hydrate ($Na_2Al_2Si_2O_8$ H_2O) and albite ($NaAlSi_3O_8$) phases responsible for crack's sealing. Albite was derived from the following phase transition pathway of dmisteinbergite/anorthite feldspars formed in 1-day-aged composite: feldspars →oligoclase/orthoclase →albite. The matrix in 30-day-aged composite included amorphous (CaO, Na_2O)-Al_2O_3-SiO_2-H_2O phase and crystalline ferrian hydrogrossular [$(Ca_3Al_{2-y}Fe_y(SiO_4)_{3-x}(OH)_{4x}$, $0.2<x<1.5$], non-ferrous hydrogrossular from phase transition of feldspars, iron-magnesium minerals, cancrinite, silica, and boehmite phases. Thus, the lack of strength recovery may be due to the larger cracks and formation of these new iron-related reaction products, but independent of excellent crack sealing efficacy.

Re-adhering performance of debonded self-healing composites to carbon steel (CS) casing and granite rock formation

To determine the re-adhering properties of three MGF-modified composites (OPC/SiO_2, TSRC, and CAP-B) debonded from CS casing, the composite-sheathed CS tube samples were prepared in 300°C- 24-hr-palin water. The unconfined bond-strength tests demonstrated that the biggest strength improvement MGF created in TSRC, leading to the bond strength of 196 psi with MGF vs. 74 psi without the glass. Thus, MGF considerably improved bond strength of TSRC sheath. However, one drawback for such high bond strength was the generation of radial cracks in composite sheath during the bond damage. This fact clearly suggested that further improvement of interfacial bond toughness to alleviate crack development is required for advanced bond performance. Although there is no experimental evidence in this limited work, if the composites are placed between casing and geological formation under the confined condition, the crack-width and- propagation, and micro-separation between casing and composite may be suppressed or minimized. Nevertheless, the 300°C- 5-day exposure of debonded sheath/CS joint samples in water triggered the re-adhering activity of debonded sheaths to CS. Despite the generation of radial cracks, the sheath bond strength of re-adhered TSRC was 97 psi, corresponding to 49% recovery rate. As a result, both MGF-modified and unmodified TSRC composites met material criterion of sheath-shear bond strength recovery >40%. The other tested composites did not meet this material criterion. When the curing time of modified TSRC was extended to 30 days, the sheath bond strength was increased by 1.3-fold to 245 psi. As expected, such excessive sheath bond strength caused the generation of undesirable multi-radial cracks in sheath during the debonding process of composite from CS. Thus, the bond recovery was only 28%, suggesting that re-adhering treatment of 5 days may be insufficient for the adequate strength recovery. On the other hand, MGF-free TSRC exhibited the best bond strength recovery of 49% and 57 % for

1-day- and 30-day-autoclaved composites, respectively, meeting the material criterion of >40% recovery. The bond strength recovery of the 30-day-autoclaved OPC/SiO_2 reference was 38%.

As for the composite/granite rock joint, MGF-modified TSRC composite cured in 300ºC-1-day plain water developed a very high bond strength of more than 300 psi. This fact clearly demonstrated that granite rock surfaces were highly susceptible to reactions with this composite, compared with CS surface. The degree of this susceptibility was directly correlated with the pH of composite slurries. In fact, this modified TSRC with the highest pH resulted in a better adherence to granite than the MGF-modified CAP-B composite with the lowest pH. Nevertheless, only 1 day curing of composites at 300°C was sufficient to establish a great interfacial bonding. Like in the case of composite-sheathed CS tube samples, the excessive sheath bond strength of ≥200 psi for TSRC/MGF and OPC/SiO_2 triggered the development of undesirable multi-radial cracks in their sheaths during the bond testing. However, two alkali-based composites, TSRC/MGF and OPC/SiO_2, revealed a good bond recovery of *>41%* meeting the material criterion after 300°C-5-day re-adhering treatment in plain water, while the recovery of CAP-B/MGF was only 25%.

Bond durability of composite/CS joint in acid and thermal shock environments

The TSRC adhesive between two CS metal plates persisted, preserving the lap-shear bond strength of 80 psi, for 30 days in pH 0.6 H_2SO_4/brine at 90°C, strongly demonstrating great TSRC-CS interfacial bond resistance to strong acid/brine. The results of post-test analyses for TSRC adhesive showed that the crystalline (analcime) and amorphous phases in sodium aluminosilicate-based reaction products played a pivotal role in preserving cement/CS bond for 30 days in this environment after calcium depletion. In contrast, OPC/SiO_2 and GBFS/SiO_2 adhesives caused interfacial bond failure within 20 days of the acid exposure.

As part of the material criteria, the composite sheath was required to withstand the 6-cycle thermal shock stresses (one cycle, 350°C heating and 25°C water cooling by passing water through inner CS casing) for 300ºC-1-day-autoclaved composites. After thermal shock, for TSRC, the sheath-shear bond strength was reduced by 51% to 36 psi. By contrast, the OPC/SiO_2 composite strikingly decreased the bond strength from 34 psi before to 7 psi after the thermal shock, corresponding to nearly 80% reduction. In contrast, GBFS/SiO_2 sheath encountered catastrophic bond failure after the first thermal cycle. Thus, TSRC possessed a great thermal shock durability and met the material criterion of possessing ≥30% higher sheath-shear bond strength than that of OPC/SiO_2 reference composite after thermal shock testing.

Corrosion mitigation of CS by composites adhering and re-adhering to CS surfaces

One important question that must be asked is how well the composite layers adhering and re-adhering to the CS surfaces protect the CS against brine-caused corrosion. To answer this question, we needed a better understanding of the interfacial bond failure modes at CS plate/composite adhesive/CS plate lap joints. Next, we evaluated the ability of re-adhered composites made under the original curing conditions to further improve the corrosion mitigation of CS.

The most desirable bond failure is cohesive failure when the bond strength of composite to CS is higher than that of the composite itself. For the 300ºC-1-day cured CS plate/ composite adhesive/CS plate join samples, all alkali-activated composites including TSRC, FAC/FAF,

GBFS/SiO_2 and phosphate-reacted CAP-B composite failed cohesively, whereas OPC-based composites like OPC/SiO_2 and FlexCem/SiO_2 revealed the mixed modes of adhesive and cohesive failure. For MGF-modified composites the lap-shear bond strength was similar in water and carbonate environments and could be ranked in the following order according to the average bond-strength value: GBFS/SiO_2 (230 psi) > TSRC (210 psi) > FAC/FAF (175 psi) > CAP-B (160 psi) > OPC/SiO_2 (80 psi) > FlexCem (50 psi). For the long-term (30 days) cured samples, the test results were similar; the very high lap-shear bond strength of almost 300 psi was measured for MGF-modified TSRC. This bond strength value was 1.3- and 3.3-fold higher than that of unmodified TSRC and OPC/SiO_2 references, respectively.

When the micro-separation of composite sheath from CS casing takes place at composite/CS joints, there are two important questions regarding the debonded composite layers that remained on entire surface of CS: One is how well the remaining composite protects CS against brine-caused corrosion; the other is related to the corrosion protection of CS after the composite re-adherence. For the latter, using the debonded CS plate samples after lap-shear bond test, the study was directed towards the evaluation of the effectiveness of the additional composite layers, superimposed on the composite remaining after the de-bonding, in further enhancing the corrosion protection of CS. The corrosion rate of CS protected by MGF-free composites was: OPC/SiO_2 (0.68 mm/year) > CAP-B (0.56 mm/year) > TSRC (0.36 mm/year). The incorporation of MGF led to the reduction of corrosion rate for all composites, compared against that of MGF-free composites, strongly demonstrating that MGF conferred the improved protection of CS against corrosion. Particularly, the lowest corrosion rate of 0.18 mm/year was determined for TSRC. A further reduction (0.16 mm/year) of the corrosion rate was observed for CS with the re-adhered TSRC/MGF composites. This reduction was due to the presence of a new re-adhered composite layer superimposed on the pre-existing composite layer, importantly suggesting that the thickness of composite layers covering CS increased by the re-adhering treatment. For the CS/TSRC composite joint samples pre-cured for 30 days had a much greater CS coverage than those of 1-day-cured ones, corresponding to nearly 2.4-fold increased thickness which provided a better protection of CS against corrosion. Furthermore, after the re-adhering treatment, the thickness of the re-adhered composite somewhat increased to 0.32 mm from 0.28 mm before re-adhering resulting in a further reduction of corrosion rate to 0.13 mm/year, underscoring that although the interfacial debondement for 30-day-aged composites occurred, the remaining composites adhering to CS surfaces provided an excellent corrosion protection of CS against corrosion. By contrast, OPC/SiO_2 not only did not show any singes of change in thickness after the re-adhering treatment, but also did not have any improvement in corrosion protection; the corrosion rate increased from 0.59 to 0.64 mm/year after the re-adhering treatment.

Maintenance of pumpability at 85^o and 100^{o}C of optimized composite slurry as well as evaluation of self-healing and re-adhering ability of pumpable composite at hydrothermal temperatures, ranging from 270^o to 300^{o}C

Commonly, the pumping time between 3 and 6 hrs may be expected for hot geothermal wells. The retarder added to slow down cement hydration and reactions of slurry components must provide controllable, predictable pumping time of the slurry without compromising development of cement mechanical properties after the set. This task focused on evaluating the pumpability, self-healing, re-adhering, and corrosion mitigation of the retarded TSRC/MGF composite

formula, modified with D-(-)-tartaric acid (TA) as the best candidate for retarding hydration of TSRC slurries.

As a result, TA confirmed its good performance with MGF-modified TSRC slurries. In fact, using HPHT consistometer, a thickening time of more than 5 hours was achieved at 100^{o}C bottom-hole-circulating temperature. Furthermore, the slurry sensitivity to temperature variations was lower than normally expected for OPC-based slurries. However, although the maintenance of pumpability for this optimized formula was very promising, an additional study will be required for evaluation of pressure and retarder content effects on thickening time, as well as, to confirm timely compressive strength development in retarded slurries.

Regarding the self-healing, re-adhering, and CS corrosion protecting properties of TA-retarded MGF-modified TSRC, the role of TA in self-healing behavior can be described as follows: The lower Ca content-associated crystalline phases including zeolite-type minerals and boehmite were preferentially formed in TA-modified cement. Importantly, the subsurface areas and the matrix were more likely to be assembled by (CaO, Na_2O)-Al_2O_3-SiO_2-H_2O amorphous phases, rather than crystal ones. This amorphous phase contributed to strength recovery and fracture sealing. The superior strength recovery and crack sealing in carbonate environment strongly suggested the importance of carbonate compounds in the healing process. Furthermore, TA served in the creation of the crack-plugging reaction products in this environment. Ca and Na cations removal through binding to TA and carbonates at early hydration times seems to help strength recovery and crack sealing possibly through the formation of Na_2O-CaO-Al_2O_3-SiO_2 gel consisting of network structure, crystallization of carbonated compounds and tobermorite in alkali carbonate. Silica also assisted in sealing the cracks.

Like TA-free composite, TA-retarded composites displayed a very high sheath bond strength of nearly 200 and 252 psi for 300^{o}C-1-and -10-day-cured composite/CS joint samples, thereby resulting in the generation of undesirable multi-radial wide cracks in the composite sheath during bond-test procedure. Thus, there is a requirement to improve the toughness of interfacial bonding by advanced reinforce composite technology leading to the creation of re-adherable crack formation attributed to minimum number of thin cracks.

As for the corrosion protection of CS by these adhesive layers covering CS surfaces, three findings can be described: 1) there was no significant difference in protection between retarding and non-retarding adhesives; 2) the re-adhered adhesive layers displayed a better protection of CS than that of before re-adhering treatment; and, 3) re-adhered 10-day-age adhesives provided the lowest corrosion rate of 0.12 mm/year for both retarding and non-retarding, responding to 33% reduction of corrosion rate compared with that of before re-adhering treatment.

Consequently, although a real field application of this upgraded TSRC composite is contingent upon its scale-up validation, these advanced properties will bring the following potential benefits: 1) Extension of CS-based casing's lifecycle; 2) reduction of capital cost by replacing corrosion-resistant expensive alloys with inexpensive CS-based materials; 3) considerable reduction of well operation and maintenance costs by eliminating expensive well abandonment, remedy-and repairing-operations including re-drilling and re-cementing for catastrophically damaged well structure after cement's failure, and 4) decrease in cement material cost due to the use of cost-effective industrial by-products as pozzolanic cement. Consequently, the upgraded

well cement composites will contribute to some reduction of the levelized cost of electricity (LCOE) generated from geothermal power stations.

1. Introduction

In hostile geothermal environments containing hypersaline brine, CO_2 and H_2S at temperatures >250°C, the well cement sheath between the casing string and rock/clay formation encounters variable mechanical-and chemical-stresses that can lead to micro-annuli and cracks, increased cement permeability, cement debondement from metal casing and formation, casing corrosion by geothermal fluids migrating through defected cement sheath and compromised zonal isolation [1–5]. Repairs of well cements are complicated, costly and sometimes impossible since the cement failure locations are challenging to find, to reach and to repair correctly.

Self-healing concepts of cement matrix

The one economical way to alleviating this concerns is to develop the cost-effective self-healing technology of defected cements in attempt to recover cement's original properties without human intervention, to prolong the cement's service-life cycles, to assure the longevity of wellbore integrity, and to avoid the abandonment of collapsed wells. There are several technical strategies for developing the self-healing cements in the building and construction as well as oil and gas industries at temperatures, ranging from 20° to 140°C. Among the major strategies, the autogenous- and autonomic-healing technologies may be suitable to geothermal cements facing high-temperature hydrothermal environments. The former strategy is directly related to the hydration of residual non-hydrated and partially hydrated cement particles by permeation of water through micro-annuli or cracks, and to the carbonation of hydrated products. The hydration and carbonation reaction products would grow as amorphous and crystalline phases and precipitate on the defected surfaces to plug and seal an opening crack spaces [6,7]. The characteristic of the latter strategy is to incorporate the pozzolan-latent cementitious materials [8–10], granulated blast furnace slag (GBFS) [11], silica fume [12], and montmorillonite [13] as healing aids into the cements; when siliceous and/or siliceous-alumina components in these pozzolans come in contact with Ca and Na ion-containing water at high pH, they initiate pozzolanic reactions with alkali solutions to form the amorphous and crystalline calcium silicate-, calcium aluminosilicate-, sodium aluminosilicate-, and calcium, sodium aluminosilicate-hydrates, which provide plugging and sealing of the cracks.

The aluminosilicate-based pozzolans can be categorized in two major groups [14]: One is natural type encompassing zeolites, metakaolin, and clays; the other is artificial ones like Class C or F fly ashes and GBFS as industrial by-products. Class F fly ash (Fly ash F, FAF) has a highly pozzolanic nature and reacts with excess of Ca- and Na-based alkaline reactants, while both the Class C fly ash (Fly ash C, FAC) and GBFS not only possess pozzolanic nature, but also are capable of self-assembly to cementitious structure in aqueous medium. Among the natural pozzolans, zeolites have abundant natural resource worldwide. In the United Sates, U.S. Geological Survey [15] estimated reserve of zeolite minerals, involving heulandite-type zeolites (heulandite and clinoptilolite), chabazite, erionite, mordenite, and phillipsite, at 120 million tons in near-surface deposits, while the total resource of zeolite-rich deposits may be as high as 10 trillion tons. In 2014, of 67,600 metric tons produced, 65,400 metric tons were consumed commercially. Further, zeolites were relatively inexpensive material, ranging in price from $0.023 to 0.36/lb, and they have a high potential for substitution of cement, gypsum, bentonite,

montmorillonite, peat, perlite, and silica sand in civil engineering fields. In fact, during the past decade, their applications in replacing cement increased.

Regarding zeolite chemistry, as well documented [14,16–23], the natural zeolite minerals, particularly clinoptilolite [$(Na,K,Ca)_{2\text{-}3}Al_3(Al,Si)_2Si_{13}O_{36}.12H_2O$] and ferrierite [$(Na,K)_2Mg(Si,Al)_{18}O_{36}(OH).9H_2O$], containing plenty of pozzolanic siliceous or siliceous-aluminous reactants can be used to totally or partially substitute Ordinary Portlander Cement (OPC). In this case, the pozzolanic reaction of clinoptilolite and ferrierite is initiated by blending it with the $Ca(OH)_2$-forming alkaline reactants like lime and OPC. Zeolites are crystalline hydrated aluminosilicate minerals and their structure is characterized by three-dimensional oxygen-linked $[SiO_4]^{4-}$ and $[AlO_4]^{5-}$ tetrahedral frameworks containing ion exchangeable counterbalanced cations (Na^+, K^+, and Ca^{2+}) and water molecules situated in their micropores and channels [24,25]. Some authors [26–28] also stated that substantial amount of Fe counter-cation is intercalated into the crystalline lattice of zeolite. When zeolite interacts with Ca^{2+} and OH^- liberated from lime and OPC in aqueous media, its aluminosilicate frameworks are disintegrated by the attack of OH^- that leads to alkali dissolution of zeolite and creates $[SiO(OH)_3]^-$ and $[Al(OH)_4]^-$ reactants. Next, these reactants bind with Ca^{2+}, leading to the formation of calcium silicate and calcium aluminosilicate hydrates as cementitious products [29].

Compared with the properties of OPC-based cements, such pozzolan cements have the following advantages: Improved resistance to sulfate-caused erosion, minimized water permeability, and elimination of the calcium silicate-related swelling hydrogel brought about by interfacial reactions between $Ca(OH)_2$ and amorphous or poorly crystallized silica phases in aggregates, thereby mitigating an undesirable expansion-caused failure of concrete. On the other hand, there are two major drawbacks: One is slow development of early strength; the other - increased water demand for accomplishing adequate slump of fresh concrete. In dealing with these drawbacks, over more than three decades, several different processing techniques involving ultra-fine pulverization [30,31], thermal-, hydrothermal-, and acid-treatments [32–35], and chemical method [36] have been employed to enhance the reactivity of pozzolans. The efficacy of these treatments in enhancing pozzolanic reactivity of clinoptilolite was due to the extraction of Al from clinoptilolite (dealumination) caused by the breakage of aluminosilicate structure, thereby resulting in a loss of crystallinity and conversion of crystal into amorphous phases. Correspondingly, Si/Al ratio of clinoptilolite significantly increases after the treatments [37–41]. Nevertheless, among these processing techniques, Shi et al. described that the most effective one was the chemical method using Na_2SO_4 and $CaCl_2$ activators [42].

On the other hand, the use of fly ashes and GBFS as industrial by-products for building the cementitious matrix would benefit the environment while offering cost-effective solutions by eliminating the use of Ordinary Portland Cement (OPC), which emits 0.9 metric tons of CO_2 and a great deal of mercury for every ton of OPC manufacturing [43–45]. In our previous study aimed at improving the thermal shock resistance of well cements, Brookhaven National Laboratory (BNL) developed cement systems consisting of refractory calcium aluminum cement (CAC), Class F fly ash (Fly ash F, FAF), and sodium metasilicate (SMS) as alkali activator. Particularly, FAF in this cement known as Thermal Shock-Resistant Cement (TSRC) further improved the thermal shock resistance of refractory CAC to coop with large temperature variations in geothermal wells [46,47]. In fact, TSRC demonstrated good thermal- and hydrothermal-stabilities at >300°C, and the retention of compressive strength of >6.89 MPa after

five superheating-cooling cycles (one cycle: 500°C heat for 24 hrs followed by 25°C water-quenching). FAF initially played an important role in packing and densifying the first binding phases of CAC hydrates at an early curing stage. Subsequently, the dissolution of FAF by the alkaline activators, followed by the pozzolanic reactions, led to the formation of a binding phase, an amorphous (Na_2O- or/and CaO)-Al_2O_3-SiO_2-H_2O gel. The reactions of FAF were slow, while the CAC hydration was fast assuring the early strength development. Such slow pozzolanic reactions of FAF may ensure that non-reacted and partially-reacted FAF remains intact in TSRC and reacts later when geo-fluids permeate through the cracks of damaged cement. These reactions may convert FAF into cementitious structure contributing to the sealing and plugging of opened cracks in damaged TSRC.

As for GBFS, our previous GTO project assessed the potential of alkali-activated GBFS as acid-resistant geothermal well cement [48]. The 200°C-autoclaved GBFS displayed an outstanding compressive strength of more than 11000 psi and a minimum water permeability of less than 3.0 x 10^{-5} Darcy. The combination of crystalline calcium-silicate-hydrate (CaO-SiO_2-H_2O, C-S-H) and tobermorite phases was responsible for developing such high compressive strength and densifying the cement structure. However, elevating autoclave temperature to 300^{o}C engendered an excessive growth of well-formed tobermorite and xonotlite crystals and the elimination of C-S-H phase, thereby resulting in the creation of undesirable porous microstructure along with the reduction of strength and increased water permeability. Nonetheless, we evaluated the susceptibility of these calcium silicate-based phases formed at 200^o and 300^{o}C to reactions with CO_2-laden H_2SO_4 solution at pH 1.1 at 90^{o}C. All calcium silicate phases were very sensitive to H_2SO_4 solution, causing the precipitation of bassanite ($CaSO_4.1/2H_2O$) scales as cement's acid-reaction and-erosion products over cement's surfaces. Nevertheless, among these calcium silicate hydrates, the most acid erosion-resistant phase was C-S-H formed at 200^{o}C. Interestingly, after partial Ca removal from C-S-H phase by H_2SO_4, these phase beneath the bassanite scale layer preferentially reacted with the Mg ions liberated from alkali-dissolved GBFS to form lizardite [$Mg_2Si_2O_5(OH)_4$] crystals. The formation of lizardite not only retarded the rate of acid erosion, but also allowed retaining the integrity of cementitious structure. In contrast, acid-eroded tobermorite and xonotlite phases did not form any crystalline MgO-containing phases. Thus, 200^{o}C-made GBFS had a potential as a very high strength and acid-resistant geothermal well cement.

The calcium aluminate phosphate (CAP) cement is among the commercially available high-temperature geothermal well cements [49]. It was originally developed by BNL as wet carbonation-resistant cement [50]. Unlike TSRC and OPC, the CAP, called chemically phosphate-bonded cement, was prepared through three-step reaction pathways in hydrothermal environment: First step was hydrolysis of sodium hexametaphosphate (SHMP) as reactant and CAC as counter-reactant; second one was chemical reactions between SP and CAC; and final step was hydration of reaction products. Correspondingly, the pH value (8.5-9.5) of CAP slurry quite differed from TSRC and OPC slurries with pH >13. The assembled CAP was composed of two major crystalline reaction products, hydroxyapatite, $Ca_5(PO_4)_3(OH)$ and boehmite, which were responsible for strengthening and densifying the cementitious structure. When FAF was incorporated into CAP, the free Na ion dissociated from SP favorably reacted with aluminosilicate in FAF to form analcime at late cement curing age. As for the self-healing behaviors of CAP/FAF blend cement, no study was made thus fur.

Earlier studies with construction cements demonstrated that one key factor for a successful self-healing process is the size of the cracks. The cracks that heal in short periods of time under ambient conditions are typically below 60 μm in width [51,52]. For evaluation of self-healing performance, designing fractures of controlled size is essential. To achieve controlled micro cracks in cementitious materials, various fibers are commonly added to the cement formulations [53–56]. In our work to improve the toughness of TSRC [57,58], the micro-carbon fiber (MCF) moderately reacting with the cement matrix was identified as the most effective high-temperature reinforcing additive that significantly enhances compressive toughness, provides excellent bridging, controlling crack development and propagation, and suppressing the post-stress cracks' opening.

Furthermore, there are two important considerations for self-healing cements: One is a re-self-healing capability of previously healed cement after repeated damages; the other is the life-span of the healing aids.

Re-adhering concepts of cement debonded from metal casing and rock formation

The other important consideration governing geothermal well integrity is the requirement of adequate bond durability at interfaces between cement and metal casing or rock formation. Our previous work on cement/metal joint system demonstrated that two factors played a pivotal role in improving the adhesive force of 300°C-autoclaved MCF-modified TSRC and CAP composites to carbon steel (CS) casing and creating a tough interfacial bond structure at the composites/CS joints under the 7-cycle 350°C heat $\rightarrow$ 25°C water cooling-induced tensional stresses [59,60]. One factor was the fact that Fe-containing interfacial reaction products formed in the critical boundary regions between TSRC or CAP and CS; in particular, the crystalline brownmillerite [$Ca_2(Al, Fe^{+3})_2O_5$] phase in TSRC and ferrowyllieite [$Na_2Fe_2Al(PO_4)_3$] phase in CAP. The quantity of brownmillerite and ferrowyllieite chemical reaction products between composites and CS increased with the extension of the number of heat-cooling thermal tensional stress cycles, thereby resulting in the enhanced coverage of CS surfaces by the composites adhering to CS after shear bond testing. This fact strongly suggested that the adhesive force of composites to CS was greater than the strength of the composite itself. The other factor was a great effect of MCF present in this composites on enhancing the shear bond tensile extension by more than two-fold, compared with that of the cements without MCF, highlighting that MCF played a pivotal role in significantly improving the bond durability between composite and CS. By contrast, the 300°C-autoclaved Class G/SiO_2 blend consisting of xonotlite, and 0.9 nm-tobermorite and –riversideite, as the major crystalline reaction products, had no significant effect on improving the shear bond strength and the bond's toughness. No chemical interaction product with CS was found in the cement adhered to CS.

However, although the cement possessed good bond durability, the extreme thermal and mechanical stresses generated in cement/casing interfacial boundary regions often raised concerns about the debondement of cement from casing surfaces. Such interfacial bond failure not only engendered a lack of well casing integrity, but also promoted the corrosion of casing [4,5,61]. An ideal solution for this issue would be self-re-adherence of debonded cement to casing. In this case, well integrity would be restored, and casing's corrosion alleviated.

In addition to the internal healing processes in cement, some researchers studied the healing potential of products formed by interactions between failed cements and chemical reactants

present in the environments [62–67]. The subterranean geothermal environments offer some special conditions for cement self-healing. Particularly, when the defected cements are exposed to reactive cations-and anions-rich fluids, these ionic reactants may participate in promoting self-healing; for instance, carbonate ions (CO_3^{2-}) lead to the carbonation of cement, following by precipitation of carbonate compounds which make it possible to seal and plug the opening cracks in the defected cements. Further, such ionic chemical reactions will be accelerated by elevated environmental temperatures. Importantly, it should be noted that since cements are placed in the confined annular spaces between casing and geological formation, such confined conditions might help in alleviating some damages of cement sheath brought about by thermo-physicochemical stresses.

Based upon the information described above, the objective of this project was to develop self-healing and re-adhering inorganic geothermal well cements possessing the hydrothermal- and thermal stability of ≥300°C, the resistance to mechanical and thermochemical stresses, and the protection of carbon steel-based casing against brine-caused corrosion as well as to gain the fundamental understanding of self-healing and re-adhering mechanisms for defected cement matrixes and debonded cement layers from CS casing and rocks. Thus far, there are no scientific and technical information on high temperature self-healing and re-adhering cementitious materials. Thus, the understanding of healing mechanisms not only has a high scientific merit in the field of high temperature cements, but also provides engineering knowledge leading to the design of the sustainable well cement structures. Furthermore, the project success offers the extended life-cycle of well integrity, the reduction of well operation and maintenance costs due to the elimination of expensive remedy-and repairing-operations including re-drilling and re-cementing for the catastrophically damaged well structure after cement's failure. Subsequently, the levelized cost of electricity (LCOE) generated from geothermal power stations may be reduced.

The following seven-step technical approaches to achieve this project goal were taken: The step 1 was to evaluate self-healing performance of various different cement systems made by short-term autoclaving for up to 10 days in four different environments such as water, alkali carbonate, acid, and hypersaline brine; step 2 was to screen the candidates for appropriate self-healing cement systems based on the information obtained from step 1; step 3 was to develop the self-healing aids for further improvement of self-healing ability of screened cement systems; using the optimized formulas gained from the results in steps 2 and 3, step 4 was to study the re-adhering performance of selected formulas to CS and rock formation; step 5 was to assess the ability of re-adhered cements to protect CS against brine-caused corrosion; step 6 involved the self-healing and re-adhering performance evaluations of cements prepared by long-term autoclaving for 30 days; and the final step was pertinent to the development of set-controlling additive for preparing the field-applicable cement slurry possessing the pumpability for at least 3 hours at 85°C, and following by obtaining the information on the self-healing, re-adhering, and corrosion protective abilities of cements modified with this additive.

From the outset, certain criteria were specified and served as guidance, setting minimum acceptable values. These ten-target criteria are listed below.

1) Maintenance of pumpability for >3 hours at 85°and 100ºC.
2) Thermal and hydrothermal stability >300°C.

3) Compressive strength >1000 psi, Young's modulus <400 x 10^3 psi, and flexure toughness >0.006 $MN/m^{3/2}$ for cement matrix after 300°C- 24-hr-autoclaving.
4) Sheath-shear bond strength to CS casing and granite rock >100 psi based upon non-confined cement sheath samples surrounding CS tube and granite cylinders.
5) For defected cements, compressive strength recovery >80% of original strength after self-healing under the conditions of the initial curing for 5 days.
6) For debonded cements, sheath-shear bond strength recovery >40% of original strength after re-adhering under the conditions of the initial curing for 5 days.
7) ≥30% higher sheath-shear bond strength than that of OPC/SiO_2 after 6 cycles of thermal shock (one cycle, 350°C heating and 25°C water cooling by passing water through inner CS casing)
8) ≥30% higher lap-shear bond strength than that of OPC/SiO_2 after exposure for 30 days in pH 0.6 H_2SO_4/brine at 90°C as well as in pH 5.5 $scCO_2$/brine at 90°C.
9) ≥50% lower corrosion rate of CS protected by cement adhered and re-adhered to CS than that of OPC/SiO_2 after autoclaving for up to 30 days at 300°C.
10) Cost no higher than 30 cents/lb (≤5× OPC cost).

Utilizing two self-healing strategies, the autogenous- and autonomic-healings, the R&D work at BNL concentrated on three major cement systems (Figure 1); 1) OPCs including Class G well cement and Type I/II OPC clinker, 2) alkali-activated cements (AACs) made with SMS as alkaline cement-forming reagent, and 3) CAP cements made with SHMP as phosphate reaction cement-forming reagent. These cement systems were modified with pozzolan reactants. As seen in Figure 1, pozzolans were categorized in three different groups, natural-, industrial by-, and artificial-products. The natural products involved zeolites, silica flour (SiO_2), and clays, and the industrial by-products encompassed FAF with pozzolanic-cementing property, and FAC and GBFS possessing both pozzolanic-cementing and self-cementing properties, while the E-type micro-glass fiber (MGF) was adapted as an artificial pozzolanic product. The zeolite, clay, and MGF were used as additives and evaluated as self-healing aids.

In AACs, three different cements were tested. Among them were TSRC consisting of CAC and FAF; FAC/FAF blend; and, GBFS/SiO_2. All these cements were activated with SMS. In CAP cements, CACs with low- and high-Fe_2O_3 content were employed as counter reactants of SHMP. These CACs also were blended with FAF. To suppress and control size of the cracks' in damaged cements, the MCF was incorporated into all blends as a high-temperature reinforcement material. Thus, all cementitious materials designed in this project can be classified as MCF-reinforced composites.

Finally, to establish the field-applicable formula, we developed the cement-set retarder suitable for potential self-healing and re-adhering cements.

2. Experimental Procedure

2.1. Starting Materials

The five cement binders (Figure 1), Secar #80-, Secar #51-, Fondu-CACs, Class G and Type I/II clinker as OPCs, were used in this study. All CACs were supplied by Kerneos Inc, while Schlumberger and Trabits group provided Class G well cement and Type I/II clinker, respectively. The X-ray powder diffraction (XRD) data showed that the crystalline compounds

of #80 CAC were the following three principal phases, calcium monoaluminate ($CaO.Al_2O_3$, CA), calcium dialuminate ($CaO.2Al_2O_3$, CA_2) and corundum (α-Al_2O_3); #51 CAC had CA as its dominant phase, coexisting with gehlenite [$Ca_2Al(Al,Si)_2O_7$] and corundum as the secondary components, while Fondu included CA as the major phase, and mayenite ($12CaO.7Al_2O_3$, $C_{12}A_7$), calcio-olivine ($2CaO.SiO_2$, C_2S), ferrites ($MgFe_2O_4$), and hematite (Fe_2O_3) as minor phases. The Class G and Type I/II clinker consisted of hatrurite ($3CaO.SiO_2$) as major, and brownmillerite ($4CaO.Al_2O_3.Fe_2O_3$), basanite ($CaSO_4.1/2H_2O$) and periclase (MgO) as minor phases for the former cement, and hatrurite ($3CaO.SiO_2$) as the major and larnite ($2CaO.SiO_2$), brownmillerite ($4CaO.Al_2O_3.Fe_2O_3$), and portlandite [$Ca(OH)_2$] as minor phases for the latter one. Among the cement-forming constituents, SMS (Na_2SiO_3), alkali-activating powder, of 93% purity, with the particles' size of 0.23- to 0.85-mm, trade named "MetsoBeads 2048," was supplied by the PQ Corporation. It had a 50.5/46.6 Na_2O/SiO_2 weight ratio. SHMP [$(NaPO_3)_6$, 60-70% P_2O_5] phosphate chemical reactant with 200 mesh granular was obtained from Sigma-Aldrich. In the pozzolans, two natural zeolites, Ferrierite [$(Na,K)_2Mg(Si,Al)_{18}O_{36}(OH).9H_2O$, FER] and Clinoptilolite [$(Na,K,Ca)_2$-$3Al_3(Al,Si)_2Si_{13}O_{36}.12H_2O$, Clin.] with a mean particle size of 24 µm, were provided by Trabits group, while silica flour was supplied by U.S. Silica Company. Three types of natural clays, bentonite, montmorillonite [$(Na,Ca)_{0.33}(Al,Mg)_2(Si_4O_{10})(OH)_2 \cdot nH_2O$], and metakaolin ($Al_4Si_2O_{10}$), were obtained from Sigma-Aldrich. Among the three industrial by-products, FAF, FAC, and GBFS, the first two products were supplied by Boral Material Technologies, and GBFS was manufactured by Lafarge North America Inc. The XRD analysis for these by-products revealed that FAF included three major crystalline phases, quartz (SiO_2), mullite ($3Al_2O_3.2SiO_2$), and hematite (Fe_2O_3), and FAC also included three major phases, tricalcium aluminate ($3CaO.Al_2O_3$, C_3A), quartz, and calcium sulfate anhydrate ($CaSO_4$); meanwhile, GBFS was essentially amorphous. The artificial pozzolanic product, powdery E-type MGF (Microglass 7280) with fiber diameter of 16 µm and length of 120 µm was supplied by Fibertec. The oxide composition of this MGF as aluminum-lime silica system determined by energy-dispersive X-ray (EDX) analysis was as follows: 55.0wt% SiO_2, 28.6wt% CaO, 11.4wt% Al_2O_3, 2.8wt% MgO, 0.9wt% Fe_2O_3, 0.7wt% TiO_2, and 0.6wt% Na_2O.

Table 1 shows the proportion of oxide compounds present in these OPC-, CAC-, and pozzolan-based starting materials determined by EDX.

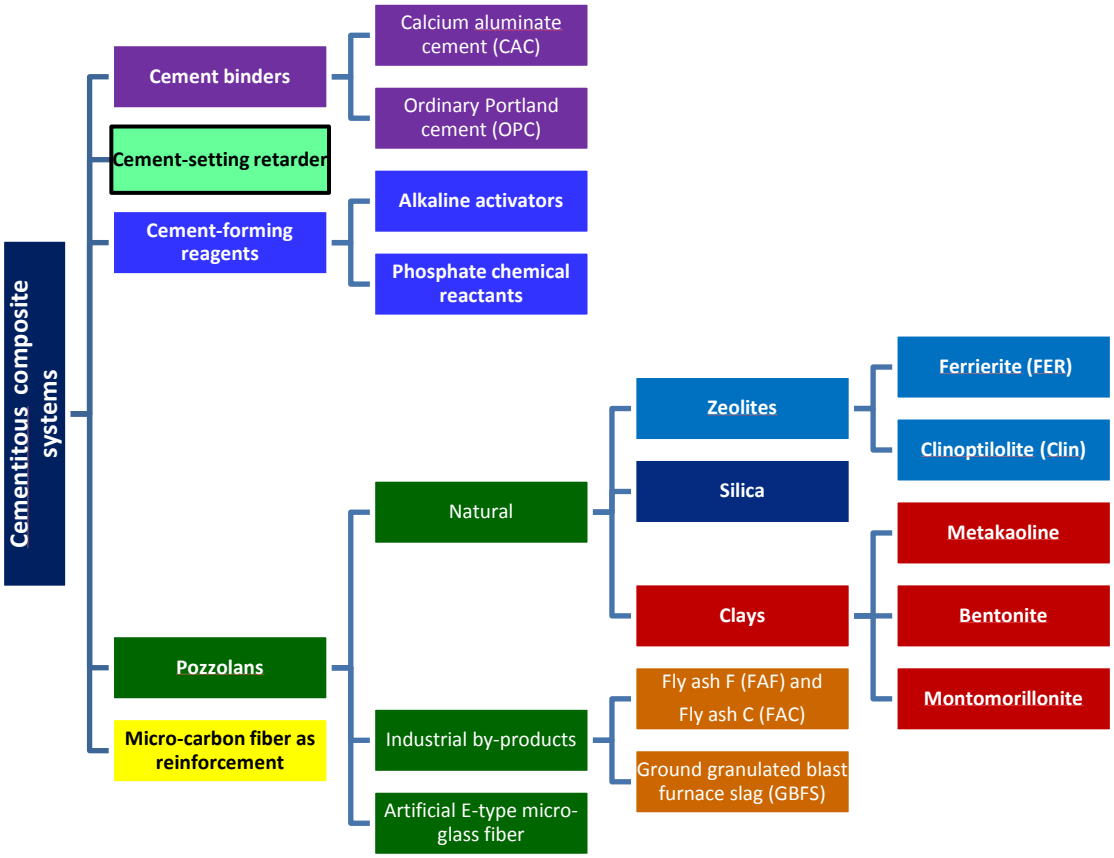

Figure 1. Diagram of cement composites used in the study and assembled from the combinations of cement binder, cement-forming reagent, pozzolan, reinforcement, and cement-setting retarder.

Table 1. Oxide compositions of these starting materials

Component	Oxide composition, wt%								
	Al_2O_3	CaO	SiO_2	Fe_2O_3	Na_2O	K_2O	TiO_2	MgO	SO_3
Class G cement	3.0	67.6	18.4	3.9	0.3	1.3	-	-	5.5
Type I/II	5.2	65.0	20.3	3.2	0.2	1.0	-	2.6	2.5
CAC, #80	75.2	24.7	-	0.1	-	-	-	-	-
CAC, #51	45.1	49.7	-	2.8	-	-	2.4	-	-
*CAC, Fondu	37.5-41.0	35.5-39.0	3.5-5.5	13.0-17.5	-	-	<4.0	<1.5	-
FAF	35.0	2.7	50.1	7.1	0.30	3.1	1.6	-	-
FAC	19.9	26.7	38.7	7.0	1.8	0.5	-	3.6	1.8
GBFS	12.9	38.6	35.3	1.1	-	-	0.4	10.7	1.0

*Product data sheet, reference FC-CF-GE-GB-LAF-032007, Kerneos

To improve the compressive toughness, and suppress and control the post-stress cracks' opening and crack width, MCF (AGM-94) derived from a polyacrylonitrile (PAN) precursor was supplied by Asbury Graphite Mills, Inc. It was 7-9 μm in diameter and 100-200 μm in length, and their visual appearance was a powder-like product.

The ASTM A-513 carbon steel (CS) tubes [125-mm-long x 25-mm-outer diam. x 3-mm-wall thickness] obtained from Aladdin Steel Inc. were used for the cement composite sheath samples surrounding the CS tubes. The AISI 1008 cold rolled steel test panel according to ASTM D 609C was supplied by ACT Test Panels, LLC and used for lap-shear bond tests. Alkaline cleaner #4429, supplied from American Chemical Products, was used to remove all surface contaminants from CS. This cleaner was diluted with deionized water to prepare 5 wt% cleaning solution.

The granite rock cylindrical column (125-mm-long x 25-mm-diam.) was provided by Gem Marble & Granite Corp (New York, USA) and was used to prepare the composite-sheathed granite column samples.

The D-(¯)-tartaric acid (TA) supplied by Sigma-Aldrich was evaluated as a set-control additive for cementitious composite slurry at 85° and 100°C circulating temperatures.

2.2. Formula of cements used for evaluation

As a starting point of this project, five different cement hydrate systems listed below were evaluated as potential candidates for self-healing cements.

1. OPC (Class G or Type I/II clinker)/Silica flour system (OPC/SiO_2): CaO-SiO_2-H_2O;
2. SMS-activated #80 CAC/FAF system (TSRC): Na_2O-CaO-Al_2O_3-SiO_2-H_2O;
3. SMS-activated FAC/FAF pozzolanic cement blend system (FAC/FAF): Na_2O-CaO-Al_2O_3-SiO_2-H_2O;
4. SMS-activated GBFS/ Silica flour system (GBFS/SiO_2): Na_2O-CaO-MgO-Al_2O_3-SiO_2-H_2O;
5. SHMP-chemically bonded #51 CAC or Fondu CAC/FAF system (CAP-A or CAP-B): Na_2O-P_2O_5-CaO-Al_2O_3-SiO_2-H_2O.

All cements were prepared as dry blend cement mixtures prior to mixing them with water. The OPC/SiO_2 system, Class G cement or Type I/II clinker/silica flour blend contained 70wt% OPC and 30wt% SiO_2. In TSRC [46], the #80/FAF ratio of 60/40 by weight was adapted, and SMS alkali activator of 6% by total weight of this dry blend was incorporated into the #80/FAF blend. The same amount of SMS also was used for two other alkali-activated cements, FAC/FAF and GBFS/SiO_2. In FAC/FAF system, to prepare the most desirable formula, the cements with FAC/FAF ratios of 100/0, 80/20, 60/40, and 40/60 by weight were prepared by hand-mixing slurries, leaving them overnight at room temperatures, then autoclaving samples for 24 hours at 85°C and 24 more hours at 300°C (for more details see “Samples preparation”). After that, the compressive strength of autoclaved cements was determined (Figure 2). As a result, we adapted the 60/40 FAC/FAF ratio blend that developed the highest compressive strength. Likewise, the best formula of GBFS blend with SiO_2 or FAF was selected from the results of compressive strength tests of samples made with 70/30 GBFS/SiO_2, and 100/0, 80/20, 60/40, and 40/60 GBFS/FAF ratios. All the samples were prepared in the same manner as FAC/FAF samples. Figure 3 shows the compressive strength of the tested GBFS blends. The highest strength of nearly 7000 psi was obtained for 70/30

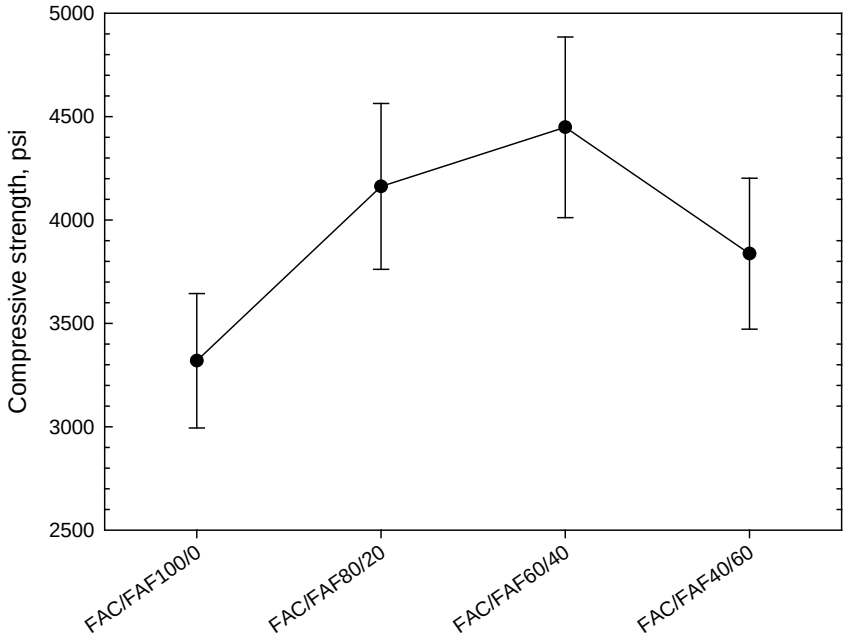

Figure 2. Compressive strength of FAC/FAF blends made with 100/0, 80/20, 60/40, and 40/60 ratios at 300ºC-1-day-autoclaving age.

GBFS/SiO_2 samples. In the CAP-A or –B systems, our previous work [68] suggested that the best formula was 60/40 CAC (#51 or Fondu)/FAF ratio dry blend mixture containing SHMP phosphate reactant at concentration of 6% by total weight of this dry blend. Furthermore, 10% of MCF by total weight of dry cement blend was incorporated into all the cements tested in this work. The water/cement (W/C) ratios to make appropriate cement slurries were as follows: 0.48 and 0.54 for OPC (Class G)/ and (Type I/II clinker) /SiO_2; 0.51 for TSRC; 0.46 for FAC/FAF; 0.45 for GBFS/SiO_2; and, 0.51 for CAP-A and –B.

The W/C ratio had to be increased by nearly 11% for blends with zeolites, FER, and Clin., added at 30% by total weight of dry cement blend. These blends included the FER-OPC clinker cement system, known as “FlexCem®”, provided by Trabits group. According to Trabits group, the OPC clinker (Type I/II) – FER – Gypsum blend (65/30/5 weight % respectively) was prepared by grinding together OPC clinker and FER. As a result, a bimodal particle size blend was obtained. As described earlier, the adequate amount of silica flour was added to FlexCem to make 70/30 Type I/II clinker/SiO_2 ratio blend for evaluations.

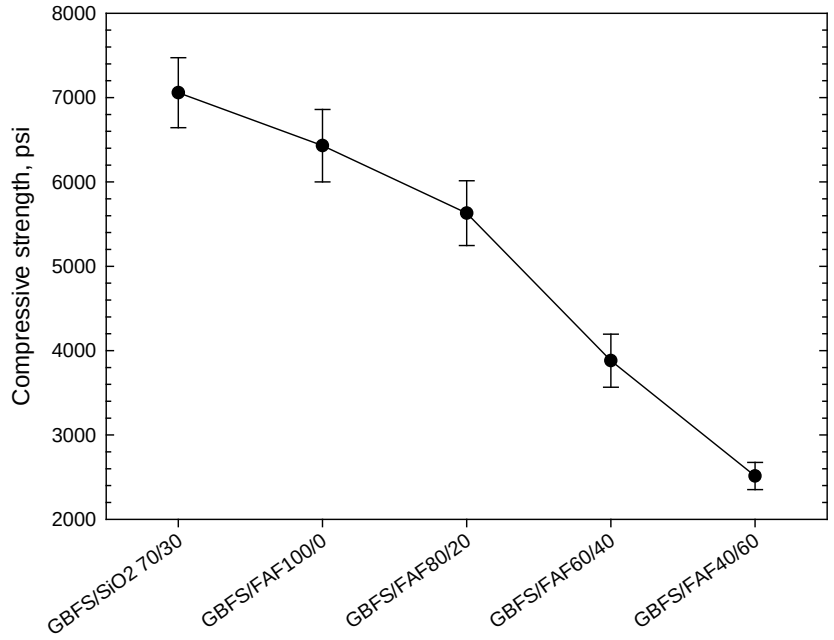

Figure 3. Compressive strength of 70/30 GBFS/SiO_2 ratio cement and cements made by varying GBFS/FAF ratios at 300ºC-1-day-autoclaving age.

Considering the environmental effect on promoting self-healing, three different environments, plain water at pH 7.4, 0.05 M sodium carbonate solution with pH 10.6 as alkali carbonate environment and simulated geothermal brine with pH 8.1 were employed. Table 2 shows the chemical ingredients of the brine fluid.

Table 2. Composition of the brine.

Major components	**Percent**	**Minor components**	**PPM**
Chlorine	13.5	Iron (ferrous)	1000
Sodium	6	Manganese	930
Calcium	2	Lithium	410
Potassium	1.5	Zinc	370
Magnesium	0.9	Boron	330
		Silicon	250
		Barium	130
		Dihydrogen sulfide	70

In assessing the acid-resistance, the 300°C-autclaved composite samples were immersed in pH 0.2 H_2SO_4 solution at 90°C for up to 28 days. Although the reactions' kinetic depends on the temperature the technical limitations did not allow conducting acid experiments at geothermal temperatures of 300ºC. The volume of the acid solutions was twice as large as the volume of the

samples and the solutions were replaced with fresh ones every 3 days to maintain <15% increase in pH during the treatment. After the acid exposure the specimens were rinsed with water, weighed, measured and tested for compressive strength. For the thermal shock testing, autoclaved samples were heated at 350°C for 24 hours, and then hot samples were dipped in 25°C water immediately after removal from the oven; such heating-water quenching cycling was repeated five times.

In evaluating the durability of interfacial bond at cement/CS casing joints, two harsh chemical environments, H_2SO_4-blended brine at pH 0.6 at 90°C and scCO_2-laden brine at pH 5.5 at 90°C, were employed for 30-day-long exposure testing.

2.3. Samples preparation

To determine the compressive strength, Young's modulus, and fracture toughness, the composite samples were prepared in the following sequences: The slurries made by hand mixing were poured in cylindrical molds (20 mm diam. and 40 mm high) for compressive strength and Young's modulus, and in beam molds (12.5 mm x 12.5 mm x 75 mm) for fracture toughness, and left to harden for 1 day at room temperature; thereafter, the hardened cements were removed from the molds, and then placed in a 99±1% relative humidity (R.H.) for 1 day at 85°C; finally, the samples were autoclaved in non-stirred Parr Reactor 4622 for 1 day at 300°C under pressure of 8.3 MPa. For fracture toughness, prior to the testing, the notch with 6.3 mm depth and 0.5 mm width was fabricated by a diamond-tipped blade on the tensile side at the center position of beam samples.

To observe cracks formation, including multi-crack development, crack-width and -propagation in composite sheath, brought about by debonding of composite from CS casing surfaces, the unconfined composite sheath samples surrounding the CS tube were prepared in the following sequences. The disk-shaped wooden tube-holder (49-mm-diam. by 13-mm-high) with a center hole (26- mm-diam.) was placed at the bottom of the cylindrical paper-mold with 48-mm-inner diam. and 100-mm length. The tube (125-mm-long x 25-mm-outer diam. x 3-mm-wall thickness) was inserted into the center hole of the wooden casing holder located at the bottom of the mold. The hand-mixed composite slurry was poured in an annular space between tube and the mold to prepare a sheath sample 23 mm thick and 74 mm high. Next, the samples were pre-cured for 24 hours in 99±1% relative humidity (R.H.) at 85°C. The pre-cured sheath sample was removed from paper mold, and then autoclaved for 24 hours at 300°C under the pressure of 8.3 MPa (1205 psi); and, finally, the autoclaved sheath sample was used for measuring the sheath- shear bond strength. The lap-shear adhesion test was conducted to determine the adhesive force of the composite coupling between CS plates according to modified ASTM D5868 for single-lap-joint sample. In preparing these samples, two plates, 32-mm-wide by 100-mm-long and 0.9-mm-thick each, were bonded together with composite adhesive; the overlapped adhesive area was 1440 mm^2 (45-mm-long by 32-mm-wide). The adhesive area was pre-cured in 100% R.H. under a loading of 16 g, and then a pre-cured adhesive without any loading was autoclaved at 300°C for 24 hours before the lap-shear bond test.

To obtain the unconfined sheath-shear bond strength between granite rock and composite, the composite sheath sample surrounding granite cylindrical column was

prepared in the same manner as the unconfined composite sheath samples surrounding the CS tube.

2.4. Measurements

Electromechanical Instron System Model 5967 was used to obtain all mechanical properties including Young's modulus, compressive strength, fracture toughness, sheath-shear bond strength, and lap-shear bond strength.

To develop set-control additive of TSRC composite slurry, TAM Air Isothermal Microcalorimetry was used to obtain the initial- and final-setting times and to determine the exothermic hydration heat energy evolved during the curing processes of these slurries at 85°C.

The fracture toughness, $K_{IC,}$ of center-notched beam samples was measured by the three-point flexure test with 50 mm span. Based upon the resulting stress-strain curves, the value of K_{IC} was computed using the following expression [69], $K_{IC}=Y.3P_{max}La^{1/2}/2bd^2$, where L is span, "a" is notch depth, "b" and "d" are breadth and depth of beam, $Y=1.93-3.07(a/d) + 14.53 (a/d)^2 – 25.11 (a/d)^3 + 25.8$.

The self-healing performance for the 300°C-atuclaved cylindrical samples was evaluated in the following manner. Firstly, the mechanical strength (compressive strength and Young's modulus) test was conducted to fabricate cracked samples. In this test, we carefully operated the Instron stopping it within no more than 40% of compressive strain after the stress-strain yield point (Figure 4). Such operation essentially avoided severe damage that would produce crumbled samples [70]. Next, the cracked sample was re-autoclaved for 5 days at the original curing temperature, and thereafter, the same mechanical test was repeated. Each test result was the average over at least three samples. The result of this test provided the strength recovery rate as one of the factors needed for evaluation of the self-healing performance. Also, since some strength recovery may be due to the progressing hydration of cement brought about by the additional 5 days in the autoclave, XRD (40 kV, 40 mA copper anode X-ray tube), thermogravimetric analysis (TGA), and Attenuated Total Reflectance-Fourier Transform Infrared Spectroscopy (ATR-FTIR) were used to identify amorphous and crystalline phase compositions and transitions responsible for strengthening cement matrix. The results of XRD tests were analyzed using PDF-4/Minerals 2015 database of International Center for Diffraction Data (ICDD). TGA (model Q50, TA Instruments) analyses were done at the heating rate of 20°C/min in a N_2 flow. Nikon Eclipse LV 150 3-D microscope was employed to obtain images of cracks' sealing and to explore the microstructures developed in sealed crack. The identification of the crystalline dissolution-precipitation products in the sealed cracks was made in non-destructive Raman chemical state mapping experiments with a Renishaw® in Via™ confocal Raman microspectrometer equipped with Leica® DM2700™ upright microscope. This information also was supported by XRD leading to crystalline phase compositions for the powder samples collected from sealed areas and JEOL 7600F Scanning Electron Microscope (SEM) image analysis coupled with EDX elemental composition survey for the typical spots of sealed areas.

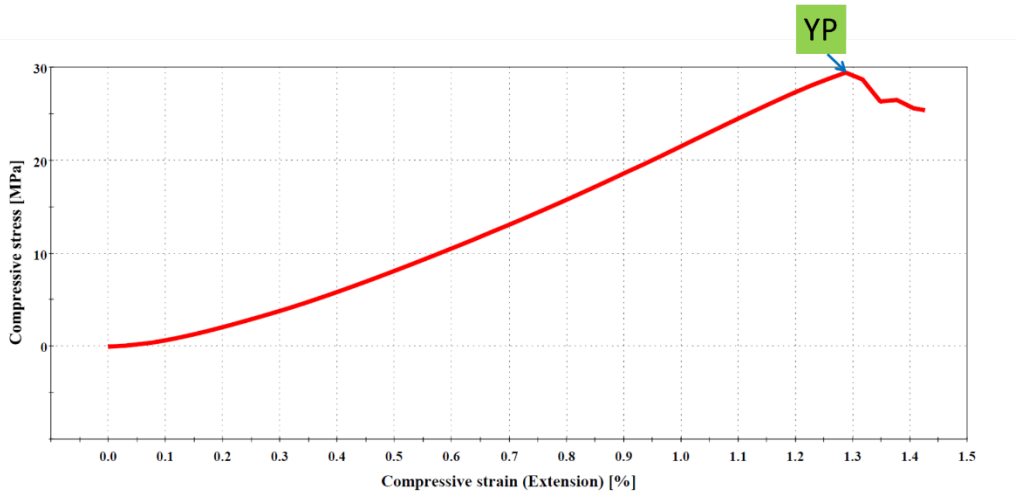

Figure 4. Stress-strain curve of MCF-reinforced cement composite.

The extent of re-adhering for 300ºC-cured CS-composite-sheath samples was determined by measuring the recovery of sheath-shear bond strength after additional 5-day-300°C-autocaving of debonded sheath samples. We also attempted to measure the recovery of lap-shear bond strength at CS plate/composite adhesive/CS plat joint. In this attempt, the two debonded CS plates were physically reattached by steel wire, and autoclaved for 5 days at 300°C. After the autoclave, the steel wire was removed from samples to assess whether the plates re-bonded. However, unlike the sheath-type bonding, the shear strength of lap-type bonding for most of re-adhered composite samples was too weak to be measured. Therefore, the attention for lap-shear bond samples before and after 300°C-5-day-re-adhering treatment was paid to not only the lap-shear bond strength for samples before re-adhering treatment, but also to identifying the locus of bond failure at interfaces between CS and composite by Shimadzu Energy Dispersive Micro X-ray Fluorescence Spectrometer, µEDX-1300, and to estimating the thickness of composite adhesive linked between CSs using Absolute Digimatic Caliper by Mitutoyo Corp. For the latter, seven different locations on each debonded CS site were subjected to thickness measurement. The resulting thickness ranged from 0.48 to 0.34 mm.

As for corrosion mitigation of CS by composites before and after the re-adhering treatment, we used the samples after lap-shear bond test and selected CS plate with the thinner composite layer. The extent of coverage of composite adhering to CS surfaces before and after re-adhering treatment was surveyed by µEDX. This extent combined with the thickness of composite layers over CS was correlated directly with the corrosion rate of CS. To obtain information on protection of CS by composite against brine-caused corrosion, DC electrochemical testing for the underlying CS was performed using Princeton Applied Research Model Versa STAT 4 Corrosion Measurement System. In this assessment, the CS plates, with composite-adhered and -re-adhered to its surface, were mounted into a holder, and then inserted into Ametex Model K0235 flat cell containing a 1.0 M sodium chloride electrolyte solution. The test was conducted under an aerated condition at 25°C, on an exposed surface area of 1.0 cm^2. The polarization curves were measured at a scan rate of 0.17 mVs^{-1} in the corrosion potential range from -0.4 to +0.6 V. The average corrosion rate, mm/year (mmpy), associated with corrosion potential, $E_{corr.}$,

mV, and corrosion current density, $I_{corr.}$, µA, was obtained by averaging Tafel fit results of polarization curves of three samples.

3. Results and Discussion

3.1. Screening of candidates for self-healing composites

3.1.1. Fracture toughness

Prior to the screening test, the effectiveness of MCF in improving the fracture toughness of all employed cements was investigated. Figure 5 shows the fracture toughness of non-reinforced and MCF-reinforced five different cement composites after 300°C-1-day-autoclaving. Among non-reinforced composites, controls, samples, the highest value of fracture toughness, K_{IC}, at 1.94 x 10^{-2} MN/$m^{3/2}$ and the lowest one at 0.58 x 10^{-2} MN/$m^{3/2}$ were determined for GBFS/SiO_2 and TSRC, respectively. The K_{IC} of the other three cements, OPC/SiO_2, CAP-A, and FAC/FAF, ranged from 1.27 x 10^{-2} to 1.53 x 10^{-2} MN/$m^{3/2}$. The incorporation of 6% by weight MCF into these cements led to a pronounced increase in fracture toughness by 1.6-, 2.3-, 2.1-, 2.1-, 2.0-fold for OPC/SiO_2, TSRC, FAC/FAF, and GBFS/SiO_2. Since the fracture toughness represents the energy, which impedes and delays the propagation of a thin crack in materials, MCF appeared to serve in resisting the propagation and grow of a thin crack present in cement matrix. Figure 6 plots the changes in K_{CI} value for TSRC as a function of MCF content. The data seems to suggest that 6wt% content of MCF is sufficient to provide a satisfying fracture toughness. However, in this work, we adapted 10% CMF by total weight of dry cement blend. Nevertheless, all MCF-free cements met the material criteria of flexure toughness >0.006 MN/$m^{3/2}$ for cement matrix after 300°C-1-day-autoclaving.

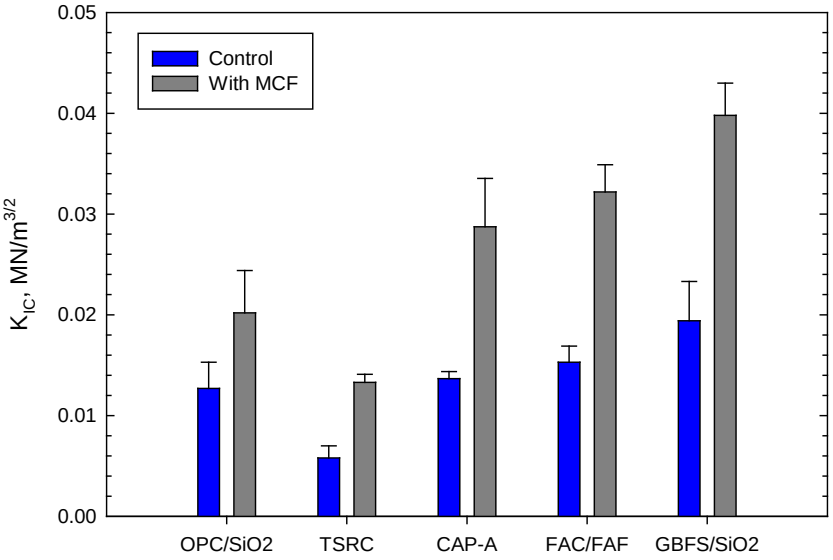

Figure 5. Effect of 10% by weight of MCF on improving fracture toughness of different cements.

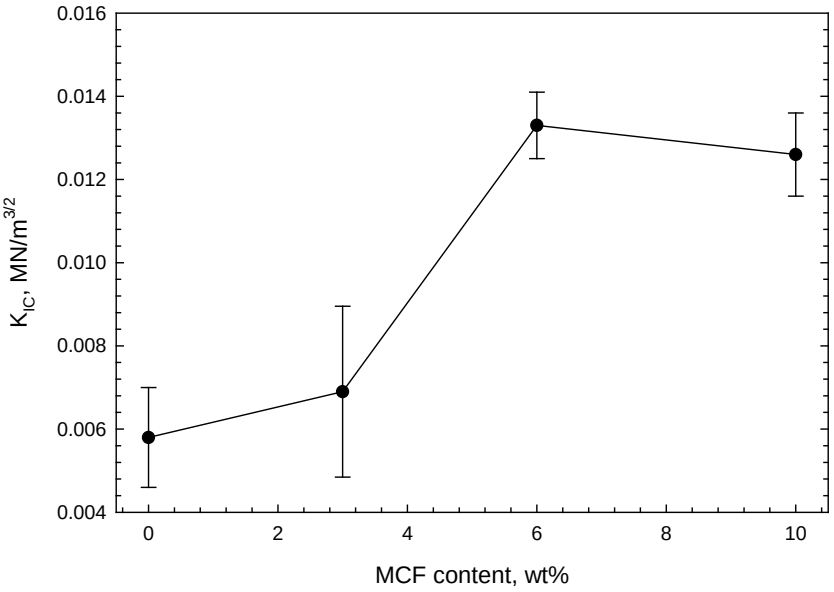

Figure 6. Changes in K_{IC} value of TSRC as a function of MCF content.

3.1.2. Brittleness and softness of cement composites made in three different environments

Figure 7 shows Young's modulus (YM) of MCF-reinforced cement composites after 24-hr exposure in three different environments, plain water, alkali carbonate, and simulated geothermal brine, at 300°C. To define the brittleness and softness of composites from YM data in a quantitative way, the fracture nature was classified as very brittle, brittle, moderate, and soft. Based upon the YM value of conventional OPC/SiO_2 well cement, we made the following quantitative classification. The very brittle mode corresponded to high YM value of more than 500 x 10^3 psi. The YMs of brittle and moderate fracture modes were in the regions of 500 x to >300 x 10^3 and 300 x to >100 x10^3 psi, respectively, and materials with YM ≤100 x 10^3 psi were classified as soft-fracture-mode ones. In plain water, four composites, OPC/SiO_2 TSRC, CAP-A, and CAP-B, had moderate YM. In contrast, two other composites, FAC/FAF and GBFS/SiO_2, had brittle and very brittle natures. Figure 8 shows the appearance of these composites after YM testing. As seen, the moderate fracture mode materials OPC/SiO_2 and TSRC developed and propagated slim and thin cracks. Compared with this, FAC/FAF with a brittle fracture mode had wider cracks, while the catastrophic fracture mode with fragmentation was observed for GBSF/SiO_2 as very brittle composite. Relating this information to the results of fracture toughness, suggests that although GBSF/SiO_2 displayed the highest fracture toughness such a brittle fractur nature caused the generation of undesirable wide cracks. In contrast, TSRC with the lowest YM generated ideal slim cracks.

Some composites were sensitive to alkali carbonate and brine environments. YM values of TSRC increased by 1.7- and 2.1-fold, respectively, in alkali carbonate and brine, compared with the plain water. Thus, TSRC was susceptible to reactions with carbonate and brine components. Nevertheless, the four composites made in three environments met the material criterion of YM <400 x 10^3 psi

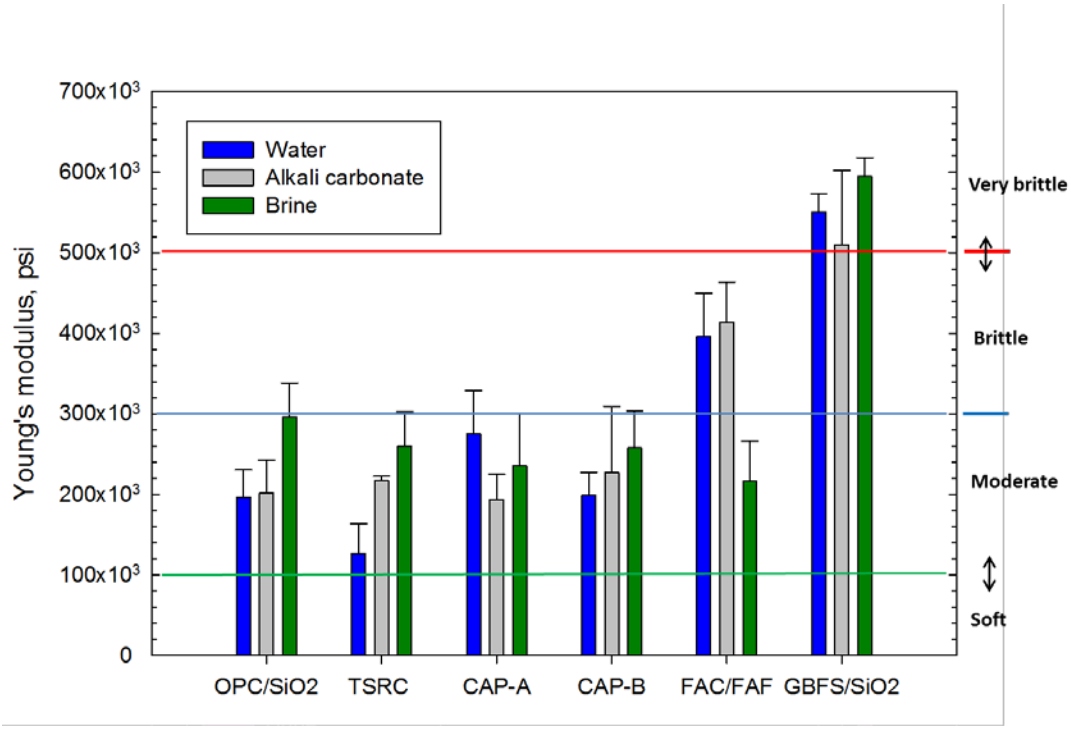

Figure 7. Young's modulus of various different cement composites after exposure for 24 hours in plain water, alkali carbonate, and simulated geothermal brine at 300°C.

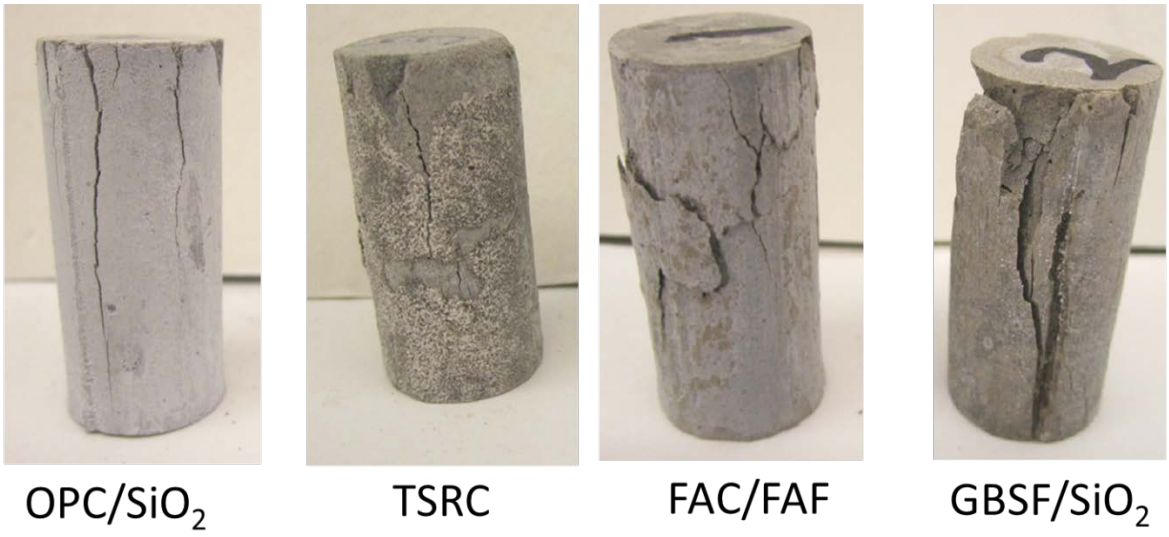

Figure 8. Appearance of various cement composites associated with the moderate, brittle, and very brittle fracture modes.

3.1.3. Compressive strength and strength recovery of various composites before and after self-healing in three different environments

Figure 9 exhibits compressive strength of various composites after 300°C-24-hr autoclaving in plain water, alkali carbonate, and brine, before and after self-healing treatment in these environments for 5 additional days at 300°C. All the composites made in these three environments had the compressive strength >1000 psi as material criterion at 24-hr-curing age. The ranking of compressive strength developed in plain water was as following: GBFS/SiO_2 (7060 psi) > FAC/FAF (4450 psi) > OPC/SiO_2 (3130 psi) > CAP-A (2920 psi) > CAP-B (2730 psi) > TSRC (1740 psi). Interestingly, GBFS/SiO_2 made in brine displayed a very high compressive strength at 8515 psi.

Figure 10 shows the recovery rate of compressive strength through self-healing of fractured composites during the repeated 5-day 300^{o}C exposure. Among these composites, only TSRC exerted the recovery >80% as material criterion in all environments; in particular, the brine led to the recovery >100%, implying that brine chemicals assisted in promoting self-healing of TSRC. Thus, the ability of brine to remedy the defected TSRC, CAP-A, FAC/FAF composites was greater than that of a plain water and alkali carbonate. By contrast, the recovery of OPC/SiO_2 was only 58, 55, and 51%, respectively, in plain water, carbonate, and brine. The data also revealed that there are two factors affecting the extent of recovery: One is the environments as described above; the other is related to the YM of composites. For the latter factor, the damage of composites with high YM was catastrophic with fragmentation and formation of wide cracks. The damaged samples were very difficult to seal and plug completely in a short-healing period of 5 days. Nevertheless, although the GBFS/SiO_2 composites made in plain water and carbonate was classified as very brittle composite, it recovered 76 and 61% of strength in plain water and carbonate. The recovery of both CAP-A and -B in all environments ranged from 53 to 71 %. Figure 11 shows the changes in appearance before and after self-healing treatment in plain water. The visual observation for all treated composites, excepting OPC/SiO_2, revealed that the crack-width and -openings became smaller. This fact clearly demonstrated that all alkali-activated composites containing pozzolan reactants are capable of self-healing and remedying cracks to some different extend in the 300°C plain water.

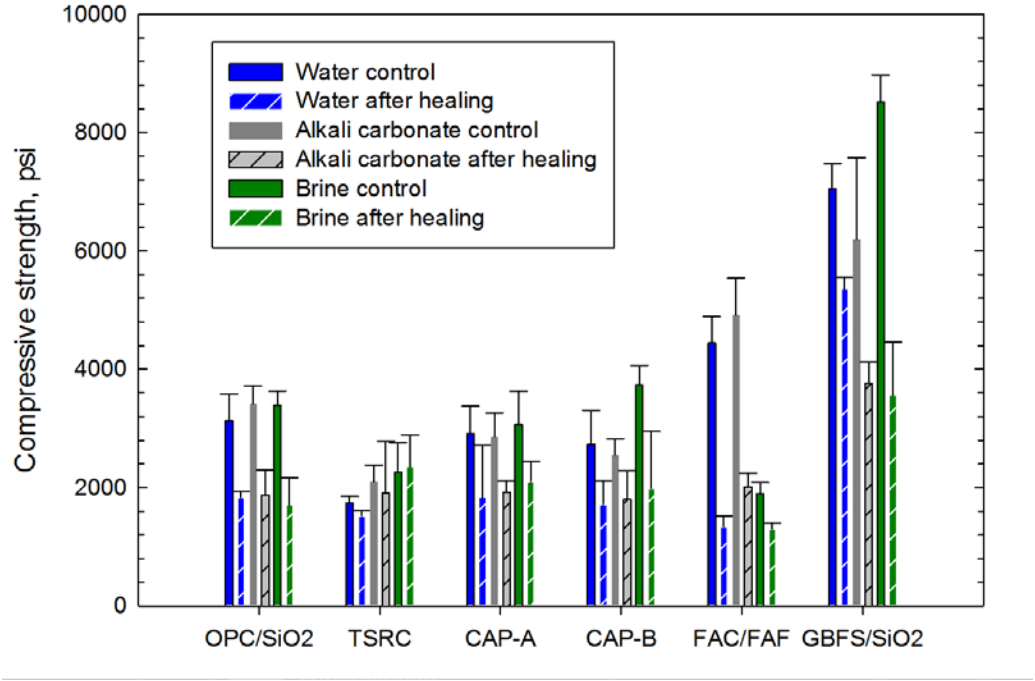

Figure 9. Compressive strength of various composites before and after self-healing treatments in 300°C plain water, carbonate, and brine.

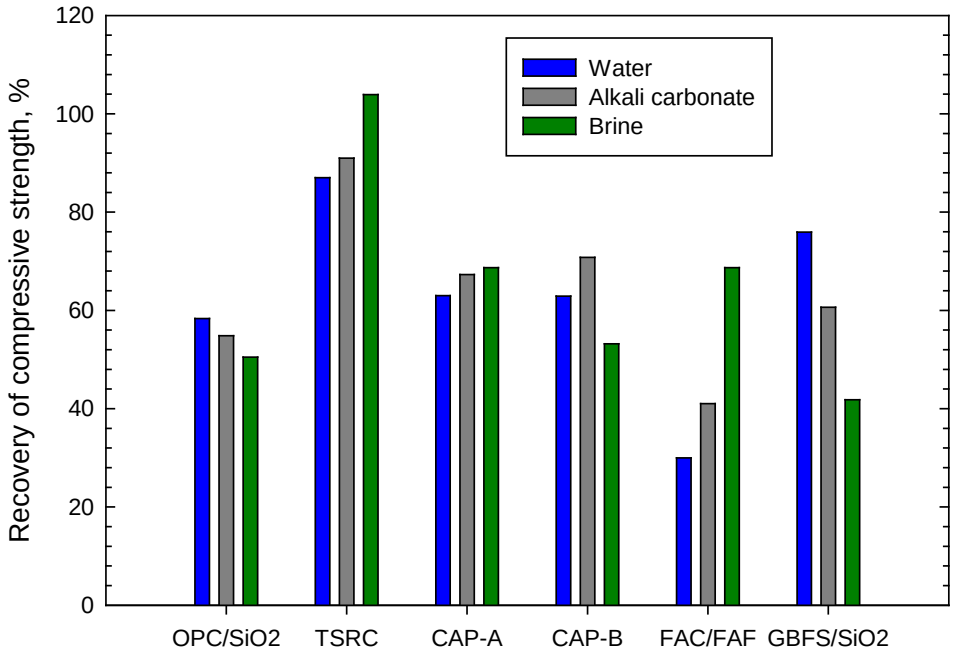

Figure 10. Recovery rate of compressive strength for various composites in plain water, carbonate, and brine.

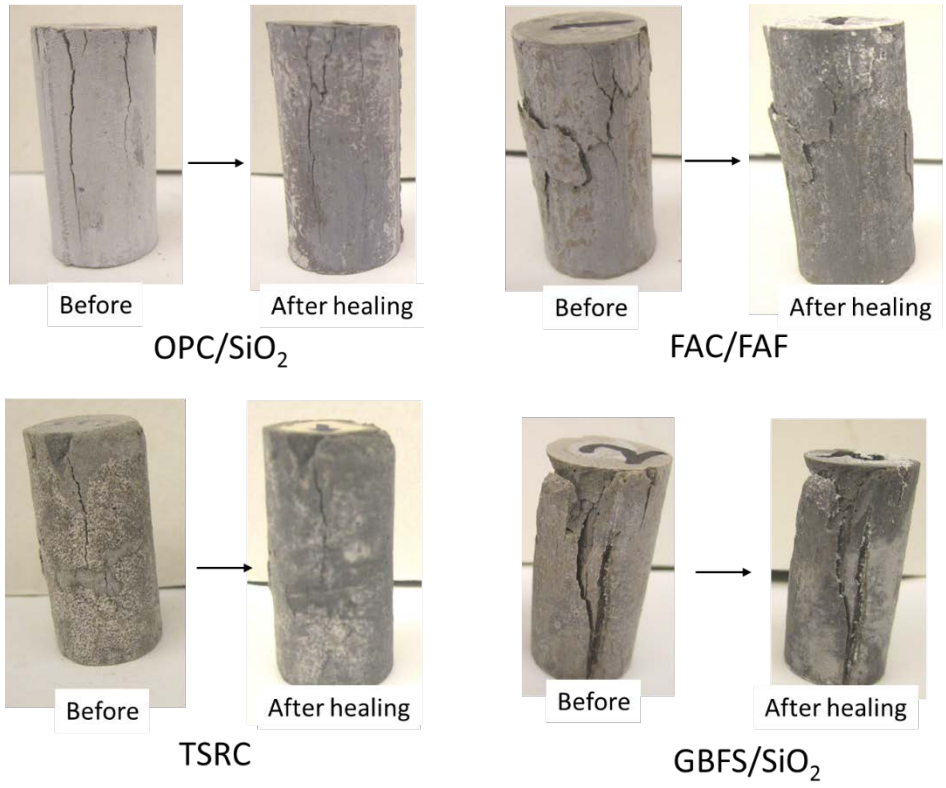

Figure 11. Changes in appearance of the damaged composites after 5-day self-healing treatment in 300°C plain water.

3.1.4. Acid resistance

To evaluate the resistance of various composites to 90°C H_2SO_4 solution at pH 0.2, 300°C-24-hr-autoclaved composites were immersed in hot acid for 14 days. After the immersion, the changes in compressive strength and diameter of composites were reported by comparison with that of non-exposed composites as controls. Afterward, the acid-exposed composites were damaged and were again exposed to acid for another 14 days to obtain information on strength recovery.

After 1st-acid immersion test, the least strength reduction, 21%, was measured for TSRC, and CAP-A showed second least reduction, while OPC/SiO_2 had the highest reduction of 37% (Figure 12). There were two different types of acid-damage modes: One was acid-scale corrosion of cements; the other was acid-erosion. In fact, the OPC/SiO_2 and GBFS/SiO_2 belonged to the former type, and the latter type involved TSRC, CAP-B, and FAC/FAF. Commonly, the acid-scale corrosion was due primary to the precipitation of the calcium sulfate reaction products between SO_4^{2-} ion from H_2SO_4 and Ca^{2+} liberated from cement at the surface and with following accumulation of scales causing volumetric expansion of cements. The accumulated scale layers were eventually segregated from cement bodies. On the other hands, acid-erosion was associated with the loss in weight of cement by its acid dissolution. In fact, the diameter of OPC/SiO_2 and GBFS/SiO_2 composite increased by nearly 10 and 6 %, respectively, and in contrast, TSRC, CAP-B, and FAC/FAF reduced their diameters due to the acid-erosion (Figure 12). As is evident

from photos in Figure 12, OPC/SiO_2 and GBFS/SiO_2 underwent the acid reaction-leading to severe expansion failure during the additional 14-day immersion. These samples could not be tested. The compressive strength of three survived acid-resistant composites was 540, 870, and 1350 psi for TSRC, CAP-B, and FAC/FAF, respectively, corresponding to the recovery rate of 39, 41, and 48%.

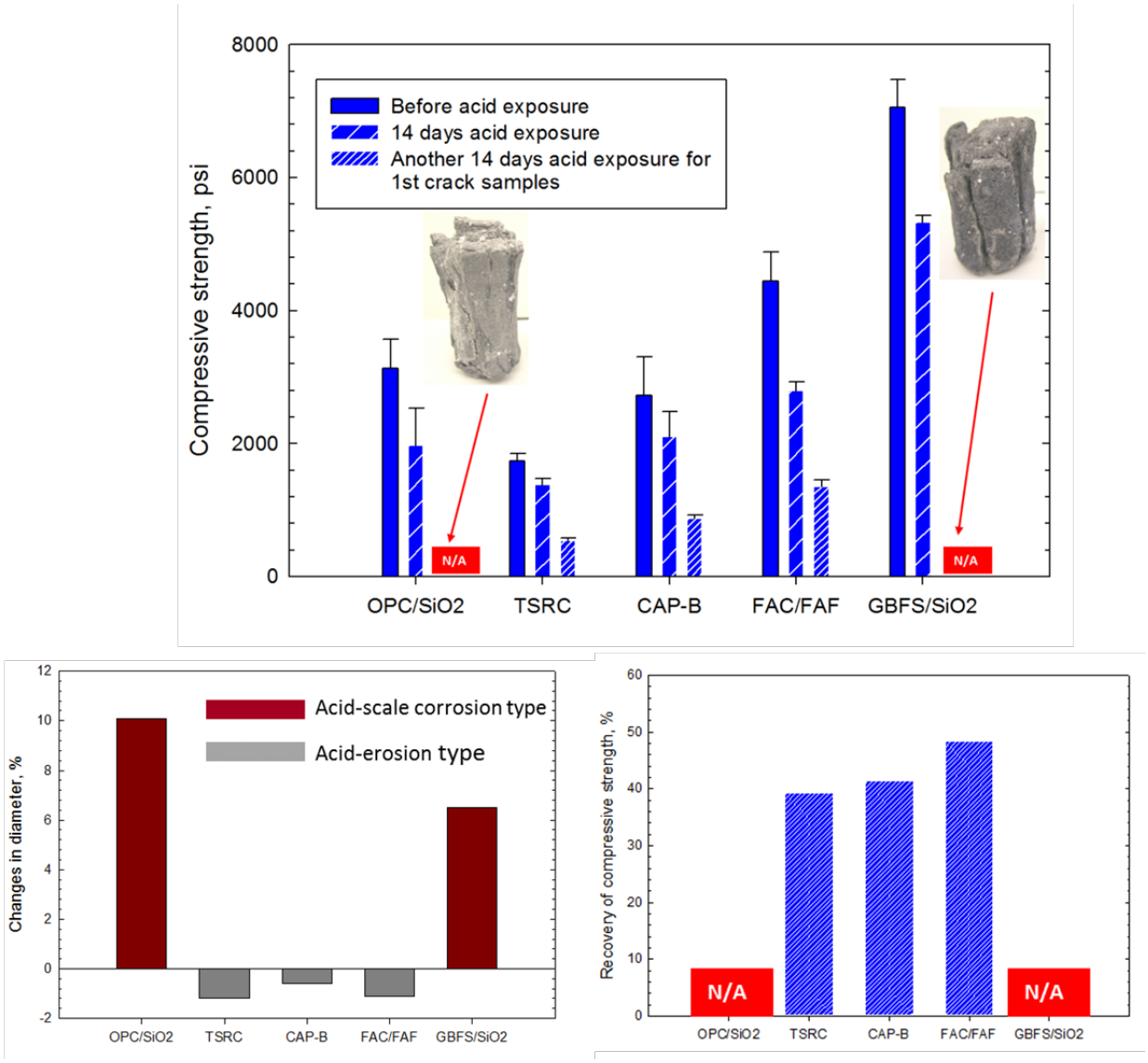

Figure 12. pH 0.2-90°C H_2SO_4 resistance tests for 300°C-1-day-autoclaved composites.

3.1.5. Thermal shock resistance

The thermal shock resistance was measured as the reduction of compressive strength for 300°C-24-hr-auctoclaved composites after 5 cycles of thermal shock (one cycle: 350°C-24-hr-heating followed by quenching in 25°C water). The recovery of compressive strength after the 5 cycles

of thermal shock and first compressive damage was measured in three different environments, plain water, carbonate, and brine. As a result (Figure 13), TSRC displayed the best thermal shock resistance with the lowest reduction of compressive strength after thermal shock test. This reduction rate was 36, 46, 47, and 34% lower than that of OPC/SiO_2, CAP-B, FAC/FAF, and GBFS/SiO_2 respectively. The recovery of compressive strength by exposing the cracked composites to plain water, carbonate, and brine for 5 days at 300°C showed that all composites, except for FAC/FAF, had the recovery of > 99% in all environments. Among these composites, the best recovery for each environment was observed for TSRC. Second best recovery performance was observed for OPC/SiO_2, while almost the same recovery was measured for CAP-B and GBFS/SiO_2. A possible interpretation of such a high recovery rate was that 350°C heating process in this test left a certain amount of non-hydrated and non-reacted cement, pozzolan in cement bodies, that reacted later. Such interpretation supports the likelihood of autogenous healing during the exposure in such environments.

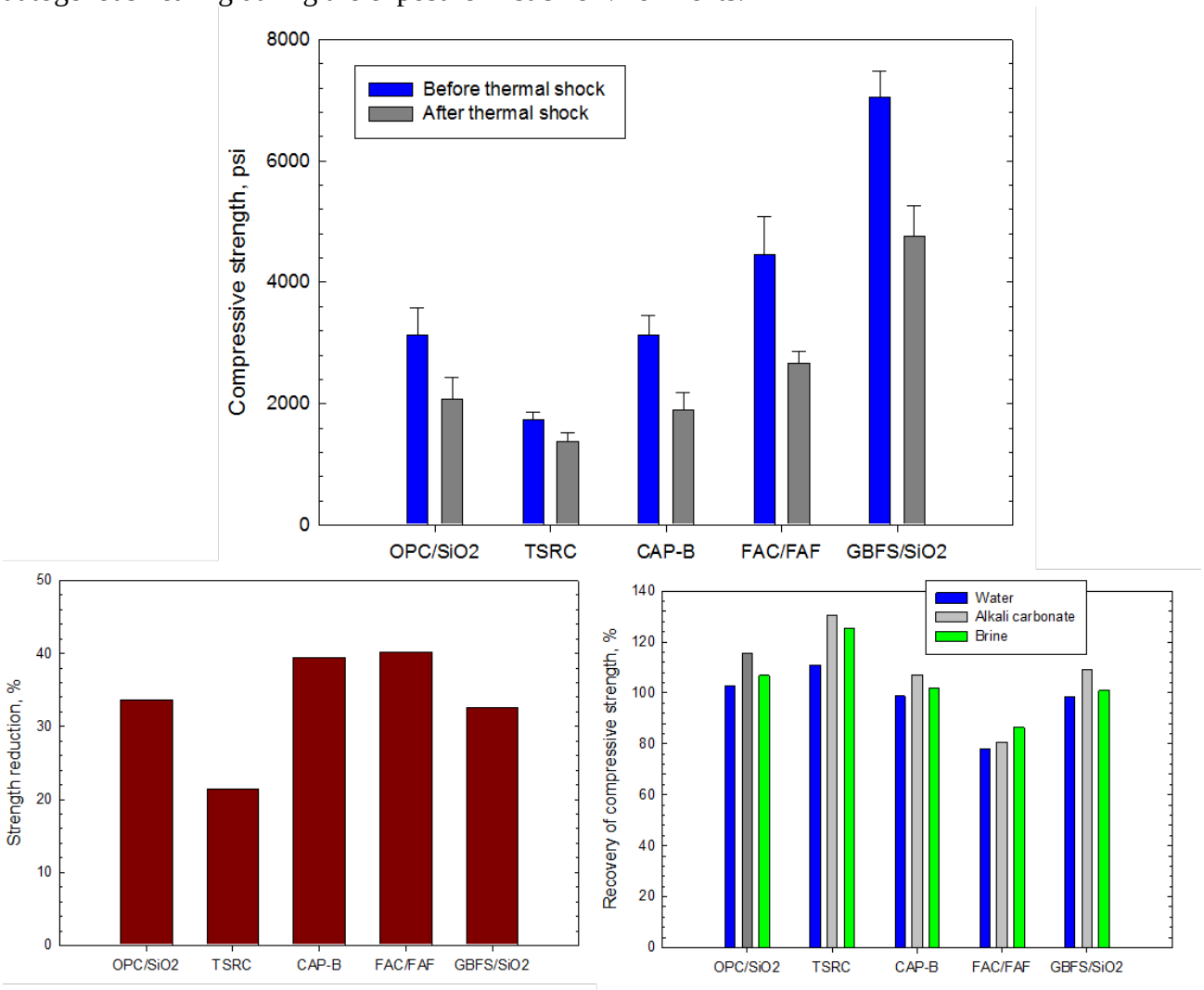

Figure 13. Thermal shock resistance of various composites, and recovery of compressive strength in plain water, carbonate, and brine at 300°C after the damage of thermally shocked composites.

All test results from the screening process described above were integrated and summarized in Table 3.

Table 3. Results of evaluation tests for various composites based on material criteria and average compressive strength recovery in 300°C plain water, carbonate, and brine environments as well as in 90°C pH 0.5 H_2SO_4.

	Thermal and hydrothermal stability >300°C	Compressive strength >1000 psi	Young's modulus <400 x 10^3 psi	Flexure toughness >0.006 $MN/m^{3/2}$	*Average strength recovery >80%	Average strength recovery >80% after thermal shock	Strength recovery in pH 0.5 acid at 90°C
OPC/SiO_2	Yes	Yes	Yes	Yes	C	A^+	Failed
TSRC	Yes	Yes	Yes	Yes	A	A^{++}	C
CAP-A	Yes	Yes	Yes	Yes	B	**N/A	N/A
CAP-B	Yes	Yes	Yes	Yes	B	A^+	C
FAC/FAF	Yes	Yes	No	Yes	C	A	C
GBFS/SiO_2	Yes	Yes	No	Yes	B	A^+	Failed

* A^{++} >120%, A^+ 199-100%, A >99-80%, B 79-60%, and C<60%, **Untested

As a result, the self-healing performance of tested candidates was arranged in the following order from the best to the worst: TSRC > CAP-B> GBFS/SiO_2 and FAC/FAF >OPC/SiO_2.

3.2. Self-healing capability of repeatedly cracked composites

One inevitable concern is the alteration in mechanical structure of composites as a function of autoclaving time; namely, the ductile nature of composites made by autoclaving for only 1 day may be converted into a brittle one during extended autoclaving periods. Furthermore, it is possible to imaging that when healed composites suffer repeated mechanical stress failure, the they not only develop new cracks in the cement bodies, but also may reopen the cracks once closed by self-healing. To respond to such intriguing questions, we investigated whether the self-healed composites are capable of re-self-healing and reclosing the reopened cracks after repeated stress loadings. The investigated factors included changes in YM and compressive strength of composites autoclaved for up to 10 days at 300°C, the strength recovery of repeatedly cracked-composites, and visual observations of healed samples. To obtain this information, the samples were prepared in the following manner: The 1st time-cracked samples as the control were autoclaved for 5 days to heal in three different environments, plain water, carbonate, and brine; this was followed by compressive strength test to yield 2nd time stress cracks, and then the 2nd time cracked composites again were treated for 5 additional days in the same environments. Afterwards, the 3rd time compressive strength test for post-self-healed composites was conducted to evaluate re-self-healing ability.

In this work, TSRC was tested as the best candidate for self-healing, and for comparison purpose, OPC/SiO_2 was employed as a reference composite. Figure 14 represents the changes in YM value of TSRC and OPC/SiO_2 composites with the extended autoclaving times for up to 10 days in 300°C-plain water, -carbonate, and –brine. As expected, the YM value of these composites increased with the prolonged exposure in all the environments, showing that the

ductile nature of composites tends to shift to brittle one after extended curing. As for the environmental effect on YM, carbonate and brine noticeably increased YM; in fact, YM of OPC/SiO_2 reference composite shifted from moderate YM to brittle one. In contrast, although TSRC was made with 10 days autoclaving, YM of this composite remained in the moderate level in all environments.

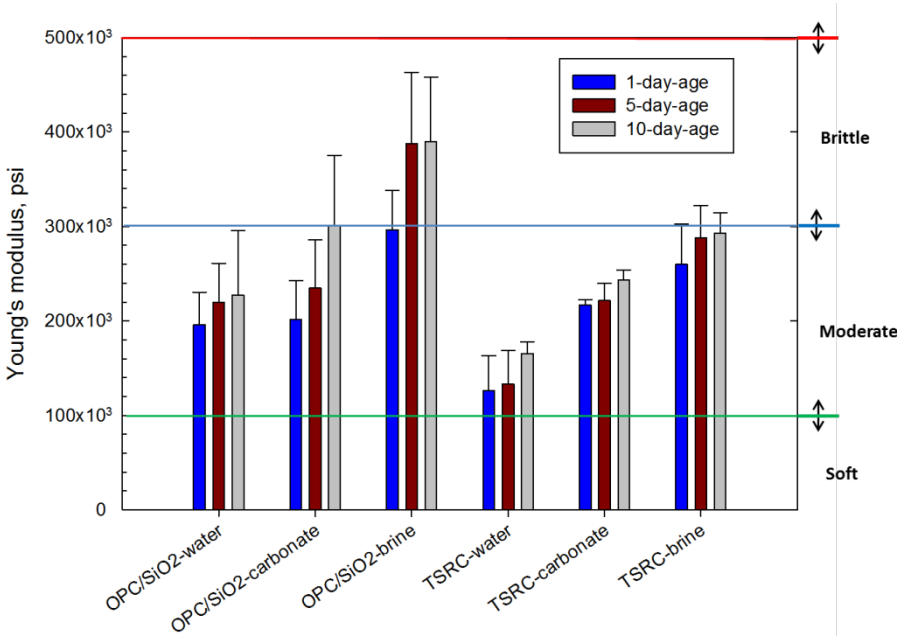

Figure 14. Young's modulus of 1-, 5-, and 10-day-autoclved OPC/SiO_2 and TSRC cured at 300°C in plain water, carbonate, and brine.

Similar changes were observed for compressive strength of OPC/SiO_2, 10 days exposure to carbonate and brine engendered the development of compressive strength >5000 psi, strongly suggesting that this composite favorably reacted with carbonate and brine chemicals (Figure 15). There was no significant difference in compressive strength of 5- and10-day-autocalved TSRC in these environments.

Figures 16 and 17 compare compressive strengths between 1st cracked as control, 2nd and 3rd cracked composites at 1-, 5-, and 10-day autoclaving ages after repeated healing treatments in plain water and their strength recovery. For OPC/SiO_2 reference composites, the recovery of 3rd time cracked sample was somewhat higher than that of 2nd cracked one, demonstrating that although self-healed composite suffered repeated mechanical stress its self-healing ability persisted after 10 days of curing. Similar results, excluding 5-day-autoclaved sample, were obtained for TSRC composite. The average strength recovery of 2nd and 3rd time cracked TSRC remedied in plain water was 92, 95, and 71%, respectively, for 1-, 5-, and 10-day autoclaved samples. In contrast, the recovery of OPC/SiO_2 reference composites was lower, 61, 55, and 44 % for 1-, 5-, and 10-day autoclaved samples. For both composites, the recovery of 10-day autoclaved samples was nearly 25% lower than the average recovery of 1- and 5-day-autoclaved samples. Nonetheless, it appeared that self-healing and re-self-healing performances of TSRC composites for 2nd and 3rd time cracked samples were far better than those of the reference OPC/SiO_2 composite.

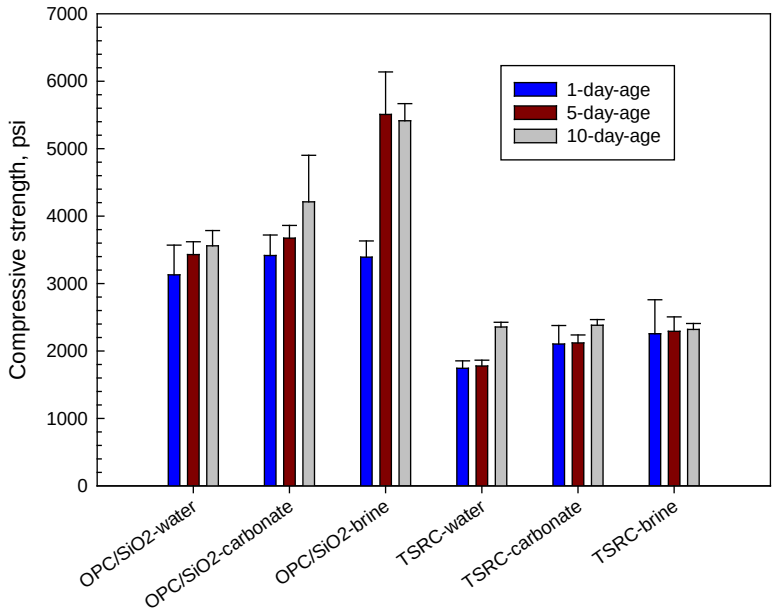

Figure 15. Compressive strength of 1-, 5-, and 10-day-autoclved OPC/SiO_2 and TSRC cured at 300°C in plain water, carbonate, and brine.

The visual analysis of re-self-healed TSRC at 10-day-age disclosed an excellent healing performance, showing formation of the healing reaction products underneath remedied composite area (Figure 18). By contrast, the re-self-healing performance of OPC/SiO_2 composite at the same age as TSRC was poor.

In reactive carbonate environment (Figures 19 and 20), as expected, the carbonation of OPC/SiO_2 at 5- and 10-day-autoclaving age resulted in rising the compressive strength by 7 and 18%, compared with that in plain water. Similarly, 18% and 1% increases in compressive strength were observed for TSRC at 5- and 10-day-atuoclaving age. The 2nd time cracked OPC/SiO_2 showed a good recovery >80% at 5- and 10-day-age in carbonate environment. However, the recovery of 3rd time cracked OPC/SiO_2 was 70 and 37% for 5- and 10-day-aged composites. The TSRC exhibited an excellent recovery >85% for all 2nd and 3rd time cracked composites, except for the 3rd time cracked 10-day-aged composite, which had a recovery of 78%. More importantly, the average recovery of re-self-healed 3rd time cracked TSRC at 1-, 5-, and 10-day-age was 87%, corresponding to 50% higher than that of OPC/SiO_2. Compared with that of plain water environment, the susceptibility of both OPC/SiO_2 and TSRC composites to carbonation obviously assisted in promoting the re-self-healing (Figure 20).

The disappearance of cracks and sealing of openings in carbonate environment could be seen visually (Figure 21), clearly verifying that carbonation was the autogenous-healing process for both composites.

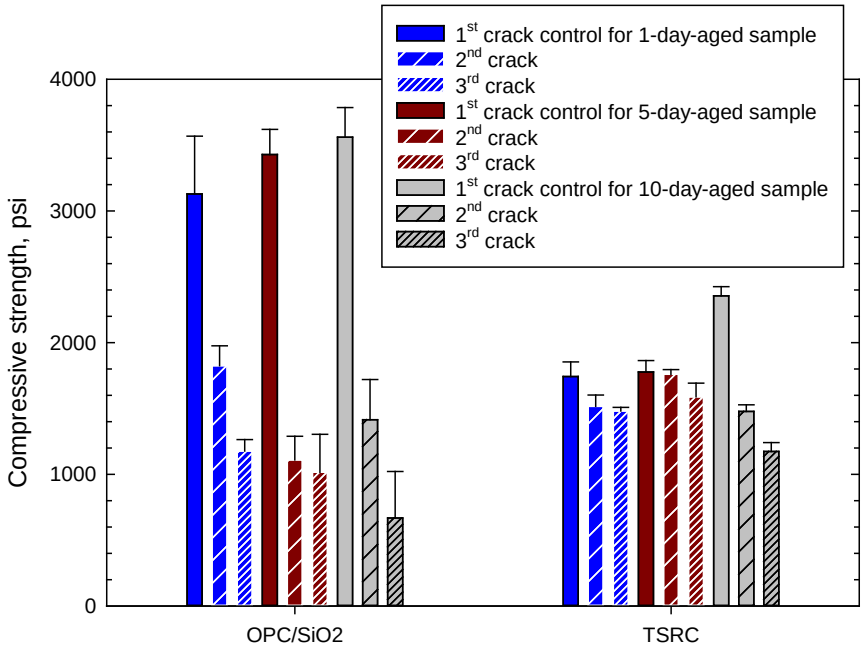

Figure 16. Compressive strength of 1st time cracked control and healed 2nd time and 3rd time cracked samples at 1-, 5-, and 10-day-autoclaving ages in plain water.

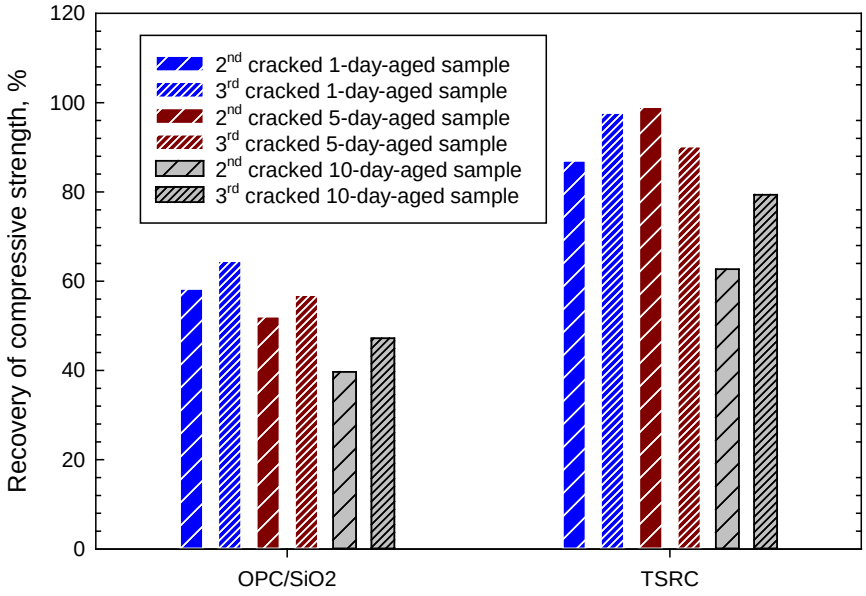

Figure 17. Strength recovery of 2st time and 3rd time cracked composites after healing in plain water.

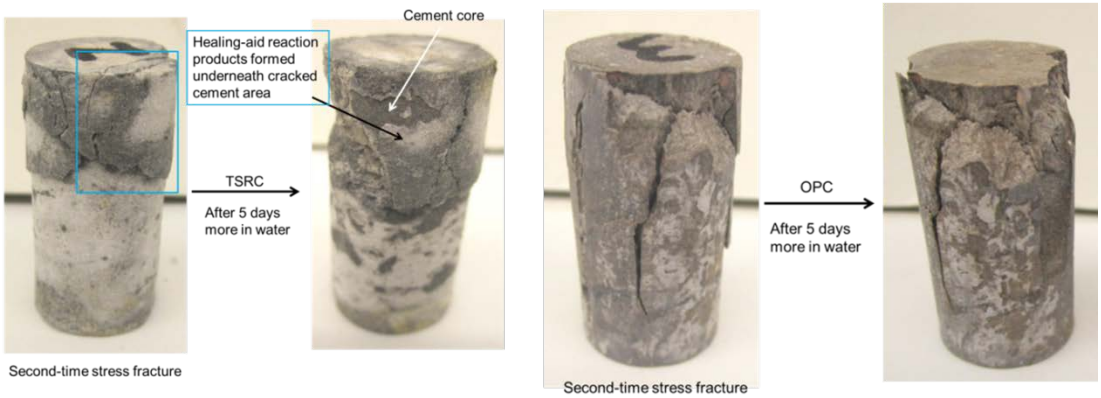

Figure 18. Changes in appearance of 3rd-time cracked TSRC and OPC/SiO_2 composites after 5 days healing treatment in plain water at 300°C.

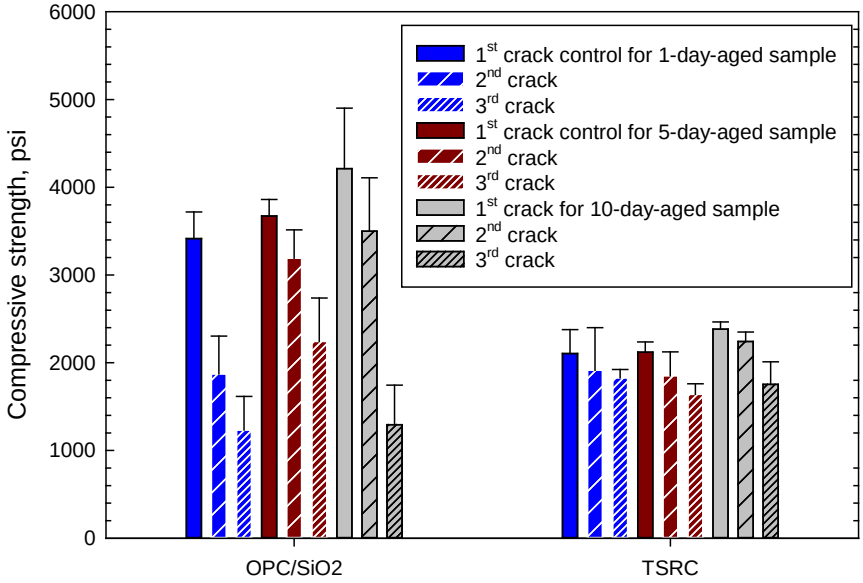

Figure 19. Compressive strength of 1st time cracked control and healed 2nd time and 3rd time cracked samples at 1-, 5-, and 10-day-autoclaving ages in carbonate.

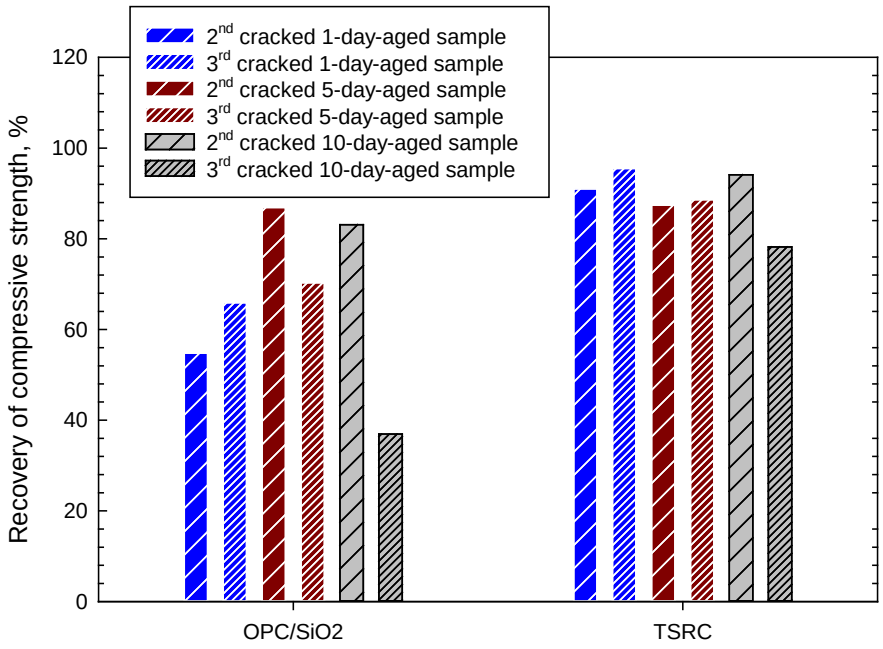

Figure 20. Strength recovery of 2nd-and 3rd- time cracked OPC/SiO_2 and TSRC composites in carbonate.

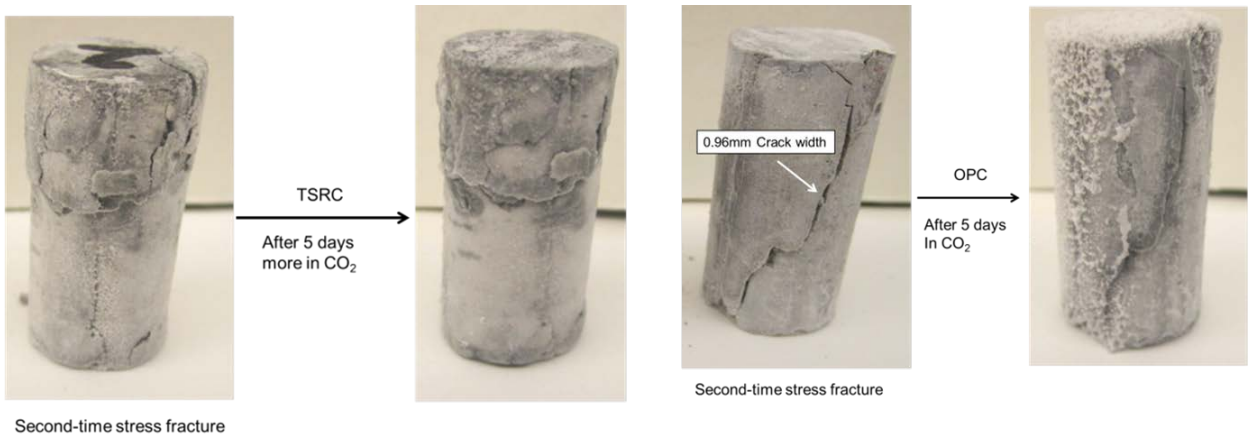

Figure 21. Changes in appearance of 3rd time cracked TSRC and OPC/SiO_2 composites after 5 days healing treatment in carbonate at 300°C.

Figures 22 and 23 compare compressive strengths of 1st time cracked control, and 2nd- and 3rd time cracked composites at 1-, 5-, and 10-day autoclaving ages after healing treatment and their strength recovery in brine environment. Brine environment strikingly enhanced YM of OPC/SiO_2 at 300°C, causing the conversion of ductile composite into a brittle one. Correspondingly, high compressive strength of nearly 5500 psi was determined for 5- and 10-day-autocaved OPC/SiO_2. The compressive strength development of 5- and 10-day-aged TSRC was similar to that in carbonate. For TSRC, the average recovery of compressive strength for 2nd- and 3rd time cracked composites made by 1-, 5-, and 10-day-autoclaving was 111% for 2nd time

cracked and 70% for the 3rd time cracked samples. The OPC/SiO_2 shoed 47% strength recovery for the 2nd time cracked and 65% for the 3rd- time cracked samples.

The data for strength recovery described above are summarized in Table 4. As is evident, TSRC possessed great self-healing and re-self-healing properties in these three different environments.

Table 4. Summary of average compressive strength for 2nd- and 3rd-time cracked composites made by 1-, 5-, and 10-day-autoclaving in plain water, carbonate, and brine at 300°C.

	Plain water		Carbonate		Brine	
	2nd crack	3rd crack	2nd crack	3rd crack	2nd crack	3rd crack
OPC/SiO_2	50 %	56 %	75 %	58 %	47 %	65 %
TSRC	83 %	89 %	91 %	88 %	111 %	70 %

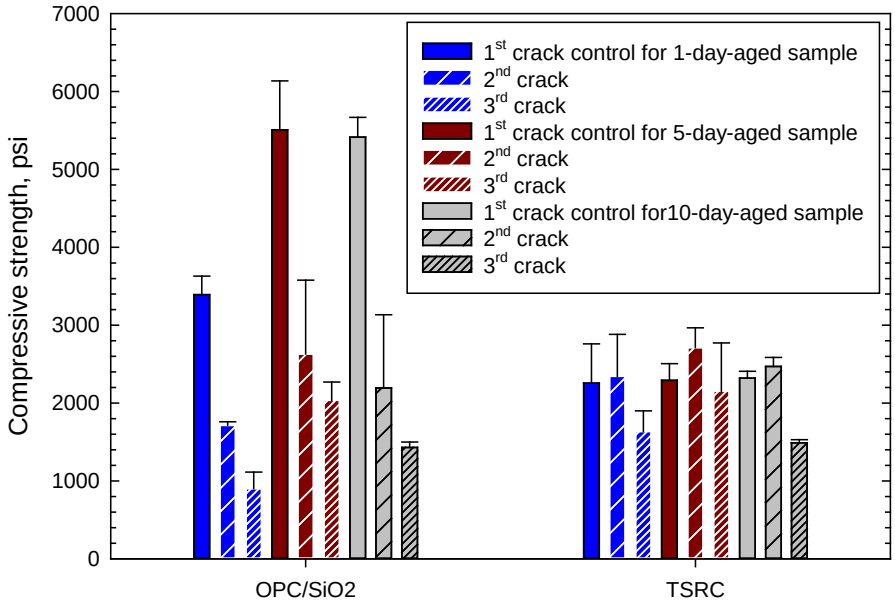

Figure 22. Compressive strength of 1st-time cracked control and healed 2nd- and 3rd-time cracked samples at 1-, 5-, and 10-day-autoclaving ages in brine at 300°C.

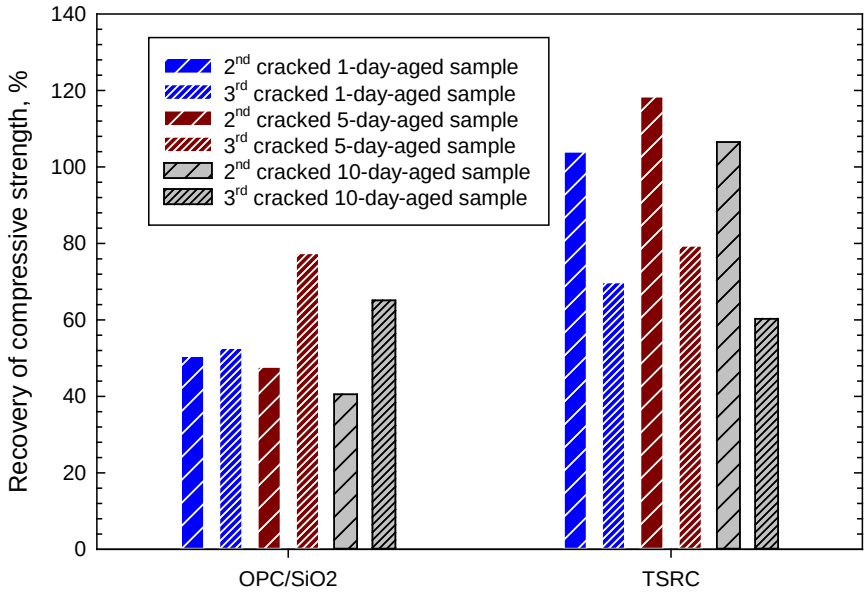

Figure 23. Strength recovery of 2nd-and 3rd-time cracked OPC/SiO_2 and TSRC composites in brine.

3.3. Study of self-healing mechanisms for TSRC

Our effort next was devoted to obtaining information on the self-healing mechanisms of TSRC. There are two major factors contributing to strength recovery after healing treatment: One is an adequate sealing and plugging of cracks by reaction and precipitation products; the other is formation of the crystalline and amorphous reaction products and their phase transitions in composite matrix during the treatment period. To study these factors, three analytical technics were used: 3D imaging of cracks, XRD, and SEM-EDX. The obtained information was directly correlated with the results from compressive strength and its recovery.

3.3.1. 3D micro-image analyses of crack's sealing after 1-day initial curing time

The crack's sealing of the damaged TSRC composite samples cured for 1 day at 270^o and 300^{o}C was analyzed using 3D micro image analyses. Figures 24-26 present examples of a typical crack sealed during the healing process in plain water, brine, and carbonate environments.

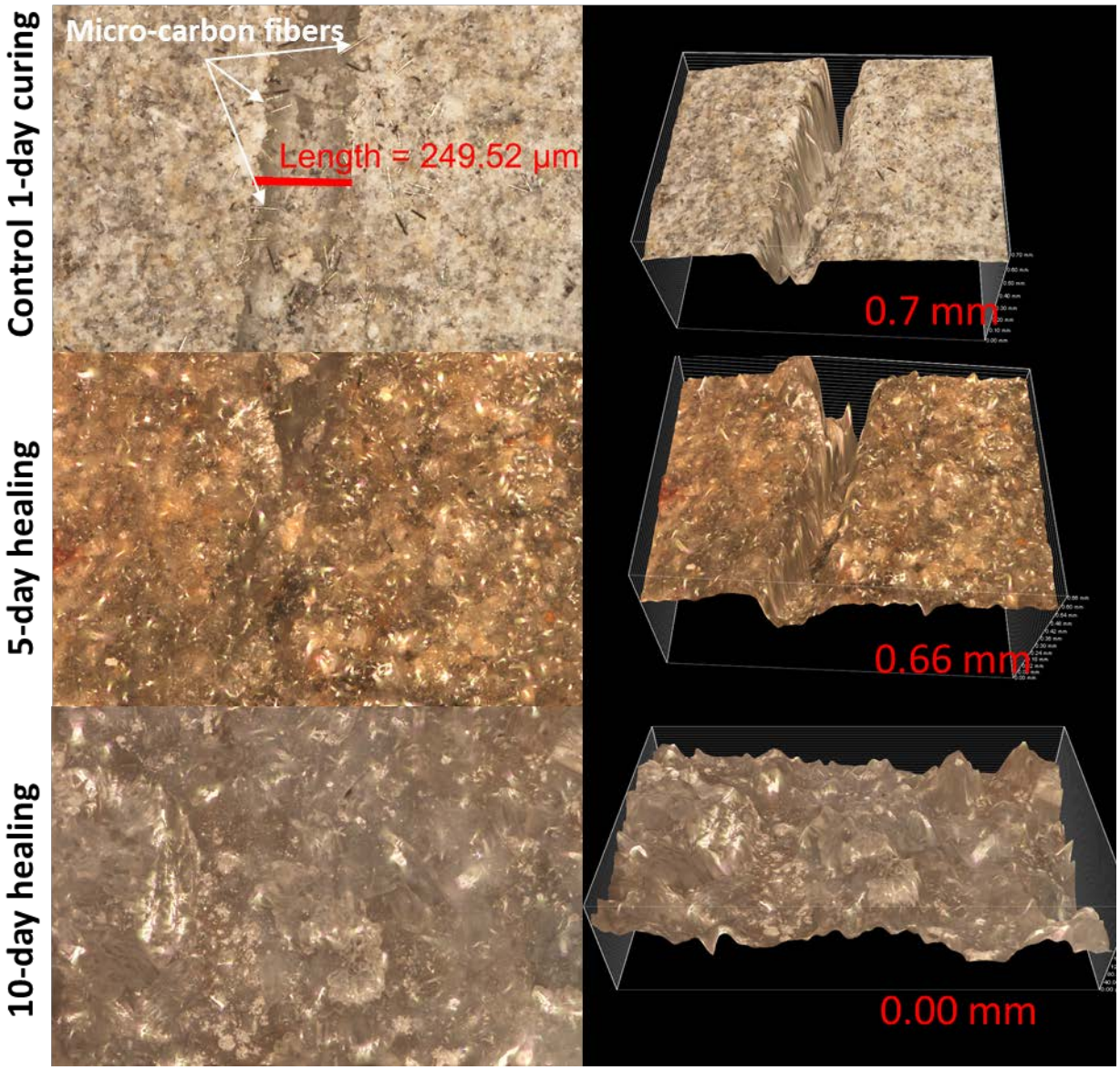

Figure 24. 1-day 300ºC plain water-cured TSRC sample after been damaged (crack size ~0.25 mm width and 0.7 mm deep) and healed for another 5 or 10 days under the same conditions.

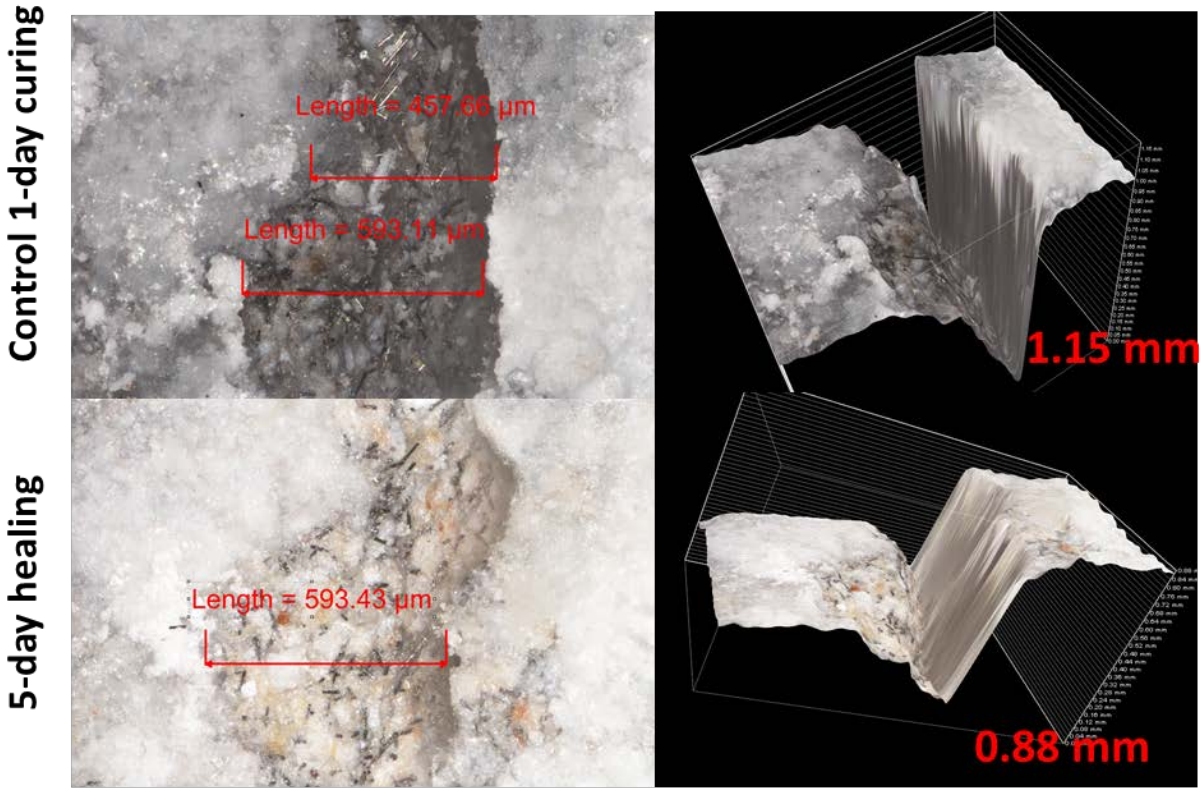

Figure 25. 1-day 270°C brine-cured TSRC sample after been damaged (crack size varies in width and is 1.15 mm deep) and healed for another 5 days under the same conditions.

TSRC's ductile nature and carbon fibers incorporated into the composite controlled the size of the cracks, preventing formation of wide deep fractures. The size of a typical crack was 0.1 – 0.3 mm wide and 0.3– 0.1 mm deep. The rate of the sealing depended on the crack size and the hydrothermal environment. As is evident from the comparison of the 3D images, the fastest sealing occurred in alkali carbonate and the slowest in geothermal brine. The sealing process in 300°C plain water environment proceeded at intermediate rate. In this environment, the crack size gradually decreased during continuous curing and the crack of ~ 0.25 mm wide and 0.7 mm deep was completely sealed with new reaction products in 10 days (Figure 24).

For 5-day healed samples in geothermal brine environment at 270°C (Figure 25), the crack before healing treatment was wider than that of water-cured samples. Although some precipitation of the crystals was observed in the cracks, there was no crystal growth on the sides of them. As a result, the width of the crack did not decrease during the short-term healing treatment of 5 days, suggesting that a longer healing time may be required for cracks sealing. In contrast, the alkali carbonate environment (Figure 26) was the most favorable for rapid cracks' sealing in damaged TSRC samples. Cracks of various sizes formed in the samples were filled after only 1 day under this condition.

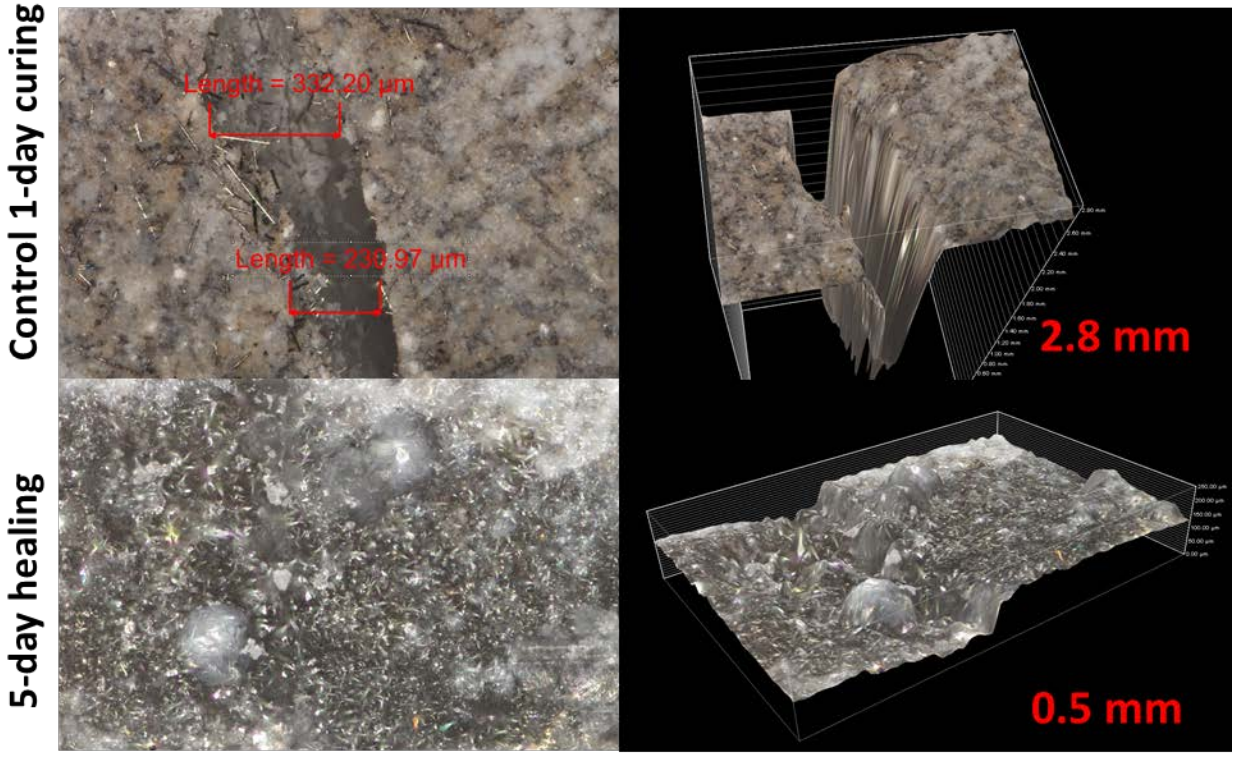

Figure 26. 1-day 270°C alkali carbonate-cured TSRC sample after been damaged (crack size varies in width and is 1.15 mm deep) and healed for another 5 days under the same conditions.

To better understand the rate of crack sealing under different environments, the changes in the surface area of crack as a function of healing time were computed for samples with artificial cracks made by the insertion of Teflon sheets of 0.5 or 0.25 mm thicknesses into the slurries (Figure 27). Although these artificial cracks made by Teflon sheets differ in the physicochemical nature including surface-chemistry and -area (physical roughness) of interior walls from those of natural cracks developed under the compressive loading, we employed the artificial cracks in this study.

Figure 27. Cement sample with a Teflon sheet of 0.5 mm thickness to create a well-defined artificial crack of 0.5 mm wide and about 2 mm deep.

Figure 28 illustrates an example of area evaluation for a TSRC sample with a crack of 0.5 mm width cured under carbonate conditions. To simplify the area evaluations of the micro-cracks, flattened images were adapted.

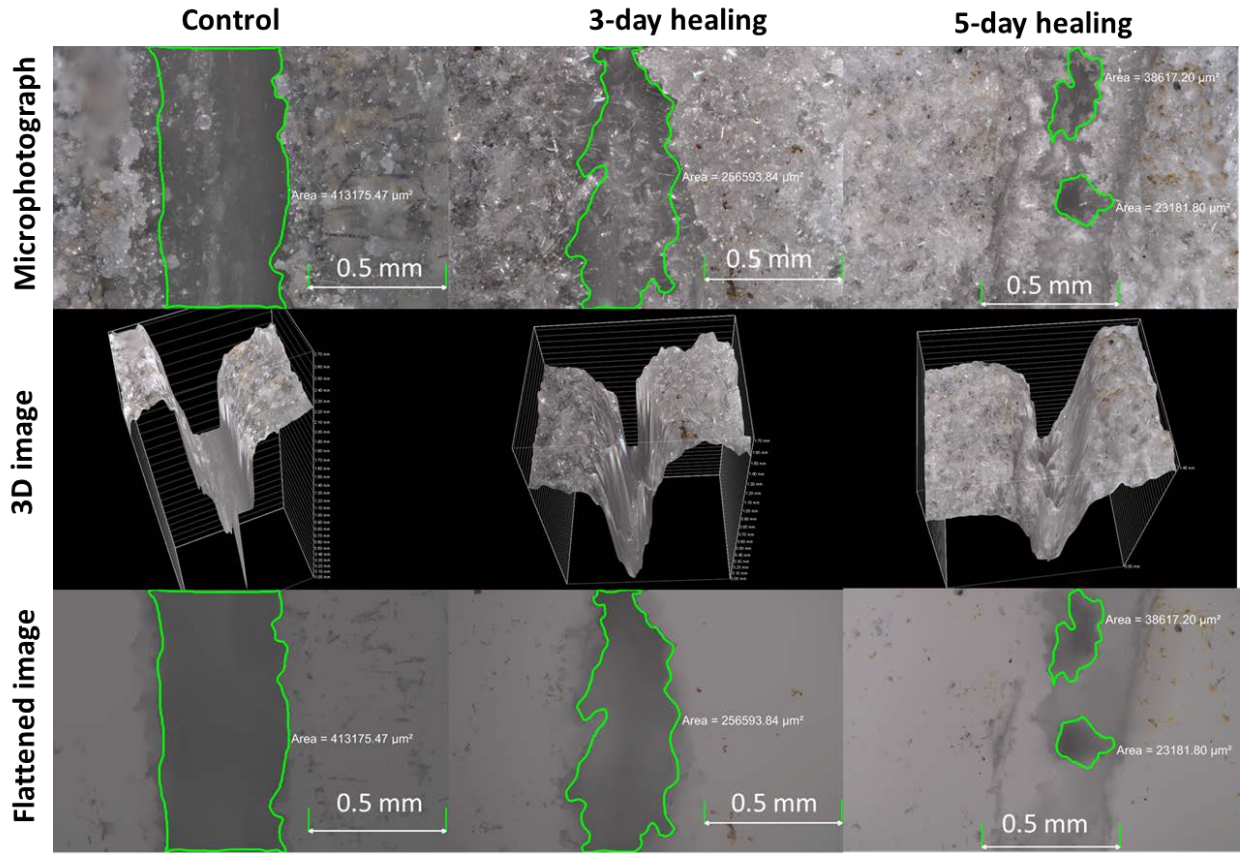

Figure 28. Evaluation of changes in cracks' areas with healing time for artificial 0.5 mm wide crack using microphotographs and flattened images.

Figure 29 depicts the changes in cracks' areas as a function of healing time for TSRC samples cured under geothermal brine, water or alkali carbonate environment. The cracks were made with a 0.5 mm wide sheets for all three environments. For comparison, 0.25 mm-wide crack sealing in alkali carbonate is also given on the graph. The data clearly demonstrate that the carbonate environment provided the fastest crack sealing for the large 0.5 mm cracks. It took 5 days to initiate the reduction of the crack's area in plain water environment. On the other hand, no significant change in crack's area was observed in bine environment for up to 8 days. Sealing of a small 0.25 mm-wide crack in carbonate was noticeably faster than for 0.5 mm crack in the first 3 days showing importance of the crack size for a fast healing process. Nevertheless, both cracks were completely sealed after 8 days.

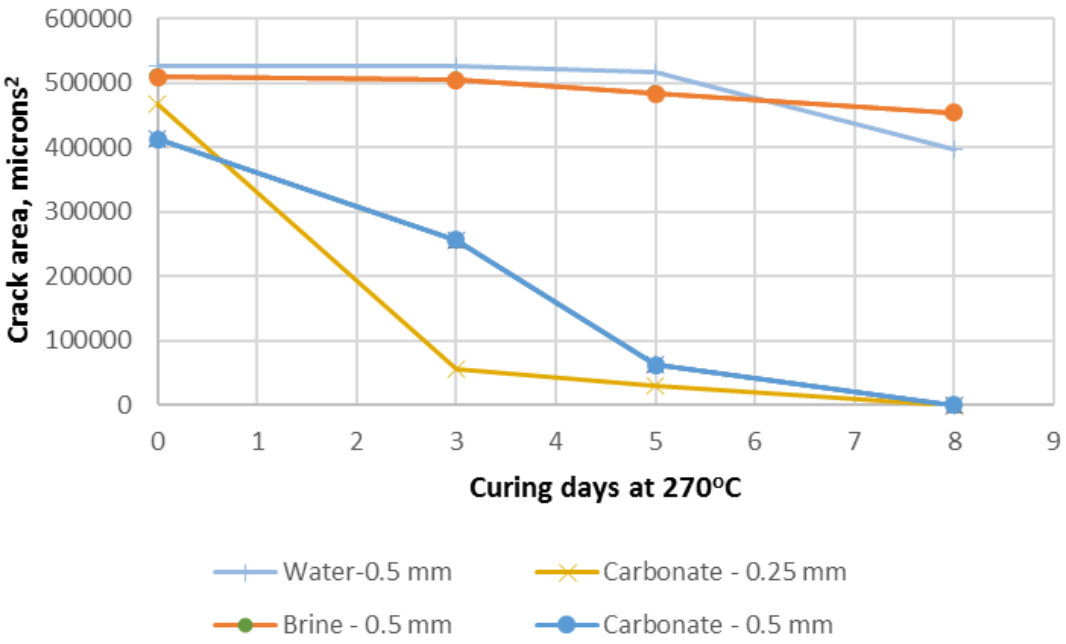

Figure 29. Changes in the artificial cracks' areas with curing time for TSRC samples cured under geothermal brine, water and alkali carbonate environments.

3.3.2. XRD study for samples with artificial cracks after 5 days healing treatment under plain water, alkali carbonate and geo-brine environments at 270°C

Table 5 summarizes the major crystalline phases of TSRC samples after 5 days of healing under water, carbonate or brine environment. The major crystalline phases under both water and alkali carbonate included feldspar mineral dmisteinbergite (anorthite); aluminum oxide hydroxide, boehmite, zeolite analcime, silica, and feldspathoid minerals, carbonated calcium-aluminum-silicate and cancrinite. Garnet, hydrogrossular was present as a minor phase with the most intense *d-spacing* peaks in carbonate environment (major peak at 2Θ ~33.34). Also, in carbonate, TSRC showed some presence of an additional zeolite, sodalite and peaks of alkali feldspar albite. All samples contained non-reacted corundum from CAC, Secar #80.

Among these minerals, feldspar and hydrogrossular were responsible for strengthening the matrix in TSRC composite, while analcime and silica crystalline phases formed in the pore solution preferentially precipitated in cracks, leading to the sealing effect. Carbonated product, cancrinite and aluminum oxide hydroxide, boehmite, detected both in the matrix and at the surface, likely contributed to both strengthening and sealing processes.

When healing treatment time was extended from 5 days to 20 days, the carbonate-cured samples showed significantly higher intensity of silica, cancrinite and albite peaks, moderately intense boehmite, and decreased signal intensities of dmisteinbergite peaks. The surface samples' peak intensities of analcime crystals of carbonate-exposed samples significantly decreased, while cancrinite peaks appeared. Boehmite content increased both in matrix and surface samples.

Alkali carbonate reacts with both the non-reacted blend components and the reaction products that contain calcium to form calcium carbonate which eventually changes in soluble bicarbonate,

$Ca(HCO_3)_2$, after longer carbonate exposure. In this process, the sodium, aluminum hydroxide and silicic acid ions are released into the pore solution or cracks. These released reactive ionic species lead to the formation and precipitation of large analcime crystals, silica and boehmite contributing to crack sealing. Later, analcime crystals present at the surface sites undergo the phase transformation by carbonate attack into cancrinite. Also, the feldspar suffers from carbonation-caused decalcification, following by the conversion of the Ca-lack feldspar into albite calcian as intermediate phase. A further Na-based alkali carbonation of albite calcian results in the formation of albite (possibly sanadine), $Na(AlSi_3O_8)$.

Based on this information, Figure 30 presents possible high-temperature alkaline carbonate phase transitions of TSRC samples. As seen in figure, the feldspar transformation likely takes place through a series of steps that decrease calcium content of the mineral. Similarly, as carbonate attack continuous sodium replaces calcium in cancrinite.

On the other hand, as more FAF were decomposes both in plain water and carbonate, reactive silicon and aluminum contents further increase in pore solution. Correspondingly, new boehmite and tohdite phases derived from aluminum hydroxide coexisting with crystalline silica form not only in the matrix, but also participate in the cracks.

Table 5. Major crystalline phase compositions of TSRC samples after 5 days healing treatment under plain water, alkaline carbonate or geothermal brine environments at 270ºC.

Plain Water
Corundum Al_2O_3 (04-006-9359) Silica SiO_2 (01-077-8620) Dmisteinbergite/anorthite $Ca(Al_2Si_2)O_8$ (04-011-6236/04-015-1492) Analcime $Na_{7.2}(Al_{7.2}Si_{16.8}O_{48})(H_2O)_8$ (04-013-2036) Cancrinite $Na_{6.02}Ca_{1.52}(Al_6Si_6O_{24})(CO_3)_{1.52}(H_2O)_{1.44}$ (01-075-8620) Tohdite $Al_5O_{7.5}(H_2O)_{0.5}$ (04-012-1638) Bohmite AlOOH (01-074-2897) Grossular hydroxylian $Ca_3Al_2(SiO_4)_2(OH)_4$ (00-042-0570)
Alkali Carbonate
Silica SiO_2 (04-011-9932) Corundum Al_2O_3 (04-006-9359) Cancrinite $Na_{6.02}Ca_{1.52}(Al_6Si_6O_{24})(CO_3)_{1.52}(H_2O)_{1.44}$ (01-075-8620) Dmisteinbergite $Ca(Al_2Si_2)O_8$ (04-011-6236) Grossular hydroxylian $Ca_3Al_2(SiO_4)_2(OH)_4$ (00-042-0570) Sodalite (Na,Ca) $(Na_{0.4}Ca_{0.3})_6(AlSiO_4)_6(H_2O)_8$ (01-073-5298) Bohmite AlOOH (01-074-2895) Tohdite $Al_5O_{7.5}(H_2O)_{0.5}$ (04-012-1638) Analcime $Na_{7.2}(Al_{7.2}Si_{16.8}O_{48})(H_2O)_8$ (04-013-2036) Albite $NaAlSi_3O_8$ (01-071-1152)

Geo-brine

Corundum Al_2O_3 (04-015-8996)
Dmisteinbergite $Ca(Al_2Si_2)O_8$ (04-011-6236)
Bohmite AlOOH (01-074-2900)
Tohdite $Al_5O_{7.5}(H_2O)_{0.5}$ (04-012-1638)
Cristobalite SiO_2 (04-018-0237/ 04-018-0233)
Magnetite Fe_3O_4 (01-082-3509)
Possible: Akermanite $Ca_2Mg(Si_2O_7)$ (01-077-9261), magnesioferrite (04-012-0929), majorite $Mg_3Fe_2(SiO_4)_3$ (00-025-0843), tetramajorite $MgSiO_3$ (00-047-1750)

In contrast, the major differences of brine-healed samples included the absence of analcime peaks and very weak intensity of silica and cancrinite peaks, as well as increased boehmite peaks' intensities. Since cancrinite is derived from carbonation of analcime, the low intensity of its peaks can be explained by the absence of analcime. It is possible that magnesium-containing minerals such as akermanite (ICDD: 01-077-9261), magnesioferrite (ICDD: 04-012-0929) and garnet group minerals, majorite (ICDD: 00-025-0843) and tetramajorite (ICDD: 00-047-1750), form in the brine environment. However, their major peaks strongly overlap with other phases and only shoulders (2Θ: 31.01, 48.47) and small peaks at 2Θ: 36.59 and 39.8 that were more pronounced in the brine-healed samples could be indicative of their presence. These minerals would be mostly responsible for strength recovery of samples treated in brine but would not contribute to the cracks' sealing. For the latter, the fact that there were no phases that form in pores through precipitation (silica and analcime), is consistent with the observed poor fracture-sealing in brine environment.

Matrix:

$CaAl_2Si_2O_8 + Na_2CO_3 + 8H_2O \rightarrow CaCO_3 + [2Na^+ + 2Al(OH)_4^- + H_3SiO_4^- + H_2SiO_4^{2-} + HSiO_4^{3-}]$

$CaCO_3 + Na_2CO_3 + 2H_2O \rightarrow Ca(HCO_3)_2 + 2Na^+ + 2OH^-$

Feldspar ($CaAl_2Si_2O_8$) → Albite calcian → Albite ($Na(AlSi_3O_8)$)

Cracks/pores:

Zeolite analcime ($Na_8Al_8Si_{16}O_{48}(H_2O)_8$) → Na-Cancrinite ($Na_8(AlSiO_4)_6(CO_3)(H_2O)_2$

$H_3SiO_4^- + H_2SiO_4^{2-} + HSiO_4^{3-} \rightarrow 3SiO_2 + 6H_2O$

Figure 30. Possible phase transitions of products formed on **surfaces of reacting blend components** (feldspar minerals) and products precipitating in **pores** (analcime and silica) under alkali carbonate at 270°C.

3.3.3. SEM-EDX study of samples healed in carbonate at 270°C

The results of SEM-EDX analyses of carbonate-cured samples agreed with the above interpretation of XRD patterns showing significant silica and analcime precipitation in the cracks of TSRC samples made with a 0.5 mm Teflon-sheet (Figure 31). The photo image shows that a 0.5 mm crack was completely sealed in 8 days under alkali carbonate conditions and the elemental composition analyses indicates silicon as the major element in the crack along with some aluminum, iron and potassium (sodium was not measured by this instrument) (Figure 31a). SEM photographs revealed a large silica precipitation in the cracks (Figure 31b). In addition to analcime and silica, some amorphous phase formed in the fractured area. This phase was rich in silicon and aluminum (Figure 31c). Importantly, the microphotograph shows carbon microfibers covered with some cementitious material and analcime crystals growth around them with formation of a coherent re-enforced structure (Figure 31d). Elemental composition analyses of the carbon fibers' surfaces and prints left after the fibers were pulled out of the cement matrix demonstrated that aluminum played an important role in providing good bonding to the fibers. In fact, as seen in Figure 32, the prints had lower than average, whereas fiber surfaces had higher than average aluminum content suggesting that aluminum remained bound to the fibers after they got detached from the matrix. Moderate fibers interaction with the cement matrix helped to

prevent cracks development and propagation, allowing formation of slimmer fractures that were easier to heal.

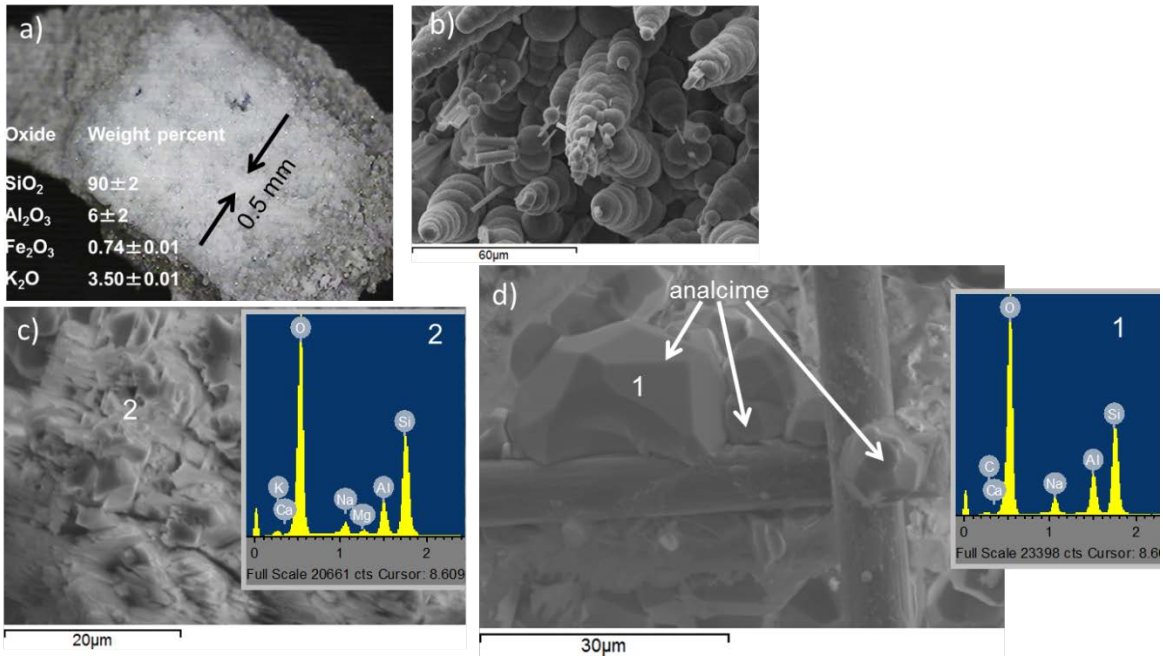

Figure 31. TSRC cracks filling in alkali carbonate at 270ºC, 8-day curing: a) a photograph of a 0.5-mm crack filled with new phases and phase composition of the material in the crack; b) a microphotograph of silica filling the crack; c) a microphotograph of an amorphous phase and its elemental composition for crack filling material; d) a microphotograph and elemental composition of analcime crystals attached to carbon microfibers in a crack area.

3.4.Study of self-healing mechanisms for CAP-B

To understand the self-healing mechanisms of CAP-B (CAC-Fondu/FAF/SHMP), we used MCF-reinforced SHMP-free Fondu/FAF (CAC/FAF) composite for comparison. Both CAP-B and CAC/FAF composites were prepared by autoclaving in 300ºC-1-day plain water. The healing treatment was performed by exposing the composites to plain water for 5 days at 300ºC.

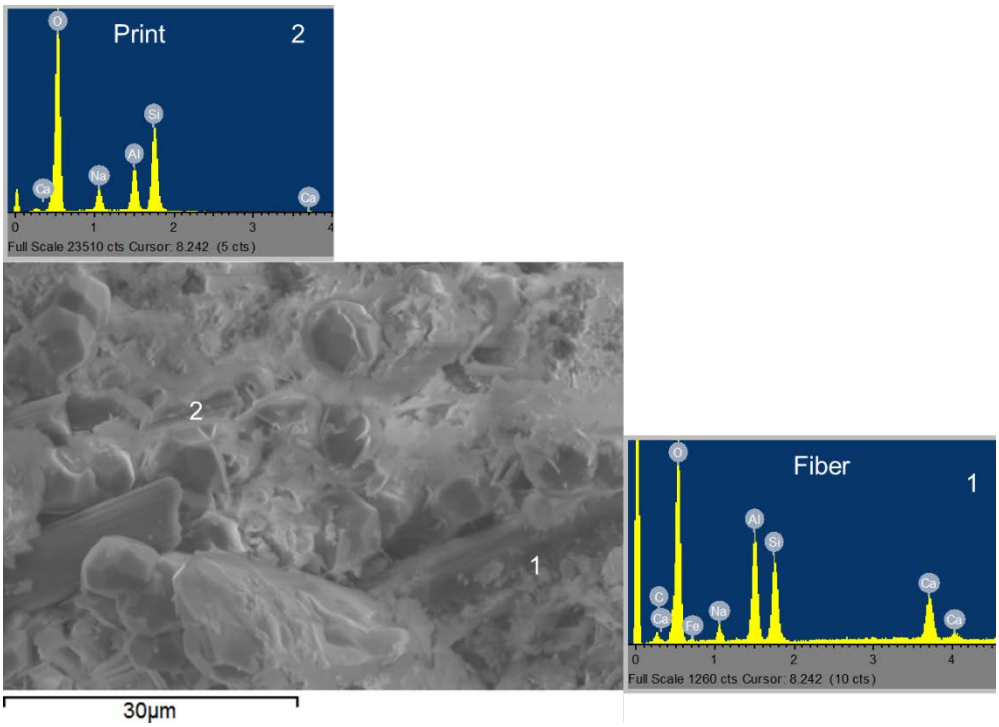

Figure 32. Microphotograph and elemental compositions of carbon fiber surface and print left after the fiber was pulled out of the matrix.

3.4.1. Compressive strength and its recovery

After a day curing at 300°C, the compressive strength of CAC/FAF reference samples was 1700 psi. When this composite was modified with SHMP chemical reactant, this strength increased by 1.6-fold to 2730 psi, strongly demonstrating that SHMP significantly enhances the strength of CAC/FAF blend. It should be noted that the compressive damage of the reference samples was typical of weak composites breaking into crumbles. Thereafter, these damaged CAP-B and CAC/FAF samples were autoclaved at 300°C for 5 days before repeated strength measurements. The results revealed that the compressive strength of the 2nd time cracked CAC/FAF reference was 710 psi, corresponding to only 42% recovery. In contrast, the recovery of CAP-B was as high as 63%.

3.4.2. Surface analyses -3D micro-imaging, Raman spectroscopy, and SEM-EDX

The original cracks of the damaged CAP-B samples were studied after the 5-day repeated exposure by 3D micro-imaging and Raman mapping. For the 3-D analyses two cracks were examined for sealing and plugging (Figure 32). The first crack was 0.31- 0.37 mm wide and 1.24 mm deep (Figure 32). The second crack was smaller – 0.21-0.29 mm wide and 0.81 mm deep. After the 5-day healing period under the initial curing conditions the depths of the cracks strikingly reduced by 2.5 and 1.7 times to 0.5 and 0.45 mm respectively. No further experimental work was done to determine the time for a complete cracks sealing. For crumbled CAC/FAF references, it was very difficult to verify whether cracks were sealed because originally developed cracks disappeared under the crumbling fragments during the healing period.

Figure 33 shows typical Raman mapping results of crack-sealing phases. The data revealed the presence of three crystalline phases, boehmite (γ-AlOOH), hematite (Fe_2O_3), and zeolite analcime ($Na_2Al_2Si_4O_{12}.2H_2O$). As is evident from the predominant pink color that represents analcime and the two typical point spectra of CAP-B showing a major analcime peak, this high-temperature stable zeolite was the major crack sealing phase. Analcime forms through reactions of sodium from SHMP with silica-aluminates of FAF. It may form through surface- or dissolution-precipitation reactions. The other sealing phase identified in the cracks was hematite due to the oxidation of the iron from CAC and/or FAF. The minor sealing phase was boehmite derived from dissolution-precipitation of CAC after calcium removal through the chemical reactions with SHMP to form CAP binder and from hydration of corundum (Al_2O_3) in CAC. Nonetheless, analcime appeared to play the major role in sealing the cracks generated in CAP-B composites after the short curing time of 5 days, possibly contributing to the strength recovery of damaged composites. This result agrees with the study of alkali-activated TSRC composites [70]. Namely, FAF acted as autonomic healing aid for both CAP-B and Na alkali-activated TSRC composites.

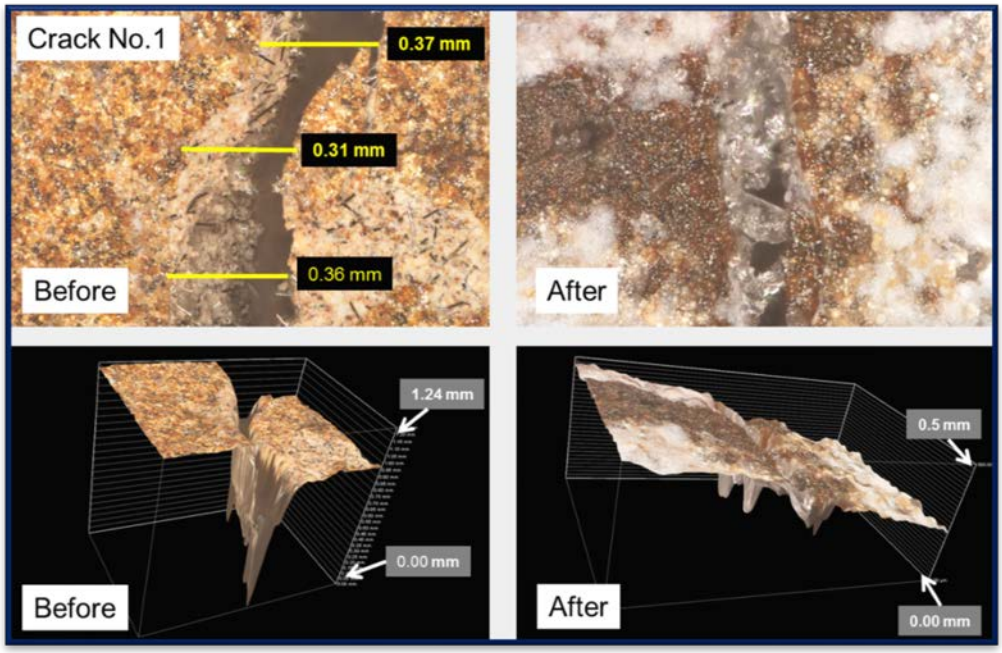

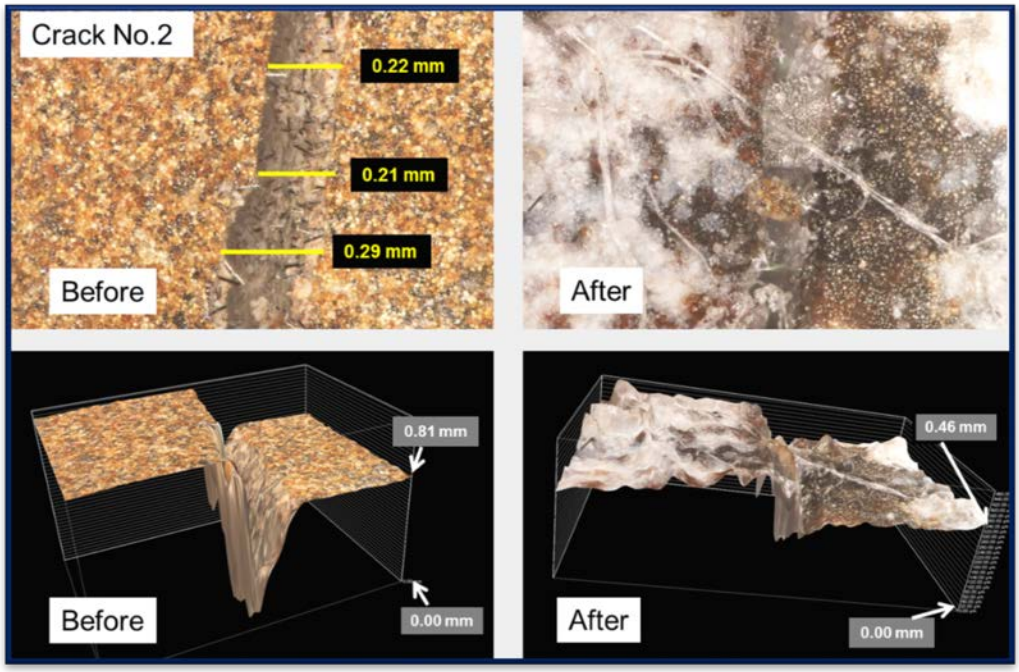

Figure 32. Micro-3D image analysis for assessing the crack-sealing effect of CAP-B after exposure in 300°C plain water for 5 days.

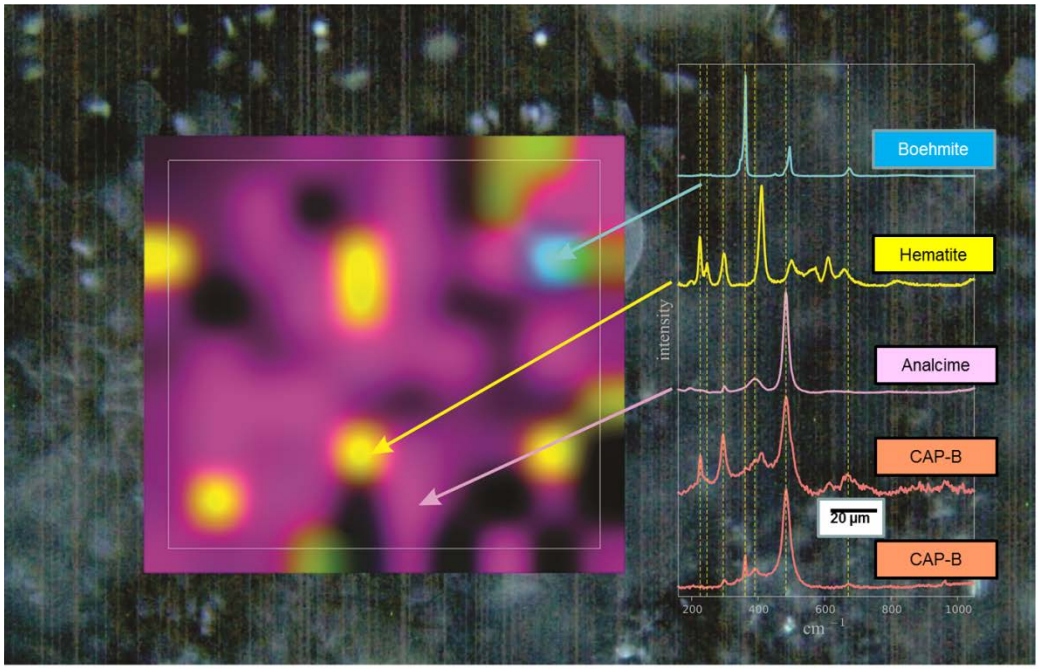

Figure 33. Raman mapping of crystalline phases occupying the surface of the sealed crack of CAP-B.

The cracks surface and underlying compositions of self-sealed samples were studied by SEM image analysis coupled with EDX elemental survey to support information obtained by Raman spectroscopy. The surface image (Figure 34) disclosed dense cubic crystals typical for well-formed analcime. Correspondingly, EDX spectrum involved five major elements, Na, Al, Si, K, and Fe; the first three elements belonging to analcime and the last two, K and Fe, coming from FAF. Au signal on the spectra came from the conductive gold coating employed to decrease the charging effects. The microstructure developed underneath the surface of the sealed cracks (Figure 35) disclosed the presence of three different morphologies. One was the intergrown rosette-like crystalline structures (area A); the second looked like almost spherical microparticles (area B); and, the third one was amorphous (area C). Correlating these morphologies with EDX results, the crystals in area A were assigned to the feldspar mineral, dmisteinbergite, and the spherical particles were identified as precursors of analcime crystals. Amorphous composite phases including Na_2O, CaO-Al_2O_3 –SiO_2 system were formed in area C. Thus, although the surface layer of sealed cracks was primarily occupied by analcime formed by the interactions between SHMP and FAF, the underlying calcium-aluminum silicate phases involved calcium from CAC.

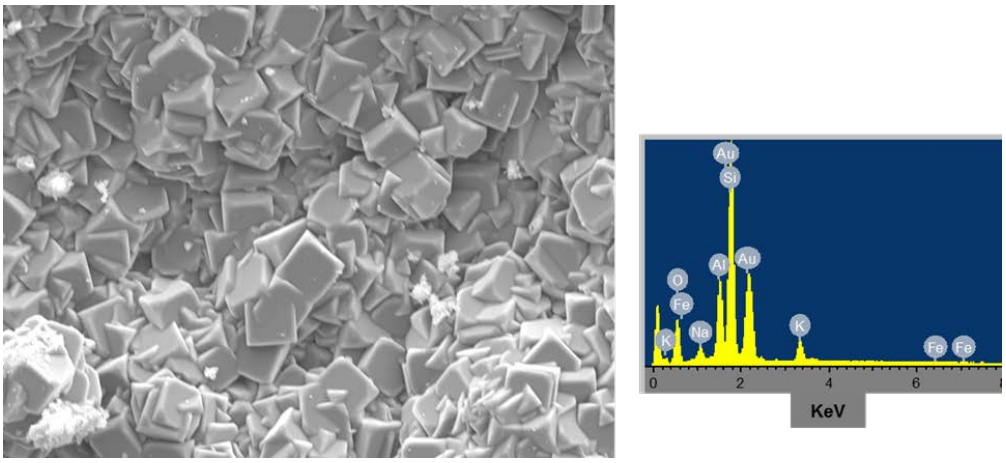

Figure 34. SEM image analysis coupled with EDX elemental survey for self-healed crack surfaces.

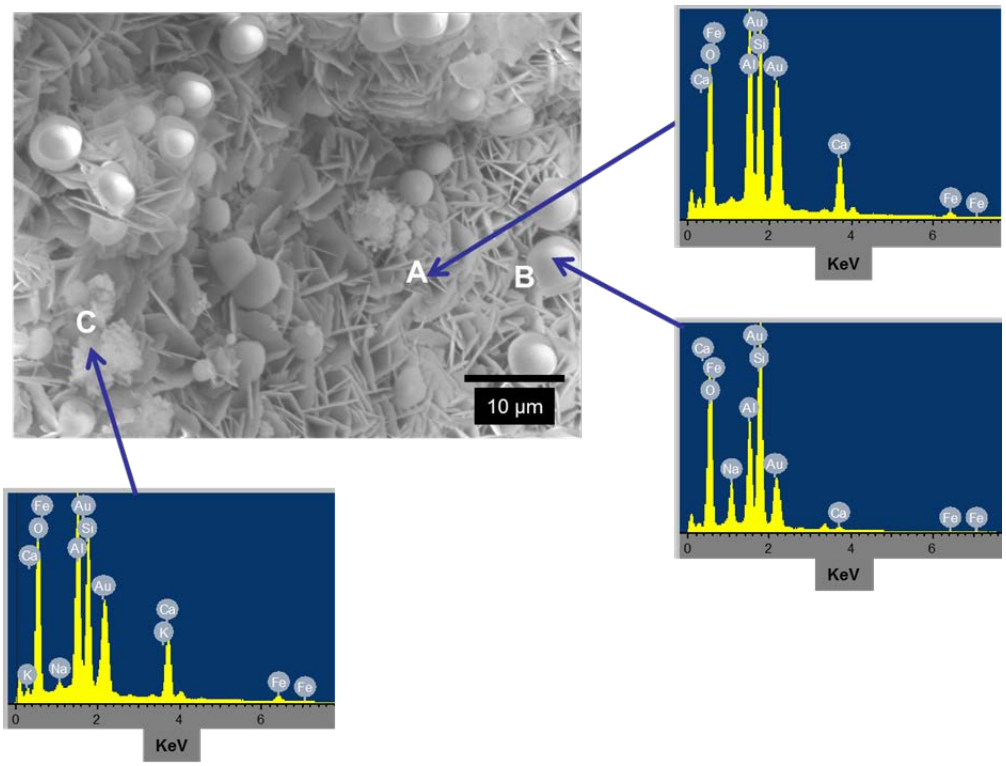

Figure 35. SEM-EDX data for samples taken from the underneath of the self-sealed cracks' surfaces.

3.4.3. Matrix analyses –XRD, FTIR, and SEM-EDX

The recovery of compressive strength is likely due to the sealing effects of cracks, and the strength improvement of matrix itself during the 5-day healing period at 300°C. Since the following three factors, 1) matrix continuous hydration, 2) phase transitions, and 3) microstructural development, are considered as the contributors to this strength improvement, our study next was directed towards obtaining information on the phase-compositions and microstructure development for CAP-B and reference core samples before and after the healing treatment, using XRD, FTIR and SEM-EDX methods

Table 6 summarizes major and minor crystalline phases, determined by XRD analyses, along with their ICDD numbers for CAC/FAF reference. For the samples before the self-healing, three major products, feldspar mineral, dmisteinbergite ($CaAl_2Si_2O_8$) and garnets, andradite ($Ca_3Fe_2Si_3O_{12}$) and aluminian andradite ($Ca_3Al_{0.84}Fe_{1.16}Si_3O_{12}$), were detected. After the self-healing, there were three main differences in the major crystalline phases. Firstly, two minor garnet phases, hydrogrossular $[Ca_3(Al_{0.849}Fe_{0.151})_2((SiO_4)_{2.43}(O_4H_4)_{0.57}]$ and grossular $[Ca_3Al_2(SiO_4)_2(OH)_4]$, became the major phases along with the earlier present andradite; secondly, margarite-2M1 $[Ca(Al_2Si_2O_{10})(OH)_2]$, mica group mineral, formed as a new major phase; and thirdly, the dmisteinbergite signals decreased, the mineral was not the major phase anymore. Thus, the combination of these three garnets and mica phases contributed to the recovery of the lost strength.

Table 7 lists the major and minor phases of CAP-B before and after the self-healing at 300°C. Three new products formed in the presence of SHMP in this blend along with the phases

detected in the reference sample. These new phases were hydroxyapatite [$Ca_5(PO_4)_3(OH)$] and carbonatious Na-hydroxyapatite [$Na_{0.4}Ca_{4.2}(PO_4)_{1.8}(CO_3)_{1.2}(OH)$] apatite group minerals, and analcime [$Na_2Al_2Si_4O_{12}.2H_2O$], a zeolite. Relating this result to the strength development, it can be noted, that the combination of apatite- and zeolite- group minerals formed in CAP-B resulted in a far better compressive strength development than the combination of dmisteinbergite, andradite, and aluminian andradite in the reference. After self-healing, there were two changes in the major phase composition. The first one was the disappearance of carbonatious Na-hydroxyapatite, analcime, and andradite; the other was the formation of hydrogrossular as a new phase. Since this cement displayed an excellent strength recovery, the principal contributors to this recovery was a well-formed hydroxyapatite. In contrast, the effectiveness of three garnets and mica phases formed in the reference after self-healing in recovering strength was less than that of apatite phase. Interestingly, there was no analcime after the self-healing treatment in the CAP-B, suggesting that analcime phase responsible primarily for crack's sealing had no effect on the strength recovery of cement cores. Additionally, boehmite that was found to be a minor crack-sealing reaction product did not contribute significantly to the strength recovery because it was formed as a minor phase. Thus, it is possible to rationalize that the reaction products contributing to the sealing effect differed from those assisting in the strength recovery of cement matrix.

Table 6. Major and minor phases formed in CAC/FAF reference samples before and after self-healing at 300°C.

Before self-healing (1-day 300ºC)	
Major phases (ICDD numbers)	**Minor phases (ICDD numbers)**
Dmisteinbergite $CaAl_2Si_2O_8$ (04-011-5220) Andradite $Ca_3Fe_2Si_3O_{12}$ (04-009-8467) Aluminian Andradite $Ca_3Al_{0.84}Fe_{1.16}Si_3O_{12}$ (01-085-1370)	Hydrogrossular $Ca_3(Al_{0.849}Fe_{0.151})_2((SiO_4)_{2.43}(O_4H_4)_{0.57}$ (01-083-7408) Grossular $Ca_3Al_2(SiO_4)_2(OH)_4$ (04-013-2153) Boehmite $Al_2(OOH)_2$ (00-005-0190)
After self-healing (5 more days 300ºC)	
Major phases (ICDD numbers)	**Minor phases (ICDD numbers)**
Hydrogrossular $Ca_3(Al_{0.849}Fe_{0.151})_2((SiO_4)_{2.43}(O_4H_4)_{0.57}$ (01-083-7408) Grossular $Ca_3Al_2(SiO_4)_2(OH)_4$ (04-013-2153) Andradite $Ca_3Fe_2Si_3O_{12}$ (04-009-8467) Margarite-2M1 $Ca(Al_2Si_2O_{10})(OH)_2$ (01-076-0883)	Dmisteinbergite $CaAl_2Si_2O_8$ (04-011-5220) Sodium-aluminum-silicates $Na_8(AlSiO_4)_6(OH)_2$/ $Na_6Al_6(SiO_4)_6(H_2O)_8$ (00-040-0100/04-016-5725) Boehmite $Al_2(OOH)_2/AlO_{1.06}(OH)_{0.94}$ (00-005-0190/01-074-6248) Magnetite $Fe_3O_4/Fe_{2.962}O_4$ (01-082-3509/04-006-6550/010861346)

Table 7. Major and minor phases formed in CAP-B samples before and after self-healing at 300°C.

Before self-healing (1-day 300ºC)	
Major phases (ICDD numbers)	**Minor phases (ICDD numbers)**
Dmisteinbergite $CaAl_2Si_2O_8$ (04-011-5220) Hydroxyapatite $Ca_5(PO_4)_3(OH)$ (01-086-	Katoite $Ca_3Al_2(SiO_4)_{1.53}(OH)_{5.88}$ (04-014-9841) Monetite $CaHPO_4$ (04-009-3755)

0740) Carbonatious Na-hydroxyapatite $Na_{0.4}Ca_{4.2}(PO_4)_{1.8}(CO_3)_{1.2}(OH)$ (04-012-7002)	Tuite $Ca_3(PO_4)_2$ (04-020-6869)
Analcime (04-019-1439) $Na_2Al_2Si_4O_{12}.2H_2O$	Senegalite $Al_2(PO_4)(OH)_3\ H_2O$ (00-036-0409)
Andradite $Ca_3Fe_2Si_3O_{12}$ (04-009-8467)	Siderite $FeCO_3$ (01-077-8369)
Aluminian Andradite $Ca_3Al_{0.84}Fe_{1.16}Si_3O_{12}$ (01-085-1370)	Mgangnesian Senegalite $Fe_{0.65}Mg_{0.35}CO_3$ (01-082-9295)
	Magnetite Fe_3O_4 (04-015-3100)
	Ferrowyllieite $AlFe_2Na_2(PO_4)_3$ (00-039-0409)
After self-healing (5 more days 300ºC)	
Major phases (ICDD numbers)	**Minor phases (ICDD numbers)**
Dmisteinbergite (04-011-5220) $CaAl_2Si_2O_8$	Cristobalite-II SiO_2 (04-018-0239)
Hydroxyapatite $Ca_5(PO_4)_3(OH)$ (01-086-0740)	Bernalite $Fe(OH)_3$ (00-046-1436)
Hydrogrossular $Ca_3(Al_{0.849}Fe_{0.151})_2(SiO_4)_{2.43}(O_4H_4)_{0.57}$ (01-083-7408)	Berlinite $AlPO_4$ (01-076-5982)
	Ferrowyllieite $AlFe_2Na_2(PO_4)_3$ (00-051-0508)
	Boehmite $Al_2(OOH)_2$ (00-005-0190)
Aluminian Andradite $Ca_3Al_{0.84}Fe_{1.16}Si_3O_{12}$ / $Ca_3Fe_{1.5}Al_{0.5}(SiO_4)_{2.8}(OH)_{0.8}$ (01-085-1370/04-012-132)	Magnetite Fe_3O_4 (04-009-8443)

To support the above information, ATR-FTIR analysis was carried out on the samples used in XRD study. Figure 36 shows the ATR-FTIR absorption spectra in region of 1800 to 650 cm^{-1} for the FAF and CAC starting materials. The bands at 1039 and 776 cm^{-1} were assigned to the M-O (M: Si or Al) asymmetric ($V_{as\ M\text{-}O}$), and symmetric ($V_{s\ M\text{-}O}$) stretching vibrations, respectively, of M-O-Si linkages in aluminosilicate [71]. The bands at 796, 730, and 690 cm^{-1} belonged to quartz; namely, the first two bands were associated with Si-O symmetric stretching ($V_{s\ Si\text{-}O}$) and 690 cm^{-1} was Si-O bending ($\delta_{\ O\text{-}Si\text{-}O}$) vibrations. The CAC had the bands at 1473 and 1449 cm^{-1} attributed to C-O asymmetric stretching ($V_{as\ C\text{-}O}$) and at 999 cm^{-1} due to C-O symmetric stretching ($V_{s\ C\text{-}O}$) in carbonate CO_3^{2-} along with carbonate-related O-C-O bending ($\delta_{\ O\text{-}C\text{-}O}$) mode at 837 cm^{-1} [72–74]. The bands at 800, 777, and 720 cm^{-1} were from the Al-O bond vibration in "condensed" AlO_4 tetrahedra network of calcium aluminate as the principal mineralogical phase of CAC [75,76] and the 677 cm^{-1} band can be accounted for by the Al-O vibration in "condensed" AlO_6 octahedral structure. Also, the latter band possibly overlaps with the Fe-O bond vibration ($V_{\ Fe\text{-}O}$) in Fe oxide compounds [75,76].

Figure 37 illustrates the spectra of CAC/FAF blend before and after self-healing in the range between 4000 and 650 cm^{-1}. For the sample before the self-healing, the spectrum showed the presence of six different compounds in the cement. One was the water related directly to the bands of stretching O-H ($V_{O\text{-}H}$) vibration at 3627 cm^{-1} and H-O-H bending ($\delta_{\ H\text{-}O\text{-}H}$) vibration at 1637 cm^{-1}; the second was the boehmite (AlOOH) attributed to $V_{as\ O\text{-}H}$ at 3301 cm^{-1}, $V_{s\ O\text{-}H}$ at 3097 cm^{-1}, and $\delta_{\ Al\text{-}OH}$ at 1070 cm^{-1} [77–79]; the third was the carbonate (CO_3^{2-}) at 1418 cm^{-1} ($V_{as\ C\text{-}O}$) and at 838 cm^{-1} ($\delta_{\ O\text{-}C\text{-}O}$); the forth was silica-related compounds including amorphous silica gel at 1247 cm^{-1} ($V_{as\ Si\text{-}OSi}$) and the quartz at 736 and 673 cm^{-1}; the fifth was iron oxide ($V_{\ Fe\text{-}O}$) overlapping with silica at 673 cm^{-1}; and the sixth were iron-, and calcium-aluminosilicate [Fe_2O_3, $CaO\text{-}Al_2O_3\text{-}SiO_2$ (F,C-A-S)] structures at 895 cm^{-1} ($V_{as\ M\text{-}OSi,}$ M: Si or Al) as the most prominent band. These structures would be directly associated with the shift of the

aluminosilicate-related band at 1039 cm^{-1} of FAF starting material to 895 cm^{-1}. This means that the aluminosilicate of FAF hydrothermally reacted with Ca^{2+} and Fe^{3+} from CAC to form amorphous and crystalline F,C-A-S phases [59]. If this assumption is valid, F,C-A-S phases are associated with crystalline dmisteinbergite (C-A-S) and andradite (F-C-S and F-C-A-S) as the major reaction products identified by XRD. Also, the presence of boehmite phase confirmed the XRD result. The spectrum of the sample after the self-healing was similar to the original one, supporting the XRD finding of the crystalline F, C-A-S phases such as grossular (F-C-A-S) and andradite as major reaction products coexisting with boehmite as a minor one.

For CAP/FAF blend before self-healing (Figure 38), there were two main differences in the spectral features. One was the absence of boehmite-related bands in agreement with the XRD data; the other was the appearance of a new band at 1029 cm^{-1} representing $V_{as\ P\text{-}O}$ stretching mode in PO_4^{-3} group in conjunction with $V_{s\ P\text{-}O}$ stretching at 895 cm^{-1} [80–85]. The phosphate, PO_4^{-3} came from hydroxyapatite phase derived from the chemical interaction-hydrations of CAC and SP. This prominent band at 895 cm^{-1} also overlapped with possible crystalline F, C-A-S phases such as dmisteinbergite and andradite identified by XRD. Amorphous and crystalline (analcime) N, C-A-S phases formed by Na^{+} (from SP) and aluminosilicate (from FAF) reactions may also contribute to this band. The spectrum of the healed sample closely resembled that of the sample before self-healing, except for the emergence of boehmite-related bands at 3301, 3097, 1070, and 750 cm^{-1}, strongly supporting the XRD result.

As for the microstructure development, the core regions of self-healed cement (Figure 39) were constituted by two different morphologies, hexagon crystals belonging to dmisteinbergite phase at site A and plate-like crystals at location B. For the latter morphology, EDX indicated two major elements, Ca and P, reflecting the formation of hydroxyapatite phase. The crystals of hydroxyapatite were closely intergrown forming a dense matrix.

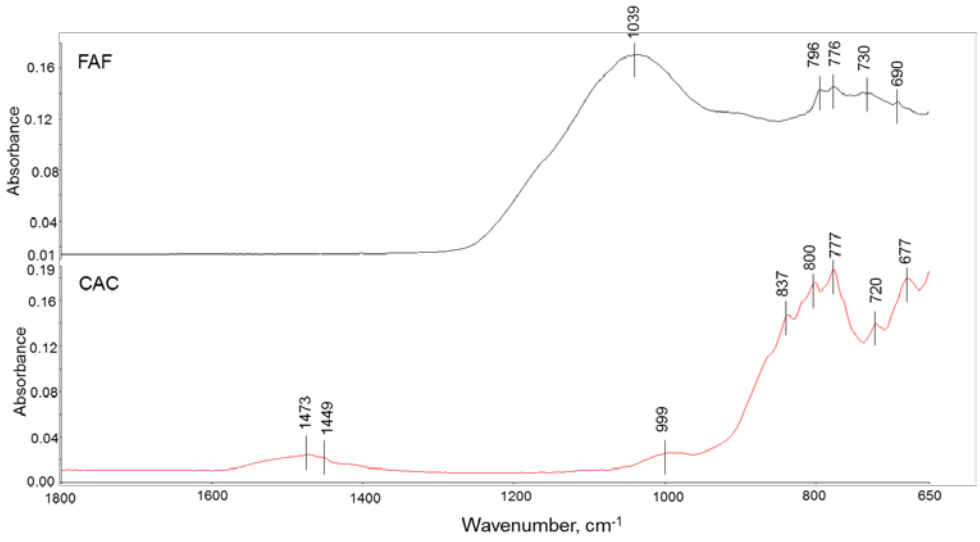

Figure 36. ATR-FTIR spectra of “as-received” FAF and CAC.

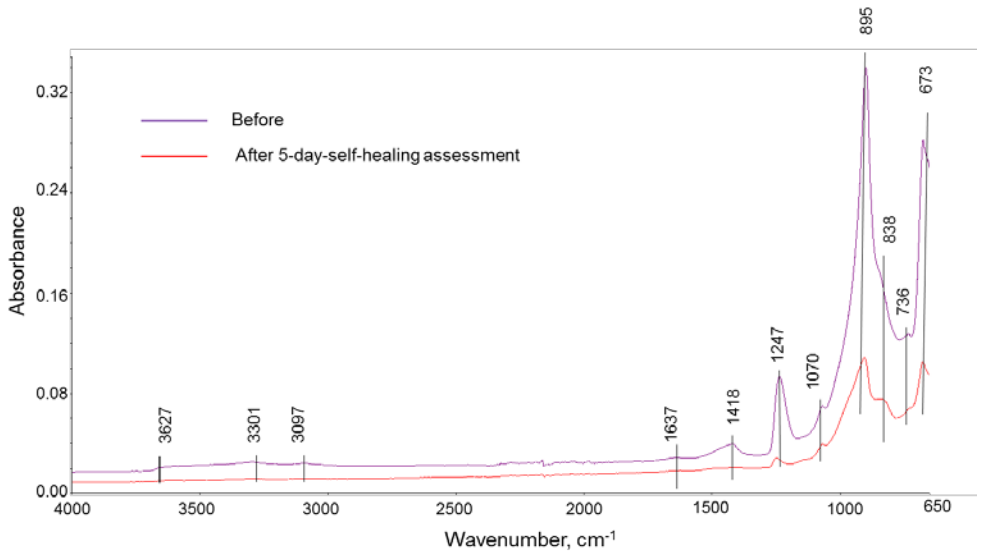

Figure 37. ATR-FTIR spectra of CAC/FAF reference before and after self-healing assessment.

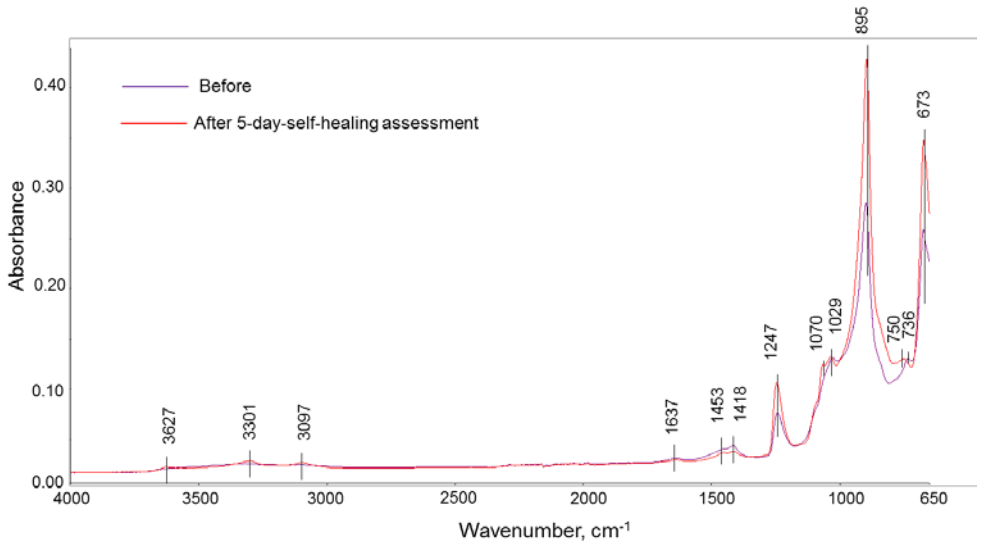

Figure 38. ATR-FTIR spectra of CAP-B before and after self-healing assessment.

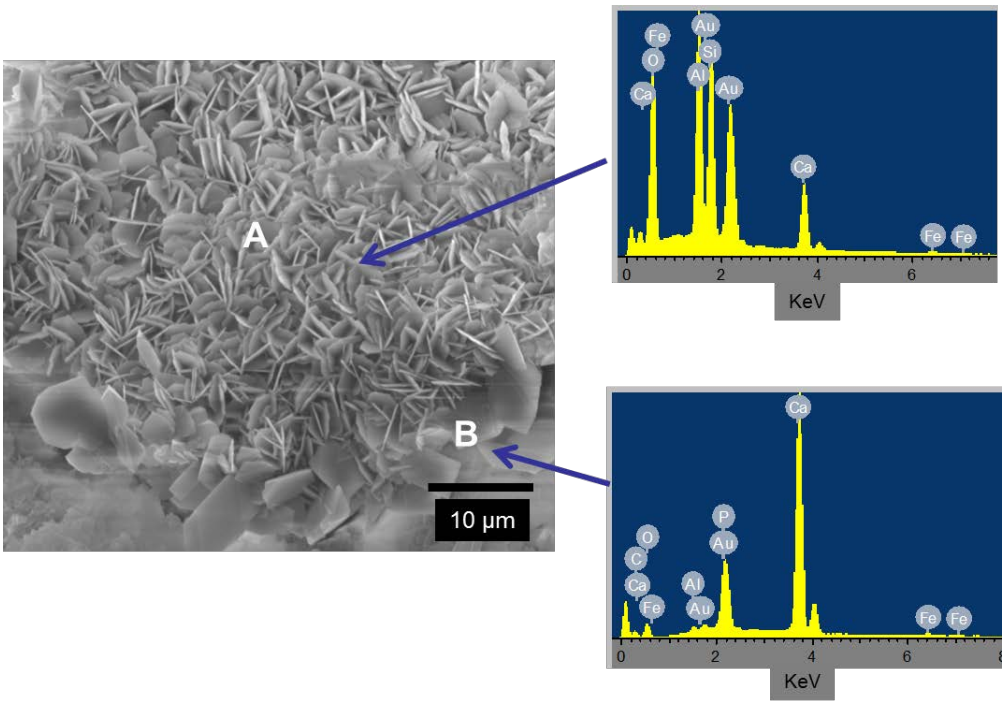

Figure 39. SEM-EDX result for the samples taken from the core region of self-healed CAP-B.

3.5. Evaluation of pozzolan additives as self-healing aides

3.5.1. Clays in natural pozzolans

To evaluate the natural pozzolan additives as self- healing aides after repeated damage, the fine clay minerals, bentonite, montmorillonite, and metakaolin, were incorporated at 5 and 10% by total weight of cement into dry OPC/SiO_2 and TSRC blends, followed by adding an appropriate water to these blends in preparing the cement slurries. Afterward, the slurries were autoclaved for 24 hours at 300°C in plain water. For OPC/SiO_2, the incorporation of 5wt% montmorillonite and 10wt% metakaolin offered improved compressive strength to nearly 4000 psi from 3420 psi for clay-free control (Figure 40). Unlike for OPC/SiO_2, these clays did not improve compressive strength of TSRC.

Figure 41 shows the strength recovery of 2^{nd}- and 3^{rd} time cracked composites with and without clays during self-healing at 300°C for 5 days in plain water treatment. For OPC/SiO_2 the most effective clay in enhancing the recovery of 2^{nd} and 3^{rd}-time cracked samples was 5wt% bentonite, which increased the recovery by 19% and 12% for the 2^{nd} and 3^{rd}- time cracked samples, in comparison with the control. The 10wt% metakaolin was not effective in improving the strength recovery of both 2^{nd} and 3^{rd}-time cracked samples.

The clays did not offer any improvement of strength recoveries for TSRC, for 2^{nd} and 3^{rd}-time cracked samples, reflecting a poor chemical affinity of clays with TSRC.

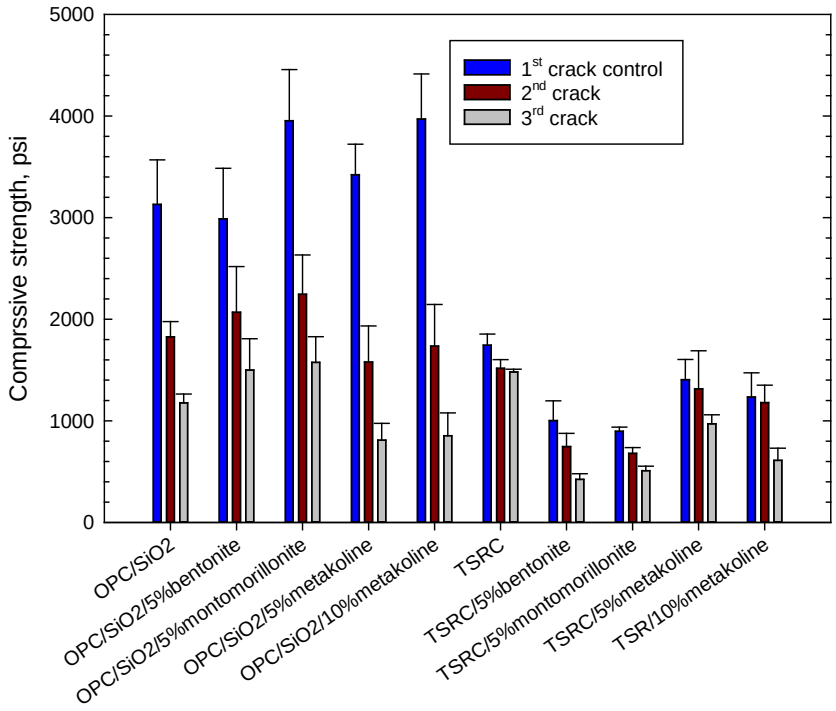

Figure 40. Compressive strength of the 1st-time cracked control, and self-healed 2nd- and 3rd-time cracked samples, containing clays, in plain water.

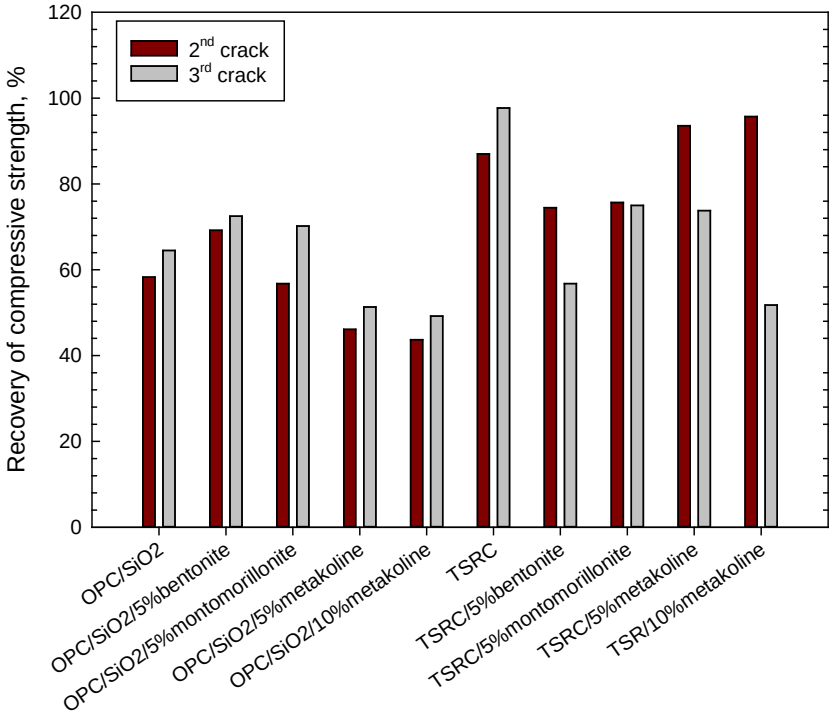

Figure 41. Strength recovery of the 2nd-and 3rd-time cracked OPC/SiO_2 and TSRC composites with clays in plain water.

3.5.2. Zeolites in natural pozzolans

Two types of naturel zeolites were used in this study on the ability of zeolites to promote self-healing of various composites: One zeolite was Clinoptilolite (Clin.); the other was Ferrierite (FER) As described in the introduction section, the zeolites containing plenty of pozzolanic siliceous or siliceous-aluminous reactants are susceptible to dissolution when they encounter alkaline reactants at high temperatures. Since the slurries of all composites, except for CAP, used in these screening tests, had pH >13, (pH of CAP slurry ranged from 8.5 to 9.5) it is possible to assume that zeolites were dissolved in these alkali slurries of the composites. Thus, in this work, we tested all composites including CAP-A and -B to obtain information on the ability of zeolites to improve the extent of self-healing.

3.5.2.1. Clinoptilolite (Clin.)

Figure 42 depicts the YM of various composites with and without Clin. cured in 300°C plain water for 24 hours. One character of all Clin.-incorporated composites was low YM; for instance, the moderate YM of TSRC and CAP-B shifted to soft YM region when Clin. was added, and furthermore, a brittle → moderate and very brittle → brittle mechanical transitions were observed when Clin. Was included into FAC/FAF and GBFS/SiO_2, respectively. Such transitions to lower YM can help restraining cracks' width and propagation, thereby improving self-healing effect for cracked composites.

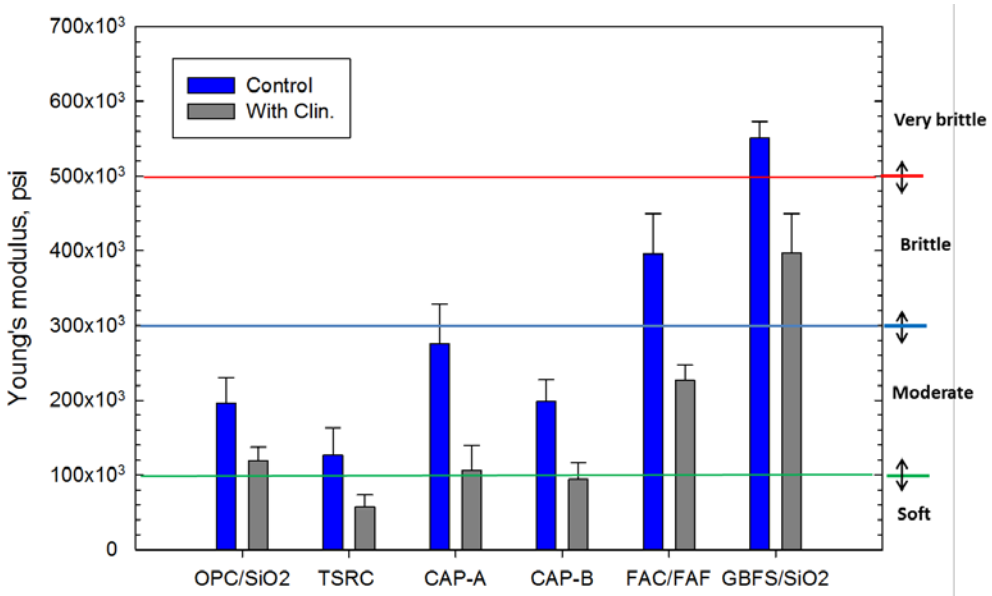

Figure 42. YM of Clin-free and Clin-modified composites after 24-hr curing in water at 300°C.

Figure 43 presents compressive strength of various composites with and without Clin. made by 300°C-1-day autoclaving before and after self-healing treatment in 300°C-5-day plain water. With Clin., the compressive strength was significantly reduced, ranging from 45 to 60% reduction for all composites, except for GBFS/SiO_2 with the strength reduction of 23%. The compressive strength of Clin-modified TSRC did not meet the material criterion of >1000 psi.

As described in section 2.2. addition of Clin. to the cements required nearly 11% increase in W/C ratio. Such increased water content along with the slow zeolite reactions that did not contribute to the strength at early curing times may be responsible for the strength reduction. Also, the dissolved Clin in composite slurry may act to inhibit the hydration of cementitious matrix at early autoclaving age.

All alkali-activated composites except for GBFS/SiO_2 displayed a great strength recovery of more than 85%; for TSRC the highest strength recovery of 168% was observed, leading to the increase in strength to 1210 psi after healing treatment from 720 psi before it (Figure 44). Interestingly, the recovery of Clin-modified CAPs with pH 8.5-9.5 was little or equal to that without Clin. The reason for this may be poor dissolution of Clin in such mild alkaline media. The GBFS/SiO_2 modified with Clin recovered only 40% of strength, compared with 76% recovery without Clin. No additional experimental work was done to understand a poor efficacy of Clin for GBFS/SiO_2.

The strength recovery involved the progressive cement hydration, reactions of non-hydrated and non-reacted cement-forming ingredients present in composite bodies and their interactions with decomposing zeolite during self-healing treatment period of 5 days.

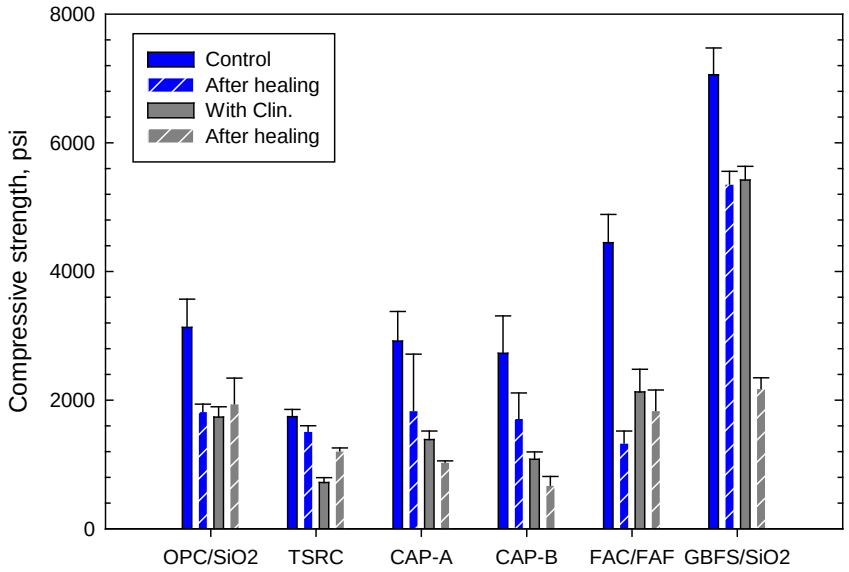

Figure 43. Compressive strength of Clin-free and Clin-modified composites before and after 5 days of self-healing at 300°C in plain water.

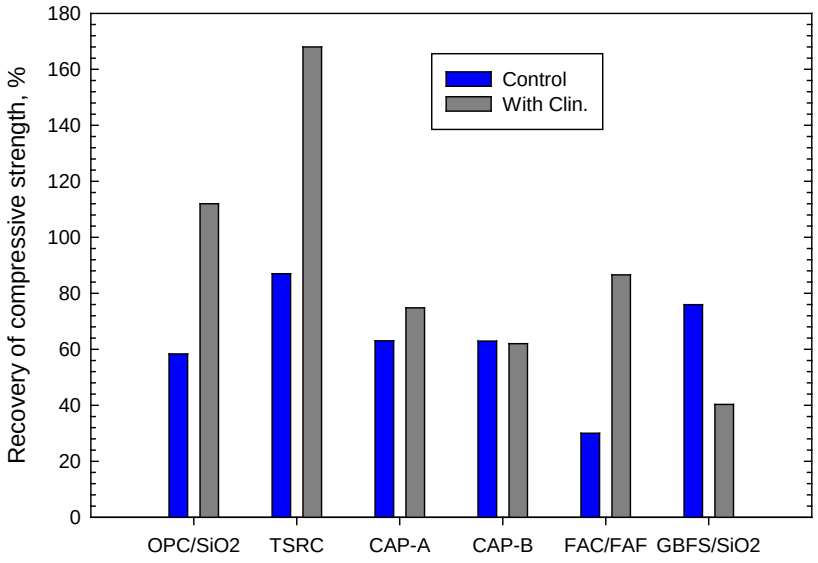

Figure 44. Strength recovery of Clin-free and Clin-modified composites after self-healing treatment.

3.5.2.2. Ferrierite (FER)

Among various zeolites, ferrierite (FER) is especially attractive for high temperature hydrothermal applications in geothermal cements because of the high stability of its structure against hydrothermal and chemical treatments [86,87]. We evaluated performance of OPC clinker– FER blend with a trade name "FlexCem®" from Trabits group under the high-temperature hydrothermal conditions relevant for geothermal wells. Based on the reported performance of zeolite-modified cements self-healing behavior may be expected from the blend at high temperatures where zeolite may become reactive under alkaline conditions of cement slurries. The purpose of the work was to establish the strength recoveries and fractures sealing of the clinker modified with FER and understand the underlying mechanisms of material's healing. Table 8 gives compositions of the tested blends. In preparing cement slurries, the water/cement ratio was 0.48 for OPC/SiO_2 and 0.54 for Clinker/FER and Clinker/FER/SiO_2.

Table 8. Tested formulations

	OPC/SiO_2	Clinker/FER	Clinker/FER/SiO_2
Type I/II Clinker/FER	-	94.3	66
OPC (Class G)	66	-	-
SiO_2	28.3	-	28.3
MCF	5.7	5.7	5.7

3.5.2.2.1. Mechanical properties and microscope study of fractures sealing

The YM values of all tested composites made in 270°C-1-day plain water and alkali carbonate were in the region of moderate brittleness, ranging from 100 x 10^3 to 300 x 10^3 (Figure 45).

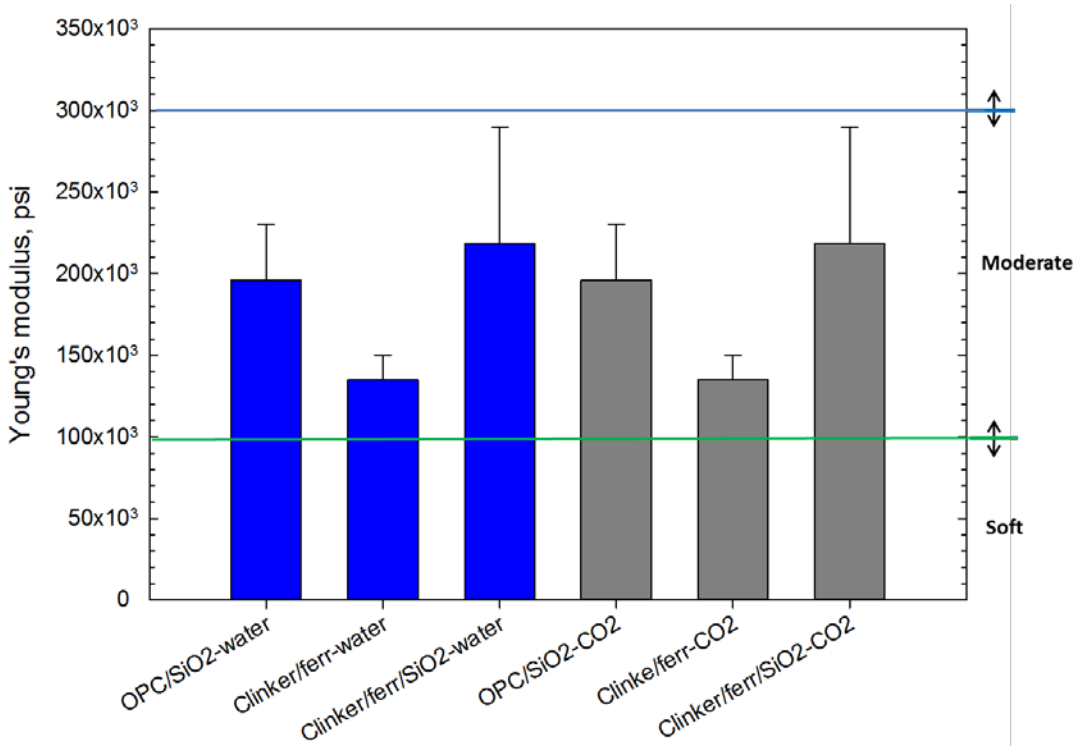

Figure 45. YM of silica (SiO_2)-modified and unmodified OPC and clinker/FER composites autoclaved in 270°C-1-day plain water or alkaline carbonate.

All the controls and healed 2nd and 3rd time cracked composites met the material criterion of compressive strength >1000 psi (Figure 46). Furthermore, outstanding compressive strength recoveries of 134 and 111% were achieved by the FER-containing blend without silica even after two crush tests in water environment and by samples modified with silica in carbonate environment, respectively. For the sample without silica cured in carbonate, the strength recovery was 170% after the first crush but only 70% after the second one. The sample with silica cured in water showed strength recoveries very close to those of OPC/SiO_2 blend (60% after the first crush and 56% after the second). Low strength recoveries were generally associated with formation of large long cracks.

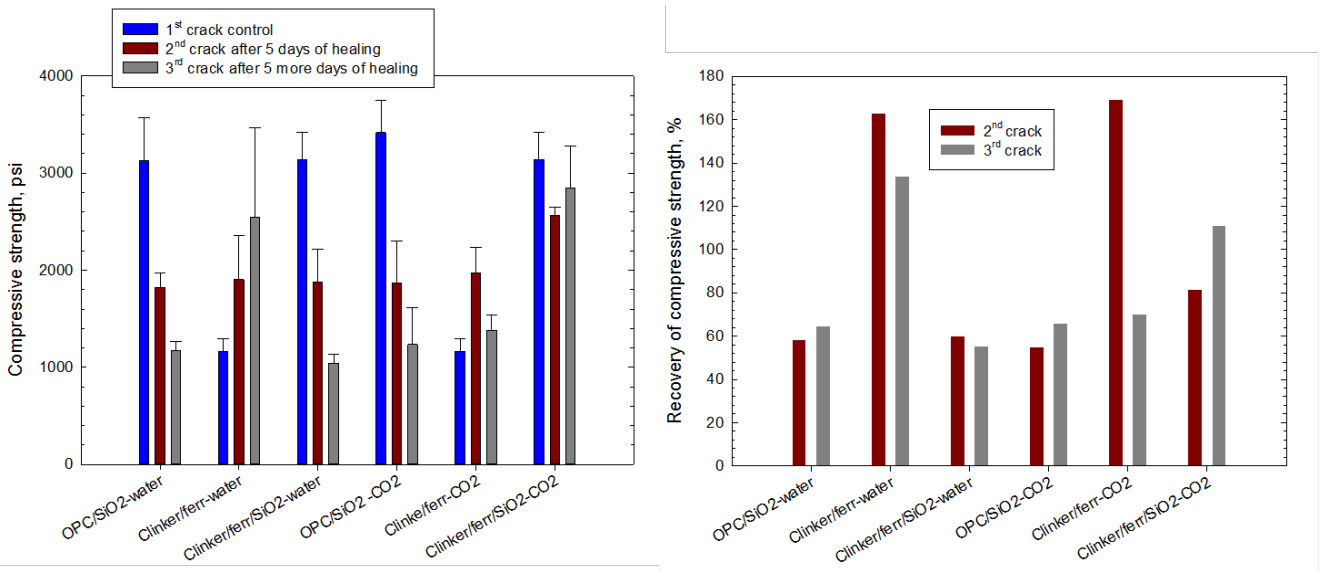

Figure 46. Compressive strengths of the control, and 2nd and 3rd time cracked composites and their recovery after 270°C-5-day self-healing treatment in plain water and carbonate.

Since the major role of the cement sheath in subterranean wells is zonal isolation, the healed cement should possess low permeability along with the recovered strength. The efficiency of crack-filling was studied by taking images and reconstructing a three-dimensional structure of pre-cracked samples after 5 or 10 days of curing in water or carbonate (Figure 47). The crack filling was noticeably better in the carbonate environment than in water. For the sample modified with silica the crack was completely sealed after 5 days. The crack of the unmodified sample was partially filled after 10 days in the carbonate solution. The additional curing time would complete the plugging. The water-healed samples had some minor solid depositions in fractures but those were not sufficient for sealing the large cracks.

The results show that the tested samples differed in strength recovery and crack filling. The filling was unambiguously better in carbonate than in water environment. The clinker-FER sample modified with silica showed the best combination of strength recovery and fracture sealing when cured in alkali carbonate environment.

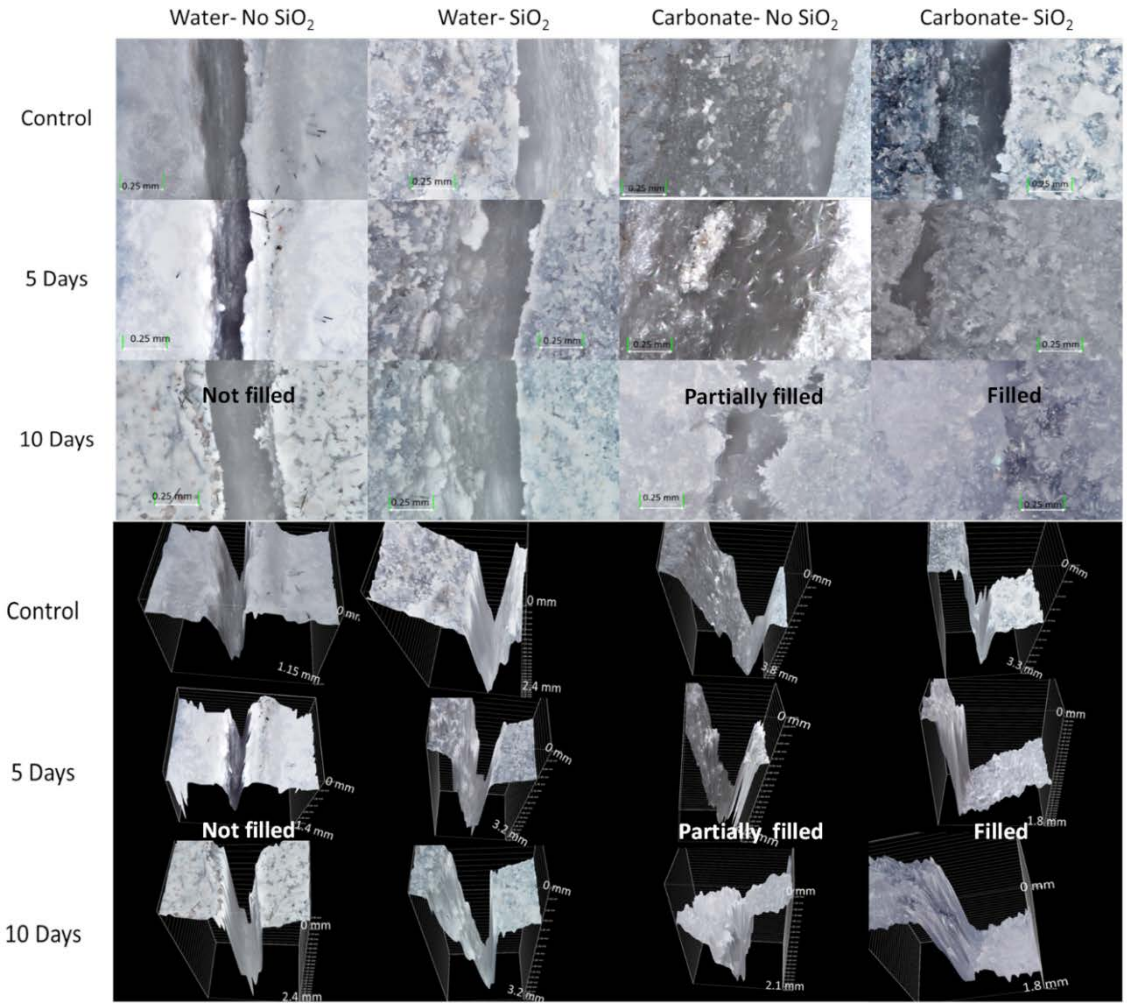

Figure 47. Photographs and 3D images of 0.25 mm crack in silica-modified or -unmodified clinker/FER samples before and after the exposures to plain water or alkali carbonate environments at 270ºC for 1- (control), 5- or 10 days.

3.5.2.2.2. Analyses of degraded samples – crystalline phases, XRD patterns

Table 9 presents crystalline phases identified in the samples cured for 1- (control), 5- or 10 days in different environments, along with their ICDD numbers and chemical formulas.

Table 9. Principal and secondary phase compositions of samples collected form core and surface areas of silica-modified and unmodified clinker/FER composites made in 270°C-1-, -5-, and -10-day plain water and carbonate.

Control			
Water-No Quartz	Water - Quartz	Carbonate – No Quartz	Carbonate – Quartz
Principal: Kilchoanite $Ca_6(SiO_4)(Si_3O_{10})$ (00-029-0370); Silica SiO_2 (04-015-7165/04-006-2057/04-012-1320) Scawtite $Ca_7(Si_6O_{18})(CO_3)\cdot 2H_2O$ (00-031-0261); Katoite $Ca_3Al_{3.5}O_{4.5}(OH)_{7.5}$ (04-017-1503); Hibschite $Ca_3Al_2(SiO_4)_2(OH)_4$ (00-042-0570); Larnite Ca_2SiO_4 (01-083-0461)	**Principal**: Xonotlite $Ca_6Si_6O_{17}(OH)_2$ (00-023-0125); Tobermorite 11A $Ca_{2.25}Si_3O_{7.5}(OH)_{1.5}(H_2O)$ (04-011-0271)	**Principal core**: Quartz SiO_2 (04-008-8440); Scawtite $Ca_7(Si_6O_{18})(CO_3)\cdot 2H_2O$ (00-031-0261); Kilchoanite $Ca_6(SiO_4)(Si_3O_{10})$ (04-009-7055); Hatrunite $Ca_3(SiO_4)O$ (04-014-8419); Calcio-olivine Ca_2SiO_4 (04-006-2363); Tobermorite aluminium $Ca_{4.95}(Si_{5.5}Al_{0.5}O_{16.3})(OH)_{0.7}(H_2O)_5$ (01-074-2878); Dolomite $CaMg(CO_3)_2$ (04-015-9842) **Principal surface**: Kilchoanite $Ca_6(SiO_4)(Si_3O_{10})$ (00-029-0370); Xonotlite $Ca_6Si_6O_{17}(OH)_2$ (00-023-0125); Silica SiO_2 (04-015-7164); Scawtite $Ca_7(Si_6O_{18})(CO_3)\cdot 2H_2O$ (00-031-0261); Tobermorite aluminium $Ca_{4.95}(Si_{5.5}Al_{0.5}O_{16.3})(OH)_{0.7}(H_2O)_5$ (01-074-2878); Dolomite $CaMg(CO_3)_2$ (01-081-8225)	**Principal core**: Xonotlite $Ca_6Si_6O_{17}(OH)_2$ (00-023-0125); Tobermorite aluminium $Ca_{4.95}(Si_{5.5}Al_{0.5}O_{16.3})(OH)_{0.7}(H_2O)_5$ (01-074-2878); Diopside $CaMgSi_2O_6$ (01-071-1067) **Principal surface**: Quartz SiO_2 (01-070-3755/01-073-1748); Xonotlite $Ca_6Si_6O_{17}(OH)_2$ (00-023-0125); Tobermorite aluminium $Ca_{4.95}(Si_{5.5}Al_{0.5}O_{16.3})(OH)_{0.7}(H_2O)_5$ (01-074-2878); Calcite $CaCO_3$ (01-81-9560/04-015-7182); Akermanite $Ca_2Mg(Si_2O_7)$ (04-014-7679)
Secondary: Spurrite $Ca_5(SiO_4)_2(CO_3)$ (00-029-0307); Tobermorite 11A $Ca_{2.25}Si_3O_{7.5}(OH)_{1.5}(H_2O)$ (04-011-0271); Akermanite $Ca_2Mg(Si_2O_7)$	**Secondary**: Anorthite $Ca(Al_2Si_2O_8)$ (01-086-1705); Diopside $CaMgSi_2O_6$ (04-011-6812); Larnite Ca_2SiO_4 (01-077-0388);	**Secondary core**: Huntite $CaMg_3(CO_3)_4$ (04-007-8886); Diopside $CaMgSi_2O_6$ (01-071-1067); Tobermorite 11A $Ca_{2.25}Si_3O_{7.5}(OH)_{1.5}(H_2O)$ (04-011-0271); Anhydrate $CaSO_4$ (04-007-9727)	**Secondary core**: Scawtite $Ca_7(Si_6O_{18})(CO_3)\cdot 2H_2O$ (00-031-0261); Anhydrate $CaSO_4$ (04-007-9727); Calcite $CaCO_3$ (04-008-0213); Valerite $CaCO_3$ (00-033-0268) **Secondary surface:** Enstatite $Ca_{0.035}Mg_{0.965}SiO_3$ (04-013-1910); Scawtite

(04-016-1459); Magnesium silicates Mg_2SiO_4 (01-087-2040/01-074-1683); Akermanite-gehlenite $Ca_2Mg_{0.08}Al_{1.84}Si_{1.08})_7$ (04-015-7935); Andradite $Ca_3Fe_{1.5}Al_{0.5}(SiO_4)_{2.8}(OH)_{0.8}$ (04-012-1320)	Cesanite $Ca_{1.31}Na_{4.32}((OH)_{0.94}(SO_4)_3)$ (01-075-1387); Anhydrate $CaSO_4$ (01-086-2270); Hematite Fe_2O_3 (04-006-9058)	**Secondary surface**: Andradite aluminian $Ca_3Fe_{1.5}Al_{0.5}(SiO_4)_{2.8}(OH)_{0.8}$ (04-012-1320); Akermanite $Ca_2Mg(Si_2O_7)$ (01-077-9261); Diopside $CaMgSi_2O_6$ (01-071-1067)	$Ca_7(Si_6O_{18})(CO_3)\cdot 2H_2O$ (00-031-0261); Diopside, sodian, ferroan $(Ca_{0.76}Na_{0.24})(Fe_{0.23}Mg_{0.77})(Si_2O_6)$ (01-082-3675)

5 days			
Water-No Quartz	Water - Quartz	Carbonate – No Quartz	Carbonate – Quartz
Principal: Xonotlite $Ca_6Si_6O_{17}(OH)_2$ (00-023-0125); Scawtite $Ca_7(Si_6O_{18})(CO_3)\cdot 2H_2O$ (00-042-1436); Coesite SiO_2 (04-015-7168); Larnite Ca_2SiO_4 (04-013-6293); Jarosite $KFe_3(SO_4)_2(OH)_6$ (04-017-4421)	**Principal**: Xonotlite $Ca_6Si_6O_{17}(OH)_2$ (00-023-0125/04-017-1287); Tobermorite 9A $Ca_5Si_6O_{16}(OH)_2$ (04-012-1761); Tobermorite – MDO2 $Ca_{4.5}Si_6O_{16}(OH)(H_2O)_5$ (04-017-1028)	**Principal core**: Spurrite $Ca_5(SiO_4)_2(CO_3)$ (04-011-9708); Scawtite $Ca_7(Si_6O_{18})(CO_3)\cdot 2H_2O$ (04-011-9710); Xonotlite-Ma2bc $Ca_6(SiO_3)_6(H_2O)$ (00-023-0125) 22% Kilchoanite $Ca_6(SiO_4)(Si_3O_{10})$ (00-029-0370); Tobermorite aluminium $Ca_{4.95}(Si_{5.5}Al_{0.5}O_{16.3})(OH)_{0.7}(H_2O)_5$ (01-074-2878) **Principal surface**: Xonotlite-Ma2bc $Ca6(SiO_3)_6(H_2O)$ (01-074-7586); Scawtite $Ca_7(Si_6O_{18})(CO_3)\cdot 2H_2O$ (01-081-1918/00-042-1436); Gismondine $(Ca,Na_2)Al_2Si_2O_8\cdot 4H_2O$ (00-021-0840); Calcite $CaCO_3$ (01-080-2791); Pseudowallastonite $CaSiO_3$ (04-011-3072)	**Principal core**: Xonotlite $Ca_6Si_6O_{17}(OH)_2$ (00-023-0125); Silica SiO_2 (04-007-0522/01-075-8322); Tobermorite $Ca_{2.25}Si_3O_{7.5}(OH)_{1.5}(H_2O)$ (04-014-8455); Calcite CaCO3 (04-019-3759/01-086-2340); Riversideite $Ca_5Si_6O_{16}(OH)_2$ (00-029-0329) **Principal surface**: Coesite SiO_2 (04-015-7168); Tridymite-M SiO_2 (00-018-1170); Xonotlite $Ca_6Si_6O_{17}(OH)_2$ (00-023-0125); Scawtite $Ca_7(Si_6O_{18})(CO_3)\cdot 2H_2O$ (00-042-1436); Tobermorite $Ca_{2.25}Si_3O_{7.5}(OH)_{1.5}(H_2O)$ (04-014-8455); Lithosite $K_3(HAl_2Si_4O_{13})$ (01-073-8490)
Secondary: Kilchoanite $Ca_6(SiO_4)(Si_3O$	**Secondary**: Diopside $CaMgSi_2O_6$ (04-015-8340);	**Secondary core**: Calcium carbonate $CaCO_3$ (04-015-4109); Andradite $Ca_3Fe_2Si_3O_{12}$ (04-009-	**Secondary core**: Bassanite $Ca_3(SO_4)_3(H_2O)_{1.8}$ (04-011-1767); Protoenstatite $MgSiO_3$ (04-

$_{10}$) (00-029-0370); Akermanite $Ca_2Mg(Si_2O_7)$ (04-016-1459); Andradite aluminian $Ca_3Fe_{1.5}Al_{0.5}(SiO_4)_{2.8}(OH)_{0.8}$ (04-012-1320); Calcite $CaCO_3$ (01-080-2803); Bassanite $Ca_3(SO_4)_3(H_2O)_{1.8}$ (04-011-1766)	Protoenstatite $MgSiO_3$ (04-008-5467); Clinoenstatite, calcian $Mg_{0.944}Ca_{0.056}SiO_3$ (01-076-0525); Hedenbergite $(Fe_{1.5}Ca_{0.5})(Si_2O_8)$ (01-082-8083)	8467/01-073-6297); Andradite, aluminian $Ca_3Fe_{1.6}Al_{0.4}(SiO_4)_{2.6}(OH)_{1.6}$ (04-012-1320); Pseudowallastonite $CaSiO_3$ (01-080-9543); Calcium magnaesium silicate $MgCa(Si_2O_6)$ (01-076-6732) **Secondary surface**: Lawsonite $CaAl_2(Si_2O_7)(OH)_2(H_2O)$ (01-073-6449); Enstatite $Ca_{0.035}Mg_{0.965}SiO_3$ (04-013-1909); Cancrinite $Na_6CaAl_6Si_6(CO_3)O_{24}{\cdot}2H_2O$ (00-048-1862); Dolomite $CaMg(CO_3)_2$ (00-011-0078)	009-2093); Diopside, ferrian $CaMg_{0.95}Fe_{0.1}Si_{1.95}O_6$ (04-013-61-03); Ilmenite $MgSiO_3$ (04-017-1488); Magnesite $MgCO_3$ (04-012-4919) **Secondary surface**: Calcium carbonate $CaCO_3$ (04-014-1601); Magnesium silicate $MgSiO_3$ (01-076-6771); Analcime – C $Na(Si_2Al)O_6{\cdot}H_2O$ (00-041-1478); Andradite, aluminian $Ca_3Fe_{1.16}Al_{0.84}(SiO_4)_3$ (04-015-1327); Gismondine $CaAl_2Si_2O_8{\cdot}4H_2O$ (00-039-1373)

10 days			
Water-No Quartz	Water - Quartz	Carbonate – No Quartz	Carbonate – Quartz
Principal: Orthoenstatite (01-082-3784) $MgSiO_3$; Xonotlite $Ca_6Si_6O_{17}(OH)_2$ (00-023-0125); Scawtite $Ca_7(Si_6O_{18})(CO_3){\cdot}2H_2O$ (00-042-1436); Spurrite $Ca_5(SiO_4)_2(CO_3)$ (04-011-9708); Kilchoanite $Ca_6(SiO_4)(Si_3O_{10})$ (00-029-0370); Andradite aluminian $Ca_3Fe_{1.5}Al_{0.5}(SiO_4)_{2.8}(OH)_{0.8}$ (04-012-1320); Jarosite $KFe_3(SO_4)_2(OH)_6$ (04-017-4421)	**Principal**: Xonotlite $Ca_6Si_6O_{17}(OH)_2$ (04-017-1287); Pseudowollastonite (04-011-3072) $CaSiO_3$	**Principal core**: Spurrite $Ca_5(SiO_4)_2(CO_3)$ (04-011-9708); Scawtite $Ca_7(Si_6O_{18})(CO_3){\cdot}2H_2O$ (01-081-1918); Xonotlite-Ma2bc $Ca_6(SiO_3)_6(H_2O)$ (01-074-7583); Pseudowallastonite $CaSiO_3$ (01-080-9543); Calcite $CaCO_3$ (01-078-3262) **Principal surface:** SiO_2 (04-017-1027/04-007-2191/04-001-7249/04-008-7824/04-013-9484/04-007-2468); Talc -1A (04-013-2941) $Mg_3Si_4O_{10}(OH)_2$; Mordenite	**Principal core**: Xonotlite-Ma2b2c $Ca_6Si_6O_{18}(H_2O)$ (01-074-7584); SiO_2 (01-075-8322/01-072-4568/04-008-8696); Pseudowollastonite (04-011-3072) $CaSiO_3$; Tobermorite $Ca_{2.25}Si_3O_{7.5}(OH)_{1.5}(H_2O)$ (04-014-8455); Calcite $CaCO_3$ (01-081-9560) **Principal surface:** SiO_2 (01-089-3607/04-012-1126/01-077-8631) 49% Xonotlite $Ca_6Si_6O_{17}(OH)_2$ (00-023-0125);Talc -1A (04-013-2941) $Mg_3Si_4O_{10}(OH)_2$

		$Na_3Al_3Si_{21}O_{48}(H_2O)_{9.2}$ (04-017-1315)	
Secondary: Bassanite $Ca_3(SO_4)_3(H_2O)_{1.8}$ (04-011-1766); Anhydrate $CaSO_4$ (04-007-9727); Magensite $MgCO_3$ (04-012-4918)	**Secondary**: Anorthite $Ca(Al_2Si_2O_8)$ (01-086-1705); Diopside aluminian $(Ca_{0.5}(Ca_{0.4}Mg_{0.1}))(Mg_{0.86}Al_{0.14})(Al_{0.15}Si_{1.85}O_6)$ (01-075-9999) Tobermorite 11A $Ca_4(Si_6O_{15})(OH)_2(H_2O)_5$ (01-077-8367); Magensite $MgCO_3$ (04-012-4918); Calcium magnesium silicate $Ca_2Mg(Si_2O_7)$ (04-014-7678); Bassanite $Ca_3(SO_4)_3(H_2O)_{1.8}$ (04-011-1767); Anhydrate $CaSO_4$ (04-007-9727); Scawtite $Ca_7Si_6(CO_3)O_{18}{\cdot}2H_2O$ (00-042-1436)	**Secondary core**: Andradite aluminian $Ca_3Fe_{1.5}Al_{0.5}(SiO_4)_{2.8}(OH)_{0.8}$ (04-012-1320); Thomsonite Ca $NaCa_2Al_5Si_5O_{20}(H_2O)_6$ (04-013-3051) **Secondary surface**: Xonotlite $Ca_6Si_6O_{17}(OH)_2$ (00-023-0125); Analcime $Na(AlSi_2O_6)(H_2O)$ (01-072-0445); Tobermorite –MDO1 $Ca_4Si_6O_{15}(OH)_2(H_2O)_5$ (04-017-1027)	**Secondary**: Calcium magnesium silicate (diopside) $CaMgSi_2O_6$ (04-011-6812); Calcium magnesium silicate $Ca_2Mg(Si_2O_7)$ (04-014-7678); Anhydrate $CaSO_4$ (01-072-0916) **Secondary surface**: Mordenite $Na_3Al_3Si_{21}O_{48}(H_2O)_{9.2}$ (04-017-1315); Magnesium iron silicate $MgFe(SiO_4)$ (04-014-7729)

Both control and 10-day cured samples showed some non-reacted clinker peaks (C_3S, ICDD: 04-014-9801 and C_2S, ICDD: 00-033-0302) and peaks of crystalline silica for silica-modified samples. The intensities of the residual clinker peaks were higher for the samples without silica and those cured in water compared against those cured in alkali carbonate (the dramatic difference in peaks intensities at ~$2\theta^o$ 29.4; 32.2 and 32.6 could not be accounted for by the lower amount of clinker in silica-modified samples), indicating acceleration of clinker hydration by carbonate in the presence of silica. FER peaks disappeared after a day of curing in all the specimens, suggesting fast alkaline decomposition of the FER. After 10 days of curing, the major types of crystalline reaction products included calcium-silicates and aluminum-modified calcium-silicate hydrates (xonotlite, tobermorite and aluminum-substituted tobermorite, pseudowollastonite) [88], kilchoanite); carbonated calcium-silicate hydrates (scawtite and spurrite); magnesium (calcium, iron) silicates; magnesium and calcium carbonates; high-temperature stable zeolites such as mordenite, analcime, thomsonite Ca; calcium sulfates such as bassanite and anhydrate. Crystalline silica was dominant in the surfaces of specimens cured in alkali carbonate even for the unmodified samples.

Crystalline compositions of silica-modified and unmodified samples noticeably varied. Calcium-silicates with the Ca:Si ratio between 0.7 and 1, such as tobermorite and predominantly xonotlite, formed as the major crystalline products in both environments for samples modified

with silica. Tobermorite persisted up to 10 days of curing and its calcium-to-silica content decreased as the curing time in carbonate solution increased, suggesting calcium removal through carbonation. Aluminum dissociated from decomposed FER was included into tobermorite detected in control samples in carbonate environment. In addition to aluminum, FER decomposition supplied silicon and magnesium for further reactions.

The crystalline composition of silica-rich samples cured in water closely resembled those of OPC/silica blend with principal products being the clinker high-temperature hydrates.
In the case of unmodified samples, kilchoanite and dicalcium silicate were the major calcium-silicate hydrates with Ca:Si ratios of 1.5 and 2 respectively formed after a day at 270^{o}C (control). Hydrothermal formation of dicalcium silicates and transformation to kilchoanite at temperatures above 220^{o}C were reported earlier [89]. Kilchoanite persisted in water cured samples after 10 days, coexisting with xonotlite that became the major calcium silicate phase both in water and alkali carbonate.
Carbonated calcium-silicate hydrates were the main hydration products in the absence of silica in both water and especially in alkali carbonate solution. They formed in the control samples and the intensity of their peaks steadily increased at longer curing times of 5 and then 10 days. These were scawtite and spurrite, possibly contributing to the increased crack sealing rate. The hydrothermal formation of carbonated calcium-silicates from dicalcium silicate and silica was reported earlier [90]. Scawtite persists under high-temperature hydrothermal conditions; it was present in natural rocks exposed to carbonates forming a stable layer during carbonation of calcium silicate hydrate-bearing rocks from Northern Ireland [91]. It was also reported to be commonly encountered in high-temperature wells where aqueous solutions of carbon dioxide entering pores of hydrating cement form scawtite and release silica that may partially seal fractures [92]. Decomposed FER was the main source of magnesium while clinker provided calcium for calcium magnesium silicates crystalized after the first day of curing (akermanite, diopside, and enstatite). At longer curing times in the alkali carbonate solution, the intensities of their peaks strongly decreased even in cores of the samples, likely because of the calcium removal through carbonation. The dolomite crystallized as one of the principle phases in unmodified samples through the calcium hydroxide attack of FER but its peaks weakened strikingly after 5 days of curing and were completely replaced by talc in the surfaces after 10 days through skarnification reactions with silica accompanied by calcium carbonate formation, which was a major crystalline phase in the surface of unmodified samples. Talc is a soft, clay-type mineral, and is unlikely to play any significant role in the strength recovery; however, it may aid sealing small crevices.
In the case of water-cured silica-modified samples, calcium magnesium silicate formed after a day curing persisted in the samples for 10 days. However, the peak intensities of this product were significantly lower than those of calcium silicates, indicating that this phase was not a major contributor to the strength recovery. In the sample without silica, magnesium silicate formed after the first day and became a major crystalline hydration product after 10 days. This phase likely played the key role in the outstanding strength recovery of the unmodified water-cured sample.
High temperature-stable zeolites formed mostly in the surface layer of carbonate-cured specimens after 10 days of curing. In the presence of silica, silica-rich zeolite, mordenite, was predominant (Si/Al = 7) and for the sample without silica peaks of thomsonite Ca with lower silica content were detected (Si/Al = 1). Notably, there were no zeolites among the principle core

products in any of the specimens. Zeolites could be crystalizing from the silica-aluminate amorphous phase after the decomposition of FER and magnesium reactions with calcium, silica and carbonate or crystalize from solution with high dissolved sodium, aluminum and silicon contents at the solids' surfaces. In both cases sodium and carbonate ions of the solution would play a major role in zeolites crystallization explaining their presence in the surface samples. Some iron-containing hydrates formed with the iron associated with FER and likely assisted in recovering the strength. After 10 days of curing, they included andradite aluminian in both environments and magnesium iron silicate in the surface of modified samples cured in carbonate solution.

In summary, the XRD analyses showed high-temperature alkaline FER decomposition after the first day of curing, persistence of unreacted clinker and silica phases for 10 days and faster clinker loss for silica-modified samples in alkali carbonate. The reactions of calcium from clinker with magnesium from FER led to the formation of calcium magnesium silicates or dolomite. These products were not stable in carbonate solution, transforming to calcium-free magnesium silicates and talc at longer curing times. The major identified crystalline phases contributing to the strength recovery were calcium silicates (xonotlite, tobermorite, kilchoanite, pseudowollastonite), magnesium silicate (orthoenstatite), calcium iron aluminate (andradite). The phases participating in sealing the cracks were mostly forming in carbonate environment and included crystalline silica, talc and high-temperature stable zeolites (mordenite, analcime, thomsonite Ca). Carbonated calcium silicates, scawtite and spurrite formed in unmodified samples as principle phases in carbonate and to a lesser extent in water contributing to the strength when present in small amounts. Sodium carbonate played an important role in formation of the reaction/hydration products stable after 10-day curing through interactions of calcium, magnesium, sodium, carbonate and bicarbonate ions and creating conditions favoring silica precipitation.

3.5.2.2.3. Derivative thermogravimetry (DTG) measurements

Table 10 gives the weight losses in different temperature ranges for specimens cured in water or the carbonate solution and Figure 48 shows the DTG curves for control (24 hours at 270°C) and 10-day cured samples. The weight losses up to 400^{o}C can be associated with (sodium, calcium) silica aluminate and calcium silicate hydrates; zeolites decomposition may also contribute to the weight loss in that temperature range (analcime, mordenite, thomsonite [93]). Between about 400 and 550^{o}C, calcium-rich calcium-silicate hydrates contribute to the weight loss [94], along with calcium hydroxide, the re-crystallization of aragonite to calcite takes place at around 450^{o}C. The losses at temperatures above 550^{o}C are for the most part due to the decomposition of carbonates such as calcite (~600^{o}C), magnetite (~620-650^{o}C), calcium magnesium carbonates (600-650^{o}C, huntite), magnesium iron calcium carbonate (~700-750^{o}C) and dolomite (750-800^{o}C) [93]. Calcium silicate carbonate, scawtite decomposes to $CaCO_3$ at ~790^{o}C and de-carbonates in the temperature range between ~830 and 850^{o}C [95,96]. Sulfate –containing mineral, jarosite decomposes at ~610^{o}C [97] contributing to the mass loss in the range 550-850^{o}C for water-cured unmodified samples. Talc decomposition also takes place in this temperature range (~800 – 840^{o}C) [98].

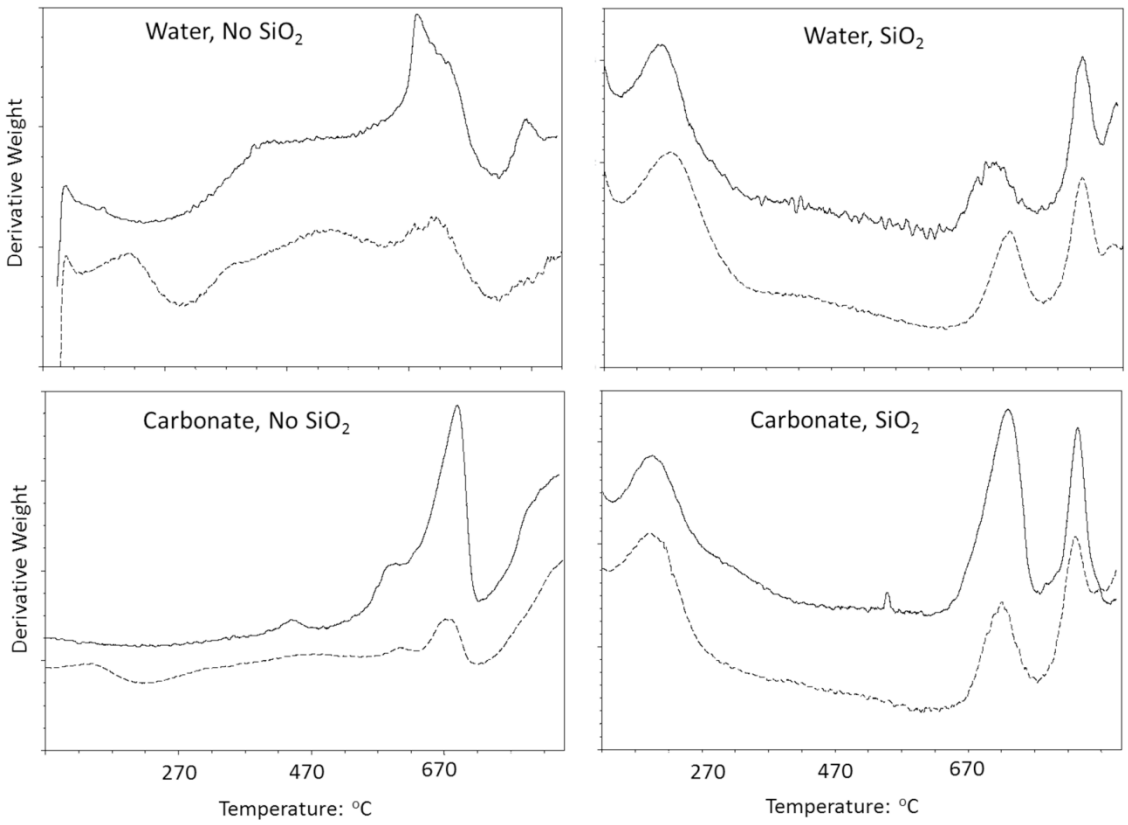

Figure 48. Differential thermal gravimetric (DTG) curves of cement blends cured for 24 hours (control; dashed lines) or 10-days (after 2 crush tests; solid lines) at 270°C in water or alkali carbonate solution.

Table 10. Thermal decomposition temperature ranges and associated weight losses for specimens cured under different conditions.

Sample	70-400°C	400-550°C	600-850°C
Water-no quartz			
Control	2.7	1.6	3.4
10 days	1.5	1.4	3.3
Water – quartz			
Control	4.1	1.0	2.5
10 days	3.8	0.8	2.4
Carbonate – no quartz			
Control	2.7	1.6	4.8
10 days	1.4	1.2	8.2
Carbonate – quartz			
Control	4.2	0.7	3.0
10 days	3.6	0.6	3.0

The decomposition peaks of various hydrates overlap strongly not allowing identification of separate phases. However, the following general trends supported findings of the XRD study. The weight losses below 400°C were about twice as high for the samples with quartz as for those without it in both water and carbonate environments, confirming formation of calcium-silicate

hydrates in the presence of silica and faster clinker reactions for silica-modified samples. On the other hand, the decomposition rate in the range between 400 and 550^{o}C associated with the calcium-rich hydrates and calcium hydroxide was greater for the samples without silica (0.6-1.0% with quartz vs. 1.2-1.6% without quartz). These hydrates are likely to be amorphous for the most part with some contribution of kilchoanite identified by XRD. The specimen without silica cured in the carbonate solution experienced the greatest weight loss above 550^{o}C (>8%). This result is in agreement with the XRD study suggesting decomposition of carbonated calcium silicate, scawtite along with the possible decompositions of dolomite and talc (a wide decomposition band above 800^{o}C). The decomposition peaks of silica-containing specimens at ~785^{o}C are likely associated with calcium magnesium carbonates.

3.5.2.2.4. ATR-FTIR measurements

Figure 49a shows the FT-IR absorption spectra in the region of 1800 to 650 cm^{-1} for the water-cured control samples (24 hours at 270°C) and for the non-hydrated clinker – FER blend. The spectrum of the blend encompassed eleven absorption bands including a wide band around 1043 cm^{-1} and the weak one at 669 cm^{-1} from T-O (T: Si or Al) bond-related anti-symmetric ($V_{as\ T\text{-}O}$) and symmetric ($V_{s\ T\text{-}O}$) stretching vibrations in three-dimensional oxygen-linked $[SiO_4]^{4-}$ and $[AlO_4]^{5-}$ tetrahedral frameworks of zeolite; two other bands of T-O bonds at 1225 (Si-O ($V_{as\ Si\text{-}O}$)) and 707 cm^{-1} (Al-O ($V_{s\ Al\text{-}O}$)) [40,99]; the prominent doublet at 921 and 889 cm^{-1} from the cement clinkers, namely, Si-O bond stretching ($V_{as\ Si\text{-}O}$) in orthosilicate of calcium-silicates (C_3S and C_2S) , and the band at 707 cm^{-1} from Al-O ($V_{s\ Al\text{-}O}$) in tricalcium aluminate (C_3A)[76,100–102]; the five bands at 1486, 1451, 853, 829, and 707 cm^{-1} associated with the CO_3^{2-} group in carbonated compounds, including two bands at 1486 and 1451 cm^{-1} due to C-O bond stretching ($V_{as\ C\text{-}O}$) and the last three bands from O-C-O bond bending ($\delta_{\ O\text{-}C\text{-}O}$) [72–74], so both Al-O and C-O contributed to the 707 cm^{-1} band; the shoulder and weak bands at 1158 and 669 cm^{-1}, respectively, attributable to the S-O stretching ($V_{as\ S\text{-}O}$) and O-S-O bending (δ_{as} o-s-o) of sulfate SO_4^{2-} tetrahedral group in gypsum [76,82,103]; finally the band at 1624 cm^{-1} was from H-O-H bending ($\delta_{\ H\text{-}O\text{-}H}$) in water.

The spectrum of the cement autoclaved in water for 24 hours at 270°C had the following new features: 1) the appearance of three new bands at 1204, 1073 and 959 cm^{-1}; 2) the attenuation in absorbance and disappearance of FER-related bands [104]; and, 3) the enhanced peak intensity of carbonate-associated bands. The new band at 1204 cm^{-1} was attributed to the Si-O stretching ($V_{as\ Si\text{-}O}$) in the amorphous silica-gel [105] and the other two new bands were Si-O ($V_{as\ Si\text{-}O}$) in calcium silicate-hydrate and -anhydrate formed during C_3S and C_2S hydration [100,102], thereby resulting in the band frequency shift from 921 cm^{-1} of orthosilicate to 959 cm^{-1} of polymerized silicate.

The attenuation in absorbance and disappearance of FER-related bands strongly suggested zeolite decomposition in reactions with Ca^{2+} and OH^- released during clinker hydration under high-temperature hydrothermal conditions [33,34]. Thus, hot alkali dissolution and hydrothermal disintegration of FER led to its disappearance and conversation into an amorphous phase. Enhanced intensity of carbonate-associated bands corresponds to a large amount of carbonated calcium silicate hydrate such as scawtite formed in cement. As is obvious from the presence of bands at 921 and 889 cm^{-1}, some non-hydrated clinkers still remained after autoclaving for a day. This fact was one of the reasons why the non-modified samples had a lower compressive strength at an early hydration age. However, importantly, cement damaged in the crush tests

recovered its compressive strength during an extended autoclave period at least partially because of the hydration of non-reacted clinker. Additionally, the bands at 1158 and 669 cm^{-1} were interpreted as the sulfate-related reaction products [106,107].

The spectrum of silica modified sample clearly differed from that of unmodified one with even more striking decay of the absorbance related to FER, clinker and carbonates, while the band at 959 cm^{-1} representing the hydrated silicate compounds becoming the principal one along with the emergence of a new band at 1073 cm^{-1} attributed to Si-O stretching in silicate. Relating these information to the XRD study it can be suggested that the silica not only promoted the formation of calcium silicate hydrates (tobermorite and xonotlite) responsible for developing an early strength of cement, but also reacted with ionic species, Na^{+}, Mg^{2+}, and Al^{3+}, liberated from the hot alkali dissolution of FER to form anorthite and diopside in the presence of Ca ions from clinker. In agreement with the XRD results, FT-IR spectrum did not show additional formation of carbonated compounds in silica-modified samples cured in water. The spectra of the samples cured in alkali-carbonate environment at 270°C for one day were similar to those of the water-cured samples except incorporating carbonate-related bands. Again, the intensity of these bands for unmodified samples was much higher than for samples modified with silica.

Figure 49b shows the FT-IR spectra for the damaged samples after 10 days of curing in water at 270°C. In agreement with the XRD results the spectra of unmodified samples indicated presence of both carbonated and non-carbonated silicate compounds with the principal and secondary bands at nearly 959 cm^{-1} and at 1073 cm^{-1}, corresponding to Si-O bond stretching, and several CO_3^{2-}-related C-O stretching bands at 1486, 1451, 853, and 829 cm^{-1}. Relating this evidence to XRD results the major crystalline non-carbonated silicates would be orthoenstatite, xonotlite [108], kilchoanite, and andradite aluminian, while carbonated silicates involve scawtite and spurrite. There were still FER- and clinker-related bands present in the samples clearly validating that the hydration of clinker and dissolution of zeolite were not completed after the 10-day exposure. The spectrum of the silica-modified cement after 10 days in water was similar to the spectrum oft of a 1-day autoclaved sample, highlighting accelerated dissolution of FER and reactions with clinker in the presence of silica.

The surface spectrum of the damaged non-modified cement exposed for 10 days to the alkali-carbonate environment (Figure 49c), showed a new reaction product identified as silica based on newly developed bands at 1023 and 785 cm^{-1}, respectively from Si-O ($V_{as\ Si\text{-}O}$) and ($V_{s\ Si\text{-}O}$) stretching vibrations [109–111]. The formation of silica as the major reaction by-product was due to the precipitation of silica in carbonate after dissolution of silicate compounds. This spectrum also showed the presence of some silicate- and carbonate-reaction products coexisting with the residue of clinker. As expected, the core of this sample had two major bands at 959 and 921 cm^{-1} attributed to silicate reaction products and clinker, but there were no quartz-related bands, emphasizing that beneath the carbonated top surface layer cement remained intact. Thus, conceivably, the precipitation of silica may create a protective barrier layer abating the rate of further carbonation- caused erosion.

For the silica-modified cement, the spectrum of the surface showed silica as a primary product in conjunction with the silicates (xonotlite and talc-1A) as secondary reaction products identified by XRD. The presence of residual clinker and carbonated compounds were negligible, supporting XRD results. The underlying core area was composed of silicate- and sulfate-related reaction products.

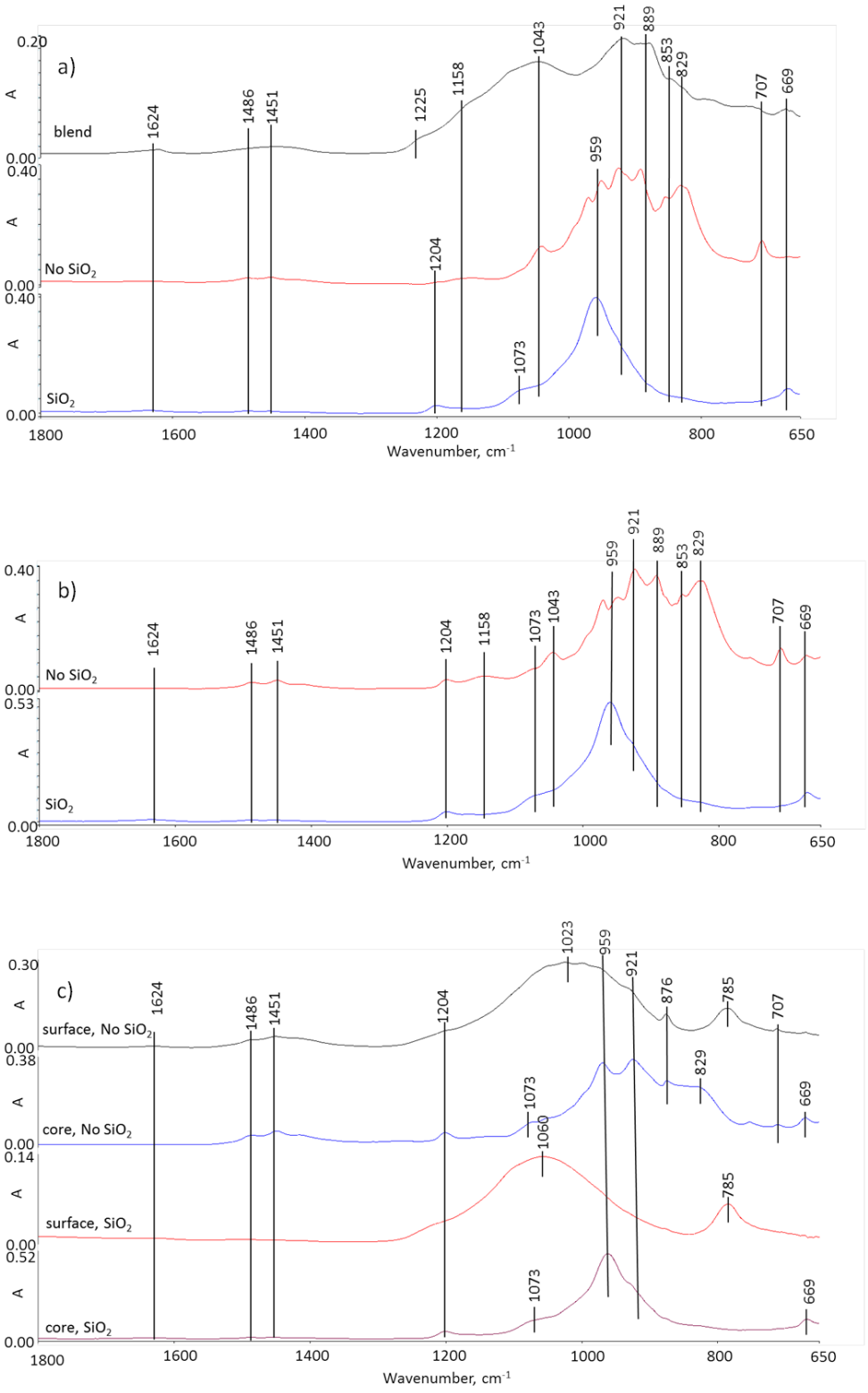

Figure 49. Fourier transform infrared spectra of non-hydrated clinker/FER blend, and control samples cured for 24 hours (a) or 10 days (b) in water at 270°C; samples cured in alkali carbonate solution at 270°C for 10 days (c).

3.5.2.2.5. Morphologies of silica-modified and unmodified samples cured in water or alkali carbonate

The core morphologies of the damaged samples autoclaved for the total of 10 days in water or carbonate were amorphous for the most part (Figure 50) with some inclusions of needle-like crystals (points 1,8,9,12). The amorphous matrix was rich in silica for silica-modified samples (points 6,7,10) and calcium for the water-cured unmodified sample (point 13). The needle-shaped crystals had compositions typical of xonotlite and scawtite (points 1 and 8) and kilchoanite (point 12), supporting XRD findings. Silica-rich mordenite composition was detected in some spots on the surfaces of the samples (2,5,14). The surface compositions of both silica-modified and unmodified cements were for the most part typical of silica and the morphologies showed depositions of amorphous and crystalline silica (points 3,4,11,15) in agreement with XRD and FT-IR results. The carbon detected in the samples was resulting from their carbonation and from the presence of carbon microfibers.

3.5.2.2.6. Acid resistance and acid strength recoveries

Geothermal wells are often highly acidic through H_2S dissolution with formation of sulfuric acid. Cements modified with pozzolanic materials are generally more acid resistance due to the lower calcium, particularly sensitive to acid attack, and higher aluminum and silicon contents. The data of OPC/SiO_2 and FlexCem exposure to sulfuric acid of pH 0.2 for 28 days at 90^{o}C summarized in Table 11 clearly support this, demonstrating a superior performance of FlexCem. The appearance of the samples after the first 14 days of acid exposure and after a crush test and 14 more days of acid exposure is given in Figure 51.
After the first 14 days of the exposure to a strong acid FlexCem lost only 9% of its strength compared against 37% loss for the OPC/SiO_2 blend and 7% of Young's modulus vs. 31% for OPC/SiO_2. There was also significantly smaller increase in samples diameter and weight indicative of scale deposition from acid reactions with cement (2.4% diameter and 12% weight increase vs. 10 and 17% increases for OPC/SiO_2 respectively). Acidification of cements accelerated after the compressive damage to the point that OPC/SiO_2 samples could not be tested anymore (see Figure 51b). FlexCem survived additional 14 days of strong-acid exposure with a residual compressive strength of 960 psi. In summary, clinker modification with FER improved its resistance to strong acid at elevated temperature.

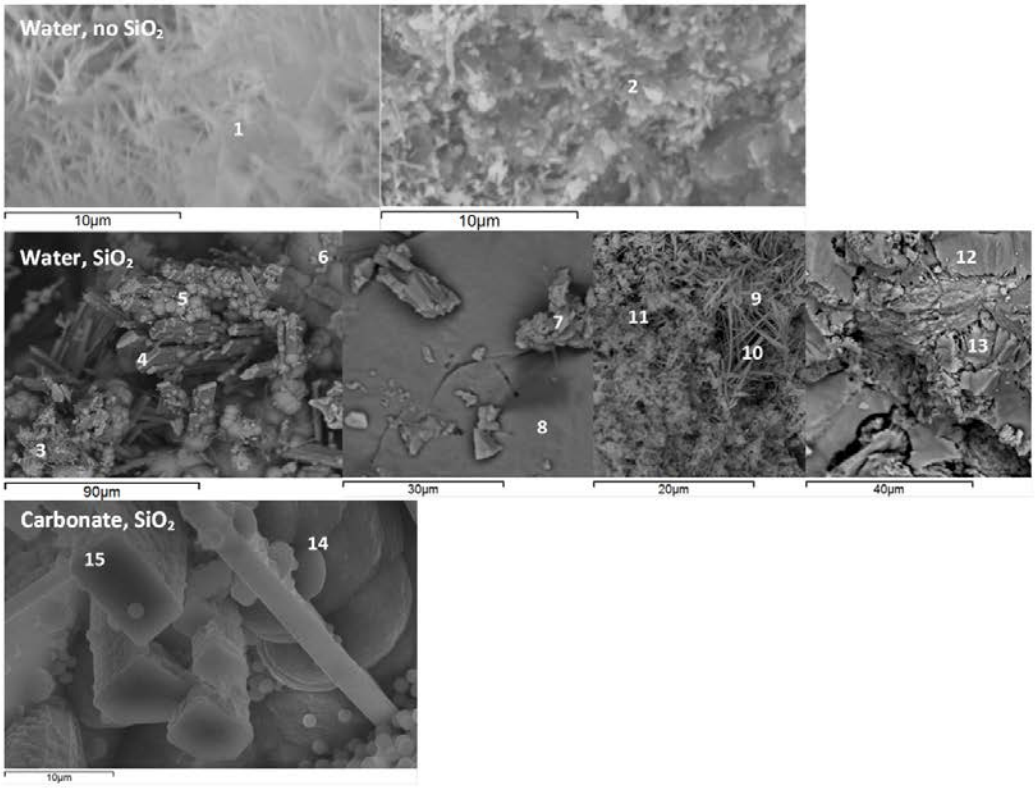

Point	C	Na	Mg	Al	Si	Ca	Fe	Possible phase
1	12	-	0.19	0.63	10	14	0.24	Kilchoanite
2	2.9	-	0.13	0.52	14	23	0.26	Amorphous matrix
3	5.4	0.39	0.42	4.6	14	14	0.81	Xonotlite; non-reacted ferrierite
4	-	1.6	-	1.6	31	-	-	Mordenite; SiO_2
5	-	0.72	-	0.39	33	-	-	SiO_2
6	-	0.56	-	0.32	33	-	-	SiO_2
7	-	3.9	-	3.2	28	-	-	Mordenite
8	-	0.23	-	0.3	33	-	-	Amorphous matrix
9	11	-	-	1.1	13	13	0.31	Xonotlite, Scawtite
10	8.3	0.31	0.64	1.2	15	13	0.3	Ferrierite, Xonotlite
11	8.8	0.43	-	1.0	14	13	0.23	Amorphous matrix
12	19	-	-	0.73	14	-	-	Amorphous silica-rich matrix
13	5.2	-	-	-	28	-	-	Silica
14	9.9	0.47	-	0.22	23	-	-	Silica
15	-	1.8	-	1.8	31	-	-	Mordenite, Silica

Figure 50. Scanning electron micrographs of typical cement microstructures and their elemental compositions for clinker/FER samples cured for 10 days at 270°C.

Table 11. Changes in mechanical properties, weight, and diameter after exposure for 14 days in 90°C-pH 0.2-H_2SO_4 and after compressive strength test and 14 more days in the same acid for OPC/SiO_2 and FlexCem

Formulation Conditions	**Compressive strength, psi**	**Youngs' modulus, psi**	**Changes in diameter, %**	**Changes in weight, %**
OPC/SiO_2				
Control	3140±640	220700±83300	N/A	N/A
After 14 days in acid	2130±560 (-37%)	152000±39000 (-31%)	+10	+17
After break and 14 more days in acid	N/A	N/A	N/A	+7.2
FlexCem				
Control	2670±60	232000±31450	N/A	N/A
After 14 days in acid	2440±250 (-9%)	216000±4900 (-7%)	+2.4	+12
After break and 14 more days in acid	960±160 (-60%)	95800±6100 (-56%)	N/A	+1.4

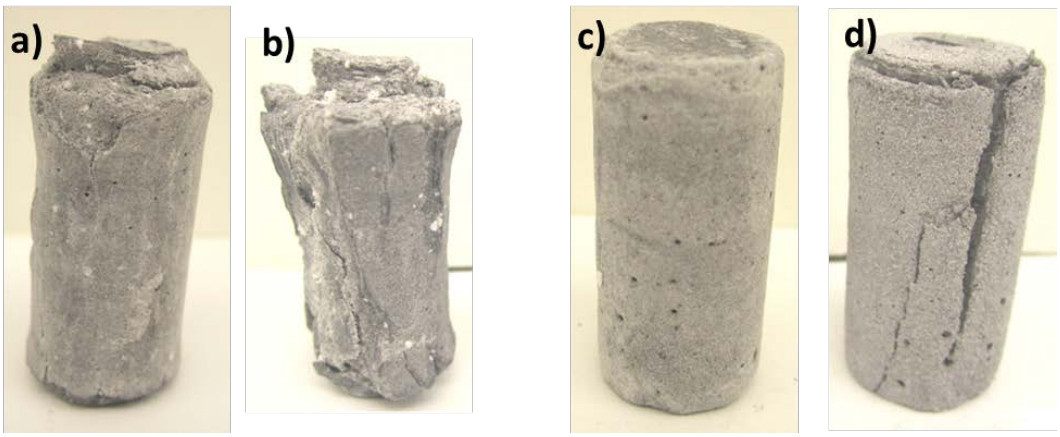

Figure 51. Sulfuric acid-treated samples (pH 0.2, 90°C): a) OPC/SiO_2 after 14 days in the acid; b) OPC/SiO_2 after 14 days in the acid, break and 14 more days in the acid; c) FlexCem after 14 days in the acid; d) FlexCem after 14 days in the acid, break and 14 more days in the acid.

3.5.3. E-type micro-glass fiber (MGF) as artificial pozzolan

Unlike Clin and FER natural pozzolans leading to the decline of YM in cement blends, the MGF as industrial pozzolan offered increased YM for OPC/SiO_2, CAP-A and –B, and GBFS/SiO_2 composites and did not change YM for TSRC made by 300°C-1-day-autoclaving in plain water, carbonate, and brine environments (Figure 52). Of the four composites with increased YM, three, OPC/SiO_2, CAP-A and –B, were transferred to brittle level from moderate brittleness. Meanwhile, a very brittle nature of GBFS/SiO_2 was further enhanced. The environmental effect on increasing YM depended on the kind of cementitious materials, especially, the plain water for CAP-A and brine for CAP-B caused the pronounced increase of YM to nearly a very brittle

level. Nevertheless, two MGF composites, OPC/SiO_2 and TSRC, met the material criterion of YM <400 x 10^3 psi.

The average compressive strength developed in MGF-modified composites autoclaved for 24 hours in 300ºC plain water, carbonate, and brine (Figure 53) was 3640, 2280, 3780, 3280, and 7450 psi, respectively, for OPC/SiO_2, TSRC, CAP-A and –B, and GBFS/SiO_2. Figure 54 compares strength recovery rates between composites with and without MGF in three environments, and the average recovery rates in these environments are summarized in Table 12. It can be seen that MGF was very effective in significantly improving the recovery of two composites, TSRC and CAP-B, while some improvement also was observed for OPC/SiO_2.

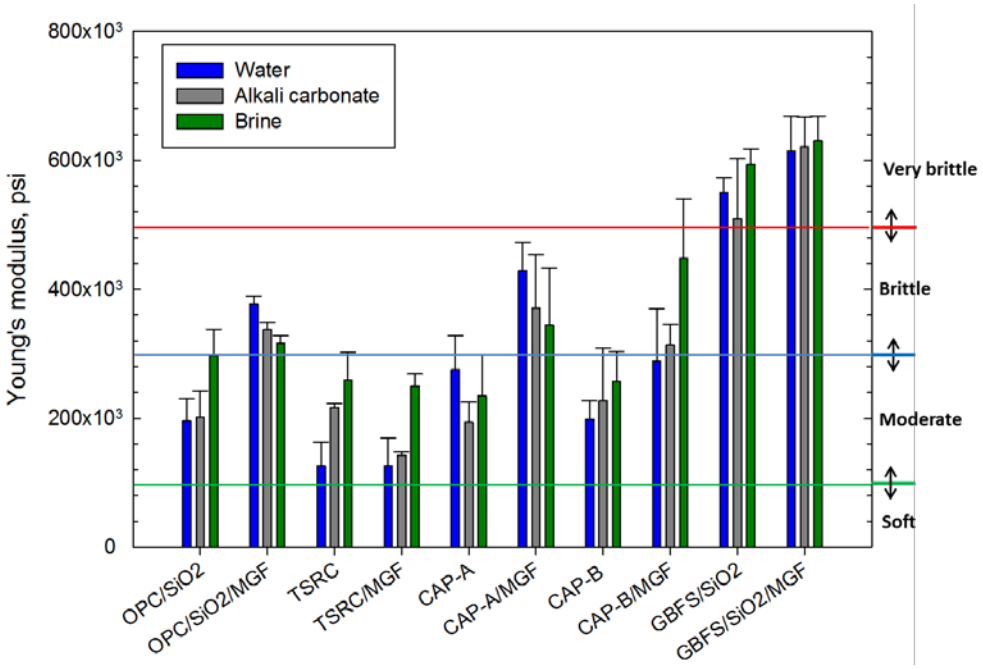

Figure 52. YM of MGF-free and MGF-modified composites made in 300°C-24-hr plain water, carbonate, and brine.

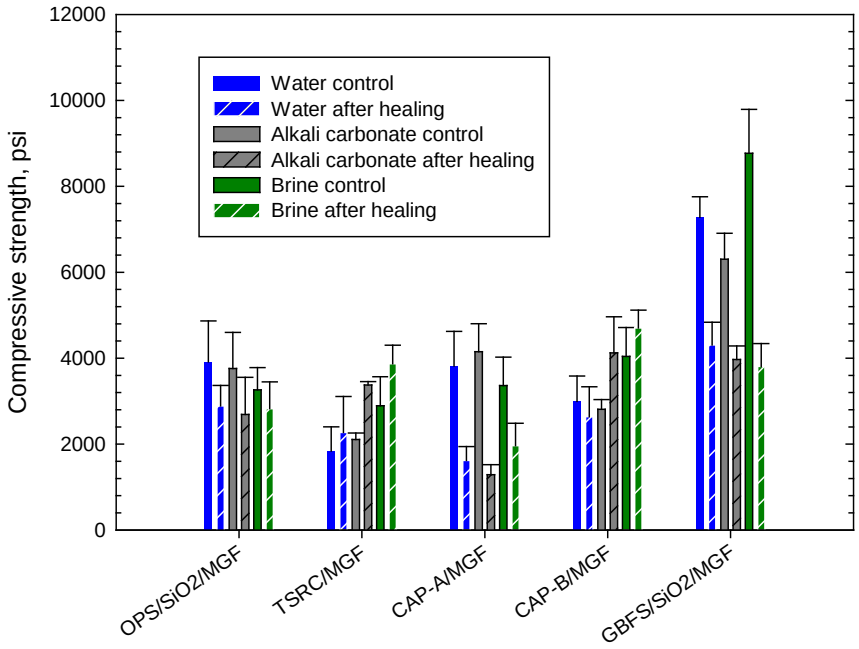

Figure 53. Compressive strength of MGF-modified composites before and after 5-day self-healing treatment in 300°C plain water, carbonate, and brine.

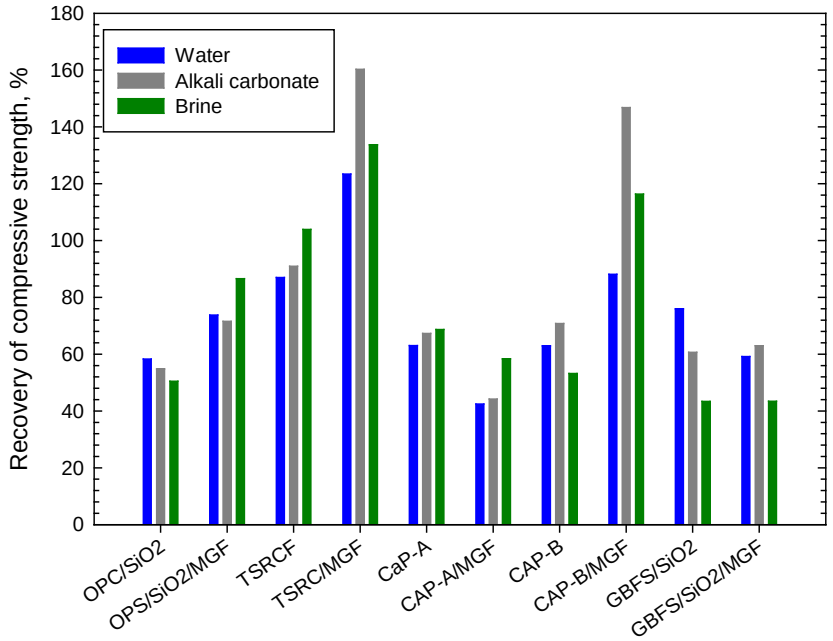

Figure 54. Strength recovery of MGF-free and MGF-modified composites after self-healing treatment in plain water, carbonate, and brine.

Table 12. Average recovery rate for various composites with and without MGF

	OPC/SiO_2	TSRC	CAP-A	CAP-B	$GBFS/SiO_2$
Without MGF	55%	94%	66%	62%	60%
With MGF	77%	139%	48%	117%	55%

It was of interest to evaluate whether broken cement fragments can self-reattach to the failed mother cement. There are two important considerations for such a reattachment: One is chemistry of cements; and the other is physical factors associated with the surface textures of fractured cements. For the latter, the undesirable texture is the smooth sharp surfaces of fractures; the ideal one is the rough surface typical for failed ductile cements. The primary benefit of rough surface is a high contact area of fracture surfaces, leading to a better interfacial bonding behavior. To verify the concept described above, our attention was centered on investigating the ability of broken fragments of MGF-modified composites to reunite with failed mother composite for brittle- and ductile-type composites. We evaluated the four composite systems, TSRC as moderate brittle composite, OPC/SiO_2 and CAP-B as brittle one, and $GBFS/SiO_2$ as very brittle one. The samples were prepared in the following manner. In the first step, the composites were broken by excessive compressive load beyond YM to fragment them. Next, the fragments isolated from intentionally broken composite were physically attached to failed mother composite body by steel wire, and the samples were autoclaved for 5 days in plain water, carbonate, or brine at 300°C. After the autoclaving, the steel wire was removed from the composite, and the samples were visually analyzed for the fragments reattachment to the main body (Figure 55). The samples with reattached fragments were tested for compressive strength to gain information on bond strength of fragments adhering to mother composite.
For OPC/SiO_2/MGF system, the fragments were not reunited with the main cement body in plain water; in fact, shortly after wire was removed, attached fragments were separated from the mother composite (Figure 39). In contrast, two other reactive environments (brine and carbonate) aided in assembling the reunited composite (Figures 55 and 56). As is evident, the broken cement fragments successfully joined the mother composite after 5-day exposures in these environments at 300°C. Figure 40 shows compressive stress-strain relation curves of reunited OPC/SiO_2/MGF composite in carbonate. There are two failure points on the curve. The initial failure (IF) point may be due to the interfacial bond breakages between the joined fragments and the mother composite. If this interpretation is reasonable, the compressive strengths at IF and at the YP (yield point) were 450 and 2620 psi. The strength recovery at YP of the 2^{nd}-time cracked sample was 68% compared to 3880 psi strength measured in the 1^{st} break. This recovery rate closely resembled the data in earlier strength recovery works. In the same carbonate environment, the shape of the stress-strain curve of TSRC/MGF system differed from that of OPC/SiO_2/MGF (Figure 57). The difference was IF point; the detected IF value of 2003 psi was tantamount to 4.5-fold greater strength than that of OPC/SiO_2/MGF. Hence, the interfacial bond of TSRC fragments to mother composite was considerably higher than that of OPC/SiO_2/MGF. Correspondingly, the strength recovery at YP was nearly 150%. There were two factors governing such high strength recovery: One was the reunited structure by an excellent interfacial bonding at fragment/failed mother composite joint; the other was continuous hydrations and reactions of non-or partially-hydrated cement particles present in cement matrix. Likewise, very

encouraging results were obtained for the other two environments, plain water and brine, (Figure 58), showing a good fragments reattachment, as well as high strength recovery of 115% in plain water and 128% in brine.

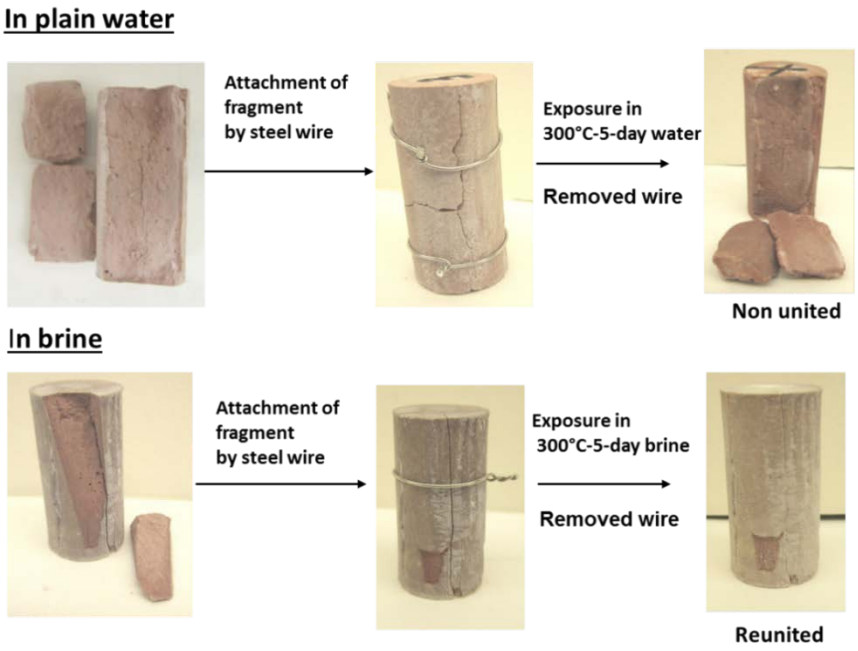

Figure 55. Visual observation for self-reuniting activity of broken OPC/SiO_2 in 300°C plain water and brine.

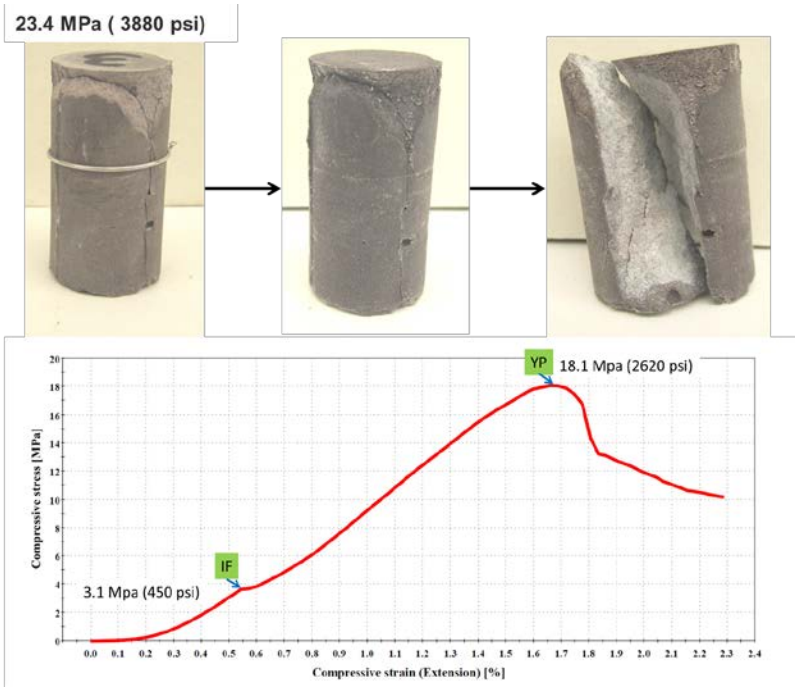

Figure 56. Compressive stress-stain curve for reunited OPC/SiO_2 composite in 300°C carbonate.

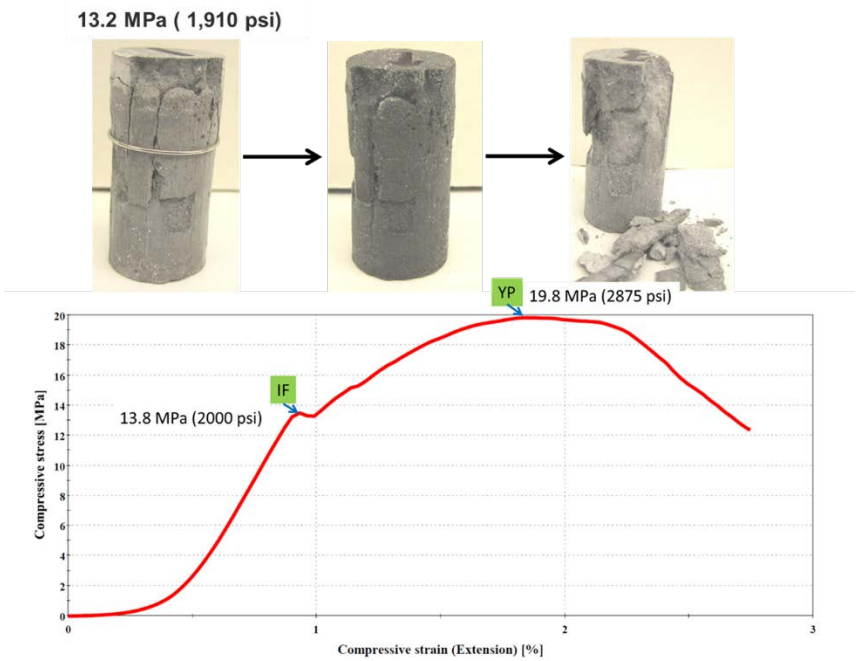

Figure 57. Compressive stress-strain curve for reunited TSRC in carbonate.

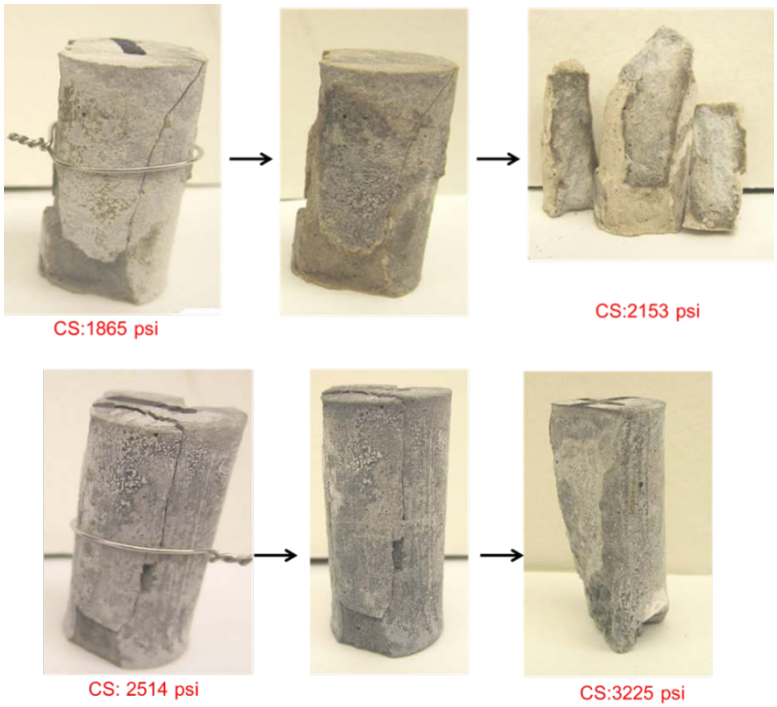

Figure 58. Appearances of reunited TSRC and failure mode after compressive strength test of reunited TSRC in water (top) and brine (bottom): CS – compressive strength before (left) and after fragments reattachment (right).

Figures 59 and 60 depict the appearance and compressive stress-stain curves for very brittle GBFS/SiO_2 prepared in carbonate and brine. After removing wire, both composites made in carbonate and brine showed an excellent reunited appearance, strongly verifying that the fragments were adequately attached to the mother composite. However, IF value was only 508 and 697 psi in carbonate and brine, respectively, implying that interfacial bonding of fragments to mother composite was considerably weaker than that of TSRC. This result was directly related to the lowering of strength recovery. Similar result also was obtained in water (Figure 61).

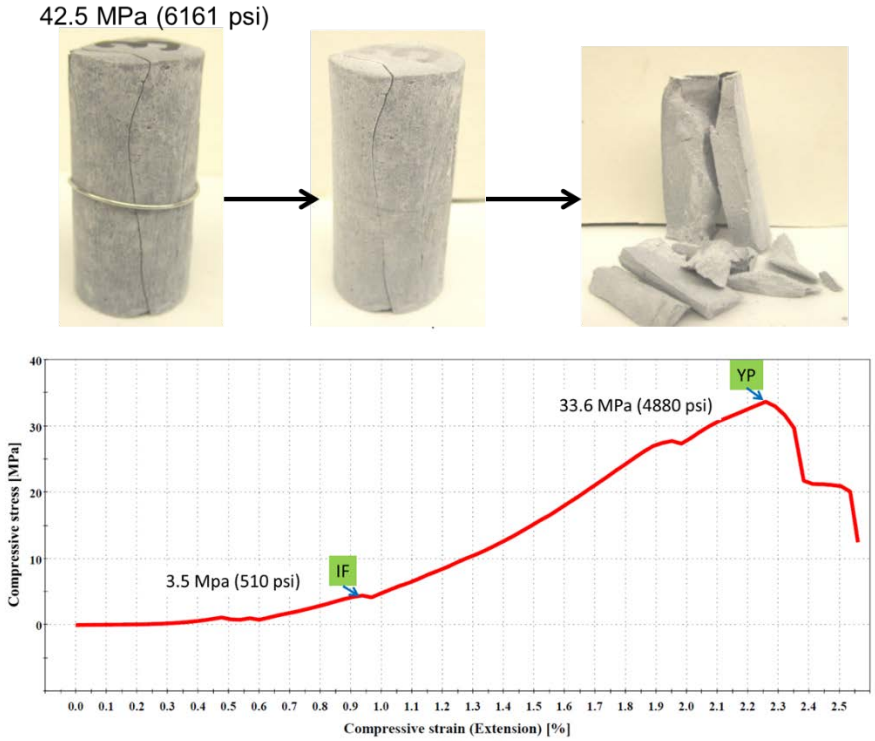

Figure 59. Compressive stress-strain curve for reunited GBFS/SiO_2 in carbonate.

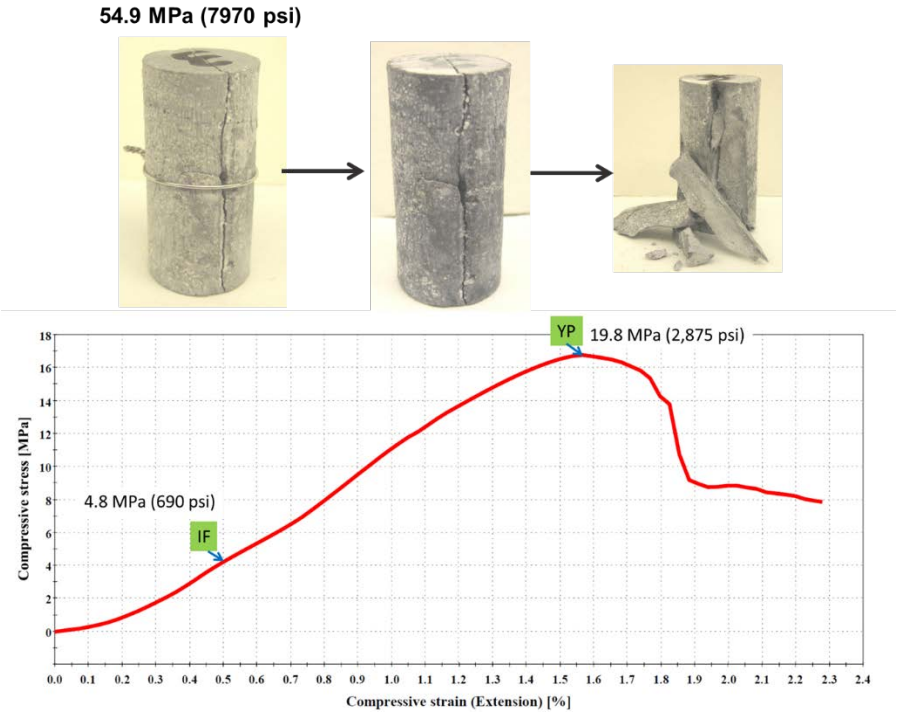

Figure 60. Compressive stress-strain curve for reunited GBFS/SiO_2 in brine.

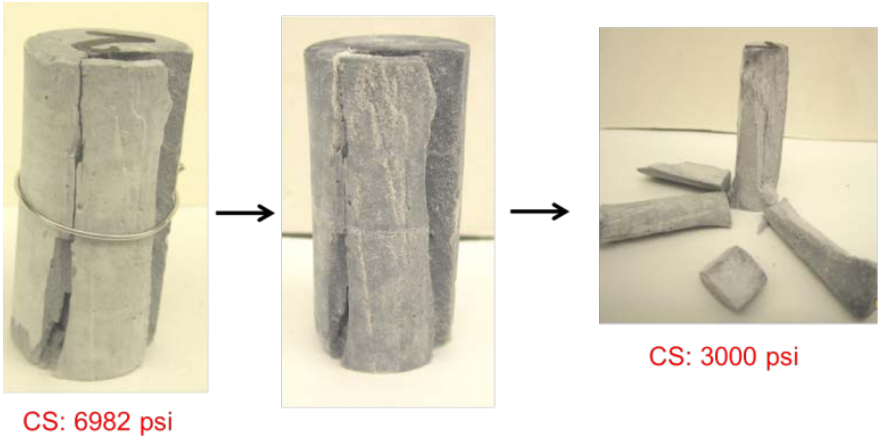

Figure 61. Appearance of reunited GBFS/SiO_2 and failure mode after compressive strength test of the healed GBFS/SiO_2 in plain water: CS - compressive strength before (left) and after fragments reattachment (right).

Figure 62 presents the appearance and compressive stress-strain curve of reunited CAP-B composite in brine. The stress-strain curve revealed the IF value of 1524 psi, which was more than 2-fold higher than that of GBFS/SiO_2. At YP, the recovery rate was 91 %, which was 60% higher than that of GBFS/SiO_2. Also, this composite disclosed a good reunited feature in water (Figure 63).

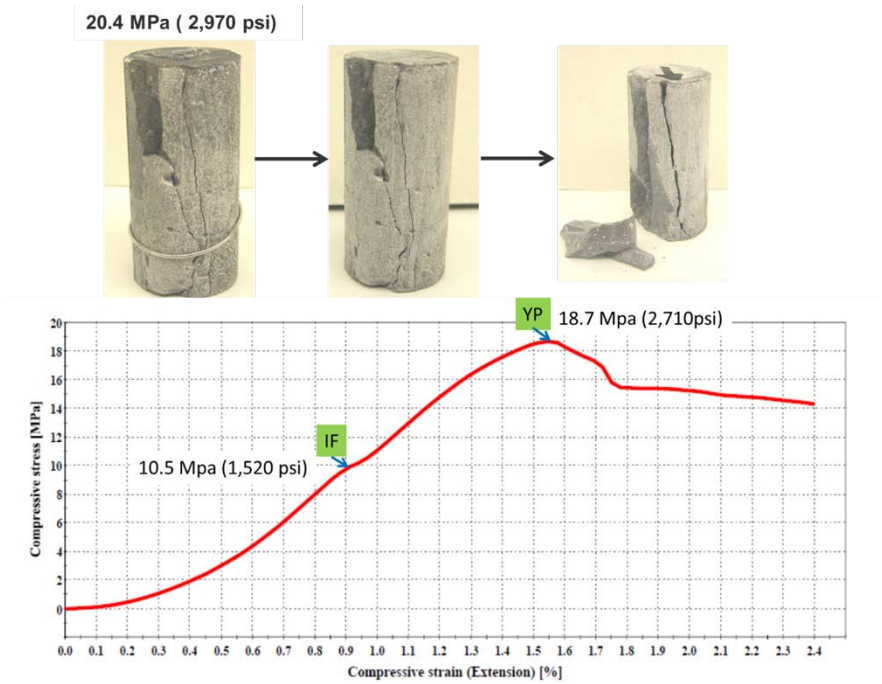

Figure 62. Compressive stress-strain curve for reunited CAP-B in brine.

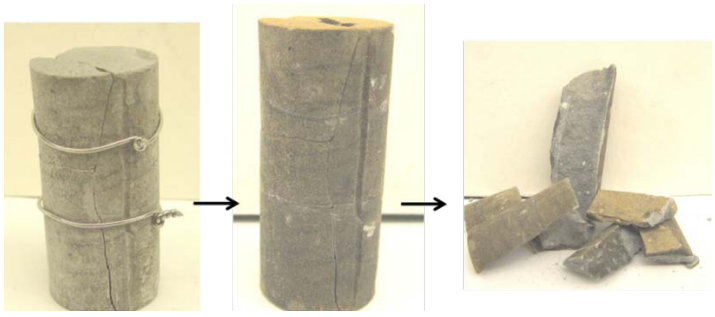

Figure 63. Appearance of reunited CAP-B and failure mode after compressive strength test of the healed sample in plain water.

The above information strongly supported our concept of interfacial bonding behavior between broken cement fragment and failed mother cement. TSRC had a great self-adherence of a fragment to the mother composite. Conceivably, there were two potential reasons for this: One was a specific chemistry of TSRC promoting the interactions between fragments and mother composite; the other was associated with the ductile failure mode; namely, both the fragment and the defected mother composite sides had rough surfaces and, as a result, high contact surface area, leading to a strong interfacial bonding. Considering these two factors, the chemistry of OPC/SiO_2 did not help self-reunion in plain water, but the re-attachment took place in carbonate and brine environments, promoted by the chemistries of the environments. On the other hand, all other composites including CAP-B and GBFS/SiO_2 were capable of fragments re-attachment in all three environments. In the case of GBFS/SiO_2 composite, despite the re-attachment of the fragment the bond was weak because of the smooth surface of the fragment and the mother cement body at the fracture interface typical for brittle composites resulting in low contact

surface area. The low contact surface area was responsible for the weak bonding of the reattached fragments.

3.5.4. 30-day-long autoclaved MGF-modified TSRC composites in plain water

In this work, the emphasis was directed towards studying the effect of MGF on YM and compressive strength of TSRC composites after longer autoclaving time of up to 30 days at 300°C. Also, we investigated the efficiency of MGF in helping to recover compressive strength of damaged TSRC. For comparison, two reference cements, MGF-free TSRC and OPC/SiO_2 composites, were employed in this work. (Figure 64), YM of OPC/SiO_2 increased in the first 15 days to 268 x 10^3 psi, and somewhat declined to 249 x 10^3 psi after 30 days. Nevertheless, after 30 days autoclaving, this composite sustained the moderate brittle nature. The YM of TSRS free of MGF increased with an extended autoclaving time from 126 x 10^3 psi after 1-day to 204 x 10^3 psi after 30 days in an autoclave. In contrast, a conspicuous increase of YM was observed for MGF-modified TSRC composite after longer autoclaving; YM value increased by nearly 3-fold to 409 x 10^3 psi after a 30-day autoclaving, compared against the 1-day autoclaved composite, thereby resulting in mechanical transition from moderate brittle nature to brittle one due to alkali dissolution and reactions of MGF, followed by densification of cement.

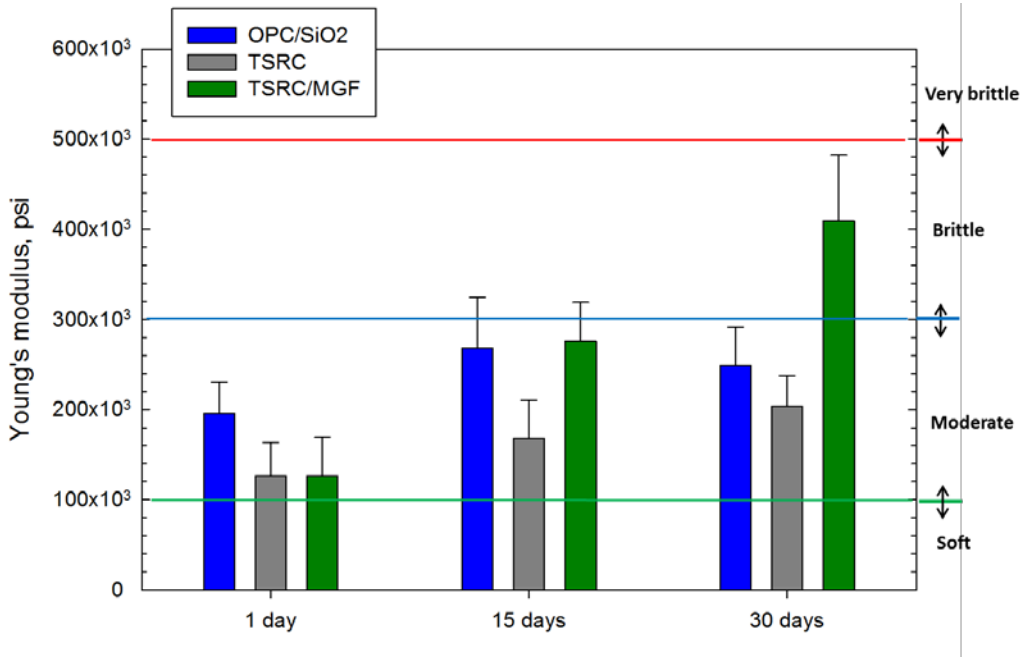

Figure 64. YM of 1-, 15-, and 30-day-autoclaved MGF-modified TSRC, and unmodified TSRC and OPC/SiO_2 reference composites.

Figure 65 gives the compressive strength of 1-, 15-, and 30-day-autoclaved composites before and after 5 days self-healing treatments. The compressive strength measurements results were similar to YM data; namely, two composites, TSRC reference and MGF-modified TSRC, exhibited increase in compressive strength as a function of autoclaving time. The compressive

strength of TSRC reference and MGF/TSRC rose to 2410 psi after 30 days from 1740 psi after 1 day for the former composite and to 2860 psi after 30 days from 1840 psi after 1 day for the latter composite. On the other hand, for OPC/SiO_2 reference, the highest strength of 3320 psi was developed after 15 days; however, extending the autoclaving period to 30 days engendered some reduction of the strength to 2965 psi.

Figure 66 represents the compressive strength recovery after 300°C-5-day-self-healing treatment in plain water. The highest recovery of 117% was observed for 1-day-autovlaved TSRC/MGF composite, strongly suggesting that MGF acts as a very effective healing aid at early autoclaving age. However, the extended autoclaving time to 15 days resulted in the reduction of recovery rate to 84%, and a further reduction to 61% was observed at 30-day-autoclaving age. TSRC reference showed no significant changes, ranging from 81 to 86%, in recovery for 1-, 15-, and 30-day autoclaved composites. Meanwhile, the recovery of 15- and 30-day-autoclaved OPC/SiO_2 reference was the average of only 37%, which was 36% lower than that of 1-day autoclaved one. Thus, it appeared that the recovery of OPC/SiO_2 reference decreases after longer curing times.

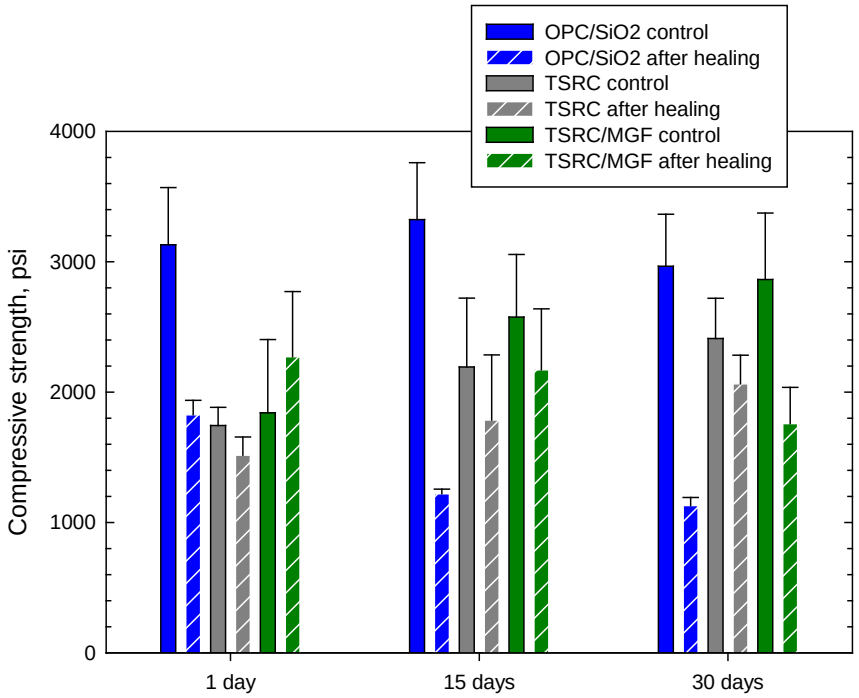

Figure 65. Compressive strength of MGF-modified TSRC, and unmodified TSRC and OPC/SiO_2 reference composites before and after 300°C-5-day-self-healing treatment.

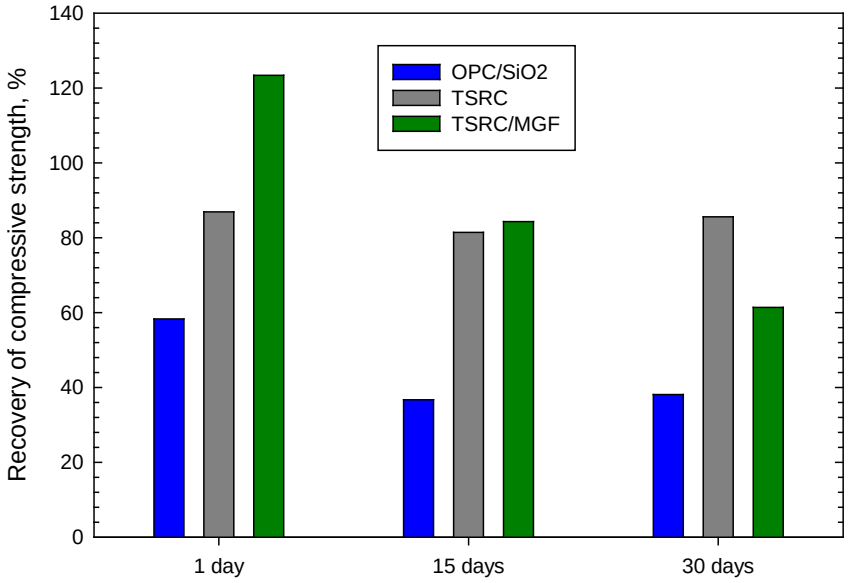

Figure 66. Recovery of compressive strength for MGF-modified TSRC, and unmodified TSRC and OPC/SiO_2 reference composites after 300°C-5-day-self-healing treatment for composites with the first compressive damage imposed after 1-, 15- or 30 days of the initial curing at 300°C.

3.5.4.1. Unmodified TSRC after 15- or 30-day initial curing time: 3D micro-image analyses of cracks sealing

Figure 67 shows images of typical natural cracks with width, ranging from 0.1 to 0.2 mm, for TSRC composite samples without MGF cured in plain water at 300°C for 15 or 30 days before and after 5-day healing treatment. After longer curing time the availability of non-reacted blend components decreases, including non-reacted cement and FAF particles due to the continues cement hydration and FAF alkaline reactions. The lack of reactive materials may cause decreased healing and sealing ability of the composites after prolonged curing. In particular, decreased FAF content can result in decreased amounts of sealing phases such as silica and high-temperature zeolites that plug the cracks, assisting the strength recovery. Additionally, water environment can provide little or none reactive ions that could help building up new phases through reactions with the cementitious composites. Moreover, longer curing times result in higher samples crystallinity and increased brittleness, promoting formation of larger cracks that are more difficult to seal.

However, the experiments revealed moderately-sized cracks formed in TSRC and effectively sealed after only 5-day exposure to the original curing conditions when the damage was imposed after 15- and even 30 days of the initial curing, while a 10-day treatment was required to seal a slightly wider crack >0.2 mm in a 1-day cured sample as described in *3.3.1. 3D micro-image analyses of crack's sealing after 1-day initial curing time*. The 30-day cured sample displayed increased surface roughness due to the deposition of new products after the additional 5 days of healing, and the small crack was effectively sealed. The healing seemed to proceed faster for the samples with the longer initial curing before the imposed damage. It is reasonable to rationalize that FAF reacted further after 15 and 30 days compared with that of the 1-day cured samples. In this case, the reactive ions released by the thermo-alkaline activation of FAF would be more

readily available to form new phases after longer curing times. Thus, this experimental evidence demonstrated that non-reacted FAFs remained in effect to assist the sealing activity.

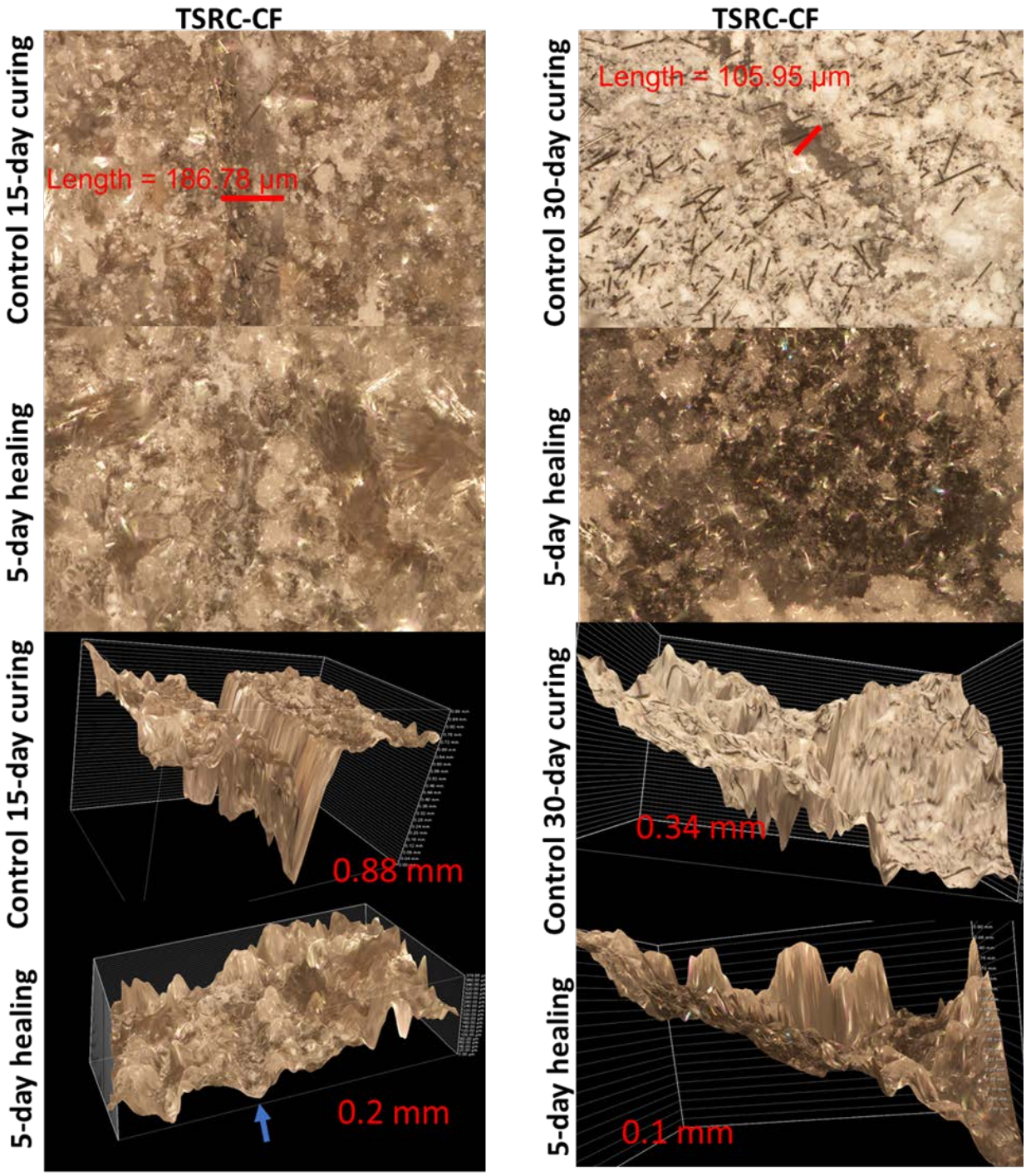

Figure 67. 15- and 30-day 300ºC cured samples damaged and healed for another 5 days under the same conditions for TSRC with Carbon fibers (CF) (crack sizes ~0.19 mm wide and 0.88 mm deep for the 15-day sample and ~0.11 mm wide and 0.34 mm deep for the 30-day cured sample).

On the other hand, the calcium-aluminate cement reaction products should be completely formed by that time and are unlikely to contribute significantly to the sealing of the cracks. Furthermore, when the initial FAF source would be exhausted at longer curing time, the phase transitions and reactions of FAF-derived reaction products with the environmental ions could further contribute to the cracks sealing. Consequently, if the above interpretation is valid, FAF is the major contributor to the phases that seal the cracks and the sealing will occur as along as the decomposition/reaction products of FAF are still available.

3.5.4.2. MGF-modified TSRC after 1-, 15- or 30-day initial curing time: 3D micro-image analyses of cracks sealing

As aforementioned, the incorporation of MGF into TSRC composite led to a highly increased YM and compressive strength with extended initial curing time compared against TSRC without MGF; particularly, YM value was in the region of brittle nature, ranging from 300 to 500 x 10^3 psi after 30 days initial curing, while 1- and 15-day cured samples had the moderate brittle nature. On the other hand, the compressive strength recovery rate of MGF-modified TSRC declined for longer initial curing. In contrast, no significant changes in recovery rate were observed for unmodified TSRC samples cured for 1, 15, or 30 days.

Figure 68 compares the microstructures of typical cracks before and after their short-term sealing for MGF-modified TSRC (denoted as TSR-CF-GF) and unmodified one (TSRC-CF) samples cured for 1 day in 300^{o}C plain water and then healed for 5 or 10 days under the same environment after the imposed damage. As can be seen, the initial crack for modified sample was larger than that of unmodified one; for instance, a typical crack shown was 0.4 mm wide and 1.25 mm deep for the composite with MGF, and 0.25 mm wide and 0.7 mm deep for that without MGF. The smaller crack of the sample without MGF sealed completely in 10 days. That of MGF-modified sample was partially sealed after the 10-day treatment, its depth decreased by only ~30% at its deepest points. However, interestingly, the top shallow area of the crack was capped and bridged by reaction and precipitation products, so that a further sealing activity was no longer needed. Conceivably, these reaction and precipitation products may come from the thermo-alkali dissolution of MGF during healing treatment; namely, the dissolved MGF may liberate reactive ionic species to form capping and bridging end-products. Such a peculiar crack sealing mechanism of composite by MGF appeared to serve in improving the strength recovery for the short initial curing time of the composite.

At longer curing time of 15 and 30 days, the efficacy of healing for the MGF-modified and unmodified TSRCs was somewhat different. The sealing became more efficient for the MGF-modified samples after longer initial curing. As is evident from Figures 69 and 70, both cracks formed after 15 and 30-day initial curing for modified samples were wider than for unmodified samples. The formation of these wider cracks seems to represent a brittle fracture mode. Interestingly, both cracks were sealed after 5-day treatment, instead of 10-day treatment which was required for the 1-day aged samples. The most likely explanation for this reduced healing time is a ready availability of reactive ionic species as healing promoters and accelerators released by the slow continuous disintegration of MGF under alkaline environment of the composite at 300°C after long-term curing. Namely, these ionic reactants released from MGF were able to form and precipitate new sealing and plugging solid state phases in crack spacing possibly because of the interactions with the composite components. This demonstrated that even after longer initial curing, the samples still possessed the sealing capacity in the presence of MGF, thereby confirming MGF's role as a healing aid. Slow disintegration of MGF was

important to ensure its healing aid activity after longer service time of the cementitious composite.

Additionally, the increase in MGF's disintegration after longer curing time is likely to form amorphous phases which could help in filling the cracks. The excellent sealing performance of MGF-modified TSRC does not correlate with the low strength recovery of the long-term cured samples. This fact suggests that lower strength recovery was due to some other factors than cracks sealing.

3.5.4.3. Phase analyses of MGF-modified and unmodified TSRC in plain water

To verify whether MGF are susceptible to a highly alkaline attack of TSRC slurries we exposed the fibers to the pore water of the slurry separated from the cement 10 minutes after the slurry mixing by centrifuging. The MGF were covered by the pore solution and autoclaved for 24 hrs at 300^{o}C. TSRC prepared with CAC#80 and iron-rich CAC Fondu were tested. Pore solution of class G/SiO_2 cement was used as a reference. MGF samples exposed to all three solutions solidified after the autoclaving. The surface elemental composition of the fibers was tested with EDX and crystalline composition determined by XRD.

The most striking change in the composition of the glass fibers after the autoclaving is appearance of aluminum signal, which was absent before the exposure (Table 13). Surprisingly the aluminum content is about the same for the samples treated with the pore solution from the aluminum-rich slurries (TSRC slurries) and OPC-based slurry with the low aluminum content. This fact suggests that MGF preferentially react with the aluminum-containing species from the pore solutions. Calcium content of MGF, on the other hand slightly decreases after the treatment. Tables 14-16 summarize crystalline compositions of pore-solution-treated MGF. For TSRC-pore solution treated MGF the two major crystalline phases forming on MGF were silica, zeolite, analcime and tobermorite aluminum. In the case of OPC-based composite the silica and sodium-calcium-aluminum silicates were predominant. Interestingly, tobermorite or xonotlite were not detected among the crystalline products formed in the MGF treated with G/SiO_2 pore solution.

Table 13. Elemental composition of MGF before any treatment and after the 24hr-300^{o}C treatment in pore solutions from TSRC (made with CAC #80 or CAC Fondu) or G/SiO_2.

Material/pore solution	SiO_2	CaO	Al_2O_3	K_2O	Fe_2O_3	SO_3	TiO_2
MGF	**57**	**42**	**-**	**-**	**0.74**	**-**	**-**
G/SiO_2	51	37	8.4	1.8	0.6	0.87	0.58
TSRC-#80	56	34	7.9	-	0.44	-	1.0
TSRC-Fondu	57	33	8.2	-	0.41	-	0.92

Based on these tests it is impossible to conclude whether the crystalline products form from the ions of the composites or MGF contribute ions to these phases because of alkaline dissolution. However, it is clear that MGF reacts forming a solid phase, which could be amorphous or both amorphous and crystalline under conditions of alkaline slurries. Also, such big species as zeolite analcime form on its surface; this type of materials can contribute to cracks plugging. It is also

important to notice that silica and aluminum-containing species are among the predominant crystalline phases.

Table 14. Crystalline phases formed with the MGF and TSRC (made with CAC #80) pore solution after autoclaving for 24hrs at 300°C.

ICDD number	Major phases	Semi quantitative evaluation
01-075-8689	Analcime, $Na_{1.71}((Al_{1.806}Si_{4.194})O_{12})(H_2O)_{2.16}$	40
04-015-7162	Coesite, SiO_2	29
01-074-2878	Tobermorite, aluminum $Ca_{4.9}(Si_{5.5}Al_{0.5})_{16.3})(OH)_{0.7}(H_2O)_{0.5}$	19
01-077-8366	Tobermorite 11A $Ca_4(Si_6O_{15})(OH)_2(H_2O)_5$	9
01-082-3579	Aklimaite $Ca_4(Si_2O_5(OH)_2)(OH)_4(H_2O)_5$	3

Table 15. Crystalline phases formed with the MGF and TSRC (made with CAC, Fondu) pore solution after autoclaving for 24hrs at 300°C.

ICDD number	Major phases	Semi quantitative evaluation
04-015-7166	Coesite, SiO_2	43
01-074-2878	Tobermorite, aluminum $Ca_{4.9}(Si_{5.5}Al_{0.5})_{16.3})(OH)_{0.7}(H_2O)_{0.5}$	21
01-077-8366	Tobermorite 11A $Ca_4(Si_6O_{15})(OH)_2(H_2O)_5$	2
00-041-1478	Analcime-C, $Na(Si_2Al)O_6(H_2O)$	20
04-015-8151	Aegirine $NaFeSi_2O_6$	14

Table 16. Crystalline phases formed with the MGF and G/SiO_2 pore solution after autoclaving for 24hrs at 300°C.

ICDD number	Major phases	Semi quantitative evaluation
04-008-8440	Coesite, SiO_2	24
04-012-5136	Vimsite, $CaB_2O_2(OH)_4$	22
04-017-9600	Analbite, $NaAlSi_3O_8$	17
04-011-1325	Gonnardite, $Na_4Ca_2Al_8Si_{12}O_{40}(H_2O)_{12}$	15
00-005-0586	Calcite, $CaCO_3$	5

The major and minor crystalline phases formed in non-modified TSRC composite under steam at 300°C after 1-day (control) and long-term curing are given in Table 17 for matrix and Table 18 for the surface.

The crystalline phases after the first day of curing included grossular hydroxylian, zeolite, analcime, feldspar mineral dmisteinbergite, some boehmite, and non-reacted species of corundum and mullite. The patterns noticeably changed after longer curing times of 15 and 30 days. Carbonated-sodium-calcium-aluminum silicate (sodium-calcium cancrinite) replaced analcime, the peaks' intensities of dmisteinbergite, katoite and mullite decreased. (Note, that multiple grossular peaks indicated various stoichiometries of hydrogrossular.) Decomposition of mullite contributed to the formation of calcium-magnesium-iron-aluminum silicates (clintonite

from mica group and possibly, khesinite – two small peaks of these mineral at 2Θ: 10.93 and 11.88 do not overlap with any other phases). After the 30-day curing, aluminum in grossular was partially substituted by ferric ion to form grossular ferrian hydroxylian. Additionally, as is evident from increasingly intense signal at 2Θ: 35.72-36, the released iron crystallized as maghemite. Decomposition of FAF also resulted in increased boehmite peaks intensities and a new peak at 2Θ: 30.26 from SiO_2 (stishovite) as well as a small peak after 30 days attributed to quartz. A strong peak at 2Θ of 20.26, partially overlapping with the dmisteinbergite peak at 20.18 was likely from some mica-type mineral. The intensity of the peak stayed the same after the 15 and 30 days of curing. Because of the complex multi-phase composition, it was difficult to ascribe this peak to an exact phase. Several minerals from mica group could fit the pattern including paraganite, margarite, muscovite or unnamed potassium-aluminum-magnesium-silicon oxide hydroxide. Similarly, the increased quartz signal after longer curing times complicated evaluation of the intensity of residual mullite peaks strongly overlapping with other phases and, in particular, with silica at ~2Θ of 26. In summary, at longer exposure of unmodified TSRC to high-temperature hydrothermal conditions, FAF further reacted with the release of aluminum, silicon, iron and magnesium ions that participated in phase transitions and formation of new minerals. The minerals such as iron-containing grossular further reinforced the matrix providing cement strength recovery even after long initial curing times, while the dissolution and precipitation of silica acted to seal the cracks. Some minerals participated in both strength recoveries and cracks sealing (cancrinite and boehmite). The complexity of XRD patterns did not allow a definite conclusion on whether some crystalline FAF was left after the 30 days of curing. Some peaks could be ascribed to feldspars with decreased calcium (albite, calcian) or alkali feldspars (albite, orthoclase, sanidine).

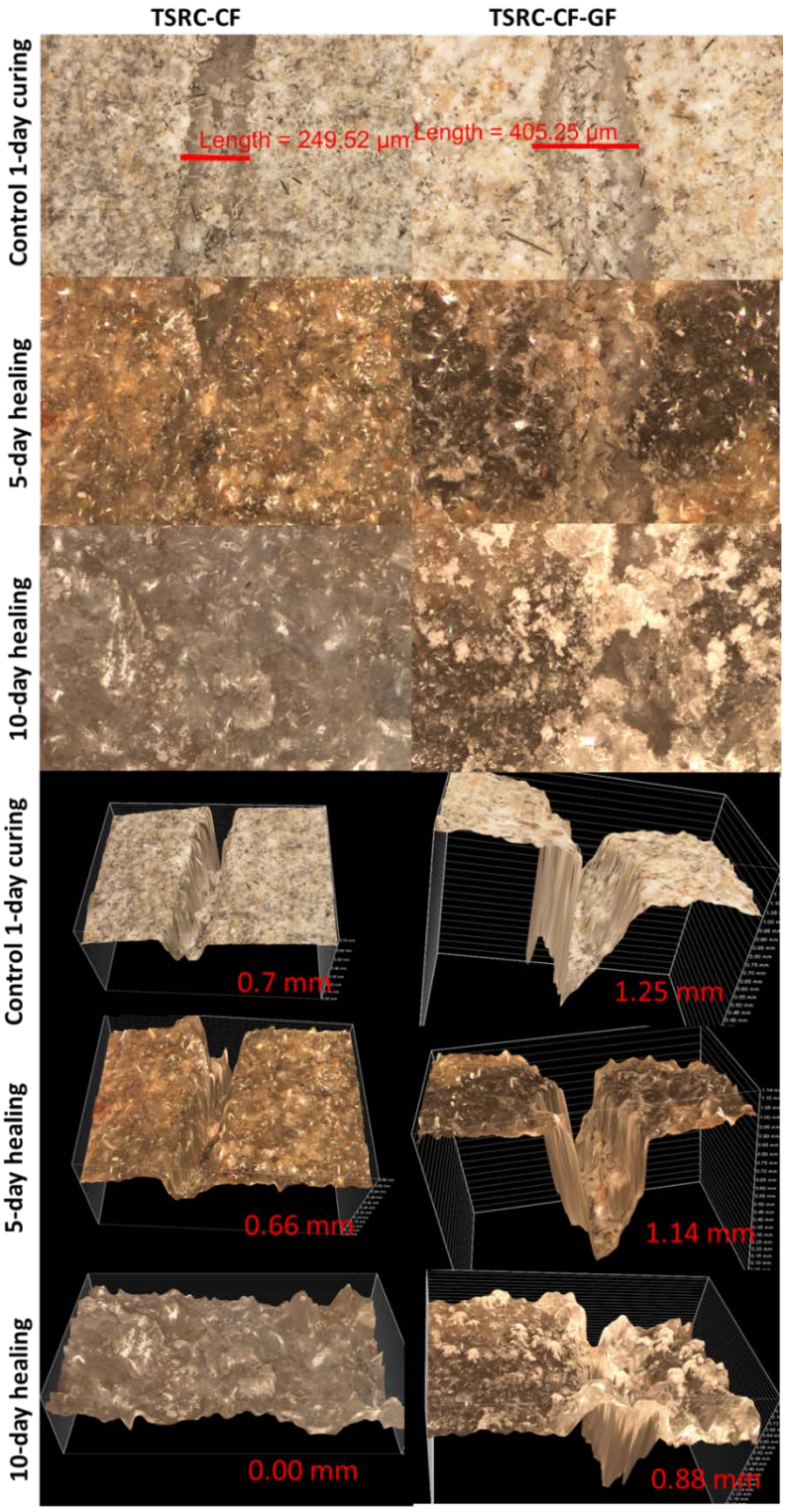

Figure 68. Comparison of short-term cracks sealing for TSRC samples modified with micro-carbon fibers (CF) (left) and both carbon and glass fibers (GF) (right) at 300°C in water. The cracks formed after 1-day 300°C hydrothermal curing of the samples.

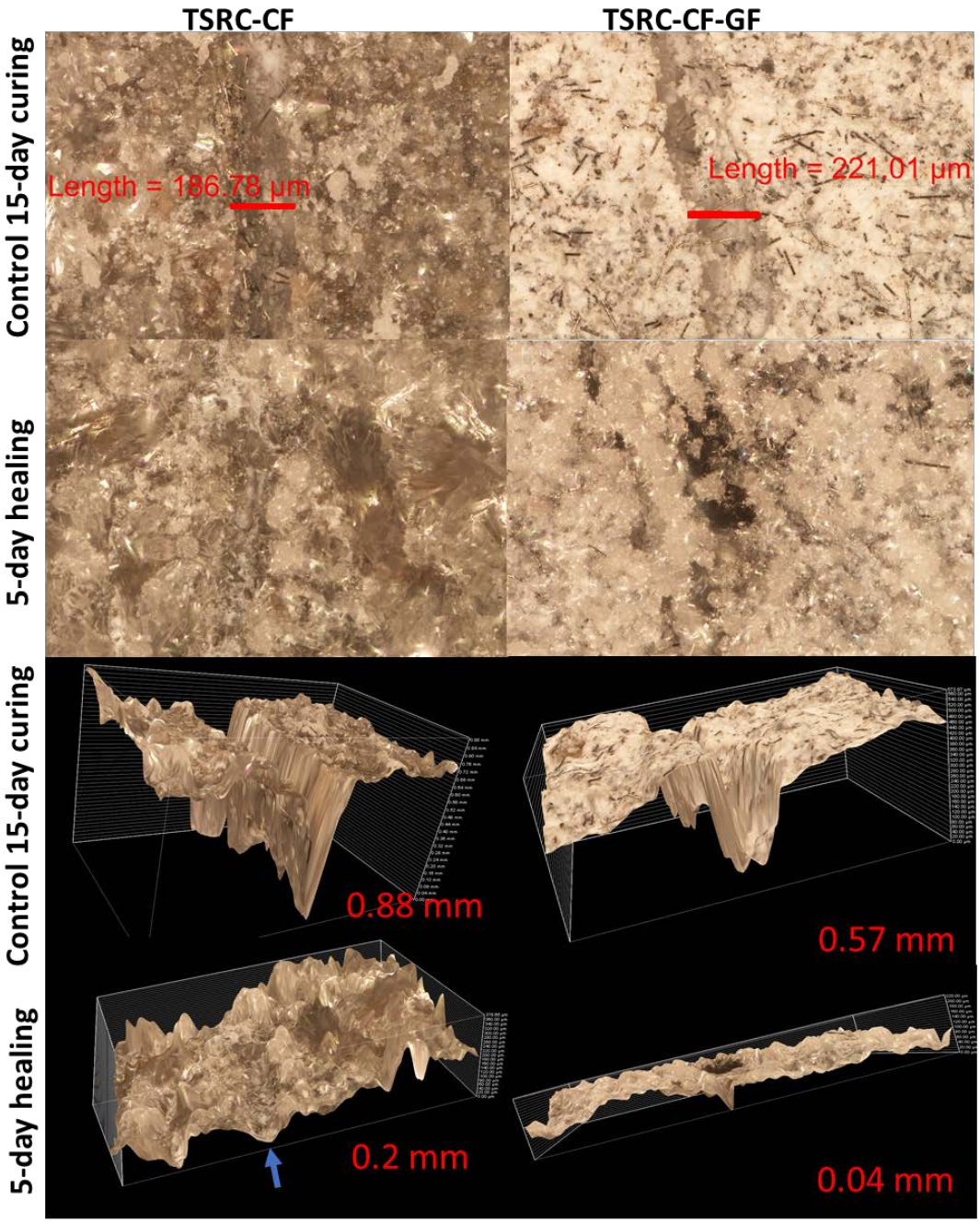

Figure 69. 15-day 300ºC cured samples damaged and healed for another 5 days under the same conditions for unmodified TSRC (crack size ~0.19 mm width and 0.88 mm deep) and TSRC modified with MGF (crack size ~0.22 mm width and 0.57 mm depth).

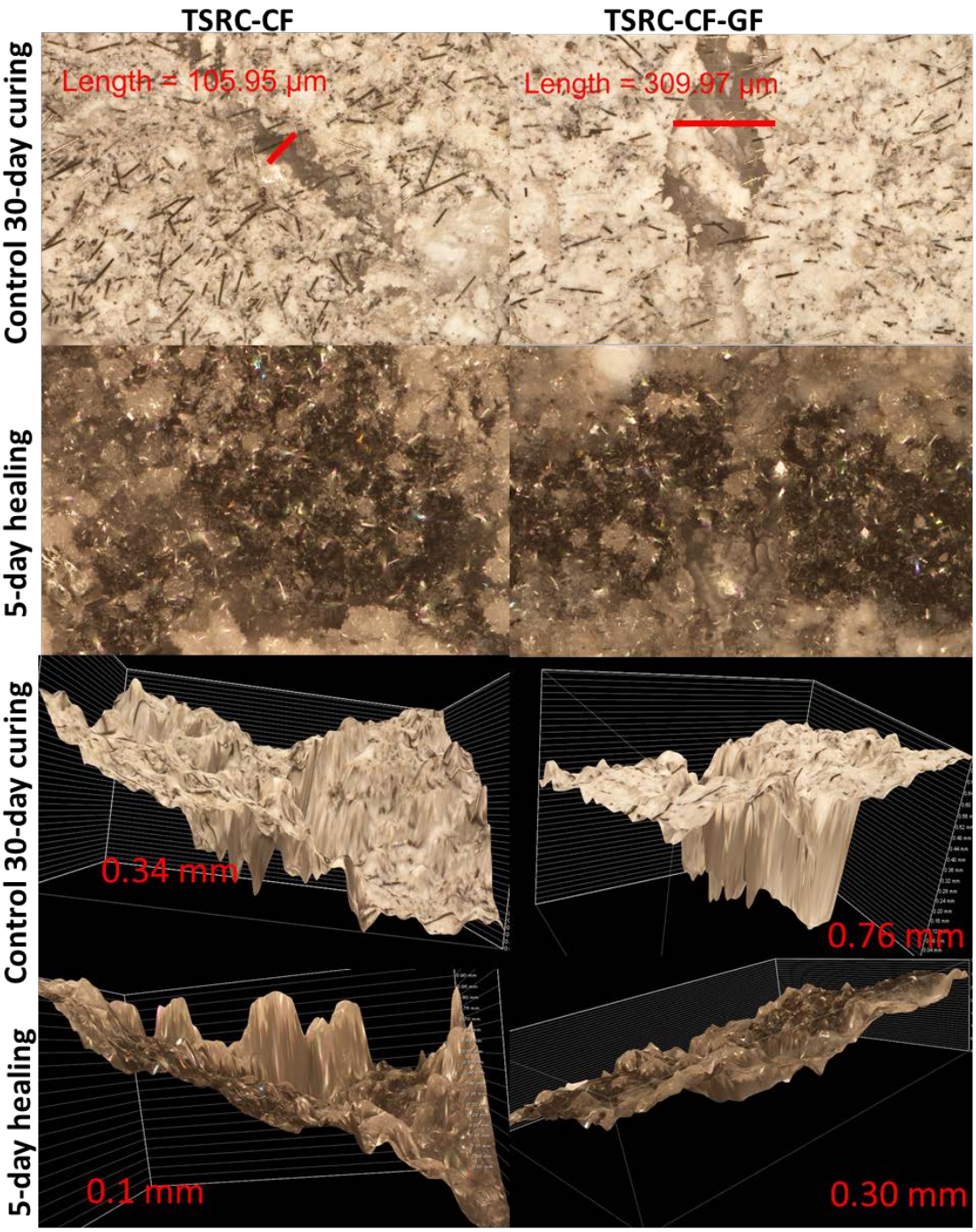

Figure 70. 30-day 300ºC cured samples damaged and healed for another 5 days under the same conditions for unmodified TSRC (crack size ~0.11 mm width and 0.34 mm depth) and TSRC modified with MGF (crack size ~ 0.31 mm width and 0.76 mm depth).

Table 17. Major, minor and possible crystalline phases formed **in matrix** under hydrothermal (water) conditions at 300°C after 1-,15- or 30-day exposure of unmodified TSRC.

Major phases (ICDD numbers)	**Minor phases (ICDD numbers)**
1-day curing	
Analcime, $Na_{0.9}((Al_{0.9}Si_2)O_6)(H_2O)$ (01-076-6569) Grossular hydroxylian $Ca_3Al_2(SiO_4)_2(OH)_4$ (and other stoichiometries) (00-042-0570) Katoites $Ca_{2.916}Al_2Si_{1.092}O_{12}H_{7.632}$/ $Ca_3Al_2(SiO_4)_{1.53}(OH)_{5.88}$ (01-075-4213/04-014-984) Dmisteinbergite $CaAl_2Si_2O_8$ (04-011-5220) Corundum Al_2O_3 (01-073-1512)	Boehmite AlOOH (04-012-5050) Mullite $Al_{2.25}Si_{0.75}O_{4.875}$ (04-014-8459)
15-day curing	
Cancrinite $Na_{7.28}Ca_{0.64}(Si_6Al_6O_{24})(CO_3)_{1.65}(H_2O)_2$ (01-081-9895) Grossular hydroxylian $Ca_3Al_2(SiO_4)_2(OH)_4$ (and other stoichiometries) (00-042-0570) Clintonite $CaMg_{2.3}Fe_{0.1}Al_{3.2}Si_{1.4}O_{10}(OH)_2$ (04-019-1584) Some mica mineral	Boehmite AlOOH (04-012-5050) Andradite $Ca_3Fe_2(SiO_4)_3$ (04-012-1284) Mullite $Al(Al_{0.83}Si_{1.08}O_{4.85})$ (01-089-2645) Corundum Al_2O_3 (04-015-8610) Stishovite SiO_2 (00-045-1374) *Possible*: Khesinite $CaMgFe_{2.2}Al_{1.7}Si_{1.1}O_{10}$ (04-013-3515)
30-day curing	
Grossular ferrian hydroxylian $Ca_3Al_{1.096}Fe_{0.904}(Si_{2.823}O_{11.292})(OH)_{0.708}$ (and other stoichiometries) (01-072-8446) Cancrinite $Na_{7.28}Ca_{0.64}(Si_6Al_6O_{24})(CO_3)_{1.65}(H_2O)_2$ (01-081-9895) Bohmite AlOOH (04-014-2197) Corundum Al_2O_3 (04-008-3293) Silicon oxide/quartz SiO_2 (01-077-8624/04-007-1808) Some mica mineral	Sodium aluminum silicate hydrate $Na_8(AlSiO_4)_6(OH)_2$ (00-040-0100) *Possible*: Albite $Na(AlSi_3O_8)$ (04-007-5009) Anorthoclase $(Na,K)(Si_3Al)O_8$ (00-009-0478) Khesinite $CaMgFe_{2.2}Al_{1.7}Si_{1.1}O_{10}$ (04-013-3515) Foshagite $Ca_4(SiO_3)_3(OH)_2$ (00-029-0377) Clintonite $CaMg_{2.3}Fe_{0.1}Al_{3.2}Si_{1.4}O_{10}(OH)_2$ (04-019-1584) Mullite $Al_{4.64}Si_{1.36}O_{9.68}$ (01-079-1453) Maghemite Fe_2O_3 (04-008-3650)

A clearly visible surface layer formed in samples cured for 15 and 30 days. It was thicker and more loosely attached to the rest of the sample after 30 days of curing than after 15 days. This stronger attachment of the matrix to the surface at 15 curing days likely resulted in collecting some part of the matrix with the surface samples for XRD analyses and, at least partially, explains higher intensity of the peaks from matrix-related calcium-containing phases, such as cancrinite, khesinite, garnet (andradite) in 15-day samples than in 30-day ones.

The major crystalline surface phase was silica. High intensity of silica peaks complicated identification of other significantly smaller peaks. These were ascribed to sodium-iron-aluminum silicate or sodium-aluminum silicate, aegirine (also detected in the MGF exposed to the TSRC

pore solution for 24 hrs at 300ºC, see above); zeolites, analcime and amicite; aluminum-oxide-hydroxide, boehmite and mica-type mineral, paragonite with limited certainty. Likewise, some peaks could be from feldspars with decreased calcium (albite, calcian) or alkali feldspars (albite, orthoclase, sanidine). These minerals crystallized after most calcium from CAC already reacted and only FAF participated in the formation of new phases.

MGF-modified TSRC cured in water had higher peak intensities of analcime, katoite and grossular. Some quartz (shoulder at 2Θ: 26.2-26.3) and some iron-containing calcium-silicate phase – srebrodolskite (shoulders, e.g. 2Θ:31.98) formed in these samples after the first day of curing at 300ºC (Table 19). A peak at 26.4 (found only in the pattern of glass-modified samples) is likely from keatite SiO_2 (04-007-1438). Presence of mica type mineral, paragonite, iron-containing grossular is possible. The samples with MGF are richer in silica already after the first curing day. The pattern shows a clear peak at 2Θ: 37.18, which likely belongs to sodium-aluminum silicate (04-015-8059). The peak strongly declines after 30 days.

Comparison of 15- and 30-day cured modified TSRC clearly demonstrates that MGF stabilize analcime. Analcime peaks at 2Θ: 15.921/30.64 are present only in the patterns of modified TSRC. Because of analcime stabilization there is less cancrinite (peaks at 2Θ: 14.16, 19.2, 24.53, 32.86, 43.11) obtained through analcime→ cancrinite transition. There are higher intensity peaks of iron-containing grossular (andradite, at 2Θ: 29.86, 33.4, 35.19, 36.79, 41.11), iron-magnesium silicate, khesinite and iron oxide peak at 2Θ: 30.1. Among the three reaction products, iron-containing grossular, iron-magnesium silicate and analcime, formed in samples of modified TSRC, the first two products enhanced the strength recovery and analcime participated in cracks' sealing.

Some mica-type mineral with the peaks at 2Θ: 20.22-20.26 was the same as for the samples without MGF. The mica minerals that fit the pattern included: paraganite-2M1 (01-083-2128); celadonite/muscovite 3T (04-021-4959); margarite 2M1 (04-013-3004) or potassium-aluminum-magnesium-iron silicate oxide hydroxide (01-079-6488(6487)). Similarly, some peaks could be ascribed to feldspars with decreased calcium (albite, calcian) or alkali feldspars (albite, orthoclase, sanidine). Additionally, presence of magnesium-containing mineral, polymorph of serpentine, lizardite, was possible in MGF-modified samples. Small amounts of magnesium could be coming from the reacting glass fibers. Magnesium minerals, in this case lizardite and khesinite, increase the strength of the cement matrix. High-temperature calcium silicate wollastonite formed only in glass-modified samples likely from silicon and calcium released by decomposing MGF.

Table 18. Major, minor and possible crystalline phases formed at the **surface** under hydrothermal (water) conditions at 300ºC after 15- or 30-day exposure of unmodified TSRC.

Major phases (ICDD numbers)	**Minor phases (ICDD numbers)**
15-day curing	
Cancrinite $Na_{7.28}Ca_{0.64}(Si_6Al_6O_{24})(CO_3)_{1.65}(H_2O)_2$ / $Na_{7.28}Ca_{0.64}(Si_6Al_6O_{24})(CO_3)_{1.66}(H_2O)_2$ (01-081-9895/9893)	Sodium-aluminum-silicate $Na_8(Al(SiO_4)_6(OH)_2$ (00-040-0100)
Khesinite $CaMgFe_{2.2}Al_{1.7}Si_{1.1}O_{10}$ (04-013-3515)	Maghemite-C Fe_2O_3 (00-039-1346)
	Analcime $Na_{7.2}Al_{7.2}Si_{16.8}O_{48}(H_2O)_8$ (04-013-2038)
	Andradite aluminian $Ca_3(Fe_{1.42}Al_{0.56})(SiO_4)_3$ (01-082-8676)

Quartz SiO_2 (01-070-8054) Some mica mineral	Mullite $Al_{2.19}Si_{0.81}O_{4.901}$ (04-008-9530) Aegirine $NaFeSi_2O_6$ (04-015-8149) Paragonite $NaAl_3Si_3O_{10}(OH)_2$ (04-017-0660) Albite, calcian/albite $Na_{0.6}Ca_{0.4}Al_{1.4}Si_{2.6}O_8/NaAlSi_3O_8$ (04-007-9876/01-080-3256)
30-day curing	
Silica SiO_2 (00-033-1161/04-008-7653) Aegirine aluminian $NaFe_{0.65}Al_{0.35}Si_2O_6$ (04-014-4678) Cancrinite $Na_{7.28}Ca_{0.64}(Si_6Al_6O_{24})(CO_3)_{1.65}(H_2O)_2$ (01-081-9895) Some mica mineral	Sodium aluminum silicate hydrate $0.99Na_2O \cdot Al_2O_3 \cdot 4.07\ SiO_2 \cdot 5.7H_2O$ (00-038-0328) Stishovite SiO_2 (04-007-3487) *Possible*: Microcline $K(AlSi_3O_8)$ (01-071-0955) Khesinite $CaMgFe_{2.2}Al_{1.7}Si_{1.1}O_{10}$ (04-013-3515) Mullite $Al_{4.868}Si_{1.132}O_{9.566}$ (01-079-1452) Sillimanite $Al_2O_3 \cdot SiO_2$ (00-001-0626) Amicite $K_2Na_2Si_4Al_4O_{16}(H_2O)_5$ (04-011-3051) Albite, calcian/albite $Na_{0.6}Ca_{0.4}Al_{1.4}Si_{2.6}O_8/NaAlSi_3O_8$ (04-007-9876/01-080-3256)
30-day plus 5-day healing, major:	**30-day plus 5-day healing**, minor:
Quartz/silica SiO_2 (00-033-1161/04-008-7653) Aegirine aluminian $NaFe_{0.65}Al_{0.35}Si_2O_6$ (04-014-4678) Carbonated sodium calcium aluminum silicate (Cancrinite) $Na_{7.28}Ca_{0.64}(Si_6Al_6O_{24})(CO_3)_{1.65}(H_2O)_2$ (01-081-9895) Some mica mineral	Maghemite-C Fe_2O_3 (00-039-1346) *Possible*: Sanidine $K(Si_3Al)O_8$ (00-025-0618) Analcime $Na_{14.4}Al_{14.4}Si_{33.6}O_{96}(H_2O)_{16}$ (04-013-2040) Bohmite AlOOH (04-014-2197) Khesinite $CaMgFe_{2.2}Al_{1.7}Si_{1.1}O_{10}$ (04-013-3515) Mullite $Al_{4.868}Si_{1.132}O_{9.566}$ (01-079-1452) Amicite $K_2Na_2Si_4Al_4O_{16}(H_2O)_5$ (04-011-3051) Albite, calcian/albite $Na_{0.6}Ca_{0.4}Al_{1.4}Si_{2.6}O_8/NaAlSi_3O_8$ (04-007-9876/01-080-3256)

Table 19. Major, minor and possible crystalline phases formed in **matrix** under hydrothermal (water) conditions at 300ºC after 1-,15- or 30-day exposure of MGF-modified TSRC.

Major phases (ICDD numbers)	**Minor phases (ICDD numbers)**
1-day curing	
Analcime $Na_{1.71}((Al_{1.806}Si_{4.194})O_{12}(H_2O)_{2.16}$ (01-075-8690) Dmisteinbergite $CaAl_2Si_2O_8$ (04-011-5220) Katoites $Ca_{2.916}Al_2Si_{1.092})_{12}H_{7.632}/Ca_3Al_2(SiO_4)_{1.53}(OH)_{5.88}$ (01-075-4213/04-014-9841) Quartz SiO_2 (01-089-8946) Grossular hydroxylian $Ca_3Al_2(SiO_4)_2(OH)_4$ (00-042-0570) Sodium-aluminum-silicate $NaAlSi_2O_6$ (04-015-8059) Corundum Al_2O_3 (04-008-3293) Sillimanite Al_2SiO_5 (00-022-0018)	Boehmite AlOOH (04-012-5050) Mullite $Al_{2.34}Si_{0.66}O_{4.83}$ (01-076-2579) Srebrodolskite $Ca_2Fe_2O_5$ (04-007-2756)
15-day curing	

Cancrinite $Na_{7.28}Ca_{0.64}(Si_6Al_6O_{24})(CO_3)_{1.65}(H_2O)_2$/ $(Na_{7.05}Ca_{0.87})(Al_6Si_6O_{24})(CO_3)_{1.76}(H_2O)_2$ (01-081-9895/01080-6875) Analcime $Na_{0.9}((Al_{0.9}Si_2)O_6)(H_2O)$ (01-076-6569) Corundum Al_2O_3 (01-073-1512) Anorthite $CaAl_2Si_2O_8$ (04-012-1276) Khesinite $CaMgFe_{2.2}Al_{1.7}Si_{1.1}O_{10}$ (04-013-3515) Some mica mineral	Boehmite AlOOH (01-074-2895) SiO_2 (01-099-8948/01-077-8634) Fe_2SiO_4 (01-071-1400) Maghemite $Fe_{21}O_{31}(OH)$ (04-009-9615) Grossular, ferrian hydroxylian $Ca_3Al_{1.096}Fe_{0.904}(Si_{2.823}O_{11.292})(OH)_{0.708}$ /Grossular hydroxylian $Ca_3Al_2(SiO_4)_2(OH)_4$ (01-072-8446/00-042-0570)
30-day curing	
Cancrinite $Na_6Ca_{1.5}Al_6Si_6O_{24}(CO_3)_{1.6}$ (00-034-0176) Grossulars $Ca_3Al_{1.096}Fe_{0.904}(Si_{2.823}O_{11.292})(OH)_{0.708}$ /$Ca_3Al_2(SiO_4)_2(OH)_4$ /$Ca_{2.81}Al_{1.89}((SiO_4)_{2.38}(O_4H_4)_{0.62})$ (01-072-8446/00-031-0250/01-083-7410) Corundum Al_2O_3 (01-073-1512)	Bohmite AlOOH (04-010-5683) Tohdite $Al_5O_{7.5}(H_2O)_{0.5}$ (04-014-1755) Silica SiO_2 (00-011-0252) Maghemite-C Fe_2O_3 (00-039-1346) Andradite aluminium $Ca_{2.82}Fe_{1.20}Al_{0.98}(SiO_4)_3$ (04-020-1960) *Possible phases*: Albite $Na(AlSi_3O_8)$ (01-071-1150) Khesinite $CaMgFe_{2.2}Al_{1.7}Si_{1.1}O_{10}$ (04-013-3515) Sillimanite Al_2O_3 SiO_2 (00-001-0626) Wollastonite $CaSiO_3$ (00-042-0550) Lizardite $(Mg,Fe)_3Si_2O_5(OH)_4$ (00-050-1606)

Like for TSRC samples, silica dominated XRD patterns of surface samples of TSRC-modified with MGF. Other possible phases included cancrinite, sodium-aluminum silicate, aegirine and feldspars with reduced calcium as in the case of the reference TSRC samples (Table 20).

Table 20. Major, minor and possible crystalline phases formed at **surface** under hydrothermal (water) conditions at 300°C after 15- or 30 days exposure of MGF-modified TSRC.

Major phases (ICDD numbers)	**Minor phases (ICDD numbers)**
15 day curing	
Cancrinite $Na_{7.28}Ca_{0.64}(Si_6Al_6O_{24})(CO_3)_{1.65}(H_2O)_2$ / $Na_{7.28}Ca_{0.64}(Si_6Al_6O_{24})(CO_3)_{1.66}(H_2O)_2$ (01-081-9895/9893) Khesinite $CaMgFe_{2.2}Al_{1.7}Si_{1.1}O_{10}$ (04-013-3515) Quartz SiO_2 (01-070-8054)	Sodium-aluminum-silicate $Na_8(Al(SiO_4)_6(OH)_2$ (00-040-0100) Analcime $Na_{7.2}Al_{7.2}Si_{16.8}O_{48}(H_2O)_8$ (04-013-2038) Andradite aluminian $Ca_3(Fe_{1.42}Al_{0.56})(SiO_4)_3$ (01-082-8676) Mullite $Al_{2.19}Si_{0.81}O_{4.901}$ (04-008-9530) Aegirine $NaFeSi_2O_6$ (04-015-8149) Paragonite $NaAl_3Si_3O_{10}(OH)_2$ (04-017-0660) Reyerite $KCa_{14}Si_{24}O_{60}(OH)_5(H_2O)_5$ (00-017-0760)
30 day curing	
Quartz SiO_2 (04-015-7194)	*Possible*: Albite, calcian (Na, Ca)$(SiAl)_4O_8$ (00-009-0456)

Cancrinite $Na_6Ca_{1.5}Al_6Si_6O_{24}(CO_3)_{1.6}$ (00-034-0176)	Anorthoclase $NaAlSi_3O_8$ (04-006-8967)
Sodium aluminum silicate $Na_2Al_2Si_2O_8\ H_2O$ (00-010-0460)	Sanidine $K(AlSi_3O_8)$ (01-080-2108)
Aegirine $NaFeSi_2O_6$ (04-014-4678)	Khesinite $CaMgFe_{2.2}Al_{1.7}Si_{1.1}O_{10}$ (04-013-3515)
	Amicite $K_2Na_2Si_4Al_4O_{16}(H_2O)_5$ (04-011-3051)

Based on the XRD test results, Figure 71 depicts a schematic of possible crystalline phase transitions in the matrix of TSRC samples cured at 300°C for different periods.

The first forming phases, crystallizing shortly after the cement set in TSRC are, for the most part, hydration and SMS-reaction products of CAC. They include hydrogrossular, feldspars (dmisteinbergite and anorthite) and boehmite. At longer exposure times garnets (various stoichiometries of hydrogrossular) become predominant. Continuous slow reactions of FAF introduce additional aluminum, silicon, iron and magnesium into the crystalline phases. Garnets with higher silicon content and with aluminum partially substituted by ferric iron replace earlier formed grossular; boehmite and silica contents noticeable increase. Additionally, mica group calcium-magnesium and calcium-magnesium-iron silicates form in the matrix. The slow reactions of FAF contributing such crystals-building ions as aluminum, silicon, iron and magnesium result in the recoveries of compressive strength for damaged samples. MGF become an additional source of silica, aluminum, calcium, and some magnesium and iron. These ions stabilize analcime for longer time, preventing its conversion into cancrinite and improving cracks sealing. Additional silica from MGF crystalizes in the fractures further filling them. MGF decomposition in alkali cement environments also introduces ions that form magnesium and iron-containing phases increasing strength of the matrix. MGF reacts slowly, and its effect becomes more noticeable after longer curing times in samples exposed to 300°C for 15 or 30 days.

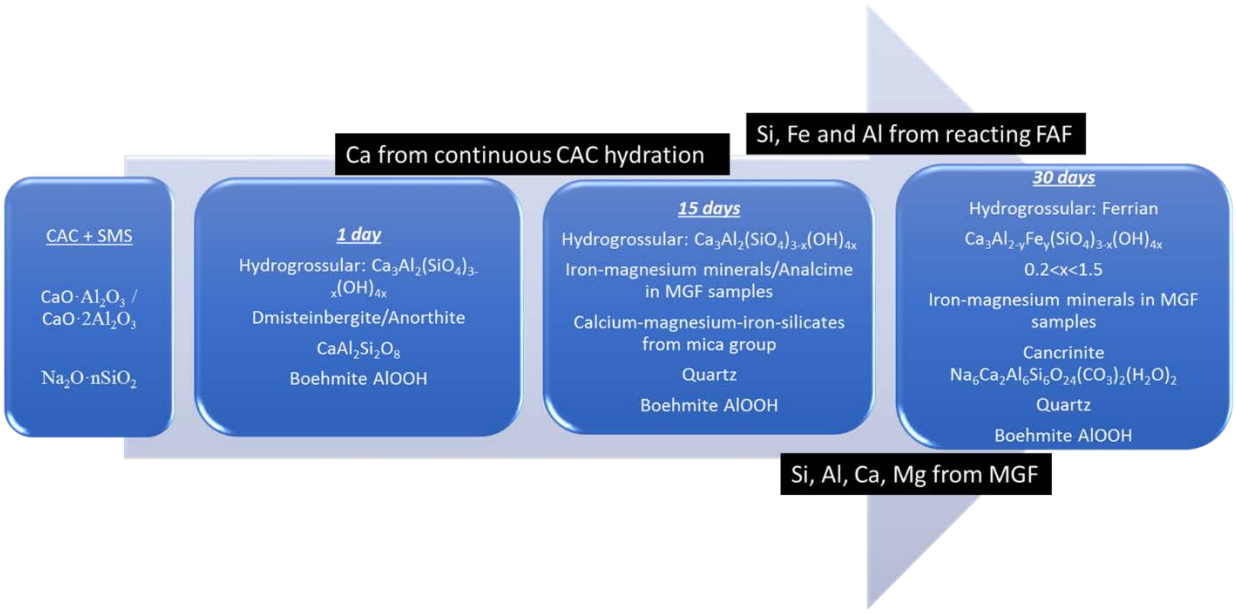

Figure 71. Crystalline phases formation and transitions with time for TSRC samples cured in water environment at 300°C.

Since XRD analyses could not unambiguously identify many of the smaller peaks especially for the surface samples, to compliment XRD phase identification Raman analyses of cracks areas were conducted on samples exposed to steam conditions after the imposed compressive damage.

3.5.4.4. Raman analyses of crack areas for long-term cured MGF-modified and unmodified TSRC samples

The Raman analyses allow targeting specific sample areas for phase identification. Crystalline phases give sharp signals while amorphous are more spread and often luminescent. This was in particular a problem for MGF-modified samples. Additionally, similar to the XRD patterns, presence of many different phases complicated the spectra and phase identification. Nevertheless, some phases, found in large quantities in crack areas were clearly identifiable for both MGF-modified and unmodified samples. Figure 72 shows a Raman spectrum of a crack area for a 15-day cured TSRC sample. The pattern unambiguously represents crystalline silica, that was a major phase filling the cracks after 15 and 30 days of curing for both control and modified samples. In addition to silica and in agreement with the XRD results Raman showed spectra corresponding to iron-containing mineral aegirine, that appears in the spectra after longer curing times when fly ash reactions proceed to release iron (Figure 73).

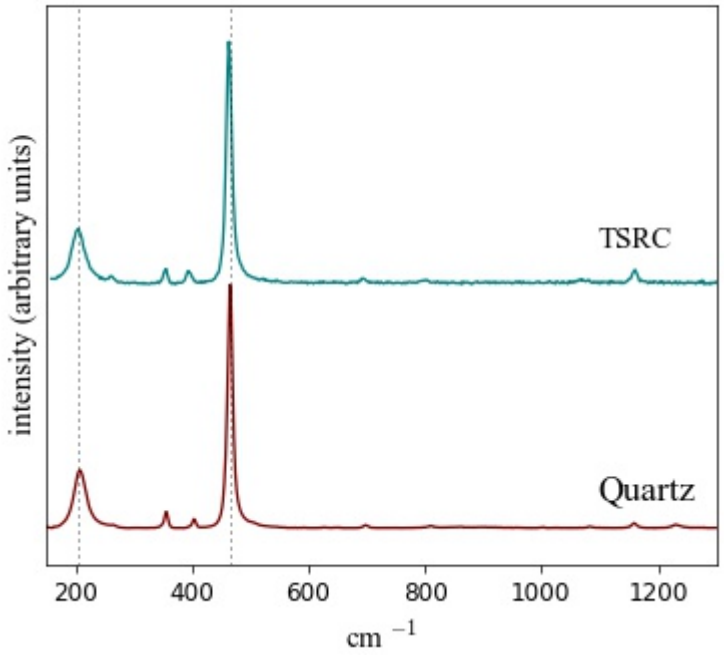

Figure 72. Raman spectrum of MGF-modified TSRC sample after 15 days of curing at 300ºC in water environment and patterns of quartz matching the spectrum.

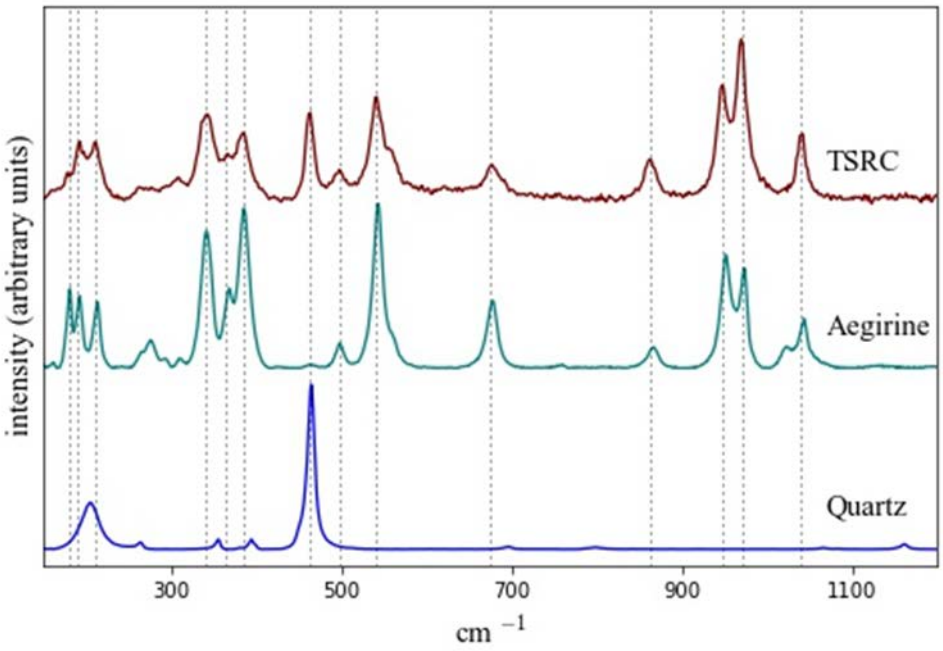

Figure 73. Raman spectrum of MGF-modified TSRC sample after 15 days of curing at 300ºC in water environment and patterns of quartz and aegirine corresponding to the spectrum.

Another 2 phases unmistakably present in the spectra of the filled-crack areas included bohmite and analcime (Figure 74). Both could be found in the samples even after short curing time of the first 5 days of cracks healing.

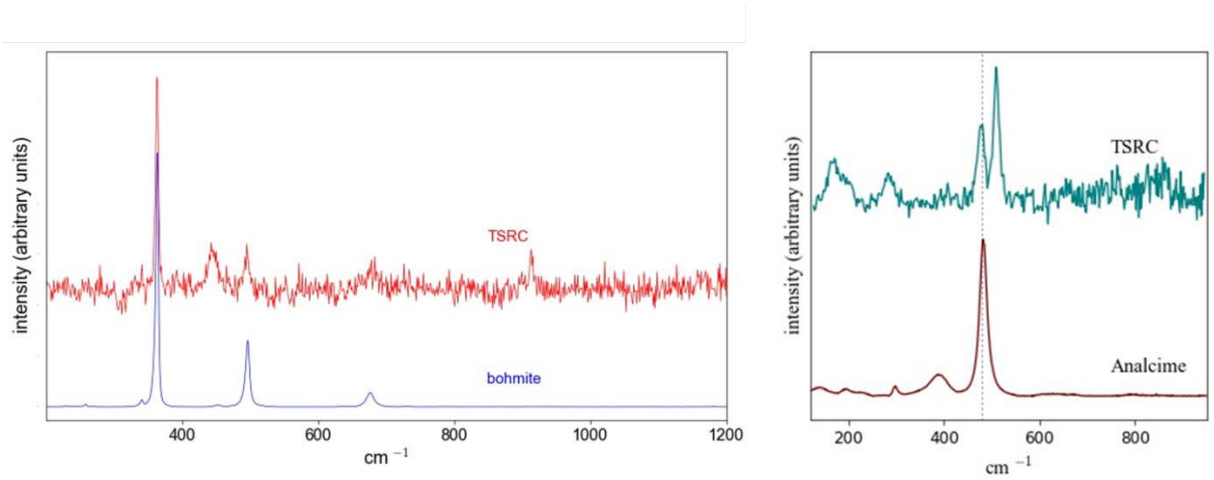

Figure 74. Raman spectra of TSRC-MCF sample after 15 days of curing at 300ºC in water environment and patterns of bohmite and analcime matching the spectra.

After longer curing time of 30 days spectrum matching that of albite was found in TSRC samples modified with glass fibers (Figure 75).

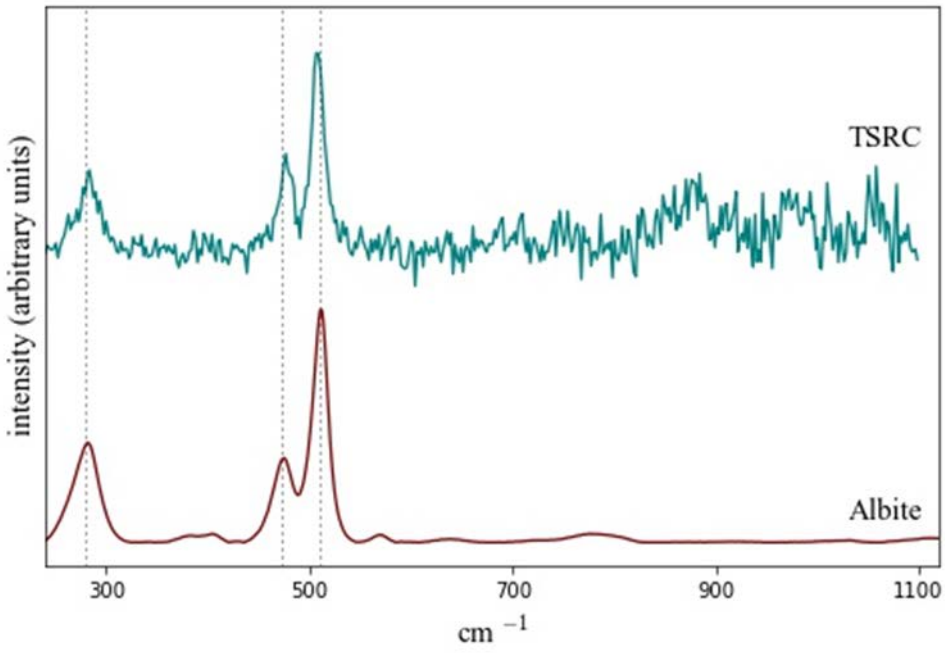

Figure 75. Raman spectrum of TSRC-MGF sample after 30 days of curing at 300ºC in water environment and pattern of albite matching the spectrum.

However, for the most part, silica spectrum dominated the spectra of the crack areas or complex overlapping spectra of many phases were obtained for the samples (Figure 76). Relatively broad peaks with shoulders indicated multiple phases contributed to the signal. In addition to earlier mentioned silica, bohmite, albite and high-temperature zeolite (amicite, in this case), the spectrum could be formed by feldspar minerals with varying calcium and potassium contents. The presence of feldspars is likely since albite matched a spectrum at another location and XRD patterns suggested possibility of these minerals in TSRC samples. Changes in calcium content after long curing times may be explained by increased contribution of silicon, aluminum and alkali metals by fly ash and glass fibers participating in high-temperature reactions.

Raman results confirmed XRD findings on surface composition of crack sealing phases in TSRC samples that for the most part included silica, high-temperature zeolites (analcime and amicite), sodium-iron-silicate (aegirine), aluminum oxide hydroxide (bohmite) and feldspar minerals with varied calcium and alkali metals content.

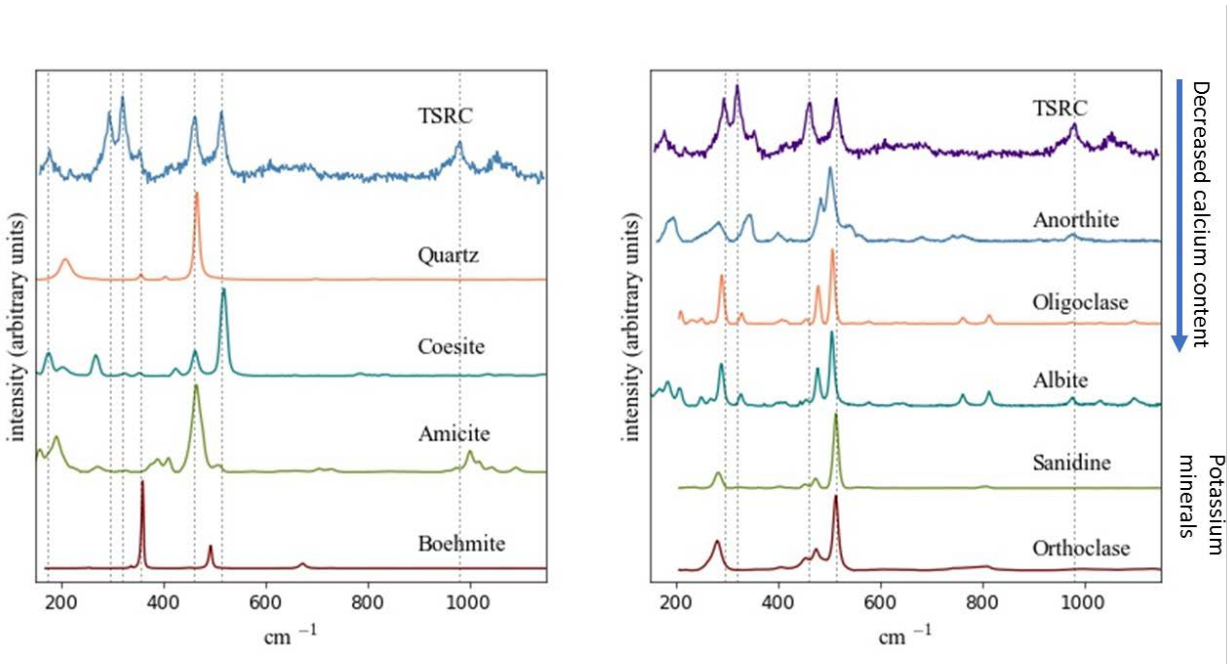

Figure 76. Raman spectrum of TSRC-MGF sample after 30 days of curing at 300ºC in water environment and reference patterns matching the spectrum.

Based on the information obtained by XRD and Raman tests, Figure 77 proposes phase transitions occurring at the surface and in the fractures of TSRC samples as the curing progresses. The major crystalline phases participating in cracks' sealing from early curing times are zeolite analcime and silica mostly from sodium silicate and calcium aluminate cement early reactions. As the curing continues analcime converts to cancrinite through carbonation, so the content of analcime declines. Another zeolite, sodalite, forms and more silica precipitates because of alkali dissolution of fly ash and MGF (for MGF-modified samples) with release of silicon and aluminum ions. Silica remains the main sealing phase throughout the healing, and especially after longer curing times when FAF and MGF dissolution releases more of silicon ions. In addition to silicon, alkali dissolution of FAF and MGF contributes more aluminum, some iron and alkalis to the pool of reacting ions after longer curing. They form (sodium, potassium, calcium)-aluminum-silicates from feldspar group of minerals with varied calcium and alkali metal contents replacing originally formed calcium-aluminum silicate feldspars, anorthite and dmisteinbergite. Sodium iron silicate, aegirine, also precipitates in the cracks.

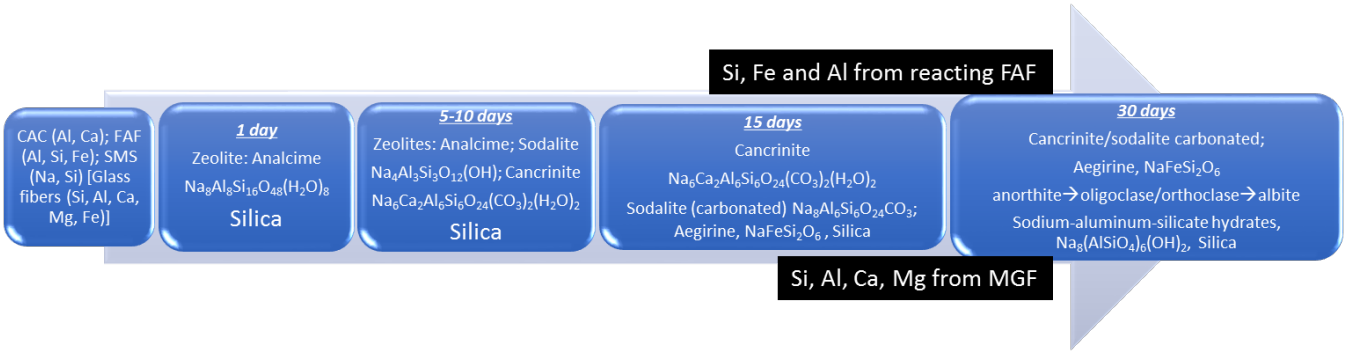

Figure 77. Crystalline phases formation and transitions with time at the surface and in the cracks of TSRC samples cured in water environment at 300°C.

3.5.4.5. Phase analyses of MGF-modified and unmodified TSRC in carbonate and brine

In this work, additional 5% MGF (10% total MGF content) was incorporated into TSRC samples to obtain the detailed information on MGF-related reaction products formed after exposure in carbonate and brine environments for 1 day at 300°C.

To analyze effect of MGF on crystalline phase composition of TSRC after a short-term curing (1 day) at 300°C in carbonate and brine environments, MGF were added to the samples at 10% by weight of blend. Crystalline compositions of MGF-modified and unmodified TSRC samples are compared in Table 21. The major crystalline phases were similar in samples with and without MGF. However, some clear differences included noticeable increase in peak intensities of high-temperature stable zeolite, analcime (at 2Θ: 15.82, 25.97, 30.54) and decreased intensities of cancrinite peaks (at 2Θ: 14.00, 19.04, 24.38, 27.66, 42.95) in modified samples. Since cancrinite forms through phase transitions of analcime during its carbonation, the increase in analcime and decrease in cancrinite peaks suggests either slower (later analcime formation) and/or later carbonation of analcime. Additionally, in carbonate and brine environments intensity of the peaks related to FAF increased (mullite and sillimanite phases) in modified samples. This means that the reactions of FAF were delayed in the presence of MGF. Since FAF is activated with SMS, it is reasonable to suppose that SMS was not as available in the presence of MGF as in the control samples for FAF activation. The most likely cause is MGF interactions with SMS that delay the activation of FAF resulting in the formation of analcime and its conversion to cancrinite through carbonation. SMS attack of MGF, on the other hand, may promote MGF dissolution, which acts to release the ionic species including silicon, aluminum, sodium, some calcium, magnesium and iron. These ions can participate in the formation/stabilization of new crystalline phases rich in silicon and aluminum such as analcime and another zeolite, sodalite, formed in MGF-containing samples. However, MGF dissolution takes some curing time and consumes SMS, so that activation of FAF is postponed. Slower reactions of FAF and limited dissolution of MGF after short curing periods limit formation of sealing crystalline phases such as silica and analcime and, as a result, samples capacities to fill the fractures. This results in inferior crack sealing for MGF-modified samples at short curing times. It also accelerates calcium-aluminate cement hydration that is known to be retarded by SMS and FAF reactions. This faster CAC hydration results in faster strength development and increased YM of MGF-modified samples.

Table 21. Major, minor and possible crystalline phases formed under hydrothermal (water), alkali carbonate and geothermal brine conditions at 300ºC after 1 day of exposure for TSRC and TSRC modified with micro-glass fibers (MGF).

Control samples (ICDD numbers)	Samples with GMF (ICDD numbers)
Alkali carbonate	
Corundum Al_2O_3 (04-006-9359)	Analcime-R $Na_8(Al_8Si_{16}O_{48})(H_2O)_8$ (04-011-7963)
Dmisteinbergite $Ca(Al_2Si_2)O_8$ (04-011-6236)	Corundum Al_2O_3 (04-006-9359)
Sodalite (Na,Ca) $(Na_{0.4}Ca_{0.3})_6(AlSiO_4)_6(H_2O)_8$ (01-073-5298)	Dmisteinbergite $Ca(Al_2Si_2)O_8$ (04-011-6236)
Cancrinite $Na_{6.02}Ca_{1.52}(Al_6Si_6O_{24})(CO_3)_{1.52}(H_2O)_{1.44}$ (01-075-8620)	Cancrinite $Na_{6.02}Ca_{1.52}(Al_6Si_6O_{24})(CO_3)_{1.52}(H_2O)_{1.44}$ (01-075-8620)
Bohmite AlOOH (01-074-2895)	Sodalite (Na,Ca) $(Na_{0.4}Ca_{0.3})_6(AlSiO_4)_6(H_2O)_8$ (01-073-5298)
Tohdite $Al_5O_{7.5}(H_2O)_{0.5}$ (04-012-1638)	Bohmite AlOOH (01-074-2895)
Analcime $Na_{7.2}(Al_{7.2}Si_{16.8}O_{48})(H_2O)_8$ (04-013-2036)	Tohdite $Al_5O_{7.5}(H_2O)_{0.5}$ (04-012-1638)
Possible:	Stishovite SiO_2 (04-008-7808)
Margarite-2M1 $CaAl_2(Si_2Al_2)O_{10}(OH)_2$ (00-018-0276)	*Possible:*
	Margarite-2M1 $CaAl_2(Si_2Al_2)O_{10}(OH)_2$ (00-018-0276)
Brine	
Corundum Al_2O_3 (04-015-8996)	Corundum Al_2O_3 (04-015-8996)
Dmisteinbergite $Ca(Al_2Si_2)O_8$ (04-011-6236)	Dmisteinbergite $Ca(Al_2Si_2)O_8$ (04-011-6236)
Cancrinite $Na_6Ca_{1.5}(Al_6Si_6O_{24})(CO_3)_{1.5}(H_2O)_{1.75}$ (04-013-1896)	Cancrinite $Na_6Ca_{1.5}(Al_6Si_6O_{24})(CO_3)_{1.5}(H_2O)_{1.75}$ (04-013-1896)
Cristobalite SiO_2 (04-018-0237/ 04-018-0233)	Sodalite octahydrate $Na_6Al_6(SiO_4)_6(H_2O)_8$ (04-009-5259)
Bohmite AlOOH (01-074-2900)	Bohmite AlOOH (01-074-2900)
Tohdite $Al_5O_{7.5}(H_2O)_{0.5}$ (04-012-1638)	Tohdite $Al_5O_{7.5}(H_2O)_{0.5}$ (04-012-1638)
Magnetite Fe_3O_4 (01-082-3509)	Cristobalite SiO_2 (04-018-0237/ 04-018-0233)
Grossular hydroxylian $Ca_3Al_2(SiO_4)_2(OH)_4$ (and other stoichiometries) (00-042-0570)	Grossular hydroxylian $Ca_3Al_2(SiO_4)_2(OH)_4$ (and other stoichiometries) (00-042-0570)
Possible:	*Possible:*
Margarite-2M1 $CaAl_2(Si_2Al_2)O_{10}(OH)_2$ (01-076-0883)	Margarite-2M1 $CaAl_2(Si_2Al_2)O_{10}(OH)_2$ (01-076-0883)
Sergeevite $Ca_2Mg_{11}(CO_3)_9(HCO_3)_4(OH)_4(H_2O)_6$ (00-041-1403)	Sergeevite $Ca_2Mg_{11}(CO_3)_9(HCO_3)_4(OH)_4(H_2O)_6$ (00-041-1403)
Magnetite Fe_3O_4 (01-082-3509)	Magnetite Fe_3O_4 (01-082-3509)

3.6. Re-adhering behaviors of debonded composite sheath to CS casing surfaces

3.6.1. Sheath-shear bond strength and its recovery

To determine the CS re-adhering properties of three debonded composites (OPC/SiO_2, TSRC, and CAP-B) modified with MGF and Clin as artificial and natural pozzolans, CS tubes with a sheath of cement composite were prepared in autoclaves at 300°C- 24-hr-palin water, and an unconfined sheath-CS tube shear-bond strength was determined. Afterward, the samples with the broken CS-composite bond were exposed for 5 days to the original curing conditions (300°C plain water) for re-adherence of the debonded sheath to the CS tube. The healing 5 days were followed by the second-time bond strength testing. As expected, for the unmodified composites, the bond strength measured in the 1st test decreased in the following order TSRC>CAP-B>OPC/SiO_2 (Figure 78). Addition of MGF improved the bond strength of all cements. The most strength improvement by MGF was achieved for TSRC: the strength of the MGF modified TSRC was almost 200 psi compared to 70 psi for non-modified one. Thus, MGF conferred the considerably improved bond strength on TSRC sheath. However, such high bond strength led to the development of wide open cracks in composite sheath during the debonding test (Figure 51), raising concern about the re-adhering ability of the damaged composite with such wide cracks. Also, this fact clearly suggested that the further improvement of interfacial bond toughness to alleviate crack development was required for high bond-strength performance composites. On the other hand, if the composites are placed between casing and geological formation under the confined condition, the crack-width and- propagation, and micro-separation between casing and composite may be suppressed or minimized. In contrast, the effect of Clin on improvement of bond strength was little, if any for TSRC. Adding Clin to the OPC/SiO_2 and CAP-B resulted in a negative effect, reducing the bond strength.

The 5-day-300°C plain water exposure triggered the re-adhering activity of these debonded sheaths to CS (Figure 79), in fact, without any healing aids, the bond strengths of re-adhered OPC/SiO_2, TSRC, and CAP-B composites were 5, 40, and 13 psi respectively, corresponding to 15, 49, and 26% bond recovery rate. Thus, TSRC displayed the best re-adhering performance, while second best performance was CAP-B. OPC/SiO_2 showed a poor performance with only 15% recovery. With MGF and Clin as healing aids, the bond strength of re-adhered TSRC was 97 psi for MGF and 31 psi for Clin, which was equivalent to 49, and 36 % recovery rate, respectively, compared with that of the 1st bond test. Since strong interfacial bond between CS and TSRC-MGF sheath (~200psi) resulted in formation of a wide crack in the composite and at the interface during debonding, the bond recovery for this formulation could require longer than 5-day healing time. Interestingly, Clin offered a better recovery for OPC/SiO_2 and CAP-B than MGF. Nonetheless, the bond recovery of composites with pozzolanic healing aids decreased in the following order: TSRC/MGF (49%) > CAP-B/Clin (40%) > OPC/SiO_2/Clin (27%). Although a 49% recovery for both TSRC with and without MGF met material criterion >40%, the critical question to be answered was whether a recovery of >45% was sufficient to plug any micro-annulus (< 1 mm) between CS tube and the composite formed during thermal and mechanical stresses.

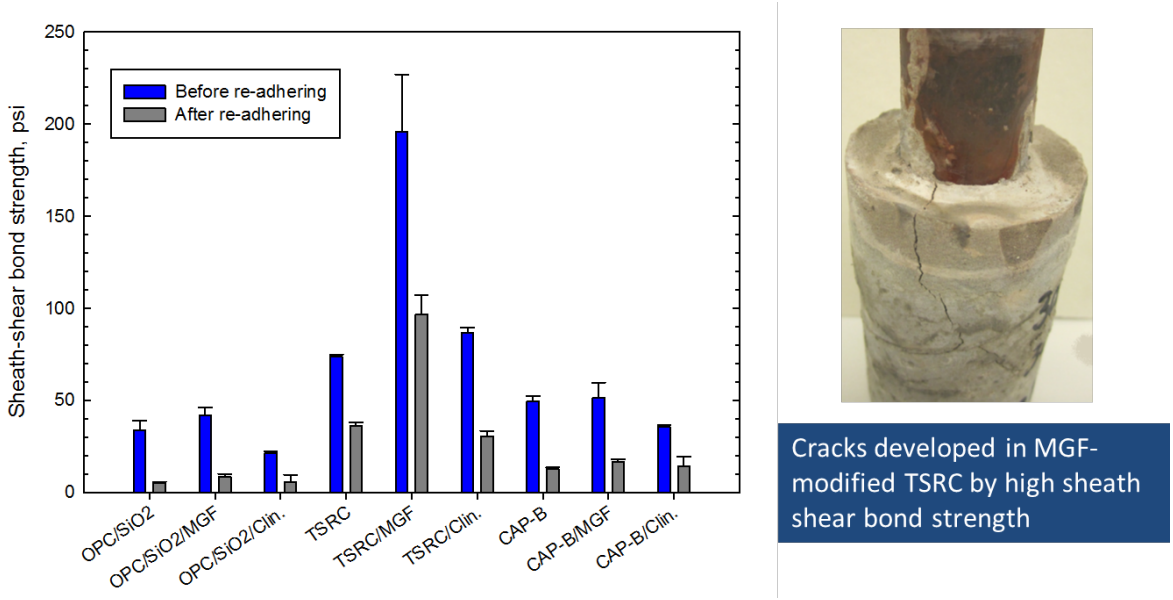

Figure 78. Sheath-shear bond strength of MGF-and Clin-modified and unmodified OPC/SiO_2, TSRC, and CAP-B composite sheaths surrounding CS casing.

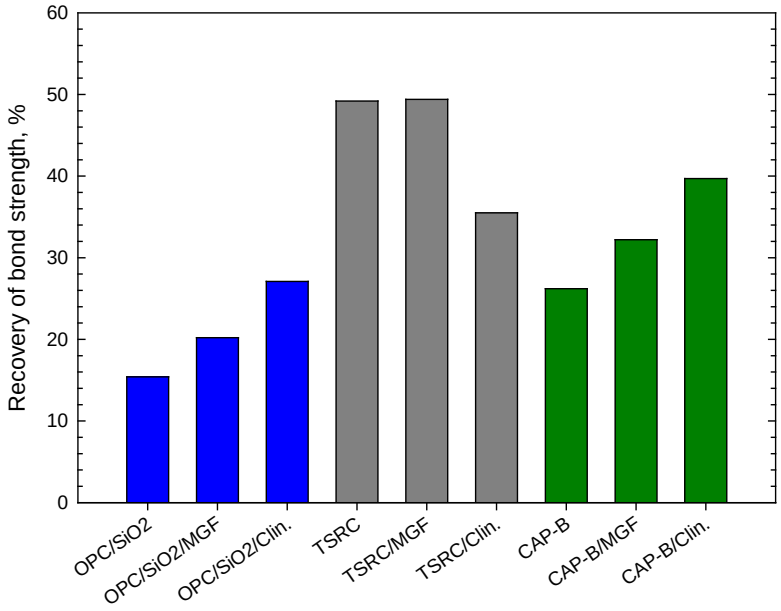

Figure 79. Recovery of composite- sheath - CS tube shear bond strength after exposure a 5-day exposure to 300°C plain water.

3.6.2. Re-adhering properties of 30-day-long autoclaved composites

Next, we studied the re-adhering properties of the long-term autoclaved strongly-bonded TSRC/MGF composite sheath. In this study, two reference composites, OPC/SiO_2 and TSRC without MGF, were employed for comparison purpose. All composites were prepared by autoclaving for 30 days in 300^oC plain water. Figure 80 compares the sheath-shear bond strengths of 1- and 30-day-autoclaved sheath samples before and after the re-adherence for 5 days in water at 300^oC. All 30-day-autoclaved composites demonstrated increased bond strength, compared with that of 1-day-autoclaved ones. The value of 30-day sheath-shear bond strength was 70 psi for OPC/SiO_2, 82 psi for TSRC, and 245 psi for TSRC/MGF, which is tantamount to 2.1-, 1.1-, and 1.3-fold rise in bond strength, respectively, over the 1-day bond strength. As expected, for strongly-bonded TSRC/MGF composite, the excessive sheath shear bond strength of nearly 250 psi caused the development of undesirable multi-radial cracks in the sheath during the second debonding test (Figure 80). Such crack development could be directly related to a low rate (28%) of bond recovery (Figure 81), suggesting that re-adhering treatment of 5 days may be insufficient for adequate composite re-adherence. No visual cracks were detected for the other two reference composites.

Overall, MGF-free TSRC exhibited the best bond recovery performance of 49% and 57 % for 1-day- and 30-day-autoclaved composites, respectively, meeting the material criterion of >40% recovery. On the other hand, the bond recovery of 30-day-autoclaved OPC/SiO_2 reference sample was 38%.

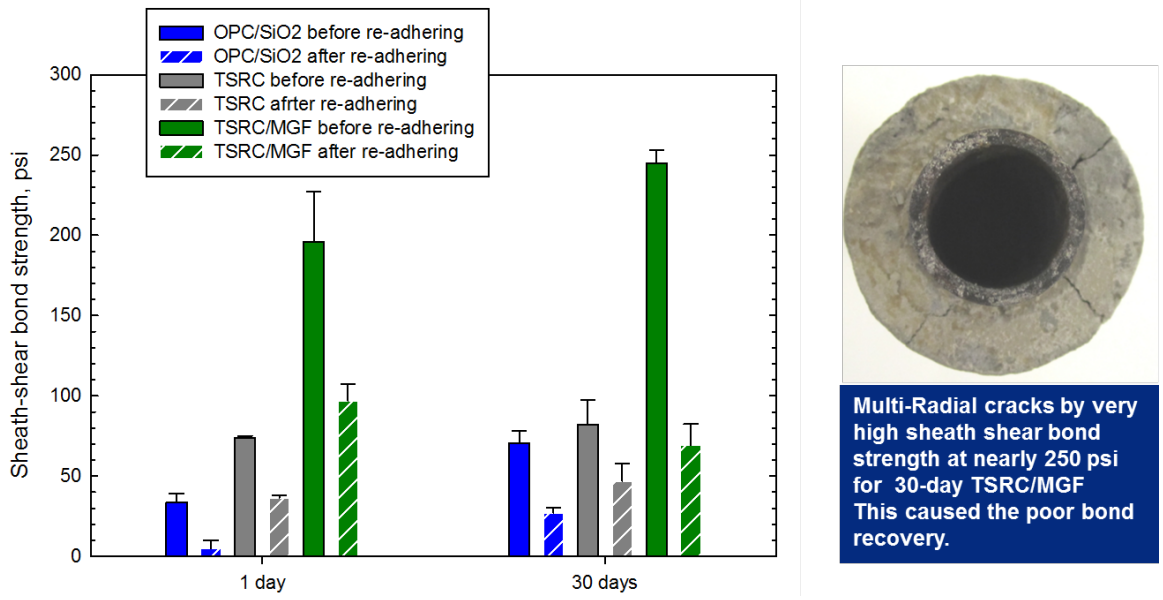

Figure 80. Sheath-shear bond strength of 1- and 30-day-acutoclaved TSRC/MGF composite sheath, and MGF-free TSRC and OPC/SiO_2 reference composite sheaths before and after the re-adherence treatment in 300^o-plain water for 5 days.

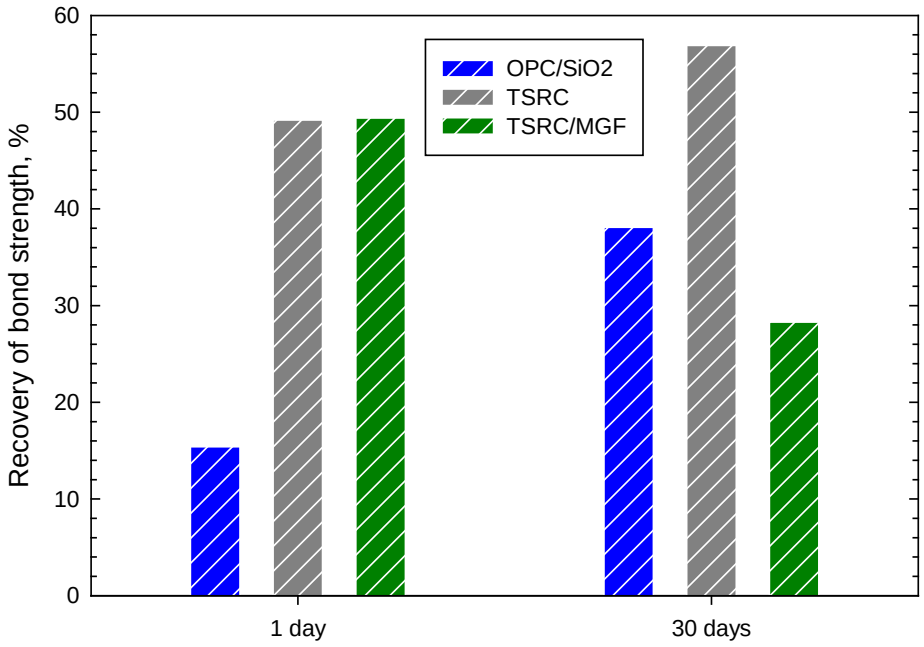

Figure 81. Bond recovery of composites debonded from CS tube after the re-adherence treatment in 300°C-plain water for 5 days.

3.6.3. Bond durability of composites adhered to CS under cyclic thermal shock stresses

Among the material criteria, the composite sheath was required to withstand 6-cycle thermal shock stresses (one cycle, 350°C heating followed by 25°C water cooling by passing water through inner CS casing) for 300°C-1-day-autoclaved composites. The criterion was as follows: The composites must have ≥30% higher sheath-shear bond strength than that of OPC/SiO_2 reference composite after thermal shock testing. As aforementioned, MGF provided very high bond strength, engendering the generation of multi-radial cracks in composite sheath during interfacial bond strength tests. So, in the bond durability test under the thermal shock stresses, three different composites (TSRC, GBFS/SiO_2, and OPC/SiO_2) without MGF were evaluated.

Figure 82 depicts the sheath-shear bond strength of these composites before and after the thermal shock tests as well as the loss of the bond strength after the thermal shock. For the unconfined sheath samples, we observed that GBFS/SiO_2 sheath generated the cracks after 300°C-1-day autoclaving. There are two potential reasons for such crack generation: One is shrinkage of

composite sheath adhering to CS surfaces; the other is the difference in thermal

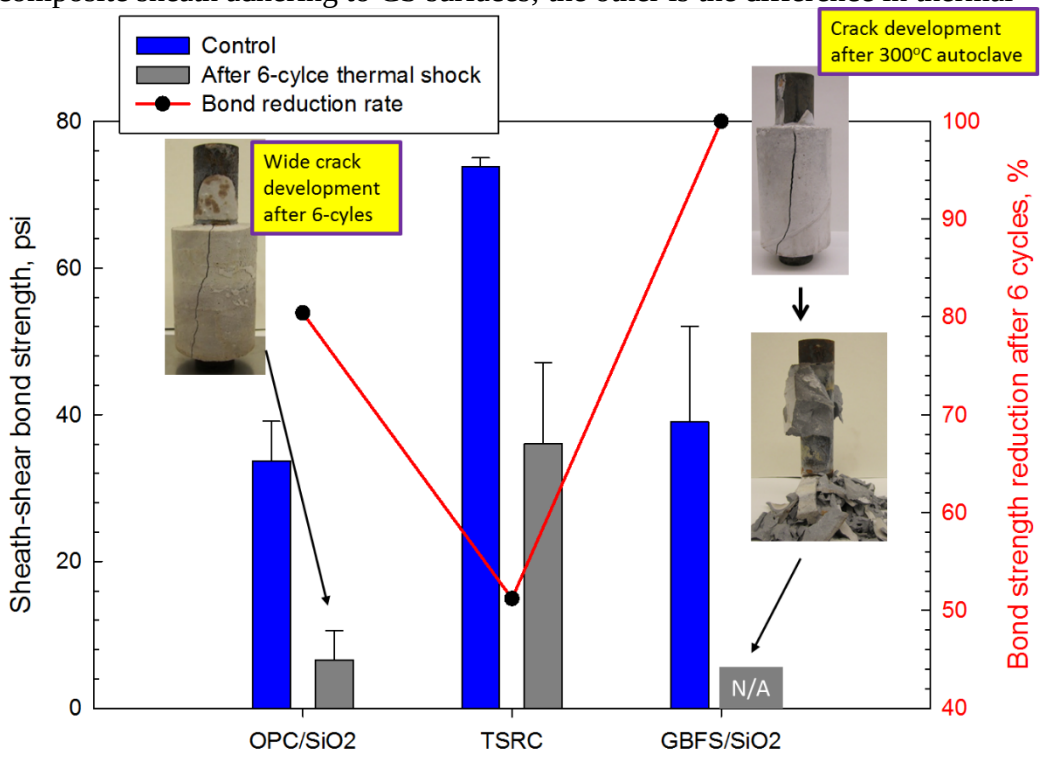

Figure 82. Sheath-shear bond strength of composites before and after 6-cycle thermal shock test.

expansion coefficients of the composite and CS tube. Although, no experimental work was done to validate these hypotheses, these two physical-thermal factors possibly caused crack generation by interfacial debondment. In fact, the sheath-shear bond strength was only 39 psi for this composite. Furthermore, the catastrophic bond failure was observed in the first thermal cycle test. Two other composites did not develop cracks before the thermal shock. After the thermal shock, for TSRC, the sheath-shear bond strength was reduced by 51% to 36 psi. By contrast, the OPC/SiO_2 reference composite strikingly lost the bond strength, which decreased from 34 psi before to 7 psi after thermal shock, corresponding to nearly 80% reduction. After 6 cycles, this composite developed some wide cracks. More importantly, for the sheath samples after thermal shock, the bond strength of TSRC was more than 5 times higher than that of OPC/SiO_2 reference composite, therefor meeting the material criterion pertinent to bond durability under the thermal shock environment.

3.7. Corrosion protection of CS by adhered and re-adhered composites for short- and long-term cured composite/CS joint samples

One important question that must be asked is how well the composite layers adhering and re-adhering to the CS surfaces protect the CS against brine-caused corrosion. To obtain this information, our first approach was to better understand the interfacial bond failure modes associated with the bond strength at CS/composite joints. Next, we studied the ability of re-adhered composites, made by the repeated exposure of samples with the broken composite-CS bond to the initial curing conditions, to further improve the corrosion mitigation of CS. In this

investigation, two CS plates were bonded together by composites to prepare the CS plate/composite adhesive/CS plate joint samples.

3.7.1. Lap-shear bond strength at CS plate/composite adhesive/CS plate joints

Figure 83 presents the lap-shear bond strength of six different MGF-free composites adhering to CS plate surfaces. The samples were made in two environments, plain water and carbonate, by 1-day autoclaving at 300°C. Six tested composite adhesives can be classified in three groups, 1) alkali-activated composites (TSRC, FAC/FAF, and GBFS/SiO_2), 2) phosphate-reacted composite (CAP-B), and 3) OPCs (OPC/SiO_2 and FlexCem/SiO_2).

As a result, in both environments, alkali-activated and phosphate-reacted composites had far greater bonding strength than OPC-based composites. The average shear bond strength in both environments decreased in the following orders; GBFS/SiO_2 (230 psi) > TSRC (210 psi) > FAC/FAF (175 psi) > CAP-B (160 psi) > OPC/SiO_2 (80 psi) > FlexCem (50 psi). For the top two composites, GBFS/SiO_2 and TSRC, the bond strengths were more than 2.5-fold higher than that of OPC/SiO_2.

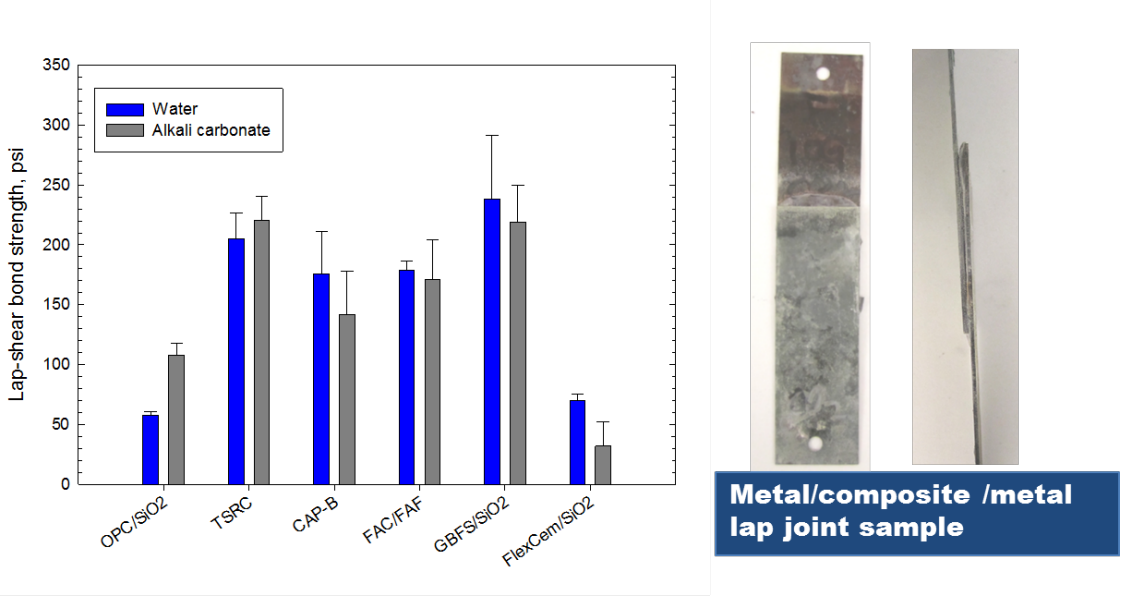

Figure 83. Lap-shear bond strength of MGF-free composites made by 1-day autoclaving at 300°C in plain water or carbonate.

The information described above was directly correlated with the identification of interfacial bond failure modes. There are three different bond failure modes, 1) cohesive failure in composite layer, 2) adhesive failure at interfaces between composite and CS, and 3) 1) and 2) mixed failure. The most ideal failure is cohesive failure, meaning that the bond strength of composite to CS is higher than the strength of the composite itself. As seen, the OPC-based composites (Figure 84) disclosed poor bonding behavior with the debondment taking place in the critical interfacial boundary regions as the cohesive/adhesive mixed failure mode. In this mode, attention was paid to the adhesively failed areas where the debondment occurred at the interfaces between CS and composite. The presence of this adhesively failed areas was the major reason why the OPC-based composites had low shear bond strength of less than 100 psi. Additionally,

the critical concern during the autoclaving curing was the corrosion of CS brought about by the following three factors; 1) a poor bond behavior, 2) undesirable chemistry of a composite and 3) porous microstructure of composite layers adhering to CS. Thus, we visually inspected the corrosion of debonded CS sites. For OPC-based composites (Figure 57), we observed some local corrosion stains at the debonded CS sites, implying that steel corrosion was related to the inadequate bonding behavior of these composites.

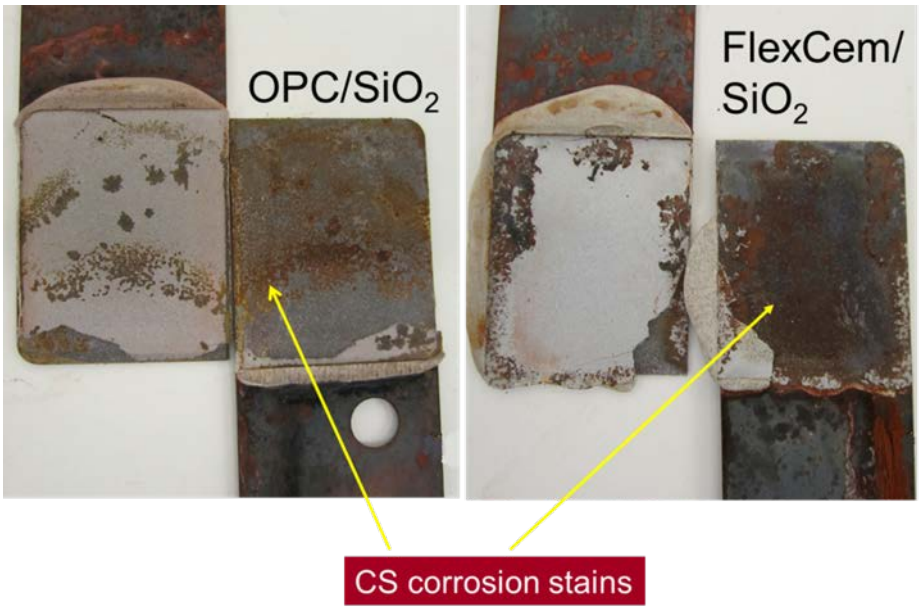

Figure 84. Appearance of the debonded OPC/SiO_2 and FlexCem/SiO_2 composite adhesive sites at CS plate/adhesive/CS joint.

Such behavior resulted in insufficient protection of CS against corrosion. In contrast, all alkali-activated and phosphate-reacted composites along with a great bond strength revealed the ideal composite coverage over CS surfaces; namely, the whole lap-jointed surface areas of both CS sites were covered with these composites. Thus, it appeared that the interfacial bond failure occurred in composite layers, that is through cohesive bond failure mode (Figure 85). However, although all the composite adhesives along with this mode visually showed a great deal of coverage over both the CS sites, attention was paid to two composites, FAC/FAF and CAP-B. These composites disclosed presence of local corrosion spots. As well known, the cement slurry with high pH value provides a better protection of CS than that with low pH. Since CAP-B slurry had a lower pH value (8.5-9.5) compared against alkali-activated cements with pH >13, this fact mentioned above as undesirable chemistry of a composite, may be the reason why corrosion stains of underlying CS were observed on the CAP-B coverage. In the case of FAC/FAF, although there is no experimental evidence, the carrion could be a result of the porous microstructure (factor 3 above) allowing the moisture to permeate through composite layer. On the other hand, TSRC and GBFS/SiO_2 composites were responsible for mitigating the corrosion of CS (Figure 85).

Furthermore, we investigated the effect of pozzolanic additives, MGF and Clin on lap-shear bond strength of three composites, OPC/SiO_2, TSRC, and CAP-B, prepared by 1-day autoclaving in water at 300°C (Figure 86). The data showed that for all composites, the incorporation of MGF led to the increase in lap-shear bond strength, ranging from 8 to 18%, compared with that of MGF-free ones, while Clin reduced this strength. Interestingly, this bond strength value of MGF-modified OPC/SiO_2 and TSRC adhesives closely resembled that obtained from sheath-shear bond strength tests of the same composites.

Also, we evaluated the effect of a long-term curing at 300°C for 30 days on the lap-shear-bond strength of TSRC/MGF composite (Figure 87). Two reference adhesives, MGF-free OPC/SiO_2 and TSRC, were used for comparison. The test results were similar to that obtained from sheath-shear bond tests; the very high lap-shear bond strength of almost 300 psi was determined for 30-day-autoclaved TSRC/MGF. This bond strength value corresponded to 1.3- and 3.3-fold higher strength than that of TSRC and OPC/SiO_2 references at the same period of autoclaving time, respectively.

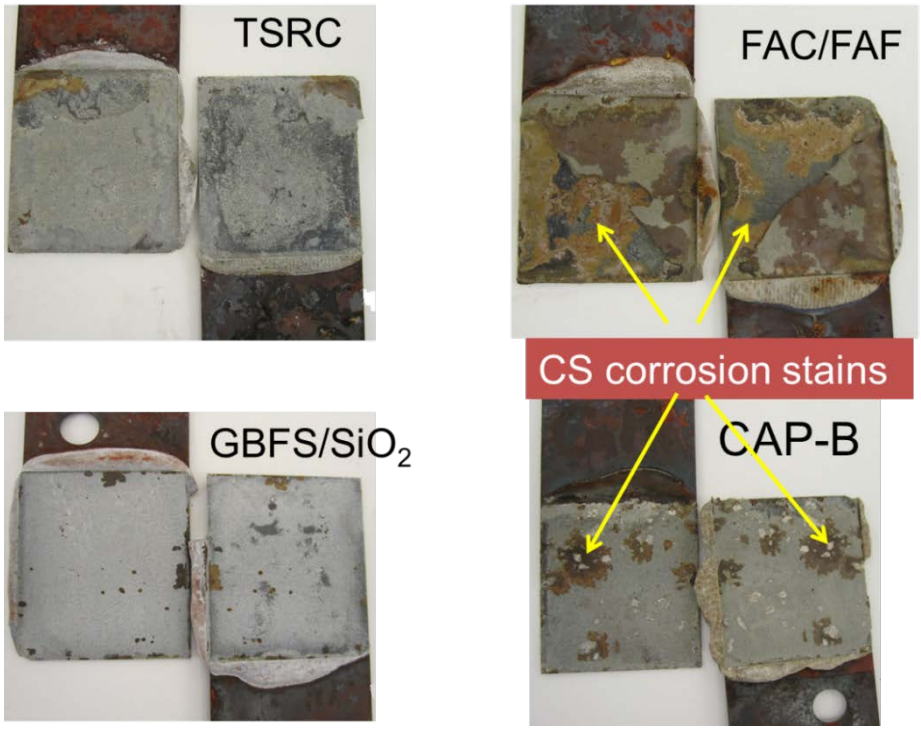

Figure 85. Appearance of debonded TSRC, GBFS/SiO_2, FAC/FAF, and CAP-B adhesive sites.

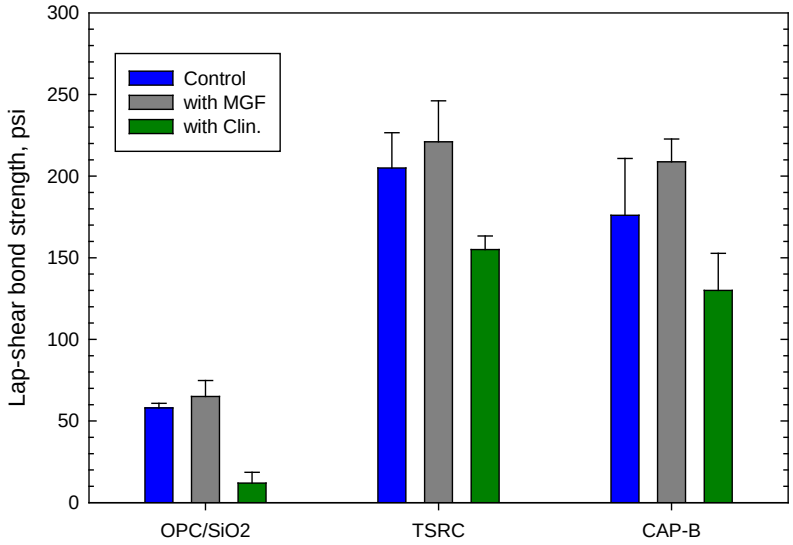

Figure 86. Lap-shear bond strength of MGF- and Clin-modified and unmodified OPC/SiO_2, TSRC, and CAP-B composites prepared by 1-day autoclaving in water at 300°C.

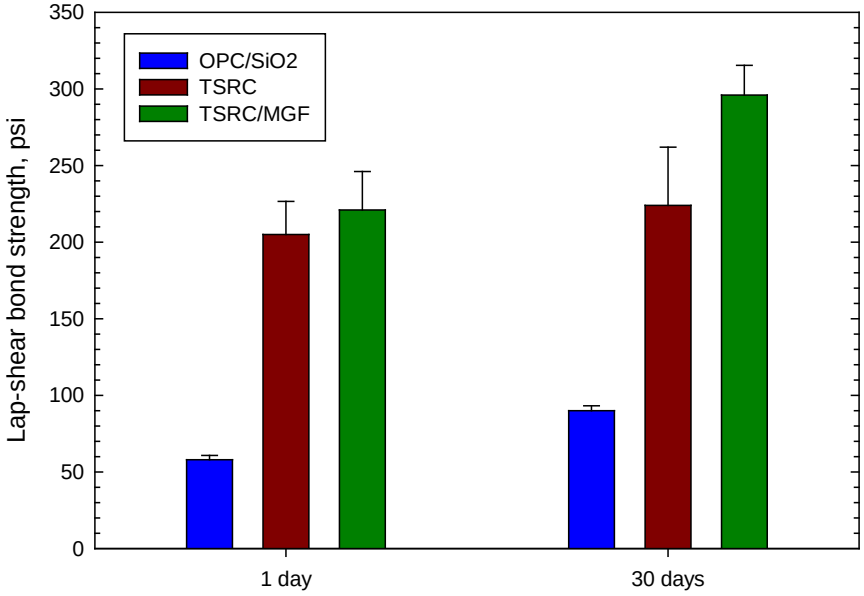

Figure 87. Lap-shear bond strength of MGF-modified TSRC, and unmodified TSRC and OPC/SiO_2 prepared by 1-day autoclaving in water at 300°C.

3.7.2. Bond durability in acids

We investigated lap-shear bond durability of MGF-free composites, OPC/SiO_2, TSRC, and GBFS/SiO_2, in two different acid environments at 90°C. One acid environment was pH 0.6 H_2SO_4/brine and the other was pH 5.5 $scCO_2$-laden brine. The lap-shear bond samples were exposed to these environments for up to 30 days. Considering highly corrosive nature of these environments for CS plates, the entire CS plate surfaces of the lap-shear bond samples were coated with acid-resistance epoxy polymer prior to acid exposure.

3.7.2.1. pH 0.6 H_2SO_4/brine environment

All composites lost some strength under these conditions in the first 15 days (Figure 88). Extended exposure of 30 days caused dramatical decrease in the bond strength for two composite adhesives, OPC/SiO_2 and GBFS/SiO_2. As seen in the photos, OPC/SiO_2 adhesive layers for the most part eroded after exposure of 18 days, engendering a catastrophic interfacial bond failure. The bond failure mode of GBFS/SiO_2 differed from that of OPC/SiO_2; the acid erosion was minor for GBFS/SiO_2. Instead, the interfacial boundary region underwent an important acidic damage through interactions with the acid and salts precipitation in the boundary region after the 20-day exposure, thereby resulting in the interfacial debondment of the composite from CS. In contrast, TSRC adhesive remained in effect for the 30-day exposure, and it still had lap-shear bond of 80 psi, strongly demonstrating a great resistance to a pH 0.6 acid/brine at 90°C of the bond structure at the interfaces between TSRC and CS and providing an outstanding bond durability in such a harsh environment.

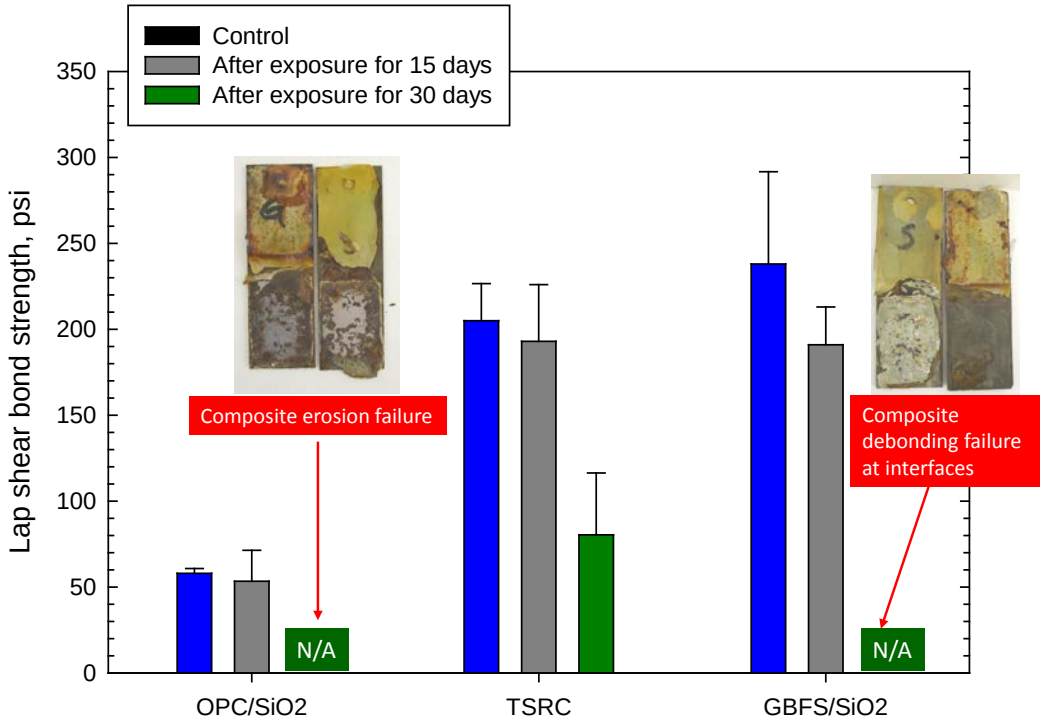

Figure 88. Bond durability in pH 0.6 H_2SO_4/brine at 90°C for up to 30 days.

To obtain a better understanding of acid degradation and stabilization of these three adhesives, the additional studies were accomplished using the combined analytical tools of XRD, µEDX, FT-IR, and Raman imaging.

3.7.2.1.1. Crystalline phase identification – XRD

Table 22 shows identified crystalline phases along with their ICDD numbers for the samples which were collected by scrubbing the adhesives covering the CS plate surfaces after acid-exposure tests. OPC/SiO_2 and GBFS/SiO_2 samples were taken after 18- and 20-day acid exposure, respectively, after the bond failure, while TSRC sample was collected after 30 days of exposure. All specimens contained some magnetite from the CS (not included into the table). The change in the crystalline composition of the samples could be attributed to the formation of new phases as a result of the acid exposure and as a result of continuous curing at 90°C [112]. The acid exposure leads to the presence of sulfonated products (both amorphous and crystalline), while the continuous curing should bring the phases stable at that temperature.

Table 22. Crystalline phase compositions of the cement composite samples between two CS plates, exposed to 90°C- pH 0.6 sulfuric acid for TSRC, OPC/SiO_2 and GBFS/SiO_2 composite adhesives.

Principal phases	**Secondary phases**
TSRC control	
Corundum Al_2O_3 (04-002-3621) Mullite $Al_{2.26}Si_{0.74}O_{4.87}$ (04-016-1587) Grossite $CaAl_4O_7$ (00-023-1037) Cristobalite-II/quartz SiO_2 (04-018-0238/01-070-7345) Garronite $Na_{0.8}Ca_{2.82}(Al_6Si_{10}O_{32})(H_2O)_{12.08}$ (01-079-1336) Dmisteinbergite $Ca(Al_2Si_2)O_8$ (00-051-0064)	Hedenbergite $CaFeSi_2O_6$ (04-013-2079) Calcite $CaCO_3$ (00-005-0586) Sodalite $Na_6Al_6(SiO_4)_6$ (04-009-5260) Analcime $Na(AlSi_2O_6)H_2O$ (01-074-2218) Bohmite AlOOH (01-074-2898)
TSRC after the acid exposure for 30 days	
Corundum Al_2O_3 (00-005-0712) Garronite $Na_{0.8}Ca_{2.82}(Al_6Si_{10}O_{32})(H_2O)_{12.08}$(01-079-1336) Dmisteinbergite/anorthite $Ca(Al_2Si_2)O_8$ (00-031-0248/00-041-1486) Silicon oxide SiO_2 (01-073-2991) Analcime $Na(AlSi_2O_6)H_2O$ (01-074-2218)	Anhydrate $CaSO_4$ (04-007-4744) Hedenbergite $CaFeSi_2O_6$ (04-013-2079) Bohmite AlOOH (01-74-2898) Sodalite $Na_6Al_6(SiO_4)_6$ (04-009-5260)
OPC/SiO_2 control	
Xonotlite $Ca_6Si_6O_{17}(OH)_2$ (00-023-0125/01-074-7586) Tobermorite 9A $Ca_5Si_6O_{17}(OH)_2$ (04-012-1761)	Quartz SiO_2 (01-075-8320)
OPC/SiO_2 after the acid exposure for 18 days	Coesite/Quartz SiO_2 (04-015-7165/00-033-1161)
Xonotlite $Ca_6Si_6O_{17}(OH)_2$ (00-023-0125); Riversideite-9A (00-029-0329)	
GBFS/SiO_2 control	
Xonotlite $Ca_6Si_6O_{17}(OH)_2$ (00-023-0125); Quartz SiO_2 (04-008-7653);	Calcite $CaCO_3$ (04-007-0049)

Tobermorite 11A (00-019-1364); Diopside, sodian, aluminian $Na_{0.3}Ca_{0.65}Mg_{0.65}Fe_{0.1}Al_{0.3}Si_2O_6$ (04-013-2121)	
GBFS/SiO_2 after the acid exposure for 20 days	Diopside ferroan (01-087-2070);
Silica/coesite SiO_2 (01-075-8322/01-072-1601);	$(Mg_{0.39}Fe_{0.52}Ca_{0.09})SiO_3$ (01-071-0712);
Xonotlite $Ca_6Si_6O_{17}(OH)_2$ (00-023-0125);	Tobermorite 11A $Ca_5Si_6O_{17}(OH)_2$ (00-019-1364);
Bassanite $CaSO_4$ 0.67 H_2O (00-047-0964)	Millosevichite $Al_2(SO_4)_3$ (04-005-9668)
	Calcite $CaCO_3$ (01-072-1937)

Non-reacted crystalline mullite was still present in the TSRC control sample, cured for a day at 300ºC. The peaks of dmisteinbergite, bohmite and analcime were small while grossite was the major calcium-aluminate hydrate. After the continuous curing during the 30-day exposure to the acid dmisteinbergite and analcime became the major crystalline phases as was expected based on the previous studies [58,112]. The changes related to the interactions with the acid included decrease in the content of such calcium-containing phases as garronite (significant decrease of the major peak intensity at 2θº 28.28) and calcium carbonate (complete disappearance of peak at 2θº 29.38). Identification of the cement-acid reaction products was problematic due to the complexity of the XRD patterns. The fitting program SIeve+ of the International Center for Diffraction data suggested a possibility of calcium, aluminum and iron sulfates in the sample (Anhydrate $CaSO_4$ (04-0070-4744), Millosevichite $Al_2(SO_4)_3$ (04-005-9668), Szomolnokite $FeSO_4(H_2O)$ (00-021-0925). However, their patterns strongly overlap with the pattern of analcime that clearly increased in intensity after the 30-day exposure. The presence of anhydrate in the exposed sample is likely since there was a noticeable rise in the intensity of the shoulder at 2θº 31.36 in comparison with the control pattern. The presence of iron sulfate could be argued based on the peak at 2θº 35.56. As for aluminum sulfate it could not be identified unambiguously in these experimental patterns. Additionally the baseline of the acid-exposed sample increased suggesting higher content of amorphous phases and decreased sample's crystallinity.

The major difference in the pattern of OPC/SiO_2 cement exposed to the acid environment was significant intensity reduction of the quartz peak at 26.72º. That could be a result of continuous cement hydration with formation of calcium-silicate hydrates. After the acid exposure there was a slight decline in intensities of xonotlite, the major calcium-silicate hydrate. Formation of calcium sulfate could not be confirmed decidedly; although bassanite presence at low concentrations was proposed by the SIeve+ fitting program. Despite little changes in the crystalline composition, the bond of this cement broke in the first 18 days under the acidic conditions, partially because of the low initial bond strength.

GBFS/SiO_2 samples clearly showed bassanite in their composition (new peak at 2θº: 14.69, 29.71, 31.97) after the acid exposure. A new small peak around 2θº 25.53 could be attributed to aluminum sulfate (04-005-9668). Formation of bassanite corresponded to the decrease in intensities of calcium-silica hydrates (xonotlite and tobermorite) that decomposed loosing calcium. The intensity of calcite peaks also decreased (major peak at 29.29). Similarly, the intensities of diopside peaks between 30.42 and about 30.74º declined, suggesting sensitivity of this phase to the attack of a strong acid. Calcium removal and, as a result, partial dissociation of major binding phases resulted in the loss of the bond strength after 20 days of the samples exposure.

3.7.2.1.2. Elemental mapping – µEDX

Figure 89 gives the elemental maps and the composition of the major oxides in TSRC covering CS plates after the acid/brine exposure tests. The color schemes give quantitative evaluations of individual elements, with the contents decreasing as the color changes from white (100% element) through red, yellow, and green colors to blue (0% element). Relating sulfur to other elements is not straight forward based on these results. There are no clearly overlaying sulfur-calcium signals (high calcium content does not always match high sulfur content in the maps). In addition to calcium, the maps of sulfur correspond to iron and aluminum. The quantitative data (in the table) show higher sulfur for the sites with higher aluminum rather than with higher calcium or iron contents (site 1 vs. sites 2 and 3). Association of sulfur with aluminum could be interpreted as possible presence of aluminum sulfate or low amounts of crystalline Millosevichite (see section 3.7.2.1.1). Presence of hydrated iron sulfate or anhydrate cannot be excluded.

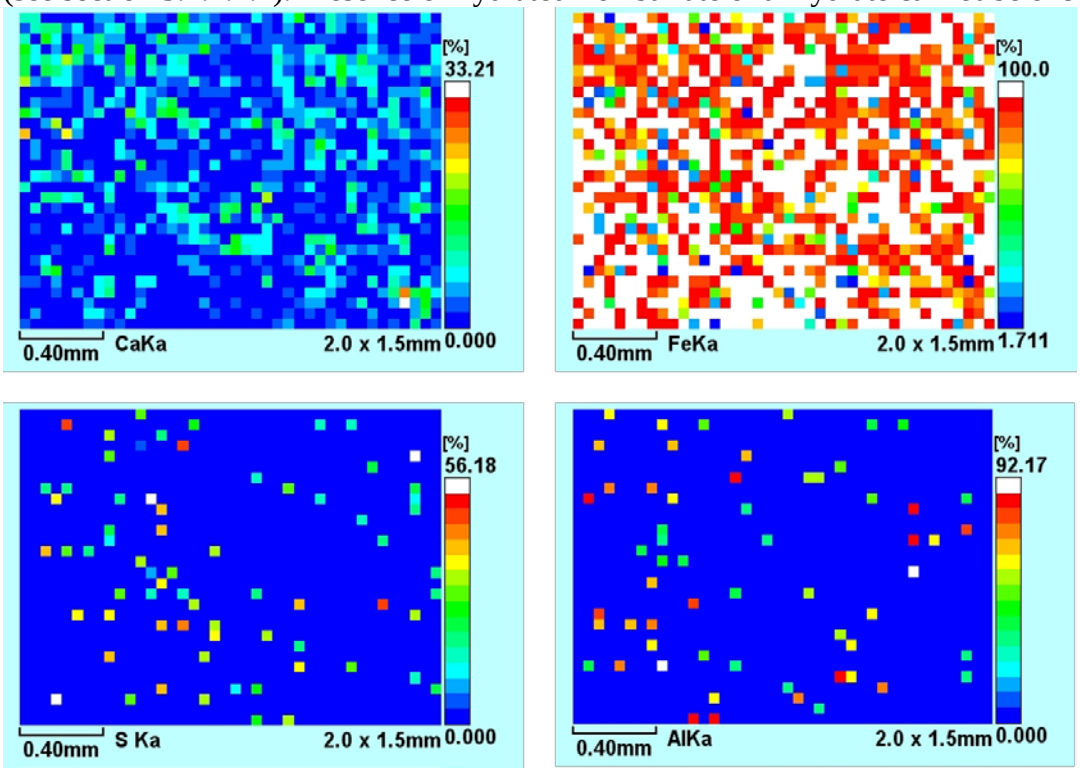

Oxide	Mass percent		
	Site-1 (shown above)	Site-2	Site-3
Al_2O_3	35	23	24
Fe_2O_3	29	40	38
SiO_2	23	22	22
SO_3	6.1	4.4	4.8
CaO	2.2	5.8	5.9

Figure 89. EDX elemental mapping and oxides composition of TSRC-covered CS samples after a 30-day exposure to H_2SO_4/brine solution at pH 0.6 and 90°C.

The quantitative data clearly suggest the depletion of calcium in the samples as a result of reaction with sulfate ions. Despite the calcium removal, there was still significant cement coverage of CS plates and the bond strength, although decreased, could be measured after 30 days of strong acid exposure (Figure 89). This indicates that some sodium-aluminum-silicate-based phases still ensured the bonding in the calcium-depleted cement.

The measurements of the GBFS/SiO_2 samples shown in Figure 90 suggest sulfur – calcium association. Both maps and the table show higher sulfur content at the locations of calcium accumulation. This result is in agreement with the XRD measurements that showed bassanite in acid-exposed GBFS/SiO_2 covering CS plates. The silicon content is low in these samples, suggesting that after calcium removal through reaction with sulfates, silicon was washed out probably as a gel. This process resulted in a gradual loss of the original bond and CS corrosion.

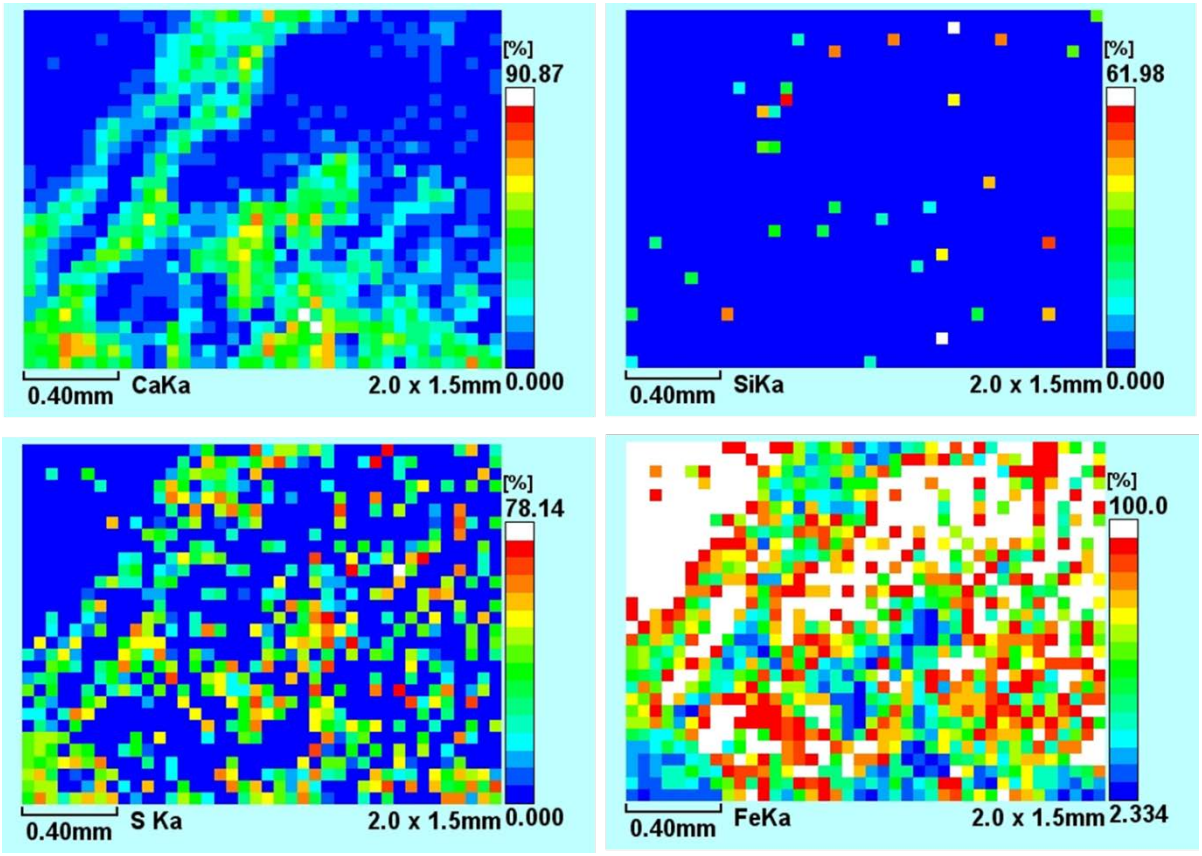

Oxide	Mass percent		
	Site-1 (shown above)	Site-2	Site-3
SO_3	34	40	19
Fe_2O_3	42	38	57
CaO	14	23	7
SiO_2	9.8	-	-

Figure 90. EDX elemental mapping and oxides composition of GBFS/SiO_2-covered CS samples after a 20-day exposure to H_2SO_4/brine solution at pH 0.6 and 90°C.

In the case of OPC/SiO_2 covered CS plates (Figure 91), there was no/or very little sulfur associated with the cement, unlike for TSRC and GBFS/SiO_2 samples. In fact, the original bond between the cement and CS was already weak. The samples survived only 18 days of acid/brine exposure. At the end of this period, the interfacial bond was broken with most of the cement staying on one of the plates. It is probable that calcium was just washed out sufficiently for the bond to break. On the other hand the maps of chlorine clearly show its association with calcium in the areas still covered by cement. This is in agreement with the quantitative data showing higher chlorine content at the sites with higher calcium. Formation of calcium silicate chloride hydrate (Rusinovite, ICDD 00-063-0365) cannot be excluded but it could not be confirmed by the XRD measurements with certainty because of the low content (if any) and complex XRD patterns with overlapping peaks of different minerals. The absence of sulfur in the cement agreed with the XRD data that did not show any noticeable peak of calcium sulfate.

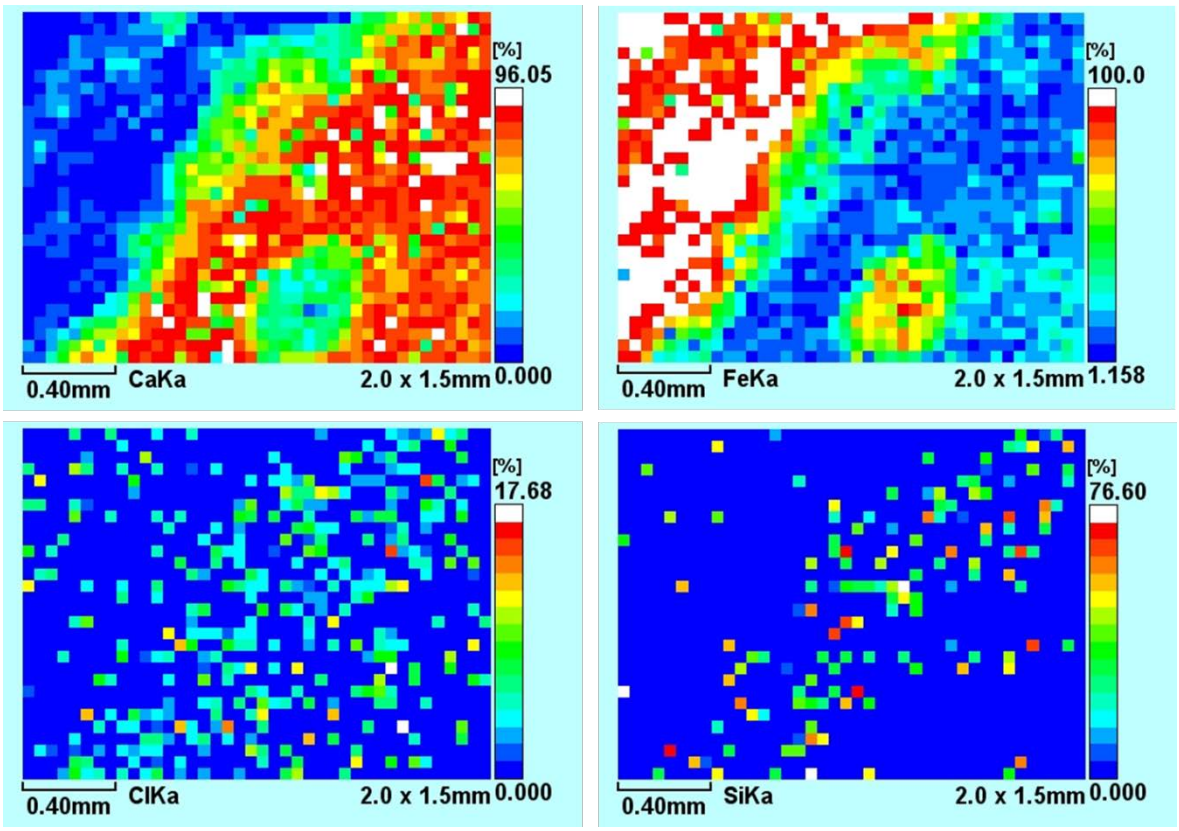

Oxide	Mass percent		
	Site-1-edge (shown above)	Site-2 (low cement coverage)	Site-3 (cement-covered)
CaO	34	2.7	52
SiO_2	27	8.8	18
Fe_2O_3	34	88	16
Cl	1.4	0.6	2.3

Figure 91. EDX elemental mapping and oxides composition of class G/SiO_2-covered CS samples after an 18-day exposure to H_2SO_4/brine solution at pH 0.6 and 90°C.

3.7.2.1.3. ATR-FTIR analyses

To support information obtained from the XRD study, ATR-FTIR analysis was carried out for the cement samples covering CS surfaces before and after the acid exposure tests. Figure 92 shows the ATR-FTIR absorption spectra in region of 2000 to 670 cm^{-1} for TSRC, OPC, and GBFS cements before the exposure. As described in our previous paper [59], the contributors to these absorption bands included the following five groups: water, carbonate, sulfate, silicate, and silica. The band at 1638 cm^{-1} was the H-O-H bending ($\delta_{H\text{-}O\text{-}H}$) in water. The carbonate group, CO_3^{2-}, was represented by 1489, 1452, and 1418 cm^{-1} bands attributed to the C-O anti-symmetrical ($V_{as\ C\text{-}O}$) stretching vibration in CO_3^{2-} and correspondingly, the band at 877 cm^{-1} belonged to O-C-O out-of-plane bending ($\delta_{O\text{-}C\text{-}O}$) in CO_3^{2-}. The presence of amorphous silica is identified by the bands at 1245 and 1204 cm^{-1}, while the crystalline silica as quartz gave the bands at 1077 cm^{-1} assigned to Si-O anti-symmetric ($V_{as\ Si\text{-}O}$) and at 799, 779, and 669 cm^{-1} corresponding to symmetric ($V_{s\ Si\text{-}O}$) stretching vibrations. There were two different types of silicate: One was calcium silicate hydrates (C-S-H) formed in class G/SiO_2 and slag/SiO_2 cements; the other was sodium, calcium aluminosilicate hydrate (N,C-A-S-H) and sodium aluminosilicate hydrate (N-A-S-H) formed in TSRC. For the former cements, the C-S-H-related Si-O anti-symmetric stretching ($V_{as\ Si\text{-}O}$) in silicate SiO_4^{-4} can be recognized by the presence of the principal band at 965 cm^{-1}. For the latter, the principal peak at 983 and shoulder peak at 901 cm^{-1}, respectively, was assigned to the M-O (M: Si or Al) anti-symmetric ($V_{as\ M\text{-}O}$) stretching mode in the Na^+ $^-$O-Ca-O-Si-O-Al and Na^+ $^-$O-Si-O-Al linkages related to amorphous- or crystalline-N,C-A-S-H and –N-A-S-H silicate reaction products. On the other hand, the sulfate group was associated with the band at 1156 cm^{-1} corresponding to the S-O symmetric stretching ($V_{s\ S\text{-}O}$) in SO_4^{2-}- related compounds.

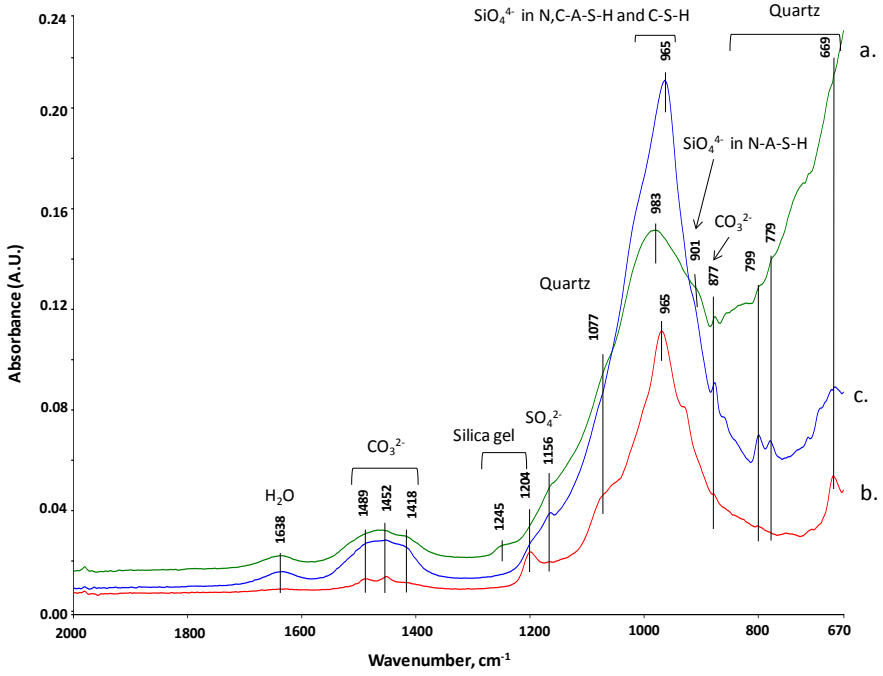

Figure 92. ATR-FTIR absorption spectra of TSRC (a), OPC/SiO_2 (b), and GBFS/SiO_2 (c) cements adhering to CS before acid exposure test.

Figure 93 gives FTIR spectra for cements remaining on the CS surfaces after acid-corrosion and –erosion damages of the cement/CS joints. We compared spectral features of the cements before and after the acid attack. For TSRC, there were three differences in the spectral features of acid-damaged cement: Firstly, $V_{as\ M\text{-}O}$ stretching at 901 cm^{-1} attributed to N-A-S-H became the major band, while N,C-A-S-H-related $V_{as\ M\text{-}O}$ at 983 cm^{-1} became secondary. This result strongly suggested that amorphous sodium-aluminum-silicate hydrates and crystalline analcime-type N-A-S-H phase not only acted to impede acid erosion of cement adhering to CS, but also offered an improved interfacial bond durability of cement to CS in acid environment; secondly, the peak intensity of carbonate-related bands was considerably reduced, implying that the carbonate compounds formed in this cement were susceptible to acid erosion; and thirdly, the additional silica gel was produced. It should be noted that the peak intensity of sulfate-related bands did not significantly increase after the acid exposure tests, if sulfate reaction products formed, their amounts were small.

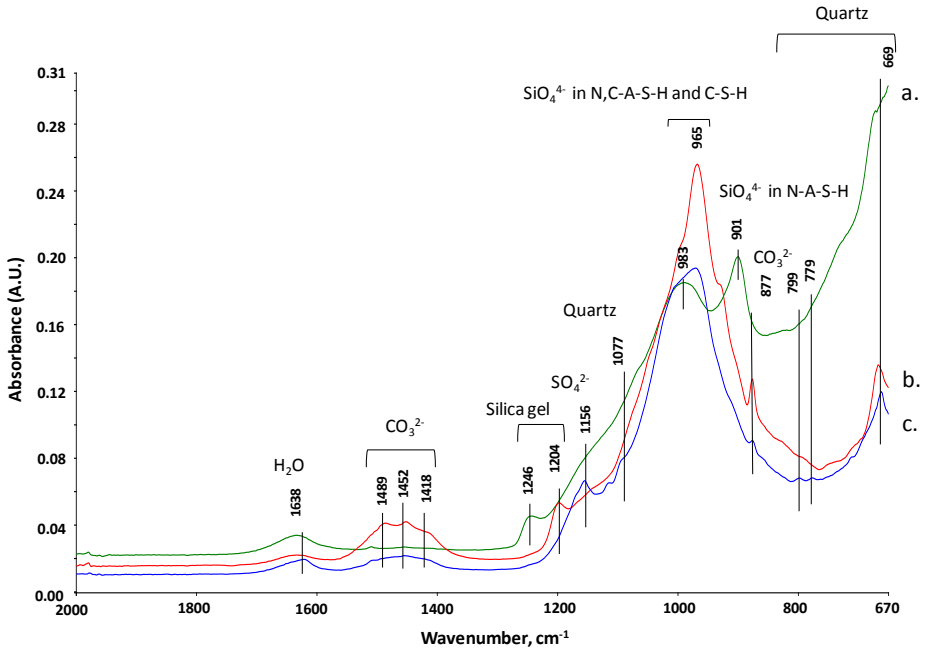

Figure 93. ATR-FTIR absorption spectra of TSRC (a), OPC/SiO_2 (b), and GBFS/SiO_2 (c) cements present at corroded and eroded cement/CS joins after acid exposure test.

For eroded OPC/SiO_2, the major difference for samples after the acid exposure was visible in the three reaction products (carbonates, silica gels, and C-S-H phases). There was no evidence whether carbonation reactions of eroded cement took place during the acid exposure or during drying of eroded cement in an air oven at 90°C. Furthermore, C-S-H compounds as the major hydrate phase were further formed in cement during acid exposure. Similarly to TSRC, the formation of sulfate reaction products was very small, if any.

For eroded GBFS/SiO_2, unlike for TSRC and OPC, two specific differences for acid exposed sample were noticeable: One was the ascent of sulfate-related band intensity, corresponding to the increase in sulfate reaction products; the other was the decline in quartz content, while there was no significant change in peak intensity at 983 cm^{-1} attributed to C-S-H phases.

There was a general agreement between the FTIR, XRD and µEDX mapping data on the composition of acid-exposed samples. In particular, FTIR results confirmed increase of sodium-aluminum-silicate hydrates in TSRC, further formation of calcium-silicate hydrates in OPC/SiO_2 and sulfates presence in the slag/SiO_2 specimens after the exposure.

3.7.2.1.4. Raman imaging

The Raman imaging was done on control samples after a day curing at 300°C and samples exposed to the acid/brine after 30 days for TSRC-, 20 days for GBFS/SiO_2- and 18 days for OPC/SiO_2 samples. An effort was made to select representative areas for the analyses. Three maps were registered for each sample. However, due to the high non-homogeneity of the samples and limited map areas the integrated information that could be obtained with this method was limited. The TSRC samples (not shown) were strongly luminescent without clear peaks that could allow phase identification.

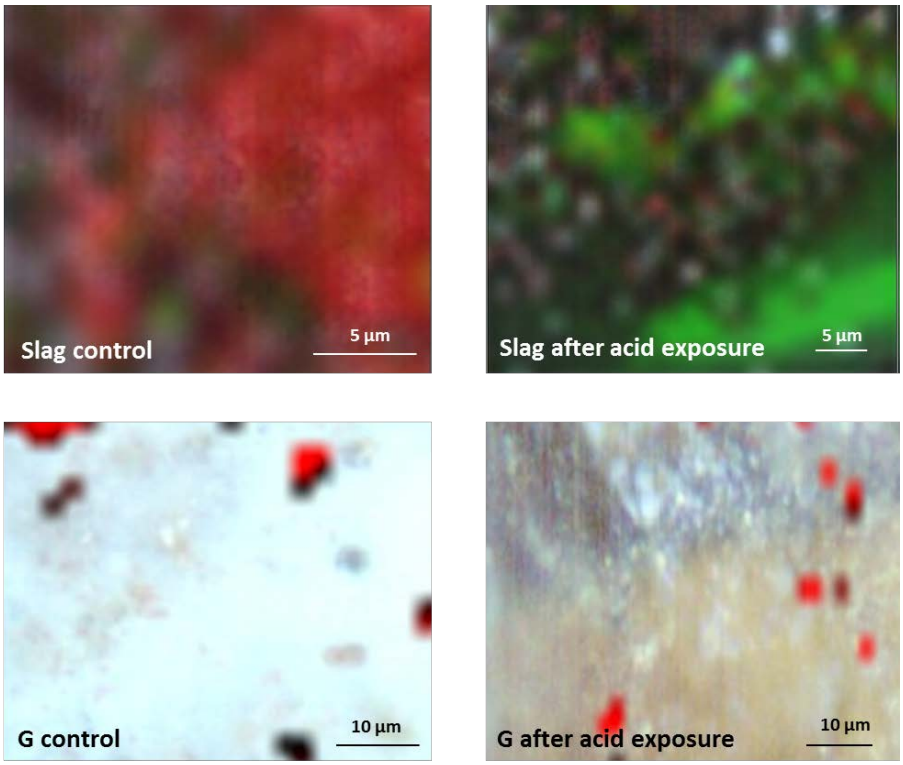

Figure 94. Raman mapping of GBFS (Slag)/SiO_2 and OPC (G)/SiO_2 samples before and after the acid/brine solution at 90°C for 20 and 18 days respectively. The red color in the GBFS/SiO_2 map shows tobermorite (660 cm^{-1}) and the green color sulfate peaks (115 cm^{-1}) intensities. The red color in the OPC/SiO_2 samples shows intensities of sulfate peaks.

GBFS (Slag)/SiO_2 and OPC (G)/SiO_2 control and acid-exposed samples' images are shown in Figure 94. The maps of tobermorite were made based on the major peak at 660 cm^{-1} and those of sulfate based on the major peak at 115 cm^{-1}. The difference in the control and treated GBFS/SiO_2 images is striking. The control sample surface composition is clearly dominated by tobermorite,

while the signal from sulfate is at the level of a background. The acid-exposed one is totally dominated by sulfate products, and the tobermorite becomes a minor component of the cement composition. This result agrees with the XRD, µEDX and FTIR studies that suggested sulfate reaction with the GBFS-based cement and sulfates accumulation. XRD data suggested bassanite presence in the samples.

3.7.2.2. pH 5.5 $scCO_2$-laden brine environment

Figure 95 shows the results of supercritical CO_2 ($scCO_2$)/brine with pH 5.5 exposure tests for up to 30 days at 90°C. In this specific environment, the lap-shear bond strength for all composite adhesives declined as the exposure time increased. The least bond strength reduction of 11%, after 30 days, was measured for TSRC. Compared with this, bond strength reduction of 36 and 35 %, respectively, was observed for the 30-day-exposed OPC/SiO_2 and GBFS/SiO_2. Nonetheless, the 30-day-exposed TSRC and GBFS/SiO_2 adhesives exhibited the lap-shear bond strength of 180 and 165 psi, respectively, which is equivalent to 5.0- and 4.5-fold higher than that of OPC/SiO_2 after the same exposure time.

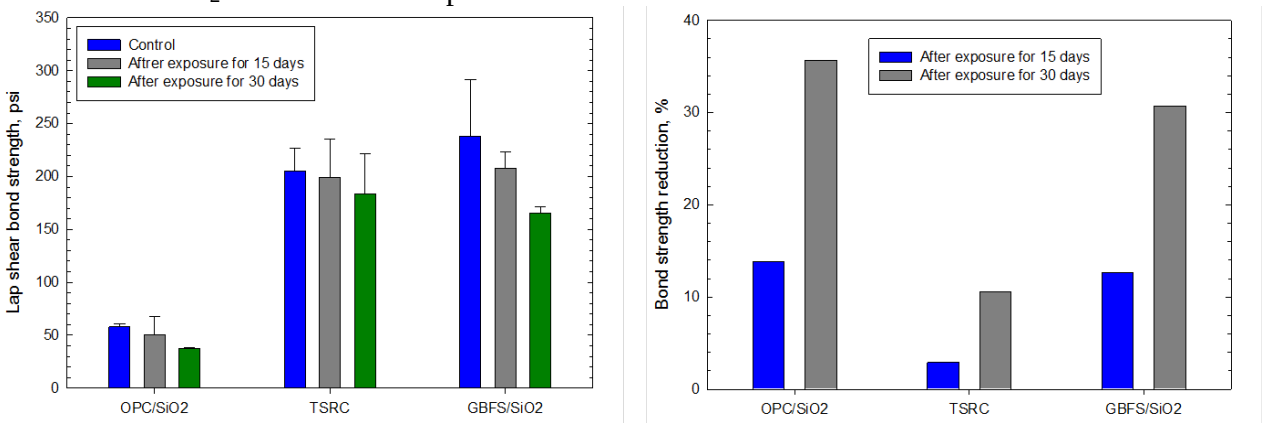

Figure 95. Bond durability in pH 5.5 $scCO_2$-laden brine at 90°C for up to 30 days.

As a result, in these tested acid environments, TSRC fully met material criterion of the lap-shear bond strength of more than 30% above that of OPC/SiO_2.

3.7.3. Corrosion mitigation

After the debonding of the composite sheath from CS the remaining composite layer must protect CS from corrosion and this protection must improve after the re-adherence treatment. We evaluated whether additional composite layers that deposit on the CS during the healing period further enhance its corrosion protection. To obtain this information, the CS plate/cement/CS plate lap joint samples were prepared by autoclaving them in 24-hrs-300°C plain water. In this work, three composites (OPC/SiO_2, TSRC, and CAP-B) modified and unmodified with MGF and Clin were employed, and their ability to inhibit corrosion of CS was evaluated for composite layer adhering to CS surfaces after the 1st and 2nd lap-shear bond tests by DC electrochemical polarization in brine. The detail of preparation for the 2nd bond strength test can be found in section 2.3. “Samples preparation”. Namely, after the 1st bond strength test, two debonded CS plates were reattached by steel wire (Figure 96), and then reattached plate samples were

autoclaved for 5 days in plain water at 300°C. After this re-adherence treatment the 2nd time bond strength test was conducted and the plate with the thinner composite layer was further tested to obtain quantitative corrosion-related data showing whether the re-adherence treatment improved corrosion protection of CS. The data included the corrosion rate of CS, coverage of composite on CS, and cathodic corrosion protection by composite. The electrochemical corrosion-related data were collected from DC potentiodynamic polarization curves (Figure 96). As was mentioned above, we selected the CS site covered with a thinner composite layer. The results were obtained by averaging data from three different locations of cement-covered CS samples. On the polarization curve the corrosion potential denoted as E_{corr} accounted for the extent of cement's coverage over CS; a high value of E_{corr} means a better coverage in terms of minimum spacing between composite and CS. The corrosion current density marked as I_{corr} provides information on the protection from cathodic corrosion that corresponds to the following half-reaction: $H_2O + 1/2O_2 + 2e^- \rightarrow 2OH$; a low I_{corr} value means a minimum permeation of water and oxygen through cement layer covering CS surfaces. In other words, the cement layers with low I_{corr} are dense, with low water and oxygen permeability.

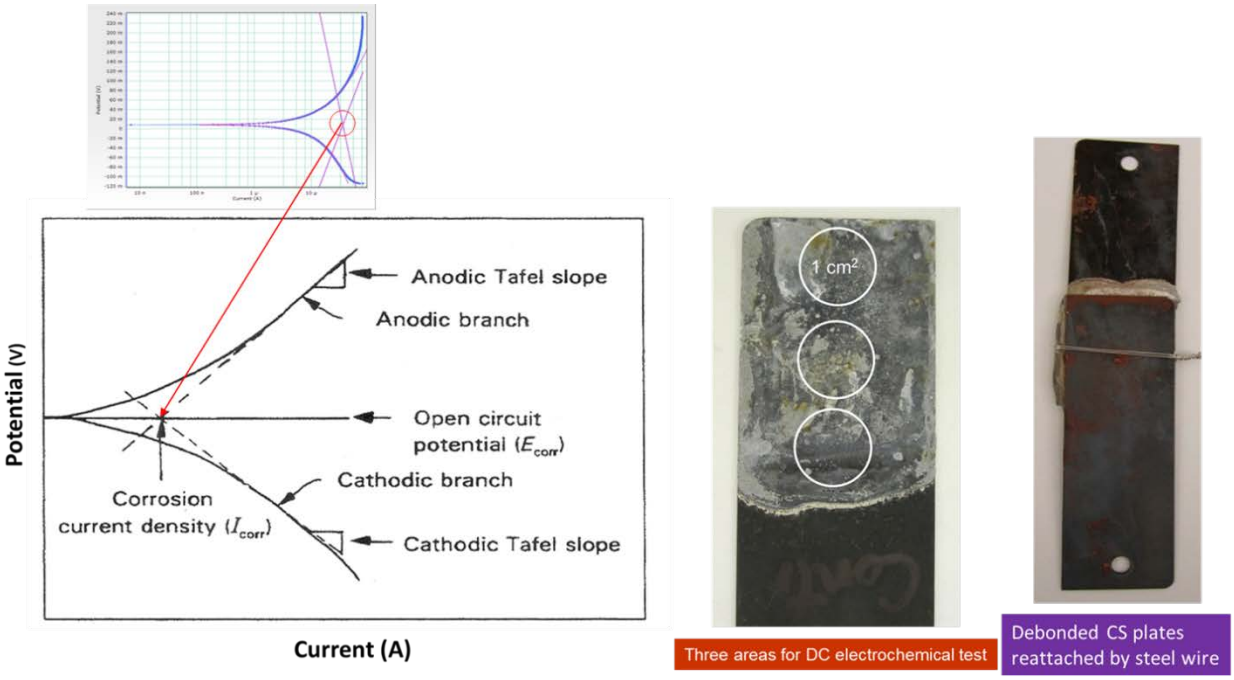

Figure 96. DC electrochemical potentiodynamic cathodic-anodic polarization diagram for composite-covered CS after lap-shear bond test.

Figure 97 depicts the average E_{corr} and I_{corr} values for CS plate covered with OPC/SiO_2, TSRC, and CAP-B composite layers modified with MGF and Clin. The obtained E_{corr} and I_{corr} data were directly correlated with the thickness of composite layers covering the CS surfaces and the corrosion rate of underlying CS (Figure 97). The corrosion rate was computed based on E_{corr} and I_{corr} values obtained from the polarization curves. The resulting data revealed that unmodified TSRC exhibited the best coverage over the CS surface, reflecting the highest E_{corr} of average +14 mV, while bear CS without any coverage had the lowest E_{corr} of -185 mV. The relatively moderate coverage in the range from ±0 to -50 mV was detected for TSRC/MGF, OPC/SiO_2/MGF, CAP-B, and CAP-B/MGF, emphasizing that MGF contributed to the moderate

coverage for all composites. Relating this finding to the results of lap-shear bond strength tests, such good coverage resulted from the increasing adhesive force of composite-modified with MGF to CS. Furthermore, MGF also helped to impede cathodic corrosion reactions of CS; in fact, the I_{corr} value of all composites was lower with MGF, especially, OPC/SiO_2 and CAP-B indicated a considerable reduction of this value. Since the lowering of I_{corr} value implies low permeability of oxygen and water as corrosion initiators through composite layer, it is possible to assume that MGF offered the densified composite structure. The effectiveness of Clin in raising the E_{corr} and lowering the I_{corr} was not as great as that of MGF.

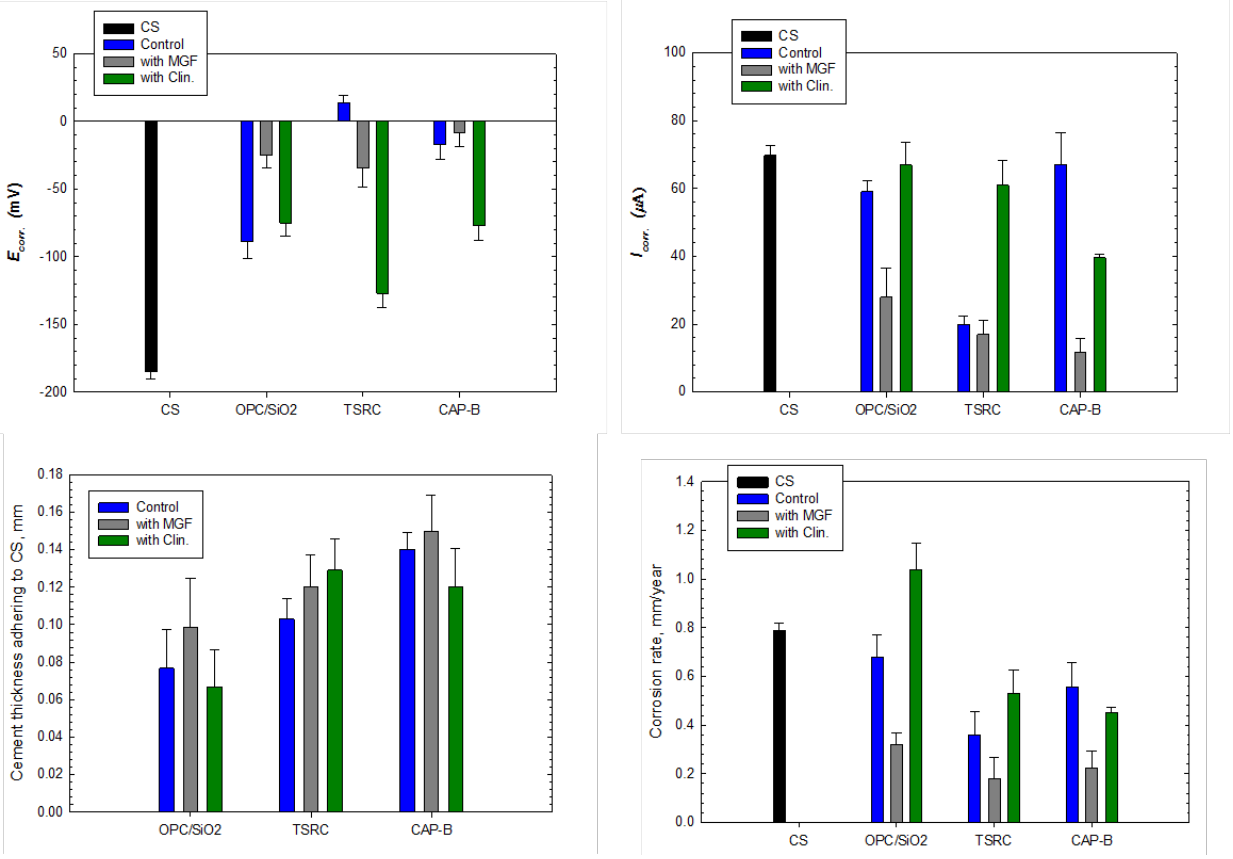

Figure 97. Comparison of $E_{corr,}$ $I_{corr,}$ and composite CS coverage thickness affecting the corrosion mitigation of CS by MGF- and Clin-modified and unmodified OPC/SiO_2, TSRC, and CAP-B composites.

Regarding the average thickness of the composite layer remaining on CS after the lap-share bond strength tests, the composites without any additives had 0.07, 0.10, and 0.14 mm thickness, respectively, for OPC/SiO_2, TSRC, and CAP-B; with MGF, this thickness increased by 28%, 17%, and 7%. With Clin, only TSRC showed an increased thickness compared with that of MGF, while the decreased thickness was observed for the two other composites.

The data strongly demonstrate that the combination of three parameters, higher E_{corr}, lower I_{corr}, and thicker composite layer adhering to CS, played a pivotal role in decreasing the corrosion rate of composite-covered CS. Without any pozzolanic additive, the corrosion rate of CS protected by tested composites decreased in the following order: OPC/SiO_2 (0.68 mm/year) > CAP-B (0.56 mm/year) >TSRC (0.36 mm/year). For all composites, the incorporation of MGF led to the

reduction of corrosion rate; particularly, OPC/SiO_2 and CAP-B modified with MGF significantly improved the corrosion mitigation of CS. The 0.32 and 0.22 mm/year for MGF-modified OPC/SiO_2 and CAP-B, respectively, corresponded to 2.1- and 2.5-fold reduction of corrosion rate, compared with that of the unmodified ones; meanwhile, the lowest corrosion rate of 0.18 mm/year was obtained with TSRC. On the other hand, Clin did not improve the protection of CS against corrosion for OPC/SiO_2 and TSRC.

Using the corrosion tested samples, we investigated ability of re-adhered composites to further mitigate corrosion of CS. As described earlier, two debonded CS plates were reattached with a wire, and then reattached plates were exposed to plain water at 300^{o}C for 5 days as a re-adherence treatment. Afterward, the re-adhered plates were again separated by lap-shear bond test. It should be noted here that the shear bond strength of re-adhered plate samples was too weak to be measured. Nonetheless, after the 2nd time lap-shear bond test, the same CS side as the one tested after the 1st lap-bond test was examined to obtain information on the corrosion protection by the re-adhered composites. Because of a typical cohesive failure, relatively large amount of TSRC and CAP-B, remained on two debonded CS sites, as a result, the two debonded CS sites re-adhered together through the composite-to-composite bonding during the re-adherence treatment. This was similar to the re-attachment of a fragment to the mother cement, as described in “E-type micro-glass fiber as artificial pozzolan” section.
Figure 98 compares the representative polarization curves, the average E_{corr} and I_{corr} values, and appearances of debonded CS site before and after the re-adherence to CS for MGF- and Clin-modified and unmodified OPC/SiO_2 composite. For the unmodified OPC/SiO_2 composites after re-adhering treatment, there were no significant changes in the average values of E_{corr} and I_{corr}, compared with that of 1st debonded samples denoted as before. The noticeable changes in E_{corr} value from -25 mV for “before” to 6 mV for “after” were observed for the MGF-modified composite, implying that MGF acted to improve the coverage of composite over CS surface after re-adherence treatment. Meanwhile, I_{corr} value somewhat increased from 28 μA for “before” to 74 μA, suggesting that the permeability of water and oxygen through re-adhered composites increased. The Clin-modified composite revealed some improvement of coverage and no significant change in permeability. Overall, more corrosion stains were generated beneath all re-adhered composite layers of OPC/SiO_2.

Unlike for OPC/SiO_2, in the case of TSRC there was less corrosion of underlying CS and a new re-adhered composite layer superimposed on the pre-existing composite layer was present, importantly suggesting that the thickness of composite layers covering CS increased during the re-adherence treatment (Figure 99). For unmodified TSRC, E_{corr} value significantly increased by 8.4-fold from 14 mV to 118 mV after re-adherence, the re-adherence treatment provided the improved coverage of CS by the composite, while no changes in I_{corr} was observed. Likewise, Clin-modified TSRC indicated a great enhancement of E_{corr} and conspicuous reduction of I_{corr} after re-adherence treatment. In contrast, for the re-adhered MGF-modified TSRC, E_{corr} value decreased to -83 mV, raising concerns that the uniform coverage of composite layer originally adhering to CS became poor during the re-adherence treatment. On the other hand, I_{corr} increased to 41 μA, causing the reduction of the cathodic corrosion protection. However, this value was still lower than that of MGF-modified OPC/SiO_2.

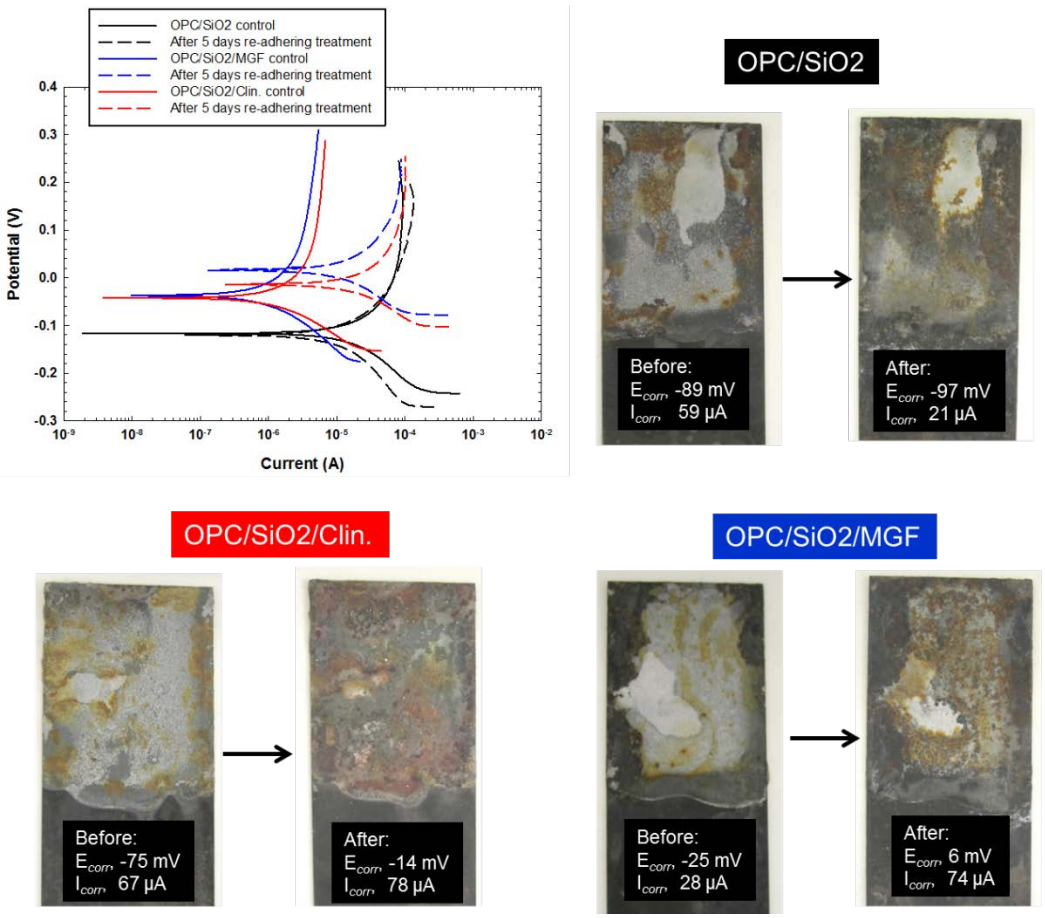

Figure 98. Changes in polarization curve features, E_{corr}, and I_{corr} values, and appearance of debonded CS surfaces for MGF-and Clin-modified and unmodified OPC/SiO_2 adhesives after re-adherence treatment.

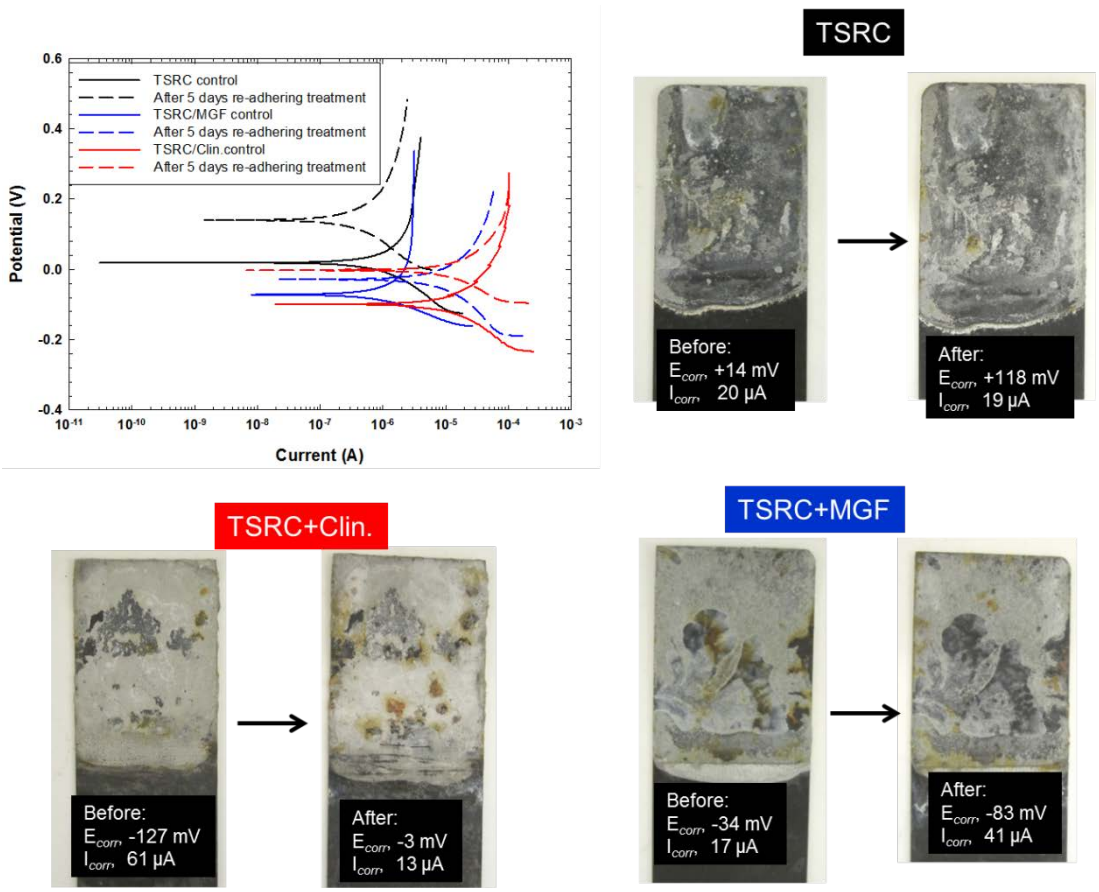

Figure 99. Changes in polarization curve feature, E_{corr}, and I_{corr} values, and appearance of debonded CS surface for MGF-and Clin-modified and unmodified TSRC adhesives after re-adherence treatment.

For all re-adhered modified and unmodified CAP-B (Figure 100), there were two negative factors affecting the corrosion protection: One was no visible new layer of the re-adhered composites superimposed on the pre-existing composite layer; the other was the increase in I_{corr} to more than 90 µA for unmodified and Clin-modified ones, engendering the increased permeability of water and oxygen because of poor cathodic corrosion protection, while E_{corr} showed a remarkable increase, reflecting an improved coverage as positive factor. Additionally, the corrosion stains seem to be reduced by re-adherence treatment.

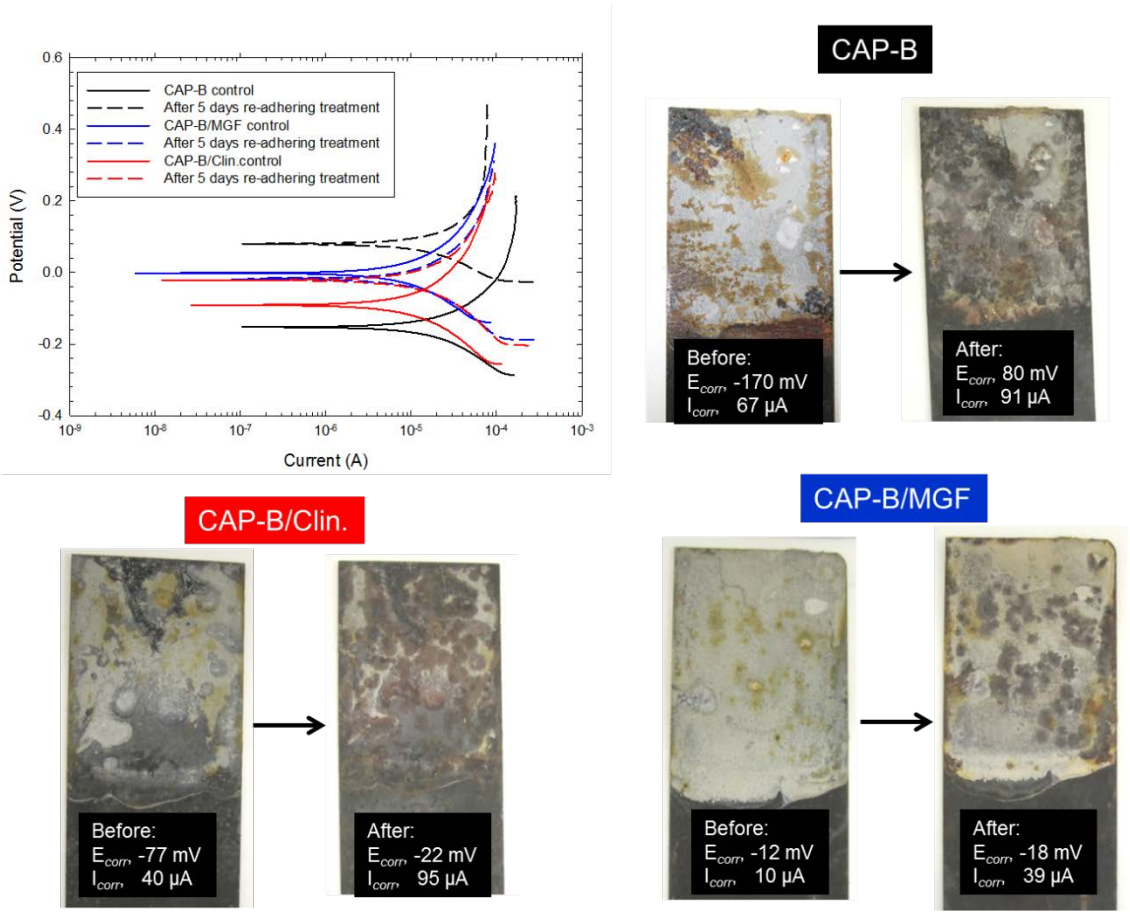

Figure 100. Changes in polarization curve features, E_{corr}, and I_{corr} values, and appearance of debonded CS surfaces for MGF-and Clin-modified and unmodified CAP-B adhesives after re-adherence treatment.

Figure 101 represents the thicknesses and corrosion rates of MGF- and Clin-modified and unmodified composite coverage before and after re-adherence treatment. As seen, MGF-modified and unmodified TSRC showed a considerable increase in thickness of composite layers after the treatment. In fact, the thickness of both MGF-modified and unmodified TSRC after 1st lap-shear bond test rose by nearly 2.3-times. The increase in thickness by Clin was only1.4-fold. For the two other composites, MGF also assisted in increasing thickness of OPC/SiO_2 and CAP-B, while the effect of Clin on increased thickness was little, if any.

Based upon the combination of these three factors ($E_{corr,}$ $I_{corr,}$ and thickness of composite coverage) contributing to the corrosion mitigation of underlying CS, Figure 101 shows corrosion rates of CS for re-adhered composites. For unmodified composites, two composites, OPC/SiO_2 and TSRC, improved the corrosion protection of CS by re-adherence treatment. The corrosion rates of 0.49 and 0.23 mm/year for OPC/SiO_2 and TSRC were reduced by 28% and 36% compared against those before the treatment as control. In contrast, the re-adhered CAP-B did not show any reduction of corrosion rate. Further corrosion mitigation was observed from re-adhered MGF-modified OPC/SiO_2 and TSRC, reflecting the corrosion rate of 0.23 and 0.16 mm/year, respectively. These encouraging results strongly demonstrated that the additional

composite coverage superimposed on pre-existing composite layer by re-adherence treatment appeared to further improve the corrosion protection of CS. On the other hand, although MGF-modified CAP-B before re-adherence had a good corrosion protection of 0.22 mm/year, the re-adherence treatment engendered negative effect of increased corrosion rate (0.45 mm/year). Such negative effect was observed for all re-adhered CAP-B composites.

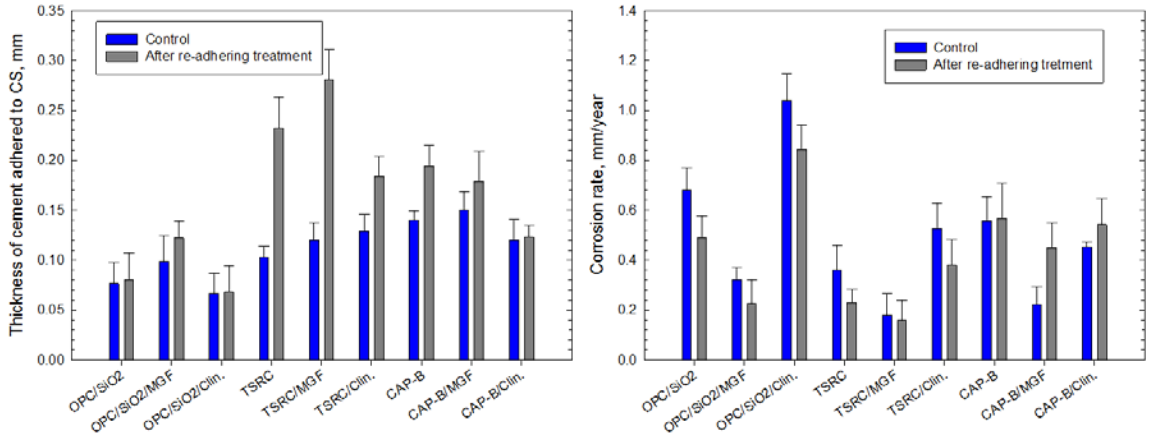

Figure 101. Thickness of composite adhesives covering on CS and corrosion rate of CS for MGF- and Clin-modified and unmodified OPC/SiO_2, TSRC, and CAP-B adhesives before and after re-adherence treatment.

Furthermore, we investigated CS corrosion protection by the 30-day-autoclaved MGF-modified TSRC. In this work, two unmodified reference composites, OPC/SiO_2 and TSRC, were used for comparison. The ideal coverage of composite over CS surfaces can be seen for TSRC and TSRC/MGF; namely, the entire lap-jointed areas of both CS sites were covered with these composites that failed cohesively (Figure 102). When these images were compared with those of the same composites at 1-day autoclave age, it appeared that the extent of coverage by 30-day-aged composites was much greater, corresponding to nearly 2.4-fold increased thickness (Figure 102). Similar increase thickness was observed for the 30-day cured OPC/SiO_2. However, one unavoidable concern was the Fe-related corrosion product known as magnetite (Fe_3O_4) formed in the composite-uncovered areas of CS. The magnetite corrosion product formed dark colored areas on CS creating a passive layer. Since magnetite passive layer is soluble in acid, it is possible to assume that this passive layer may act as barrier to delay further corrosion of CS in plain water, but not in acidic environments. As expected, the increased coverages directly reflected the reduction of corrosion rate (Figure 102). In fact, compared with that of 1-day-autoclved ones, the corrosion rate of CS for 30-day-autoclaved composites before re-adherence treatment was reduced from 0.18 to 0.16 mm/year for TSRC/MGF, from 0.36 to 0.25 mm/year for TSRC, and from 0.68 to 0.59 mm/year for OPC/SiO_2.

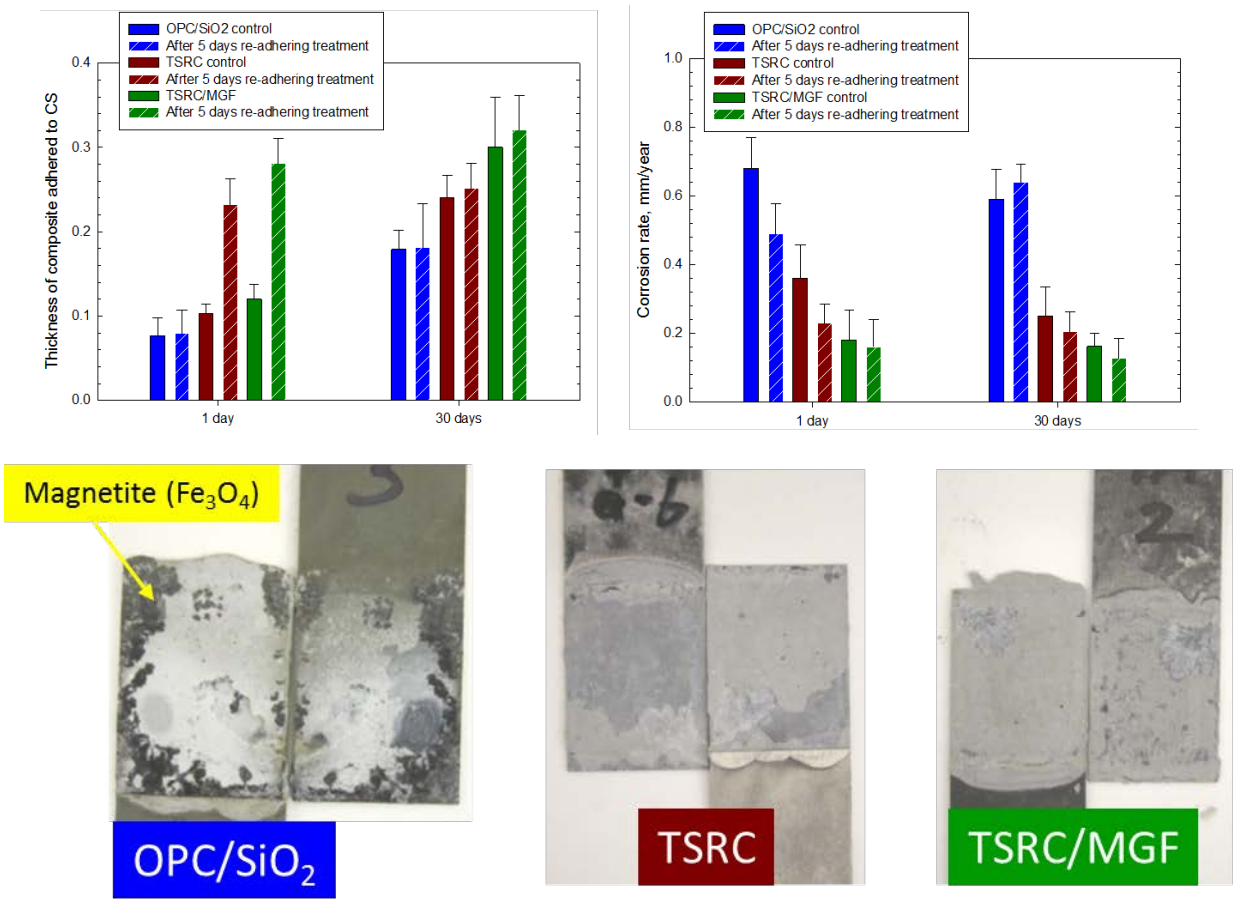

Figure 102. Thickness of composite adhesive at CS surfaces, corrosion rate of CS, and appearance of debonded CS sites for 300^{O}C-30-day-autoclaved MGF-modified TSRC, and unmodified TSRC and OPC/SiO_2 composites.

After the re-adherence treatment, the thickness of re-adhered 30-day-autocalved TSRC/MGF and TSRC composites over CS, somewhat increased to 0.32 mm from 0.28 mm and to 0.25 mm from 0.23 mm, respectively, decreasing corrosion rate to 0.13 mm/year for TSRC/MGF and 0.2 mm/year for TSRC, underscoring that although the interfacial debondement for 30-day-aged TSRC/MGF and TSRC composites occurred, the composites remaining on the CS surface provided an excellent corrosion protection of CS against brine-caused corrosion. By contrast, the OPC/SiO_2 layer thickness did not change after re-adherence treatment and the corrosion rate increased from 0.59 to 0.64 mm/year.

The integrated information of all adhesion- and corrosion-related data described above strongly verified that the adequate corrosion protection of CS was essentially governed by the following two principal factors: One was a good wetting and spreading behavior of composite slurries over CS surfaces, reflecting uniform coverage by the composite layer; the other was an outstanding adhesive behavior of composite to CS, leading to the development of high interfacial bond strength between composite and CS. From this point of view, alkali-activated TSRC/MGF demonstrated the best wetting and adhesive behaviors, while such behaviors of non-activated OPC/SiO_2 were relatively poor.

3.8. Bond strength between composites and granite rock before and after re-adhering

Figure 103 shows the unconfined sheath-shear bond strengths between composite sheath and granite cylindrical column before and after re-adhering for OPC/SiO_2, TSRC/MGF, and CAP-B/MGF. The samples were made by 1-day autoclaving in plain water at 300°C.

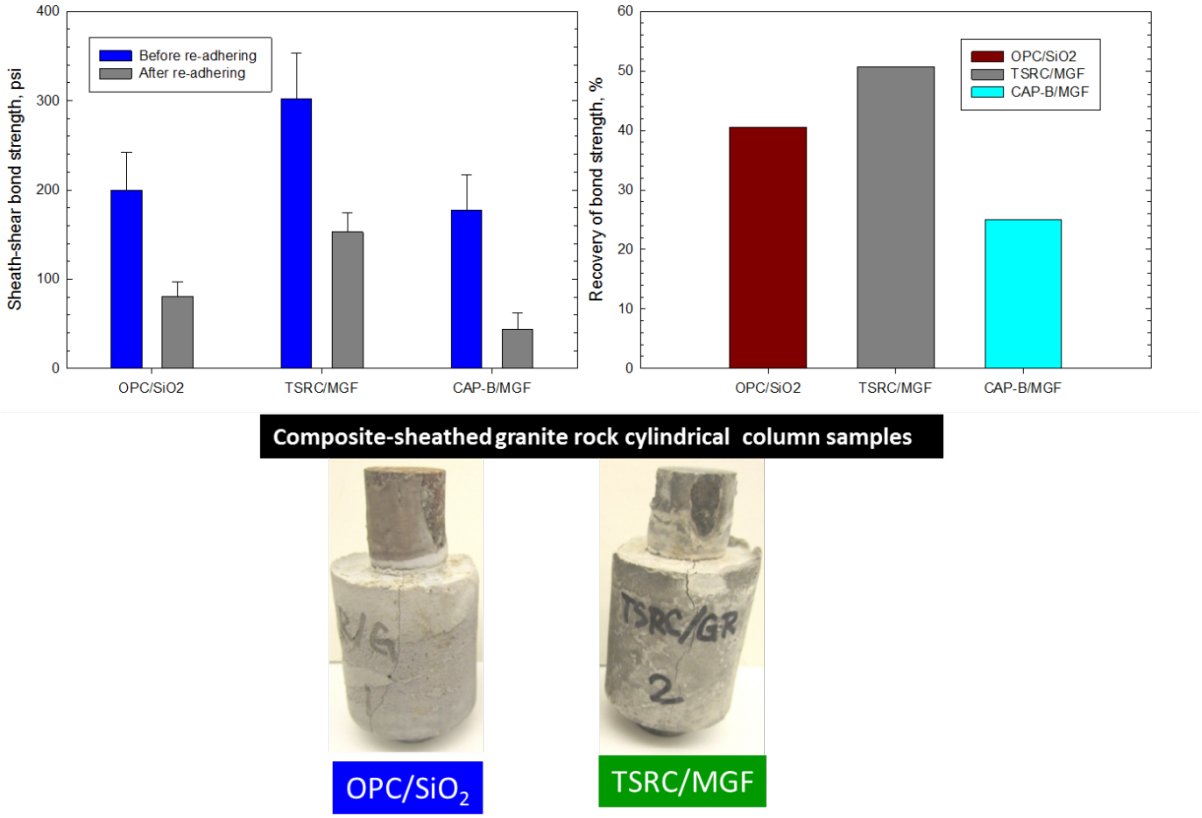

Figure 103. Sheath-shear bond strength of OPC/SiO_2-, TSRC/MGF-, and CAP-B/MGF composites to cylindrical granite rock column and bond strength recovery after re-adhering treatment.

All the composites exerted high sheath-shear bond strength of more than 170 psi with granite rock. In particular, TSRC/MGF developed a very high bond strength of 300 psi. This fact clearly demonstrated that granite rock surfaces were highly susceptible to reactions with these composites, compared with CS surface. In fact, the 300, 200, and 180 psi bond strength, respectively, for TSRC/MGF, OPC/SiO_2, and CAP-B/MGF, was tantamount to the increases in 1.5-, 5.9- and 3.5-fold, compared with that of CS joint samples. If the degree of this susceptibility is directly related to the sheath bond strength, TSRC/MGF along with the highest pH resulted in a better adherence to granite than that of the lowest pH of CAP-B. Nevertheless, the surfaces of granite formation appeared to have a great attraction to alkaline composites. Consequently, only 1 day curing of composites at 300°C was sufficient to establish a great interfacial bonding. Thus, there was no further experimental work on investigating the bond behaviors of the samples made by the extended autoclave curing. Like the composite-sheathed

CS tube samples, the excessive sheath bond strength ≥200 psi for TSRC/MGF and OPC/SiO_2 triggered the development of undesirable multi-cracks in the composites during the bond testing.

Despite the cracks' development, two alkali-based composites, TSRC/MGF and OPC/SiO_2, revealed a good bond recovery of >41% after 300°C-5-day re-adhering treatment in plain water, while the recovery of CAP-B/MGF was only 25%.

3.9. Placement technology of self-healing TSRC composite: Set control, properties of retarded cements

Generally, the pumping time between 3 and 6 hrs may be expected for cement slurries in hot geothermal wells. The retarder added to slow down cement hydration and reactions of slurry components must provide controllable, predictable pumping time of the slurry without compromising development of cement mechanical properties after the set. The challenges of controllable and predictable pumping time include exponential acceleration of hydration reactions with the increase of temperature, which means that, as a rule of thumb, the rate doubles for each 10^{o}C, usually accelerated set at higher pressures and uncertainty in these parameters in the field, especially for geothermal wells that are commonly drilled in highly fractured unstable environments.
Additional concerns arise for cement blends where components react at different times and their reaction rates are mutually affected. In the case of TSRC blend hydration of calcium-aluminate cement was slowed down by SMS activator of FAF and by the reactions of the ash. The reactivity of FAF, in turn will strongly depend on the temperature and rate of the temperature increase. In the case of fast temperature increase, the alkaline dissolution of FAF will start earlier slowing down reactions of calcium-aluminate cement and producing products with ions coming from both the cement and the ash. For the slow rate of temperature increase, the FAF reactions may take place well after the calcium-aluminate cement hydration. Presence of a third reacting component (MGF in the case of TSRC) further complicates the situation. All these factors must be considered during the development of the placement technology.

Our previous work identified D-(-)-tartaric acid (TA) as the best candidate for retarding hydration of TSRC slurries at 85^{o}C bottom-hole circulating temperature (BHCT) [47]. The pumping time evaluated as the beginning of thickening or point of departure of the consistency increase in API thickening time tests was shown to be predictably dependent on TA concentration (Figure 104). TA was identified as an efficient set retarder of TSRC. There were three important reasons why TA was desirable as set-controlling additive for TSRC under the final curing conditions (after short curing periods of up to three days at temperatures of up to 300 °C) [113]: The first reason was creation of a microstructure consisting of uniform small pores; the second was the development of high compressive strength; the third was minimal phase transitions with preferential formation of the stable phases in the presence of TA.

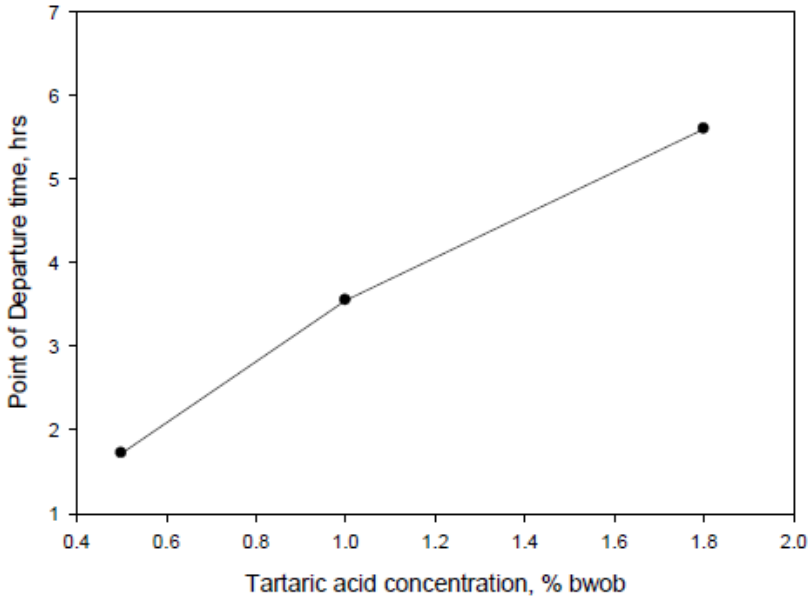

Figure 104. Point of departure time for TSRC slurry thickening time tests (API 10B) as a function of tartaric acid concentration [47].

This work focused on evaluating TA effect on self-healing, re-adhering, and corrosion mitigating ability of MGF-modified and unmodified TSRC composites in water and carbonate environments at 270° and 300°C.
TA was dry-blended with the composites at 1% by total weight of the blend in this experimental work.

3.9.1. MGF-free TSRC

To prepare the samples, the slurries were hand-mixed at water-to-blend ratio of 0.5 and cast into cylindrical molds (25-mm diameter and about 40-mm length). Borosilicate glass tubes (25 mm × 150 mm cylinders) were used as the molds. The walls of the tubes were covered with Teflon sheets to avoid cement slurry contact with the glass. The tubes were filled with the slurry up to about 40 mm height. The final samples of cement were measured before mechanical testing and the exact size of each sample was used to calculate the compressive strength. The molds were placed into an autoclave partially filled with water (20% of volume) at 85 °C for a 3-day curing, and then the temperature was increased to the final 270 °C for 24 h. The preliminary low curing temperature imitated placement conditions in geothermal wells. The volumetric proportion of cement-to-fluid was 1-to-3.5 and the pressure in the autoclaves was 8.27 MPa (1200 psi). The fluid used as a curing environment was either plain water or 0.05 M solution of sodium carbonate. Mechanical properties of the samples cured for 3 days at 85°C and 24 h at 270°C were determined in crush tests. Damaged samples were returned into the autoclaves and cured for 10 more days at 270°C. Then, the crush tests were repeated to evaluate strength recoveries and damage the samples for the second time. The second-time damaged samples were cured for 5 more days under the same conditions followed by the final crush tests. Each result was averaged over at least three samples. The experimental steps are summarized below.

3days at 85 °C→ 24 h at 270 °C→ 1st crack test → 10days at 270 °C→ 2nd crack test → 5days at 270 °C→ 3rd crack test.

3.9.1.1. Compressive strength and its recovery

Figure 105 gives the strength values of the 1st-, 2nd- and 3rd-time cracked samples under the compressive load. The data for the 1st crack (original strength) revealed that TA-modified samples displayed a better development of compressive strength at the curing age of 24 h than control cement. In fact, the compressive strength of 1553 and 1553 psi, respectively, for TA samples cured in water and carbonate, was 32% and 23% higher than that of control samples. The value of compressive strength for all 1st-time cracked samples after the first 10 days of healing in these environments was somewhat lower, compared with that of the original strength. Nevertheless, we observed a good strength recovery rate, ranging from 80% to 95%. The average strength recovery rates after the third crack and additional 5-day healing were 89 and 98% for TA-modified samples in water and carbonate, respectively, which was a better recovery than after the second crack. In contrast, the recovery rate of the 3rd time cracked samples without TA decreased by 23 and 20% in water and carbonate compared against the 2nd time crack. Thus, TA appeared to offer the improved cement strength recovery.

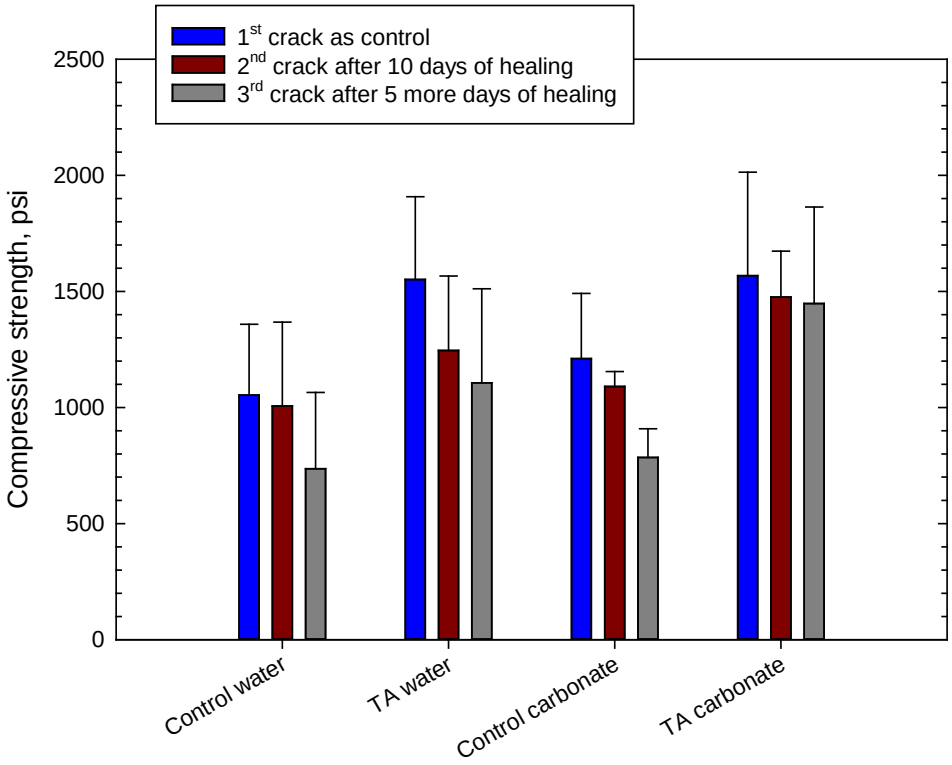

Figure 105. Compressive strength for the first-, second- and third-time cracked TA-modified and unmodified (control) samples after exposure to water or alkali carbonate solution at 270 °C.

3.9.1.2. Crack sealing, optical microscope and µEDX elemental analyses

Figures 106–109 show optical microscope images of TA-free control and TA-modified samples exposed to water or carbonate environments after the crush tests. The photographs and the corresponding 3D images (images with the black background to the right of the photographs) show the same cracks before and after the healing (the "before" image for the crack in location B of Figure 106 is not shown).

All samples underwent some crack sealing. The nature of the healing material visually differed depending on the curing environment. The water-cured samples showed a smooth gel-like (glassy in the case of the control) filling, while it was rougher in the alkaline carbonate especially for TA-samples.

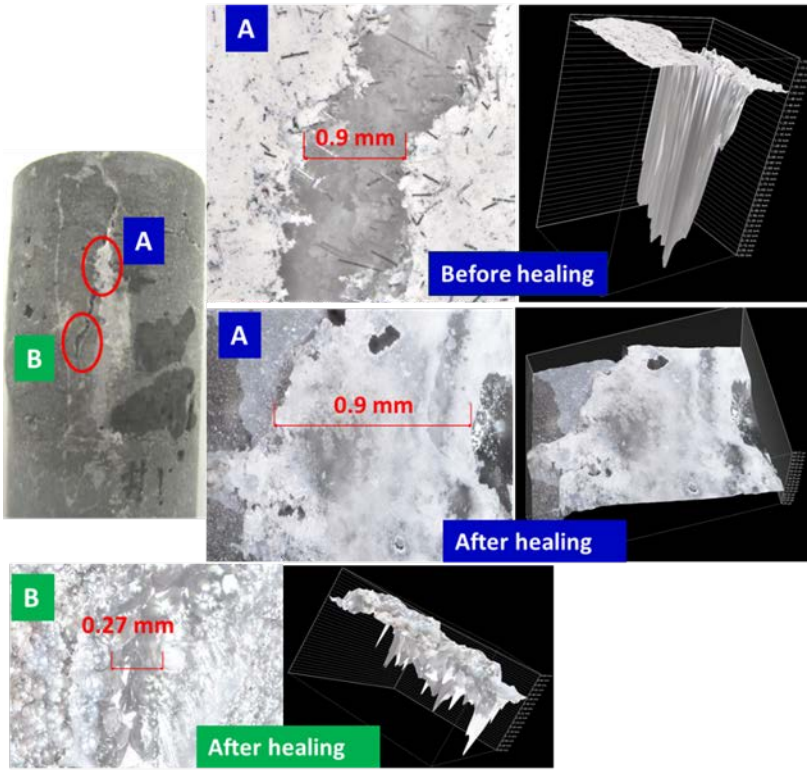

Figure 106. Optical microscope images of cracks in damaged TA-free control samples before and after healing in water for 10 days at 270 °C.

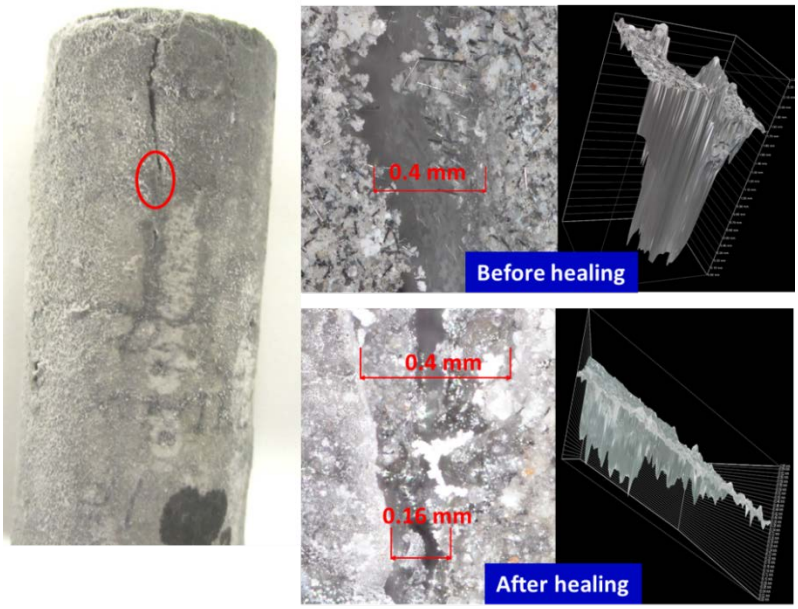

Figure 107. Optical microscope images of cracks in damaged control samples before and after healing in alkali carbonate for 10 days at 270 °C.

Impressively, the gel completely sealed the 0.9 mm wide and 1.75 mm deep crack and partially filled a narrower 0.27 mm crack in some crack areas of the control sample (Figure 106). The 3D images reveal the flat gel surface covering the 0.9 mm crack. Similarly, for the TA-modified sample, the 0.24 mm wide and 1.1 mm deep crack was totally closed with a solid gel (Figure 108). In fact, the 3D image clearly demonstrated the absence of the depth in the healed crack area.

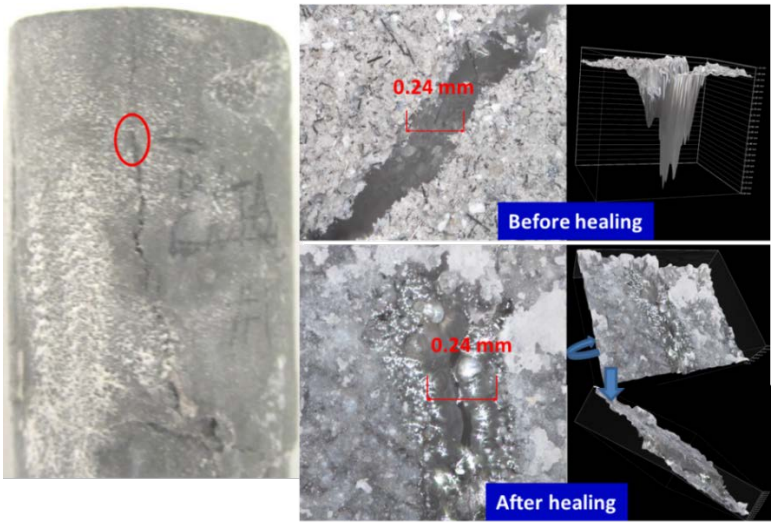

Figure 108. Optical microscope images of cracks in damaged TA-modified samples before and after healing in water for 10 days at 270 °C.

The sealing was more efficient for TA-modified samples than for control in alkaline carbonate. For example, 0.16 mm crack in control sample was only partially healed, while 0.27 mm crack in TA-modified sample was sealed completely (Figures 107 and 109). The sealing material was rougher with a visible build up above the crack area for this environment. Unlike the gel formed in water, this material was more likely to fill the cracks, rather than to cover them. The filling was lesser for the deeper/wider fractures.
The results of the elemental composition mapping for the cores of the samples and the healed crack areas are given in Table 23. The data were obtained by grinding samples collected from cores or scratched out of the healed crack areas.

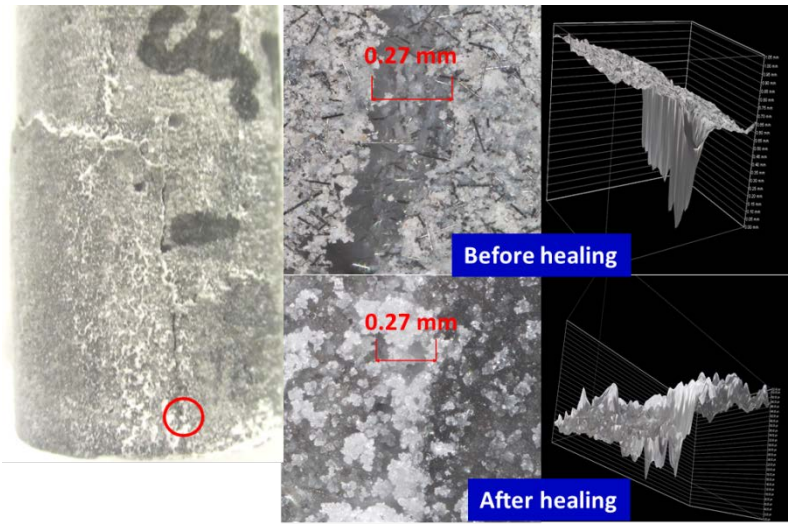

Figure 109. Optical microscope images of cracks in damaged TA-modified samples before and after healing in alkali carbonate for 10 days at 270 °C.

Table 23. Major oxides composition in the cracks and cores of the healed Thermal Shock Resistant Cement (TSRC) samples with or without tartaric acid (TA).

Sample	SiO_2	Al_2O_3	CaO	CaO/ Al_2O_3	CaO/ SiO_2	Al_2O_3/ SiO_2
Samples from Healed Cracks						
Control Water	78	11	3.9	0.35	0.05	0.14
Control Carbonate	79	11	5.6	0.51	0.07	0.14
TA Water	69	19	3.2	0.17	0.05	0.27
TA Carbonate	81	13	3.2	0.25	0.04	0.16
Core Samples						
Control Water	22	51	19	0.37	0.86	2.3
Control Carbonate	22	52	20	0.38	0.91	2.4
TA Water	23	51	19	0.37	0.83	2.2
TA Carbonate	23	52	18	0.35	0.78	2.3

Comparison of the core and crack compositions can provide information on the elements preferentially participating in the healing process. The data presented in Table 23 clearly indicate

silicon-rich material accumulation in the crack areas. Concentrations of SiO_2 in the cracks are 3.1–3.5 times higher than in the cores of the samples. Accordingly, the CaO/SiO_2 and Al_2O_3/SiO_2 ratios in the ranges 0.78–0.91 and 2.2–2.4 in the cores drop to 0.04–0.07 and 0.14–0.27, respectively, in the healed cracks.

The CaO/Al_2O_3 ratio of control samples did not change significantly in water environment but increased in carbonate, possibly as a result of calcium carbonate precipitation in the cracks. TA-modified samples seemed to have lower calcium and higher aluminum contents in the healed areas than in the cores, which resulted in lower CaO/Al_2O_3 ratio for the crack material. In the sealed areas, the lesser drop in Al_2O_3/SiO_2 ratio for TA-modified samples than for controls is in agreement with this observation. Elemental mapping of aluminum (not shown) demonstrated that it was present in low amounts throughout the crack areas in both environments.

In summary, the micro-images show that both control and TA-modified samples undergo sealing of the fractures accompanied by the increase of silicon surface content and in the case of TA-modified samples some increase in aluminum in the crack sealing material. TA enhances sealing of the cracks especially in carbonate environment.

3.9.1.3. XRD study

Figures 110 and 111 show major crystalline phases for control and TA-modified samples cured in water or alkali carbonate at 270 °C for total of 15 days and Table 24 lists these phases with their respective ICDD numbers. The phases appear in the table in the order of higher to lower abundance according to the semi-quantitative analyses of the PDF-4/Minerals 2015 database. The major crystalline phases were for the most part similar in control and TA-modified samples after total 15 days of curing. In addition to the listed phases all the samples showed peaks of corundum, some hematite (from non-reacted fly ash) and the crack areas had some calcium carbonate-related minerals (calcite and vaterite).

The major crystalline reaction products for all samples included: feldspar-type mineral dmisteinbergite; mica-type mineral margarite-2M1; zeolites thomsonite with varied calcium content and analcime. In the case of the control aluminum oxide hydroxides bohmite and tohdite (split bohmite peaks at 2θ 38.3° and peak shoulders at 20.3° and 42.9°) along with the small amounts of feldspathoid group mineral cancrinite were mostly present in the core of the sample. For the TA-modified cement, additional crystalline phases included garnet-group mineral grossular in water-cured samples and clinotobermorite (or distorted tobermorite) that gave a visible low-angle peak at 2θ 9.43° in the crack areas of TA-modified sample cured in alkali carbonate. This phase was absent from all other samples. Small peaks of paragonite, sodium-aluminum silicate, mica-type mineral appeared in cracks of the TA-sample cured in alkali carbonate.

Although the major crystalline phases were similar in both control and TA-modified samples there were noticeable differences in their manifestation. The same mineral phases including predominantly dmisteinbergite, margarite, grossular and aluminum oxide hydroxides formed in the cores of control and modified samples. However, water-cured control samples showed higher core intensities of dmistenbergite (peaks at 2θ°: 23.5, 24.1, 31.6, 35.3) and aluminum oxide

hydroxides (peaks at 2θ°: 14.52, 28.25, 38.34 and between 48.93 and 49.34) while TA-modified ones were richer in margarite (2θ°: 35.6) and zeolite thomsonite (peaks at 2θ°: 13.4, 15.0, 30.45, 33.6).

For the crack zones, the major phases included zeolites and cancrinite for both control and modified samples. However, TA-samples crack areas were richer in zeolites (analcime and thomsonite). Thus, the intensities of analcime's peaks (2θ° 15.8) were more important for TA-samples and thomsonite was present only in the patterns of water-cured TA-modified cement. In contrast, cancrinite (a likely carbonation product of analcime and dmisteinbergite) forming mostly in carbonate environment had higher peak intensities in control samples than in TA-modified ones.
As mentioned above, sodium-aluminum silicate paragonite and calcium-silicate hydrate, clinotobermorite formed only in the cracks of TA-modified sample cured in alkali carbonate. It is possible that clinotobermorite contained aluminum since its inclusion into tobermorite does not necessarily change the XRD pattern. Additionally, gonnardite was possibly present in the cracks of TA-modified sample cured in alkali carbonate since its patterns largely overlap with those of thomsonite.

In summary, the principal crystalline phases in TA-modified samples were poorer in calcium compared against the crystals in controls. The calcium-to-aluminum ratio of margarite preferentially crystalizing in TA-modified samples is lower than that of dmisteinbergite, predominant in control ones (1-to-4 ratio vs. 1-to-2 ratio, respectively), analcime, a major crystalline product in the material sealing the cracks in TA-samples does not contain any calcium, while peak intensities of calcium-containing cancrinite are higher for controls. This confirms earlier findings where minerals with lower calcium content formed in TA-modified samples after short curing time. The lower calcium content of crystals suggests a possibility of higher calcium presence in the amorphous hydrates in TA-samples. Crystalline phases identified by XRD cannot account for the high silicon content detected by µEDX. This suggests existence of amorphous silica in both control and TA-modified samples.

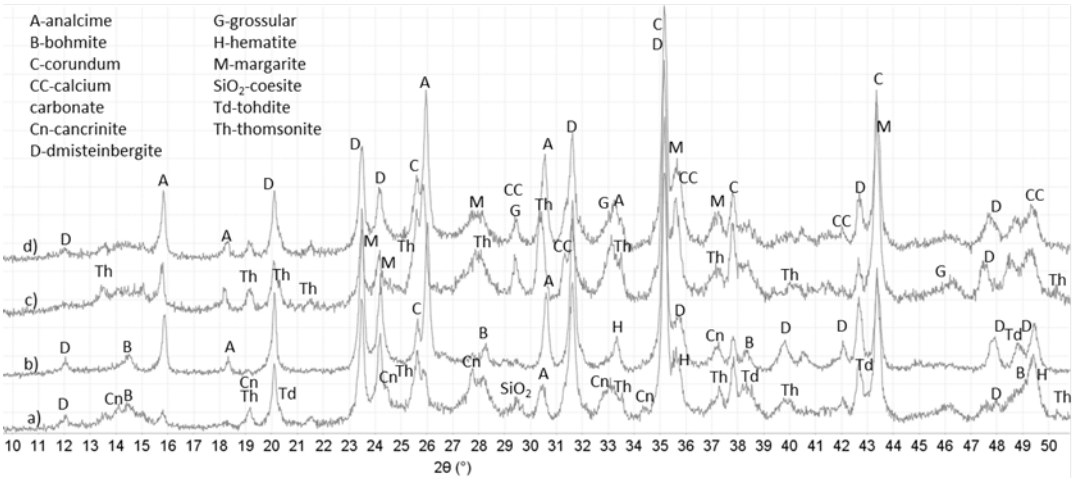

Figure 110. Diffractograms for control and TA-modified TSRC samples after total of 15 days in water at 270 °C: (**a**) control-core; (**b**) control-cracks; (**c**) TA-core; and (**d**) TA-cracks.

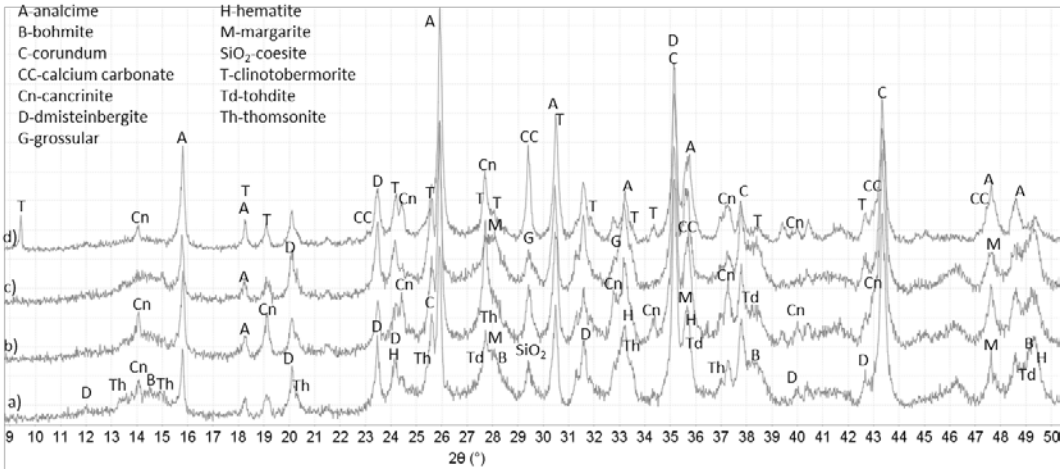

Figure 111. Diffractograms for control and TA-modified TSRC samples after total of 15 days in alkali carbonate at 270 °C: (**a**) control-core; (**b**) control-cracks; (**c**) TA-core; and (**d**) TA-cracks.

Table 24. Main crystalline phases identified by XRD with corresponding The International Center for Diffraction Data (ICDD) numbers.

Control	**TA-Modified**
Core—Water	
04-011-5220 Dmisteinbergite $CaAl_2Si_2O_8$; 04-013-3004 Margarite-2M1 $CaAl_4Si_2O_{10}(OH)_2$; 01-078-0296 Thomsonite-Ca $NaCa_2Al_5Si_5O_{20}(H_2O)_6$; 04-012-1749 Analcime $Na_{7.6}Al_{7.6}Si_{16.4}O_{48}(H_2O)_8$; 04-014-1755 Tohdite $Al_5O_{7.5}(H_2O)_{0.5}$; 00-005-0190 Bohmite $Al_2(OOH)_2$; 00-011-0401 Hydroxysodalite $Na_4Al_3Si_3O_{12}OH$	04-013-3004 Margarite-2M1 $CaAl_4Si_2O_{10}(OH)_2$; 01-078-0296 Thomsonite $NaCa_2Al_5Si_5O_{20}(H_2O)_6$; 04-011-5220 Dmisteinbergite $CaAl_2Si_2O_8$; 04-013-2153 Grossular $Ca_3Al_2(SiO_4)_2(OH)_4$; 01-072-0445 Analcime $Na(AlSi_2O_6)(H_2O)$
Crack—Water	
04-011-5220 Dmisteinbergite $CaAl_2Si_2O_8$; 01-076-6569 Analcime $Na_{0.9}((Al_{0.9}Si_2)O_6(H_2O)$; 04-013-3004 Margarite-2M1 $CaAl_4Si_2O_{10}(OH)_2$; 04-014-1755 Tohdite $Al_5O_{7.5}(H_2O)_{0.5}$; 00-005-0190 Bohmite $Al_2(OOH)_2$	00-018-0276 Margarite-2M1 $CaAl_4Si_2O_{10}(OH)_2$; 01-088-2093 Thomsonite-Ca $Na_{1.26}Ca_{1.74}(Si_{5.26}Al_{4.74}O_{20})(H_2O)_6$; 04-011-6755 Analcime $Na_8Al_8Si_{16}O_{48}(H_2O)_8$; 04-014-1755 Tohdite $Al_5O_{7.5}(H_2O)_{0.5}$; 04-011-5220 Dmisteinbergite $CaAl_2Si_2O_8$; 04-013-2153 Grossular $Ca_3Al_2(SiO_4)_2(OH)_4$
Core—Alkali Carbonate	
00-018-0276 Margarite-2M1 $CaAl_2(Si_2Al_2)O_{10}(OH)_2$; 04-011-6755 Analcime $Na_8Al_8Si_{16}O_{48}(H_2O)_8$; 01-080-6030 Cancrinite $Na_{7.4}Ca_{0.54}(Si_{6.42}Al_{5.58}O_{24})(CO_3)_{1.47}(H_2O)_2$; 04-011-5220 Dmisteinbergite $CaSi_2Al_2O_8$; 04-013-2153 Grossular $Ca_3Al_2(SiO_4)_2(OH)_4$; 00-005-0190 Bohmite $Al_2(OOH)_2$	00-018-0276 Margarite-2M1 $CaAl_2(Si_2Al_2)O_{10}(OH)_2$; 04-011-7963 Analcime-R $Na_8Al_8Si_{16}O_{48}(H_2O)_8$; 01-078-0296 Thomsonite-Ca $NaCa_2Al_5Si_5O_{20}(H_2O)_6$; 01-075-8619 Cancrinite $Na_{6.02}Ca_{1.52}(Si_6Al_6O_{24})(CO_3)_{1.52}(H_2O)_{1.56}$;

	04-011-5220 Dmisteinbergite $CaSi_2Al_2O_8$; 04-013-2153 Grossular $Ca_3Al_2(SiO_4)_2(OH)_4$; 04-014-1755 Tohdite $Al_5O_{7.5}(H_2O)_{0.5}$
Crack—Alkali Carbonate	
04-013-1895 Cancrinite $Na_6Ca_{1.5}Al_6(SiO_4)_6(CO_3)_{1.5}(H_2O)_{1.75}$ 04-011-7963 Analcime-R $Na_8Al_8Si_{16}O_{48}(H_2O)_8$; 04-015-7167 Coesite SiO_2; 00-018-0276 Margarite-2M1 $CaAl_4Si_2O_{10}(OH)_2$; 04-011-5220 Dmisteinbergite $CaSi_2Al_2O_8$; 00-005-0190 Bohmite $Al_2(OOH)_2$	01-074-2596 Clinotobermorite $Ca_5(Si_6O_{16})(OH)_2$; 04-011-7963 Analcime-R $Na_8Al_8Si_{16}O_{48}(H_2O)_8$; 01-075-8620 Cancrinite $Na_{6.02}Ca_{1.52}(Al_6Si_6O_{24})(CO_3)_{1.52}$; 04-011-5220 Dmisteinbergite $CaSi_2Al_2O_8$; 01-082-2720 Paragonite-2M1 $Na_4Al_{12}Si_{12}O_{40}(OH)_8$

3.9.1.4. DTG Study

The differential thermogravimetric analyses complimented the XRD studies for identification of both crystalline and amorphous phases that decompose with the weight loss at temperatures up to 1000 °C. The results are shown in Table 25. The weight losses below about 200 °C were attributed to poorly crystalline (sodium, calcium)-aluminosilicate hydrates and calcium-silicate hydrates[82,114,115] along with the water loss from zeolite-type phases such as gonnardite and possibly sodalite that showed minor peaks in XRD studies [93]. Analcime and thomsonite decompose for the most part in 200–400 °C temperature range, although increasing CaO content may shift analcime decomposition temperature up to 700 °C [116]. Garnet phases, such as grossular also have decomposition peaks in that temperature range[117–119]. Bohmite loses its hydroxyl groups between 400 °C and 550 °C. There is a possible contribution from thomsonite structure collapse above 500 °C[120]. Carbonates decompose at temperatures above 550 °C, including cancrinite decomposition at about 680 °C and 950°C[121], iron calcium carbonate decomposition may take place in two steps (650–700 °C and 850–950 °C), sodium carbonate decomposes between 900 °C and 1200 °C. Mica group minerals decompose between about 820 and 920°C [93].

For the water environment the major differences between control and TA-modified samples included: (1) higher weight losses in TA-modified samples up to 400 °C associated with amorphous and poorly crystalline hydrates (<200 °C) and zeolites and garnet phases (200–400 °C); and (2) lower losses in TA-samples from bohmite (400–550 °C).
These results are in general agreement with the XRD-study that suggested higher zeolites content (analcime and thomsonite), grossular and smaller amount of aluminum oxide hydroxide (bohmite) in TA-modified samples. Additionally, it suggests more amorphous hydrates in composition of the TA-samples. It should be noted that the loss in 400–550 °C temperature range assigned to bohmite could be overestimated for TA-samples because of the possible contribution from zeolites. However, the fact that for both control and TA-samples the loss in that temperature range was larger in the core than in the crack areas suggests bohmite, which predominantly forms in cores, to be the main contributor to these losses. The decomposition temperature was lower for TA-modified samples in this range likely because of the lower

crystallinity and possibly different nature of the decomposing phases (bohmite in the case of control, contribution of zeolites in the case of TA-samples).
The losses above 550 °C were assigned to carbonates and mica group mineral, margarite. The carbonate-related peaks at about 630 °C were larger for TA-modified samples in agreement with the XRD results. Large decomposition peaks at temperatures above about 750 °C for control samples may be associated with margarite. However, it is also possible that they are associated with the carbonation and further decomposition of (CaO,Na_2O)-Al_2O_3-SiO_2-H_2O gel [122].
The weight losses of control and modified samples cured in carbonate were for the most part similar. The main difference was in noticeably higher weight losses above 800 °C for TA-samples. These are likely associated with the carbonation of cations originally bound to TA so removed from the pool of ions participating in formation of other minerals. Other contributors to this mass loss include cancrinite and margarite. The sample from TA crack area had two peaks at around 680 and 912 °C that are likely related to cancrinite or its precursor while the core sample had a wide peak above about 850 °C with probable contribution of margarite (not shown).
Interpretation of specific peaks in complex blends of the samples is problematic. However, some general trends confirm XRD observations such as likely presence of zeolites, aluminum oxide hydroxides, margarite and cancrinite minerals in the healed samples. There are higher losses associated with amorphous phases and zeolites in TA-modified interface samples and lower losses from aluminum oxide hydroxides in the cores of these samples.

Table 25. Mass losses in different temperature ranges for the 15-day cured interface (IF) and core samples.

Specimen	Decomposition Temperature Range, °C									
	<200 Ca(Na)-Al-Si-H Clinotobermorite (Zeolites)		2004400 Zeolites Grossular		400–550 Bohmite (Zeolites)		>550 Carbonates Mica group		Total	
	crack	core	crack	core	crack	core	crack	core	crack	core
Carbonate-Control	1.4	1.5	2.1	2.0	1.9	2.4	3.2	2.2	8.6	8.0
Carbonate-TA	1.1	1.5	2.3	1.9	1.2	2.3	9.4	7.1	14.1	12.8
Water-Control	0.94	1.3	1.6	1.5	1.3	2.2	7.5	7.1	11.4	12.0
Water-TA	1.5	1.7	2.1	1.9	1.6	2.1	2.2	4.2	7.3	9.9

3.9.1.5. ATR-FTIR Studies

ATR-FTIR study was performed to support XRD results on the core and interface samples of specimens after 15 days of total healing and the third brake. The ATR-FTIR spectra of starting materials , CAC #80 and FAF (not shown), disclosed a very strong band at 770 cm^{-1} associated with the Al-O bond of “condensed” AlO_4 tetrahedra network of mono-calcium aluminate (CA), the principal mineralogical phase of CAC[75,123]. The two major components of FAF were: the aluminosilicate anhydrous compounds showing the strong and weak bands at 1035 and 776 cm^{-1}, respectively, belonging to the M-O (M: Si or Al) anti-symmetrical ($V_{as\ M\text{-}O}$) and symmetric ($V_{s\ M\text{-}O}$) stretching vibration in the Si-O-Si and Si-O-Al linkages[124,125]; the second component was

quartz with weak 740 and 680 cm^{-1} bands attributed to Si-O symmetric stretching ($V_{s\ Si-O}$) and Si-O bending (δ_{O-Si-O}) vibrations, respectively [109,111].

Figure 112 depicts the ATR-FTIR absorption spectra in the region of 1600 to 650 cm^{-1} for the core and inner-surface of cracks samples exposed to 270 °C alkali carbonate solution for 15 days. The spectral features closely resembled each other containing the same frequency nine representative frequency bands with the following contributors. The C-O ($V_{as\ C-O}$) stretching vibration in carbonate CO_3^{2-} emerged in the region of 1510 to 1400 cm^{-1} [72,74,126], the Si-O-Si linkage-associated $V_{as\ Si-O}$ vibration in silica gel at 1243 cm^{-1} [105,127,128], the Al-OH bending ($\delta_{as\ Al-OH}$) and ($\delta_{s\ Al-OH}$) vibrations, and AlO_4 tetrahedral (V_{Al-O}) stretching in bohmite (γ-AlOOH), were respectively, at 1148, 1068, and 777 cm^{-1}, reflecting the presence of typical bohmite-related doublet peaks of O-H group at 3307 ($V_{as\ O-H}$) and 3086 ($V_{s\ O-H}$) cm^{-1} bands (not shown) [77,78,129,130], the M-O (M: Si or Al) ($V_{as\ M-O}$) in amorphous and crystalline Na_2O-Al_2O_3-SiO_2-H_2O (N-A-S-H), CaO-Al_2O_3-SiO_2-H_2O (C-A-S-H), and CaO,Na_2O-Al_2O_3-SiO_2-H_2O (C,N-A-S-H) hydrates appeared at 990 and 902 cm^{-1} [80,112,131], and the Si-O stretching ($V_{s\ Si-O}$) and Si-O bending (δ_{O-Si-O}) modes in quartz at 738 and 675 cm^{-1}, respectively with a possible quartz contribution to the band at 1068 cm^{-1} ($V_{s\ Si-O}$)[111]. The N-A-S-H, C-A-S-H, and C,N-A-S-H phases were assembled by the interactions between Na^+ and Ca^{2+} released by SMS activator and CAC, and the aluminosilicate anhydrous compounds in FAF[71]. The rest of the aluminum from CAC appeared in bohmite. The carbonates formed with the carbonate ion from the curing environment. Additional amorphous and crystalline silica showing prominent bands were derived from alkaline degradation of FAF and alkali carbonate environment as well as from the dissolution of SMS.

Comparison of absorbance peak heights of the bands representative of carbonate, silica gel, bohmite, N-A-S-H, C-A-S-H, and C,N-A-S-H reaction products, and quartz for core and the inner crack surface areas of control and TA-modified samples in carbonate environment led to the identification of potential sealing and plugging reaction products. The cracks in TA-modified cement were plugged by carbonate-, silica-, N-A-S-H-, C-A-S-H-, and C,N-A-S-H-related products; in fact, the height of band peaks belonging to all these reaction products strikingly increased in the samples from crack surfaces, compared with the cores. In contrast, the bohmite-related peak height was reduced in the crack areas, so underscoring that the bohmite did not contribute significantly to the sealing of the cracks. This finding strongly supported the results from XRD study and is in agreement with the DTG analyses showing higher zeolite- and amorphous phases-related decomposition peaks for TA-modified samples. It is possible to rationalize that the principal reaction products have the highest peaks. Thus, the N-A-S-H-, C-A-S-H-, and C,N-A-S-H-related products are the major contributors to crack's plugging. If this interpretation is valid, the secondary contributor was quartz, while the carbonates and silica gel role was minor. Unlike TA-modified cement, control cement was not as effective in plugging the cracks. In fact, the heights of the peaks were similar for the core and crack areas for all identified components. Accordingly, it appeared that TA served in the creation of the crack-plugging reaction products in alkali carbonate environment. Relating these findings to XRD data, the crystalline reaction products involved analcime and paragonite, in N-A-S-H system, cancrinite as carbonated-C,N-A-S-H, and dmisteinbergite in C-A-S system. In addition, tobermorite (or possibly aluminum-containing tobermorite) formed in the carbonate environment, contributing to the C-A-S-H peak.

The overall appearance of the spectral features of the samples cured at 270 °C in water environment for total of 15 days was similar to that of the samples cured in carbonate (Figure 113). Similar to the carbonate environment for TA-modified samples, the heights of the peaks of N-A-S-H-, C-A-S-H-, and C,N-A-S-H-related products, silica gel and quartz were higher in the crack areas than in the core samples.

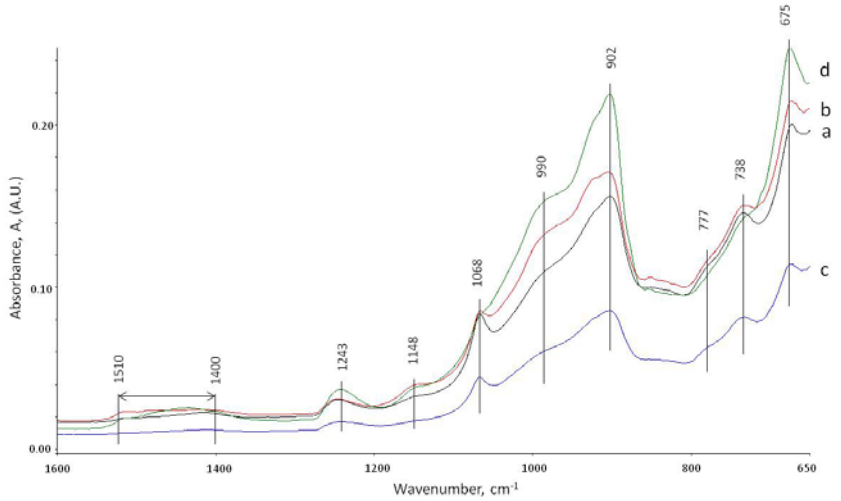

Figure 112. ATR-FTIR spectra of the: core (**a**); and crack (**b**) areas for control cements; and the: core (**c**); and crack (**d**) areas for TA-modified cements in alkali carbonate environment at 270 °C.

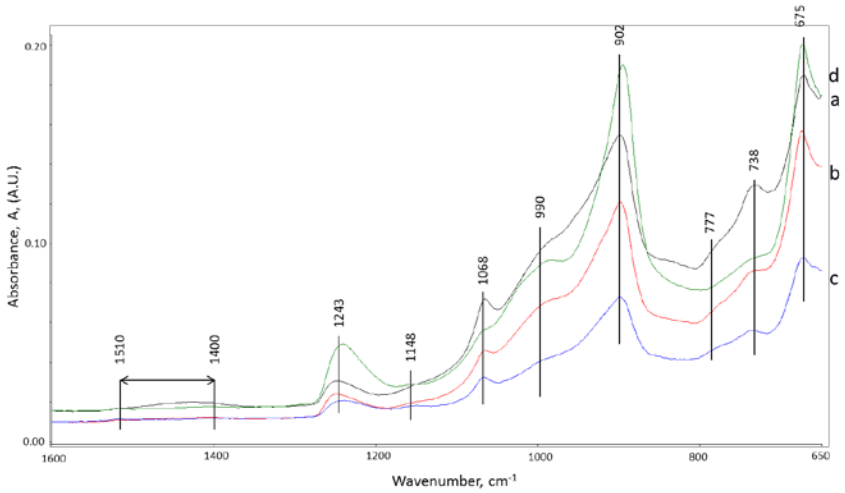

Figure 113. ATR-FTIR spectra of the: core (**a**); and crack (**b**) areas for control cements; and the: core (**c**); and crack (**d**) areas for TA-modified cements in water environment at 270 °C.

Thus, there was no doubt that although the water environment differed from alkali carbonate, TA favorably promoted the formation of these reaction products in crack areas. However, despite this fact, the recovery rate of strength in water was lower than that in the carbonate, suggesting that the formation of carbonate compounds may be required to achieve a better strength recovery.

The crack-plugging effects by the reaction products formed in TA-retarded cement exposed to alkali carbonation environment appeared to play a pivotal role in enhancing the recovery rate of compressive strength for the repeatedly crushed cements.

3.9.1.6. Microstructural Characterization

To observe the morphological features and support the XRD findings, the SEM-EDX studies were conducted on freshly fractured samples. The samples of crack surfaces and the undelaying areas were examined after the total of 15 days of healing in water or alkaline carbonate at 270 °C (Figures 114 and 115, and Table 26 for point compositions).

Morphological features of control and TA-modified samples were generally similar with the major difference being a lower crystallinity of TA-modified samples compared against control ones. The samples' surfaces were composed of agglomerates, likely precipitated from the interstitial solution [132] (Figure 114 and 82 left, points 1 and 4). The silicon-surface content was clearly higher compared against that of the core for all the samples in agreement with EDX and FTIR measurements. With increasing distance from the surface, analcime cubic crystals were visible under the precipitated surface agglomerates in control samples (Figure 114 left, point 2). The cores of these samples included areas with elevated calcium typical for feldspar minerals (Figure 114 right, point 3) confirming the XRD data.

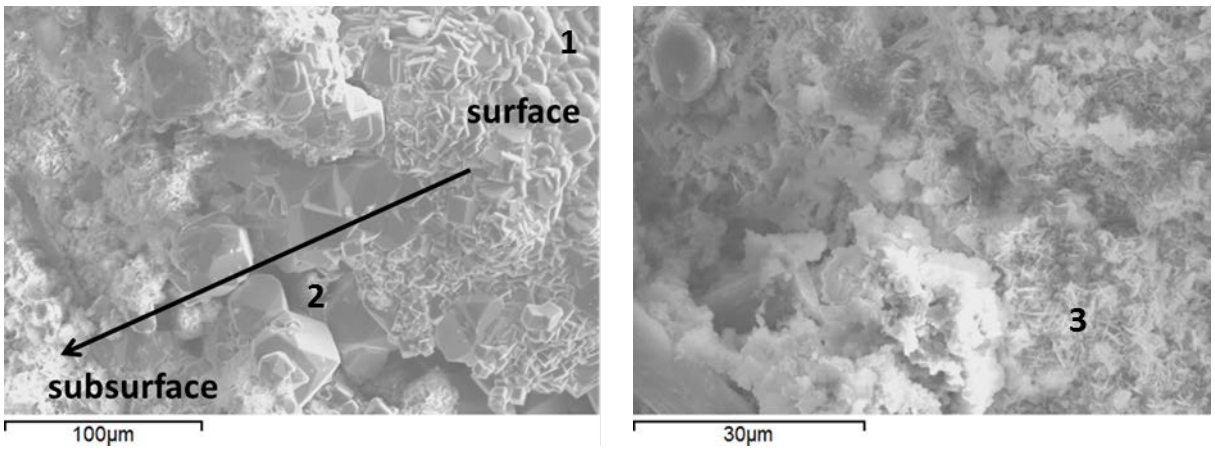

Figure 114. Scanning electron micrographs and point EDX data of typical cement microstructures for control specimens cured in: water (**left**); or alkaline carbonate (**right**) at 270 °C.

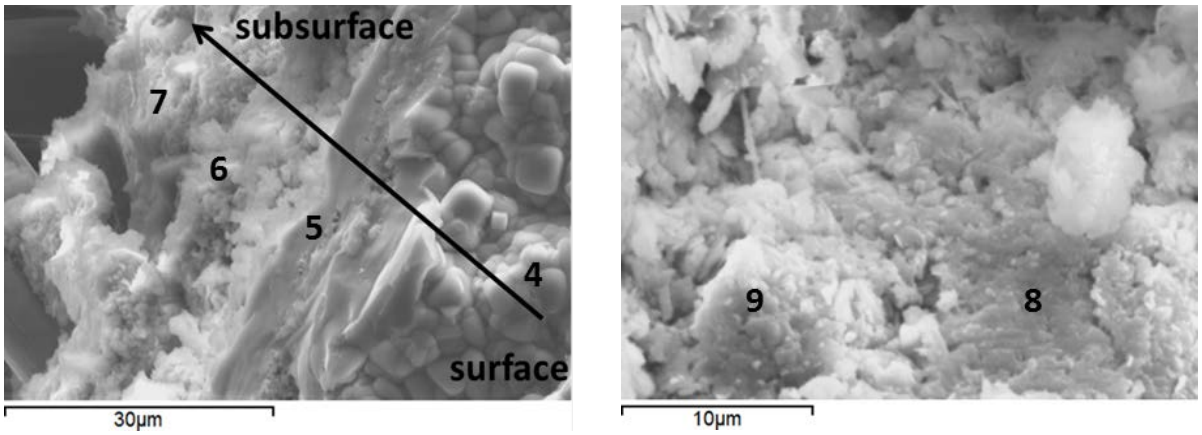

Figure 115. Scanning electron micrographs and point EDX data of typical cement microstructures for TA-modified specimens cured in alkali carbonate at 270 °C.

For TA-modified samples, the subsurface hydrates were more amorphous with growing aluminum content further from the surface (Figure 115 left, points 5–7). The amorphous cores of TA-modified samples showed calcium included into the gel composition (Figure 115 right, point 8), which agrees with the lower calcium content of the crystalline hydrates in these specimens suggested by the XRD study. Some units with zeolite-type composition forming on FAF particles were identified in the cores of these samples (Figure 115 right; point 9).

Table 26. Point compositions of typical cement microstructures shown in Figure 81.

Sample	Point	Al	Ca	K	Na	Si	Possible phase
Water-Control	1	5.89	0.33	1.85	1.28	26.65	Si-rich gel
	2	9.61	0.53	0.16	4.68	22.55	Analcime
Carbonate-Control	3	24.86	4.11	0.23	1.3	9.12	Al-rich gel, dmisteinbergite precursor
Carbonate-TA	4	6.15	0.14	1.17	3.71	25.68	Si-rich gel
	5	10.93	1.62	0.1	6.0	20.09	Si-rich gel
	6	13.38	3.6	0.25	4.14	17.58	Si-Al-rich gel
	7	23.23	3.13	0.78	1.19	9.51	Ca(Na)-Al-Si gel
	8	20.75	5.97	0.21	1.58	11.16	Ca(Na)-Al-Si gel
	9 [1]	10.11	1.53	0.24	14.93	7.20	Carbonated zeolite or cancrinite precursor

[1] – 9% carbon in composition.

3.9.1.7. Discussion

A previous work demonstrated that TA alters cement phase compositions, improves compressive strength development and increases the number of pores below 500 microns after three days of curing at temperatures up to 300 °C[113]. The present study confirms that some differences in TA-modified cements remain after longer curing times of 15 days at 270 °C. Specifically, the compressive strength of the retarded samples remains higher compared against control, the predominant crystalline phases have lower calcium content (analcime and margarite vs. dmisteinbergite) and the general crystallinity of modified samples remains lower.

The retarder also changes self-healing properties of the cement that undergoes compressive damage with the crack formation. It affects both crack-plugging ability and strength regaining properties, which are superior for the retarded slurries.

High temperature hydration of TSRC results in calcium-aluminum silicates, zeolite-family crystalline products and (C,N)-A-S-H amorphous phase [47,70]. The crystalline calcium-aluminum-silicate hydrates include hydrogrossular phases at earlier hydration times (katoite, grossular, and hibschite) and feldspar (dmisteinbergite and anorthite) or feldspathoid (cancrinite in carbonate-rich environment) type minerals after longer curing at temperature above about 250 °C. Tartaric acid that acts as a set retarder for TSRC slurries changes the early-time phase composition favoring fewer calcium- and aluminum- rich phases such as feldspar minerals, bohmite and more high-temperature stable zeolites in the set cement [113]. Calcium and aluminum interactions with tartaric acid in the first minutes of hydration decrease their availability for crystals formation [47]. These cations eventually are included into amorphous (C,N)-A-S-H gel, which even at 270 °C is among the major phases of hydrated TSRC [133]. Kinetics of gel crystallization into zeolites are generally very slow; in time zeolites such as thomsonite and especially high-temperature stable analcime crystalize from the gel phase.
If this hypothesis is correct, the first-minute interactions in slurries are critically important for the phase composition of the set cement. Thus, cation-binding molecules such as tartaric acid effectively remove certain cations from the early developing crystals and transport them into the amorphous phase that forms later. In addition to tartaric acid any other cation-binding molecules from the environment may affect the solid phase composition of the hydrating blend. Carboxylic acid anions in CO_2-rich environments may effectively bind calcium ions and, similar to tartaric acid, interfere with crystallization of calcium-containing feldspar minerals promoting formation of feldspathoids in their place [113]. Silicon from fly ash and sodium meta-silicate activator precipitates as silicon-rich gel with calcium, sodium and aluminum ions reserved through earlier interactions with TA. Carbonate environment especially favors silica precipitation lowering its solubility or assisting in its release from calcium-aluminum silicate phases through calcium dissolution by formation of soluble calcium bicarbonates. Inclusion of calcium and aluminum cations changes the structure and stability of this silicon-rich amorphous phase. At longer curing periods zeolites crystallize from the silica-aluminum-rich amorphous gel or precipitate from the solution.

There is a general agreement between the experimental results. XRD, ATR-FTIR and DTG show larger zeolites and limited bohmite presence in cements modified with tartaric acid. ATR-FTIR data also indicate higher abundance of (C,N)-A-S-H type products in these samples. XRD data suggest restricted crystallization of calcium-rich phases in modified samples. SEM morphological measurements confirm lower crystallinity with fewer calcium-rich feldspar type crystals in the presence of TA. Finally, EDX results clearly point out silicon enrichment at the surface of both control and TA-modified samples especially in the crack areas. Combining all these evidences the following strength recovery and sealing mechanism may be proposed. The binding phase providing matrix strength and fractures sealing is mostly amorphous of general (C,N)-A-S-H composition. Aluminum presence in the silicate gel increases the cross-linking in-between silicate chains [132]. In TA-modified samples, especially in carbonate environments, in addition to aluminum calcium joins the amorphous products. Both calcium and aluminum strengthen the silicate gel structure. Aluminum incorporation in the C-S-H gel was reported to

entail formation of 3D aluminum-silicate skeletons with partial healing effect in the C-A-S-H nanostructure potentially increasing durability and strength of the hydration product [134,135]. Aluminum was also reported to accelerate formation and stabilize tobermorite at temperatures that are normally above its stability domain [136]. The crystallization of tobermorite in carbonate environment in TA-modified samples is in agreement with this hypothesis. In fact, grossular presence in this sample suggested by XRD data also confirms this argument since at high aluminum content grossular crystalizes from C-A-S-H gels. At longer curing times zeolites crystallize from the amorphous phase.

In summary, TA favors formation of amorphous hydrates rich in silicon with calcium and aluminum inclusions strengthening the gel and crystallization of zeolites. In the case of a carbonate environment where calcium may additionally solubilize through formation of calcium bicarbonate and precipitate later with the silicate, eventual crystallization of tobermorite in the fractures takes place, contributing not only to the sealing but also helping to bind the broken cement pieces to the matrix.

3.9.2. MGF-modified TSRC

To enhance self-healing properties, the original TSRC formulation was modified with MGF. It was demonstrated that MGF was very susceptible to alkali dissolution in hot alkaline composite slurries, and then liberated the reactive ionic species to promote the formation of new healing reaction phases. Because of such a high reactivity of the MGFs, their effect on placement technology had to be evaluated.

Thus, we investigated the potential of MGF healing aid to further retard TSRC slurry set at 85 and 100°C. We also studied self-healing and re-adhering performances of TA-retarded TSRC/MGF composites at 300°C-1- and 10-day autoclave curing ages in plain water environment.

3.9.2.1. Micro-calorimetry and HPHT Consistometer studies

As described earlier, TA was identified as the most promising retarder for TSRC slurry. Furthermore, it was also demonstrated that effect of the retarder on the setting and thickening time of a slurry could be monitored by the release of the heat during cement hydration in isothermal calorimeter. However, although the general trend of setting time becoming longer or shorter was similar in standard API thickening time tests and calorimetric experiments, the time to the thickening was significantly shorter in API tests than time to the major heat release events in calorimetric measurements. The difference could be accounted for by the absence of shear and pressure in calorimetric tests. The API blending procedure adopted before the calorimetric tests allowed significant decrease in the difference between API thickening time test and calorimetric results. Nonetheless, calorimetric hand-mixed tests were adopted for initial evaluations of setting time and were followed by the tests with slurries prepared in Warring blender according to the API mixing procedure.

Several important factors were taken into consideration: 1) the time to the main heat release event; 2) the intensity and total time of the major heat release event to ensure sufficient hydration

in the presence of the retarder so that development of mechanical properties is not compromised; 3) the intensity of the initial heat release peak corresponding to early wetting and hydration reactions that could cause significant gelation of the slurry resulting in non-pumpable formulations; 4) total retarder concentration to minimize amount of the organic retarder added to the slurry so that when organics degrade at high static temperatures, the cement properties are not compromised by its degradation products (e.g. increased carbonation through CO_2 release); 5) predictable change of the setting time with the change of the retarder, so that the set could be controlled in function of the field conditions; and, 6) low sensitivity to variations in the slurry composition and well conditions (as a rule of thumb, at least +/- 10% variations in retarder content and temperature should be acceptable so that the placement is still safe). Other parameters that may affect retarders performance include schedule of temperature and pressure increase and pumping interruptions. The schedules will affect how fast different parts of the blended cements start reacting. This may be important for TSRC where slow reacting FAF, when activated retards CAC hydration. If the temperature increase is very slow, the activation of FAF may take longer times and counterintuitively the setting may be faster at lower temperatures. The pumping interruptions will affect the slurry consistency and further pumping if a strong gelation takes place during the static period. To verify whether that may be a problem "go/no-go" tests are conducted where consistometer is stopped for some periods of times during the thickening time tests. The consistency after each consistometer restart indicates whether stops during slurry placement may cause problems due to the slurry gelation. Because of the limited resources only few thickening time tests were conducted.

In addition to TA retarder, another experimental retarder (Ret.2) was tested for improved performance. The results of calorimetric tests are given in Table 27 and thickening time tests are shown for the original TSRC slurry for comparison. Examples of calorimetric curves are given in Figure 116 and the calorimetric setting time for TA-retarded TSRC slurries modified with MGF as a function of TA concentration is shown in Figure 117. OPC/SiO_2 high-temperature formulations heat release curve is given for comparison.

Table 27. TSRC calorimetric curves for MGF-modified formulations and thickening time (TT) results for formulations without fibers.

[TA], % bwob	**Hand mixed TSRC-MGF**		**TSRC, TT hrs**	**Warring mixed TSRC-MGF**	
	TA	**TA+Ret.2**		**TA**	**TA+Ret.2**
0.5	-	>24	1.75	-	2.7
0.6	-	-	-	3.31	-
0.8	-	>24	-	9.82	>24
1.0	>40	-	3.5	13.22	>24
1.5	>40	-	-	23.93	-
1.8	>40	-	5.6	-	-

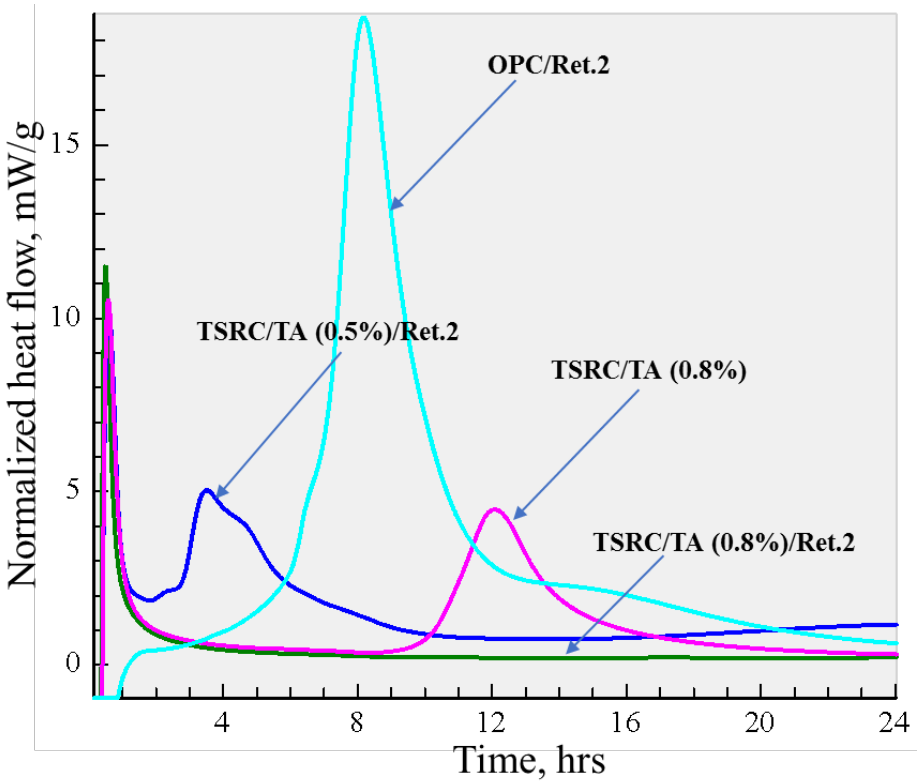

Figure 116. Examples of calorimetric curves for tested formulations.

There are some clear differences in calorimetric curves of TSRC and OPC-based slurries. Firstly, the major peak of heat flow for the OPC-based slurry is noticeably larger than for TSRC slurries. This agrees with the higher initial compressive strength of the OPC-based samples because of massif cement hydration in a limited time. Secondly, there is no any significant initial heat flow peak for this slurry; in fact, the normalized heat flow curve is flat until the cement hydration begins and heat is released in hydration reactions. On the other hand, the major heat flow peaks for the retarded TSRC slurries are smaller and arrive after the initial sharp peak. The difference in the intensity of the heat flow peaks is partly a result of different retarder concentrations (TSRC needs twice as much retarder as the OPC-based slurry for equivalent retardation) and from the fact that 40% of the slurry is slowly reacting FAF that contributed little to the heat flow at the time of the major peak. The first sharp heat flow peak is a result of strongly exothermic SMS dissolution. This fast SMS dissolution and its early reactions may cause gelation of the slurry impairing its pumpability. However, whether this is a problem needs to be evaluated by thickening time tests and rheological measurements while limiting intensity of the initial heat flow registered in calorimetric measurements only allows increasing probability of successful thickening time tests.

The data clearly confirm strong retarding effect of TA on TSRC blends including TSRC modified with MGF at 85^{o}C. They are also in agreement with earlier study showing much longer setting times for hand mixed slurries compared against those prepared in Warring blender

following API procedures (Table 27). Although the setting times in calorimetric measurements cannot be directly compared with the thickening times, the data suggest that setting may be slower in the presence of MGF. The setting time of TSRC-MGF slurry retarded with 1% TA was more than 13 hrs in calorimetric measurements after Warring mixing of the slurry, while for the slurry without MGF the thickening time was only 3.5 hrs. Although some time difference is coming from the differences in pressure, temperature increase schedules and shear during the thickening time tests, the difference in almost 10 hrs is too large to be explained solely by these factors. The MGF may slow down the set of the TSRC slurries due to the release of SMS from the surface of MGF or some other retarding species.

Addition of a second retarder (Ret.2) allows obtaining much longer setting times than those achieved with TA alone. The slurry retarded with 0.8% TA sets within 10 hrs, while addition of the second retarder extends the set beyond 24 hrs. The second retarder is effective alone for the OPC-based slurry (Figure 116); however, it was shown not to be effective for TSRC slurries. On the other hand, TA alone seems to provide sufficient retardation at the test temperature. It also increases the setting time in predictable manner; the setting time as a function of the retarder concentration curve is almost linear (Figure 117). Since the content of organic retarders in the slurries should be limited as much as possible to prevent set cement degradation at high temperatures because of the degradation of the organics, further testing using API thickening time tests were performed with TA alone by Oilfield Testing & Consulting Corporation.

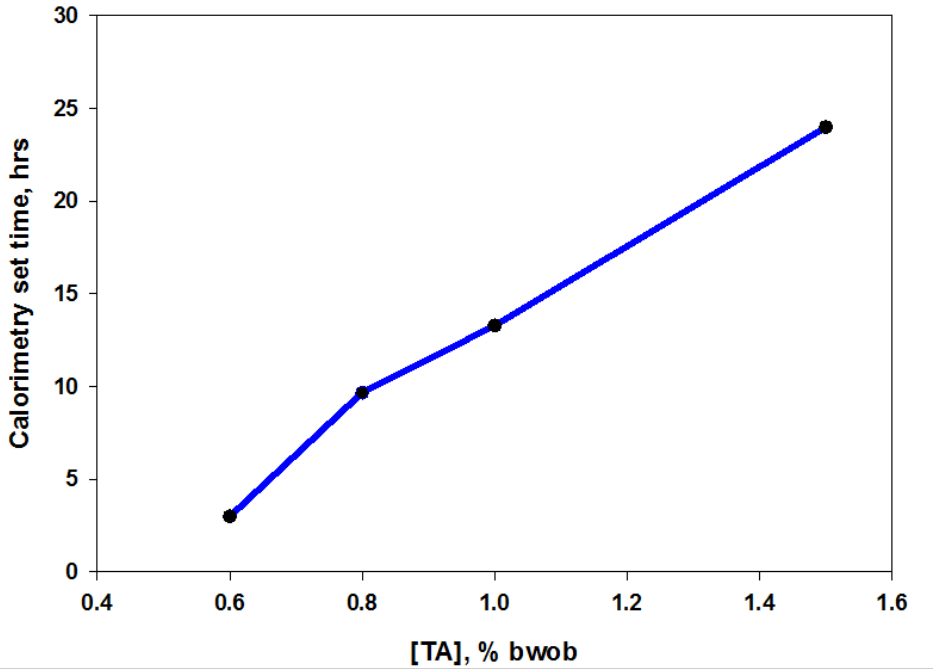

Figure 117. Calorimetry setting time for TSRC-MGF samples retarded with TA and mixed with Warring blender.

Thickening time curves of the TSRC-MGF slurry at two bottom-hole-circulating temperatures of 85 and 100°C are shown in Figure 118. The following important curve features should be noticed. The initial

consistency of the slurry after the mixing in both cases is around 30 Bc. This consistency reflects the effect of fast dissolving SMS, where gelation could be expected. In fact, the consistency of 30 Bc does not pose any pumping problems. Moreover, it is not too low suggesting that the slurry does not have any serious instability problems (e.g. particles precipitation). Predictably, as the temperature increases the consistency decreases. However, it does not drop below 6 Bc at 85°C and below 10 Bc at 100°C suggesting that the slurries stay stable in both tests. The consistency increase leading to the slurry set starts after about 6 hrs at 85°C and 5.5 hrs at 100°C. Then the consistency goes up in two steps with a shorter time to the set at 100°C. Thus, the two slurries set with the right angle set shape of the consistency curve. This does not indicate a delay in compressive strength development after the set since the slurry is sheared in the consistometer and the temperature is well below the static level of geothermal temperatures. The compressive strength development time would need to be further evaluated in API UCA tests.

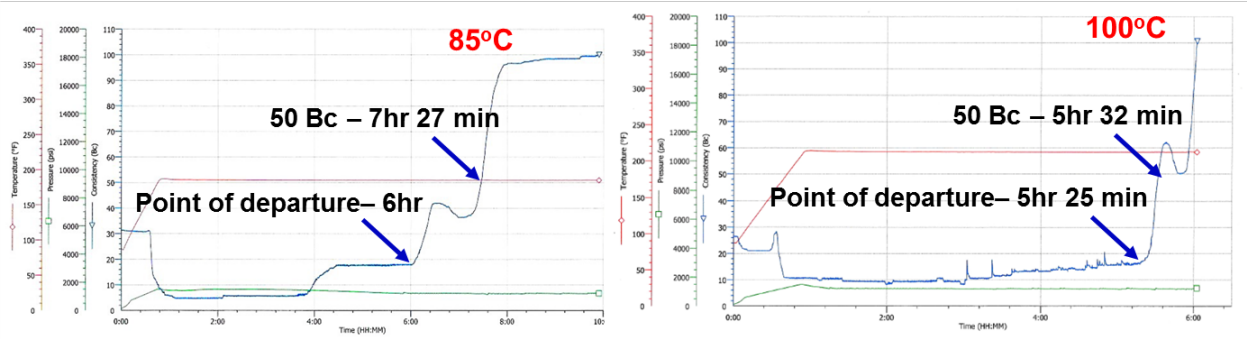

Figure 118. Thickening time tests for TSRC-MGF formulation retarded with 1% bwob TA at 85°C and 100°C.

As rule of a thumb, cement set is generally accelerated by a factor of 2 for each 10°C of temperature increase. This is not the case for the TSRC-MGF-TA blend. The 15°C-temperature increase decreased the thickening time only by a factor of 1.4. The lower sensitivity to temperature variations is very attractive especially for geothermal wells where exact temperatures are difficult to determine because of common lost circulation problems in weak underground formations.

Overall, TA confirmed its good performance with TSRC slurries modified with MGF. The retardation can be further enhanced with an additional retarder that effectively increased the setting time of TSRC-MGF slurries in calorimetric tests. Thickening time of more than 5 hours was achieved at 100°C bottom-hole-circulating temperature. The slurry sensitivity to temperature variations was lower than normally expected for OPC-based slurries. Only 2 thickening time tests were performed. Further study would require evaluation of pressure and retarder content effects on thickening time, as well as, to confirm timely compressive strength development in retarded slurries.

3.9.2.2. Compressive strength and its recovery

Figure 119 encompasses the compressive strength of TA-retarded and -free TSRC/MGF composites before and after the self-healing treatment in 300°C- plain water for 5 days and the

strength recovery after the healing treatment. For 1-day-aged composites, the incorporation of TA into TSRC/MGF resulted in a somewhat lower compressive strength compared with that of without TA. However, when autoclaving period was extended to 10 days, the combination of TA and MGF revealed an excellent strength development of 3250 psi which was equivalent to nearly 44% higher than that of the composite without TA. This fact may be due to a hindering effect of TA on the alkali dissolution of MGF because of preferential reactions of TA with Ca and Na hydroxides to form tartrate complexes in a short curing period of only 1 day. The 10-day curing may result in decomposition of TA complexes, thereby liberating free Ca and Na ionic species from decomposed tartrates as well as increasing alkalinity of composites. So, if this interpretation is right, the enhanced alkali dissolution and reactivity of MGF might be responsible for strengthening the composite after longer curing periods. Hence, it is possible to assume that 5-day self-healing treatment also assists in enhancing the decomposition of TA complexes, leading to the increased dissolution and reactivity of MGF. In fact, both TA-retarded composites of 1-and 10-day age after self-healing treatment exhibited increased compressive strength compared with that of before the treatment. Interestingly, the compressive strength of 10-day-aged TA-free composite after healing treatment was nearly 18% lower than the original strength.

Nevertheless, the recovery rate of compressive strength for both TA-retarded composites at 1- and 10-day ages was more than 110%. In contrast, this recovery rate of TA-free composite at 10-day age was only 82%, suggesting that TA conferred the improved strength recovery on TSRC/MGF composites after short curing times.

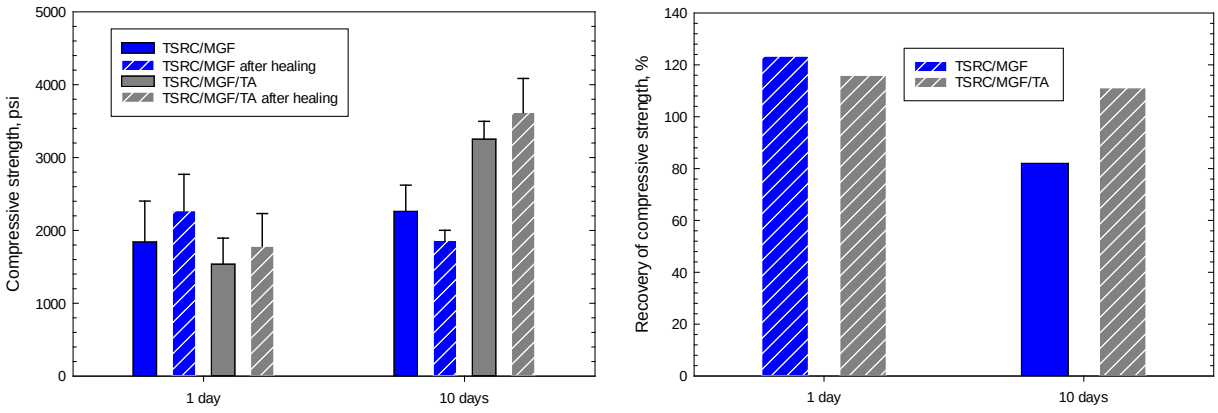

Figure 119. Compressive strength of TA-retarded and non-retarded TSRC/MGF composites at 1- and 10-day autoclaving ages and strength recovery of 1st cracked composites after 300°C-5-day self-healing treatment in plain water.

3.9.2.3. Sheath-shear bond strength and its recovery

Figure 120 gives the sheath-shear bond strength of unconfined TA-retarded and non-retarded TSRC/MGF composite sheath surrounding CS tube made by autoclaving for 1 day at 300°C before (control) and after re-adhering treatment in 300°C- plain water for 5 days as well as the

recovery rate of the bond strength for re-adhered composites. As can be seen, both the 1-day-autoclaved TA-retarded and non-retarded composites developed high sheath-shear bond strength of nearly 200 psi, causing the initiation and propagation of multi-radial cracks in sheath from central CS tube during the debonding test of cement sheath from the CS tube. Further excessive bond strength of 220 and 250 psi for non-retarded and retarded composites, respectively, was developed after prolonged curing period of 10 days. As expected, the numerous wide cracks developed by such very high bond strength were difficult to seal sufficiently in a short-term re-adhering treatment of 5 days. In fact, the recovery rate of bond strength was as low as 35 and 24 % for non-retarded and retarded composites.
As a result, for a better re-adherence of the composites with very high sheath bond strength the toughness of the interfacial bond must be improved by advanced reinforced composite technology that would lead to a minimum number of thin cracks.

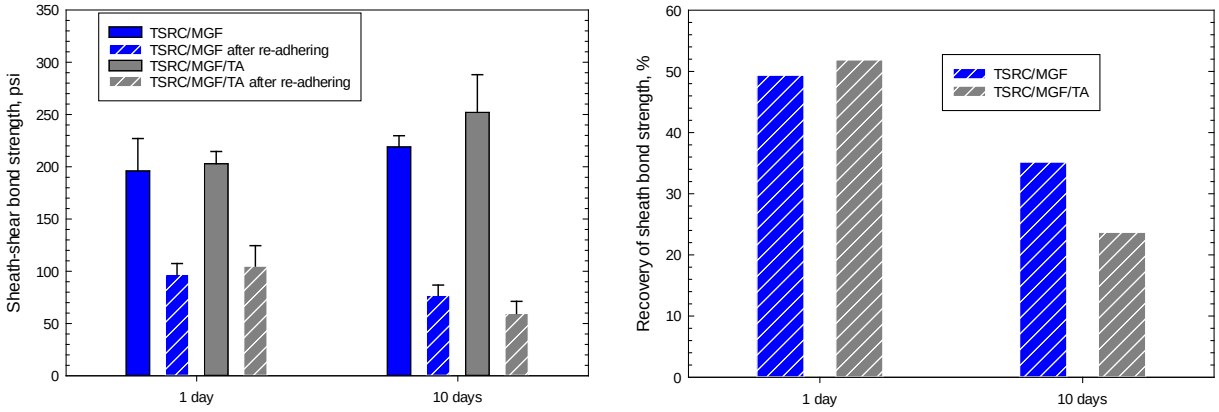

Figure 120. Shear bond strength of TA retarded and non-retarded TSRC/MGF composite sheath surrounding CS tube before and after 300°C re-adhering treatment for 5 days, as well as, recovery rate of shear bond strength.

3.9.2.4. Corrosion mitigation of CS by composite adhering to CS

The lap-shear bond strength at CS plate/composite adhesive/CS plate joints (Figure 121) closely resembled that of sheath-shear bond strength; namely, the lap-shear bond strength of nearly 200 psi was obtained from the both 1-day-aged TA-retarded and non-retarded adhesives, while very high shear bond strength >250 psi was determined for 10-day-aged TA-retarded adhesive. The thickness of adhesive layer that remained on CS after the debonding was 0.12 and 0.23 mm for 1- and 10-day-aged non-retarded adhesives, respectively, and 0.21 and 0.28 mm for 1- and 10-day-aged TA-retarded adhesives, demonstrating that TA-modified cement provided a better coverage of CS compared with that of TA-free one.

After re-adhering treatment, for the adhesives at 1-day-curing age, the thickness of adhesive layer covering CS surfaces increased by 2.3- and 1.4-fold to 0.28 mm for non-retarded adhesive and to 0.30 mm for retarded one, clearly verifying that both non-retarded and retarded adhesives re-adhered after the 5 days at 300°C. For the 10-day-aged adhesives, no pronounced increase in thickness was found for both retarded and non-retarded composites.

As for the corrosion protection of CS by these adhesive layers covering CS surfaces, three findings can be described: 1) there was no significant difference in protection between retarded and non-retarded adhesives; 2) the re-adhered adhesive layers displayed a better protection of CS than the original ones; and, 3) re-adhered 10-day-age adhesives provided the lowest corrosion rate of 0.12 mm/year for both retarded and non-retarded composites, corresponding to 33% reduction of corrosion rate compared with that of before the re-adhering treatment. Consequently, although TA offered the improved bond strength to CS, it did not affect corrosion rate of CS protected by TSRC.

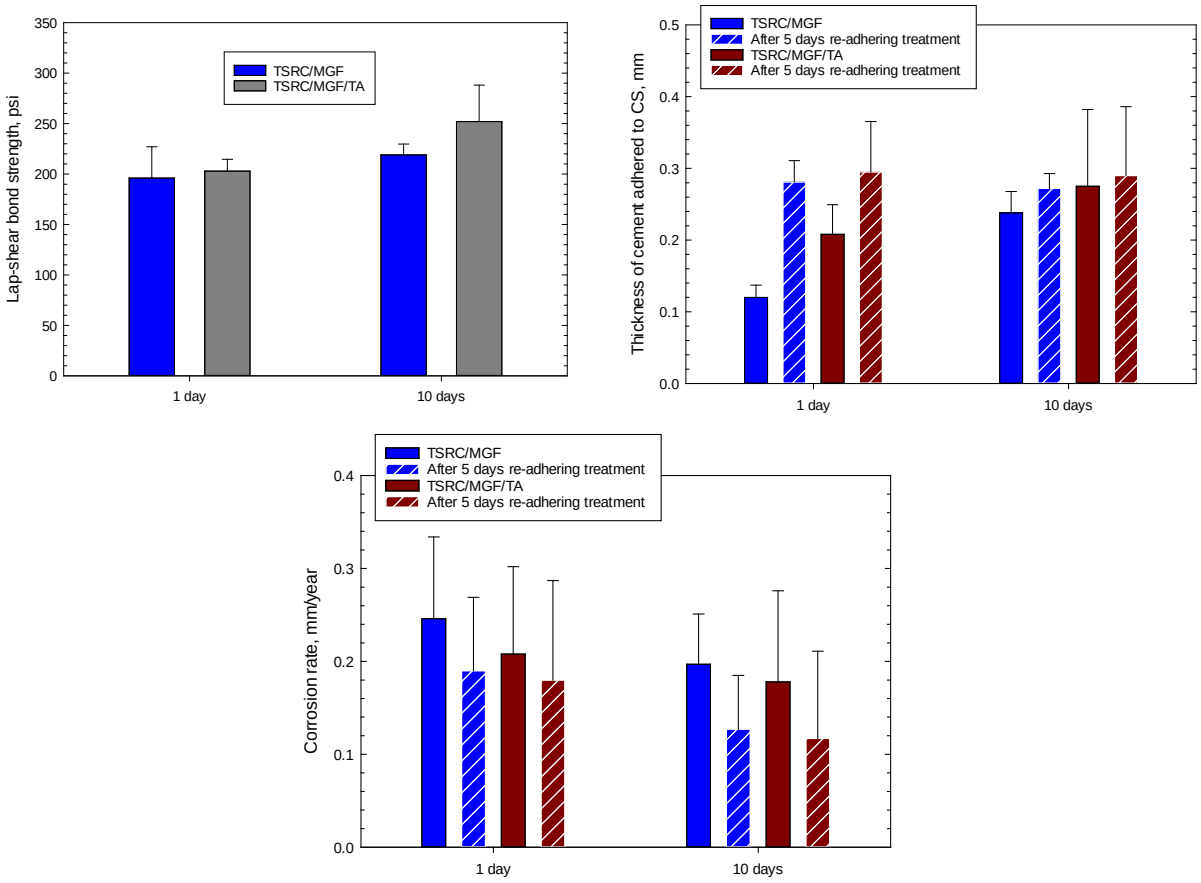

Figure 121. Lap-shear bond strength, thickness of adhesive layers covering CS surface, and corrosion protection of CS by adhesive layers before and after re-adhering treatment.

4. Conclusions

To achieve the project goals the work was divided into eleven major tasks: 1) evaluating the self-healing performance of composite systems in different environments; 2) screening the candidates for alternative self-healing composites; 3) exploring re-self-healing ability of repeatedly cracked candidate composites: 4) studying self-healing mechanisms of candidate composites; 5) evaluating pozzolan additives as self-healing aides for further improvement of the healing

ability; 6) examining self-healing and crack sealing abilities of 30-day-long autoclaved MGF-modified TSRC in plain water and obtaining fundamental understanding of these abilities; 7) assessing the re-adhering performance of debonded candidate composites to carbon steel (CS) casing and granite rock formation; 8) surveying re-adhering properties of 30-day-long autoclaved composites; 9) investigating the bond durability in acid and thermal shock environments; 10) inspecting the ability of adhered and re-adhered composites to protect CS against brine-caused corrosion for short- and long-term cured composites; and, 11) validating placement technology of optimized cement composite as well as evaluating set control and self-healing properties of retarded cements.

Task 1. Evaluating self-healing performance of composite systems in different environments

Among all the tested composites including OPC/SiO_2, TSRC, CAP-A (with Secar #51), CAP-B (with calcium-aluminate cement Fondu), FAC/FAF, and GBFS/SiO_2, the GBFS/SiO_2 system exhibited a very brittle nature in all three environments, plain water, carbonate, and brine, while FAC/FAF system showed a brittle nature in two environments, plain water and carbonate. YM values of all the other composite systems were in the region of moderate brittleness as *YM criteria <400 x 10^3 psi*, which was the ideal facture mode of formation and propagation of slim cracks in all environments. In contrast, larger cracks formed in the FAC/FAF system with brittle nature. Compared with these fracture modes, the GBFS/SiO_2 system, possessing a very brittle nature, disclosed an undesirable fracture mode of fragmental breakages.

The compressive strength of all composite systems made with 300°C-1-day autoclaving met the *material criterion >1000 psi* in plain water, carbonate, and geo-brine. The ranking of compressive strength developed in plain water was in the following order: GBFS/SiO_2 (7058 psi) > FAC/FAF (4448 psi) > OPC/SiO_2 (3130 psi) > CAP-A (2917 psi) > CAP-B (2728 psi) > TSRC (1743 psi). After self-healing treatment of 1st-time cracked composites for 5 days in these same environments, although the recovery rate of compressive strength depended on the environments, TSRC revealed the highest average recovery rate of 94 %. Furthermore, among these composites, only TSRC met the material criterion described as the *recovery rate >80%*. A secondary high recovery rate of 66% was obtained for CAP-A. The average recovery rates of OPC/SiO_2, CAP-B, FAC/FAF, and GBFS/SiO_2 were 55, 62, 47, and 60 %, respectively.

Regarding the capacity of acid resistance in pH 0.2 H_2SO_4 at 90^{o}C, there were two different types of acid degradation: One was acid-scale corrosion type involving OPC/SiO_2 and GBFS/SiO_2; the other was acid-erosion type of TSRC, CAPs, and FAC/FAF. The scale corrosion type caused severe expansion failure of composites after 14 days acid exposure, resulting in no recovery of compressive strength. On the other hand, the erosion-type composites were capable of recovering the compressive strength. In fact, after 14 days of acid immersion of 1st-time cracked TSRC, CAP-B, and FAC/FAF, the recovery rates of their strength were 39, 41, and 48%, respectively. There were two approaches to evaluating the thermal shock resistance: One was minimum reduction rate of compressive strength after 5-cycle thermal shock testing (one cycle; 350°C-24-hr-heating of cement-carbon steel sheath samples and quenching in 25°C water); the other was the recovery rate of compressive strength for 2nd-time-cracked composites of the post-thermal shock test after 5-day healing treatment in plain water, carbonate, or brine at 300°C. TSRC displayed the best thermal shock resistance responsible for the lowest strength reduction rate of 21%, while the strength reduction rates of all other composites ranged from 33

to 40%. Furthermore, TSRC had the highest average compressive strength recovery rate (131%) after the 5-day healing exposure in these three environments.

Task 2. Screening the candidates for alternative self-healing composites

All test results described in task 1 were summarized below and evaluated as to whether composites met material criteria. Consequently, the candidates for self-healing were ranked in the following order: TSRC > CAP-B> GBFS/SiO_2 and FAC/FAF >OPC/SiO_2.

	Thermal and hydrothermal stability >300°C	Compressive strength >1000 psi	Young's modulus <400 x 10^3 psi	Flexure toughness >0.006 $MN/m^{3/2}$	*Average strength recovery >80%	Average strength recovery >80% after thermal shock	Strength recovery in pH 0.5 acid at 90°C
OPC/SiO_2	Yes	Yes	Yes	Yes	C	A^+	Failed
TSRC	Yes	Yes	Yes	Yes	A	A^{++}	C
CAP-A	Yes	Yes	Yes	Yes	B	**N/A	N/A
CAP-B	Yes	Yes	Yes	Yes	B	A^+	C
FAC/FAF	Yes	Yes	No	Yes	C	A	C
GBFS/SiO_2	Yes	Yes	No	Yes	B	A^+	Failed

* A^{++} >120%, A^+ 199-100%, A >99-80%, B 79-60%, and C<60%, **Untested

Task 3. Exploring re-self-healing ability of repeatedly cracked samples

In this work, TSRC as the best candidate for self-healing composite was used, and for comparison purpose, OPC/SiO_2 was employed as the reference composite. TSRC exhibited an excellent recovery >85% for all 2nd and 3rd time cracked composites cured for 1 or 5 days before the first damage, except for 3rd-time cracked composite aged for 10-days before the damage, where the recovery was 78%. The averaged recovery of re-self-healed 3rd-time cracked TSRC cured for 1-, 5-, and 10-days before the first damage was 87%, which was 50% higher than that of OPC/SiO_2. Compared with a plain water environment, for both OPC/SiO_2 and TSRC composites carbonation obviously assisted in promoting the re-self-healing. The visual image revealed the disappearance of smaller cracks as well as partial of bigger (≥0.5 mm) cracks in carbonate environment, clearly verifying that carbonation served as the autogenous-healing processing for both composites.

Task 4. Studying self-healing mechanisms

There are two major factors contributing to strength recovery after healing treatment at 270°-300°C: One is the adequate sealing and plugging crack spacing by reaction and precipitation products; the other is formation of crystalline and amorphous reaction products and their phase transitions in composite matrix during the treatment period. In this task, two candidate composites, TSRC and CAP-B (with calcium-aluminate cement Fondu), were studied, while OPC/SiO_2 composite was used as reference.

TSRC composites

The moderately brittle nature of 270-300°C-1-day cured TSRC, further improved by the incorporation of micro-carbon fibers, allowed formation of controlled-size cracks, thereby

preventing the formation of wide as well as deep fractures. The size of a typical crack was 0.1 – 0.3 mm in width and 0.3– 0.1 mm in depth. The rate of the sealing depended on the crack size and the hydrothermal environment. The fastest sealing occurred in alkali carbonate and the slowest was in geothermal brine. The sealing process in 300^{o}C plain water environment proceeded at an intermediate rate. In this environment, the crack size gradually decreased during continuous curing as self-healing treatment and crack of ~ 0.25 mm width and 0.7 mm depth was completely sealed with new reaction products in 10 days. Thus, TSRC displayed an excellent sealing effect of cracks in plain water and carbonate, but not brine.

The major crystalline phases that contributed to self-healing in water and carbonate included dmisteinbergite (anorthite) as feldspar mineral; aluminum oxide hydroxide, boehmite, analcime as zeolite mineral, silica, and carbonated calcium-aluminum-silicate, cancrinite, as feldspathoid mineral. Also, hydrogrossular as garnet mineral was present in carbonate environment. Among these detected minerals, feldspar and hydrogrossular were responsible for strengthening the matrix in TSRC composite, while analcime and silica crystalline phases formed in the pore solution preferentially precipitated in cracks, leading to the sealing effect. Carbonated product, cancrinite and aluminum oxide hydroxide, boehmite, detected both in the matrix and at the surface, likely contributed to both strengthening and sealing processes.

In contrast, the brine-healed composites differed from water- and carbonate-healed ones. The major differences were the absence of analcime, boehmite as major phases and silica as minor phase. The lack of silica and analcime precipitation resulted in poor fracture-sealing in brine. The brine chemistry led to the formation of magnesium-containing minerals such as akermanite, magnesioferrite, majorite and tetramajorite. These minerals assisted in strength recovery of samples in brine but did not help sealing the cracks.

When healing treatment time was extended from 5 days to 20 days, the carbonate-cured composites were characterized by the phase compositions consisting of silica, cancrinite, and albite as the major crystalline compounds and boehmite as a minor one, while the quantity of dmisteinbergite phase was considerable reduced. On the other hand, analcime phase precipitated in cracks transformed into cancrinite phase. Boehmite content increased both in matrix and cracks.

Furthermore, alkali carbonate reacted with both the non-reacted blend components and the reaction products that contain calcium to form calcium carbonate which eventually changes into soluble bicarbonate, $Ca(HCO_3)_2$, after longer carbonate exposure. In this process, the sodium, aluminum hydroxide and silicic acid ions are released into the pore solution or cracks. These released reactive ionic species lead to the formation and precipitation of large analcime crystals, silica and boehmite contributing to crack sealing. Later, analcime crystals present at the surface sites undergo a phase transformation by carbonate attack into cancrinite. Also, the feldspar suffers from carbonation-caused decalcification, following by the conversion of the Ca- feldspar into albite calcian as intermediate phase. A further Na-based alkali carbonation of albite calcian results in the formation of albite (possibly sanadine), $Na(AlSi_3O_8)$.

As more FAF decomposed in plain water and carbonate, reactive silicon and aluminum contents further increased in pore solution. In fact, new boehmite and tohdite phases derived from aluminum hydroxide coexisting with crystalline silica not only formed in the matrix, but also participated in cracks sealing.

CAP-B (cement Fondu-based) composites

Like for TSRC, the strength recovery of CAP was due to two principal factors, 1) cracks' sealing effect and 2) strength improvement by progressive hydration during the healing period. For the former factor, 1.24 mm deep and 0.31 - 0.37 mm wide crack generated in CAP-B reduced 2.5-fold to 0.5 mm by sealing reaction products. Among the sealing reaction/precipitation products, zeolite analcime was the major phase, and dmisteinbergite, boehmite, Ca-substituted analcime and amorphous (CaO, Na_2O)-Al_2O_3 –SiO_2-H_2O phases were minor ones. The formation of zeolite analcime as major sealing product was like that of TSRC. The microstructure developed in sealed cracks was formed by dense cubic crystals of analcime derived from FAF reactions contributing to autonomic healing. Three major crystalline phases, hydroxyapatite, carbonatious Na-hydroxyapatite, and analcime, were responsible for the initial strength development of the CAP-B composite matrix after the first 24hrs of curing at 300^{o}C. After the self-healing of damaged composites, the principal contributor to strength recovery of CAP-B was a well-formed hydroxyapatite, which was characterized by dense microstructure of plate-like crystals. Analcime, on the other hand, was identified as the major sealing product but not a strength-recovery one, underscoring that the products promoting the sealing of cracks differed from those assisting in strength recovery of cement matrix.

Task 5. Evaluating pozzolan additives as self-healing aides for further improvement of healing ability

In this task, two natural pozzolans, clays and zeolites, and one artificial pozzolan as micro-E type glass (MGF), were evaluated as self-healing enhancing additives for TSRC composite system. As a result, all clays including bentonite, montomorillonite, and metakoline, employed in this work did not offer any significant strength recovery for repeatedly 2nd and 3rd times cracked TSRC samples, seemingly suggesting a poor chemical affinity of these clays with TSRC.

Two types of zeolite mineral family, Clinoptilolite (Clin.) and Ferrierite (FER), were used to evaluate their ability to promote self-healing of various cementitious composites. These zeolites containing plenty of pozzolanic siliceous or siliceous-aluminous reactants are susceptible to dissolution in alkaline environment. Since the slurries of all composites, except CAPs, used in this screening tests, have pH >13, (pH of CAP slurry ranged from 8.5 to 9.5), it is possible to assume that zeolites dissolve in these alkali slurries.

Using Clinoptilolite (Clin.), two specific changes in physical and mechanical behaviors were observed in the presence of Clin: One was an increase in water/cement ratio demand of composite slurry; the other correlated with the former change was a reduction of initial YM and compressive strength. The reduced YM resulted in the mechanical transitions from moderate brittleness to soft nature for TSRC and CAP-B, and the brittle → moderate for FAC/FAF, as well as very brittle → brittle for GBFS/SiO_2. Such transitions restrained both crack-width and -propagation, thereby improving self-healing effect for cracked composites. Thus, the strength recovery was not only due to the crack-sealing and -plugging performance by Clin pozzolan as autonomy-type healing, but also involved the progressive hydrations and reactions of non-hydrated and non-reacted cement-forming ingredients present in composite bodies as autogenic-type healing during self-healing treatment period of 5 days in 300°C plain water.

With Ferrierite (FER), OPC Type I/II clinker/natural zeolite, ferrierite/silica or silica-free blends under the trade name "FlexCem®," from Trabits group were tested for compressive strength recoveries and fracture sealing under hydrothermal conditions at 270^{o}C in alkali carbonate or plain water environments after imposed mechanical damage. The following general conclusions were drawn from the study: Compressive strength recoveries were outstanding (above 100%) for repeatedly damaged silica-modified samples healed in alkali carbonate and for unmodified samples healed in water at 270^{o}C for 10 days. The strength recoveries of the unmodified samples in carbonate were comparable to OPC/silica blends and those of the silica-modified samples were more than 100% after the first damage and less than 60% for the second one. The recovery decrease was due to the increased sample brittleness after the first healing period, resulting in the formation of long wide cracks in second damage that were difficult to repair. The 2.5 mm cracks were closed after 10 days in carbonate for the silica-modified samples and partially closed for the unmodified ones. On the other hand, the sealing was insignificant for the samples healed in water. The recoveries of compressive strength were the result of continuous clinker hydration and fast high-temperature alkali decomposition and interactions of ferrierite. The crystalline structure of ferrierite was lost after the first 24 hours of 270^{o}C exposure both in carbonate and water. The decomposed zeolite released silicon, magnesium, aluminum and iron that participated in the creation of new phases, allowing the strength and fracture to recover and seal. Formation of mixed calcium-aluminate and calcium-magnesium silicates suggested that decomposition and reactions of the zeolite and hydration of the clinker phases were concurrent. The new crystalline phases responsible for strength recoveries included various magnesium silicates, calcium silicates, calcium-aluminum silicates and calcium-aluminum-iron silicates. The crystalline products sealing the cracks were mostly silica, talc and high-temperature stable zeolites (mordenite, analcime, thomsonite).Decomposition of ferrierite was faster in alkali carbonate environment than in water. This along with the partial calcium removal as soluble calcium bicarbonate, and lower solubility of silicon led to a larger precipitation of crystalline and amorphous silica, resulting in a more efficient sealing of the cracks in carbonate. Formation of talc through transformation of calcium-magnesium silicates (diopside and akermanite) to various magnesium silicates (protoenstatite, ilmenite) as a result of calcium removal by carbonation and through dolomite skarnification also contributed to the process of fracture filling.

The major crystalline hydration products of clinker were xonotlite in silica-modified samples and kilchoanite along with carbonated calcium silicates scawtite and spurrite that became principal crystalline products in carbonate environment for unmodified samples. Carbonated calcium silicate hydrates were persistent after 10 days of curing and likely responsible for good initial strength build up and first-time recoveries but increased samples' brittleness and, consequently, decreased second-time recoveries. The study showed that natural zeolites unstable under high-temperature alkaline conditions may serve as a latent source of aluminum, silica and other cations for new phases and strength recovery of damaged cements under high-temperature geothermal conditions.

FlexCem® clearly outperformed OPC blend with silica in acid-resistance tests surviving 28 days at pH 0.2 and 90^{o}C. This excellent performance of FlexCem may be explained by the decreased calcium content and pozzolanic reactions of ferrierite.

With E-type micro-glass fiber (MGF), contrary to Clin and FER natural pozzolans leading to the decline of YM, the MGF as artificial pozzolan offered notably increased YMs for OPC/SiO_2,

CAP-A and –B, and GBFS/SiO_2 composites, while no significant changes in YM was observed for MGF-modified TSRC, compared against the original TSRC made by 300^{o}C-1-day-autoclaving in plain water, carbonate, or brine environments. Thus, of the five composites, two MGF composites, OPC/SiO_2 and TSRC, met the *material criterion of YM <400 x 10^3 psi* in these three environments. The average compressive strength developed in these three environments was 3640, 2280, 3780, 3280, and 7450 psi, respectively, for OPC/SiO_2, TSRC, CAP-A and –B, and GBFS/SiO_2. The strength recovery assessment in these environments demonstrated that for two composites (TSRC and CAP-B), MGF was very effective in significantly improving this average recovery, compared with that of MGF-free composites, while some improvement also was observed for OPC/SiO_2. In fact, the average recovery rate of MGF-modified TSRC and CAP-B raised to 139 and 117% from 94% and 62% of unmodified ones, respectively. In contrast, the recovery rate of OPC/SiO_2 by MGF was as small as 77%. In the case of CAP-A and GBFS/SiO_2, the recovery rate reduced.

In this self-healing cement studies, of particular interest was an assessment of whether broken cement fragments can be reattached to the main body of cement samples. So, our attention was centered on investigating the ability of broken fragments separated from MGF-incorporated composites to rebind to the original sample for brittle- and ductile-type composites. We evaluated four composite systems, TSRC as moderately brittle composite, OPC/SiO_2 and CAP-B as brittle ones, and GBFS/SiO_2 as very brittle one.

As a result, the broken fragments of all composites were successfully re-bound to the original samples after exposure of 5 days in plain water, carbonate, and brine environments at 300°C. Among these composites, the interfacial bond of TSRC fragments to the main sample body was considerably higher than that of OPC/SiO_2. Correspondingly, the strength recovery of TSRC was nearly 120, 150, and 128% in plain water, carbonate, and brine, respectively. There were two factors governing such high strength recoveries: One was the reunited structure by an excellent interfacial bonding at fragment/failed mother composite joint; the other was progressive hydrations and reactions of non-or partially-hydrated cement particles and non-reacted alkali activators present in cement matrix. By contrast, although a very brittle GBFS/SiO_2 composite revealed an excellent reunited appearance, the compressive strength value at the initial failure (IF) point attributed to the interfacial bond between the jointed fragments and the rest of the sample was only 508 and 697 psi in carbonate and brine, respectively, implying that interfacial bonding of fragments to the main body was considerably weaker than that of TSRC. This result was directly related to the lower strength recovery. A similar result was also obtained in water.

Thus, MGF-modified TSRC composite possessed a great self-reattaching capability of fragments to the main cement body. There were two potential reasons for this: One was a specific chemistry of TSRC promoting interactions between fragments and main body; the other was associated with ductile failure mode; namely, both the fracture and defected body sides had a rough surface texture along with high surface contact area, leading to a strong interfacial bonding. Whereas very brittle GBFS/SiO_2 composite had an undesirable smooth sharpening features of its fractures, thereby resulting in a weak interfacial bonding.

Task 6. Examining self-healing and crack sealing abilities of 30-day-long autoclaved MGF-modified TSRC in plain water and obtaining fundamental understanding of these abilities

A conspicuous increase of YM was observed from MGF-modified TSRC composite as a function of autoclaving time; YM value increased by nearly 3-fold to 409 x 10^3 psi at 300^{o}C- 30-day autoclave curing in plain water, compared with that of 1-day curing, thereby resulting in mechanical transition from moderate brittle nature to brittle one due to alkali dissolution and reaction of MGF, followed by densification of cement. Meanwhile, unmodified OPC/SiO_2 and TSRC composites at 30-day curing sustained a moderate brittle nature. Similarly, the compressive strength of modified TSRC rose to 2860 psi after 30 days from 1840 psi at 1 day. The unmodified OPC/SiO_2 and TSRC at 30 days had compressive strength of 2965 and 2410 psi, respectively.

As for the compressive strength recovery of MGF-modified TSRC after 300°C-5-day-self-healing treatment in plain water, although a grate recovery of 117% was observed from this 1-day-autoclaved composite, the extended autoclaving time to 30 days resulted in the reduction of recovery rate to 61%. Unlike modified TSRC, unmodified TSRC at the same 30-day curing exhibited 86% recovery. The low recovery of only 36% was observed for unmodified OPC/SiO_2 after 30 days of curing.

The efficacy of healing between the MGF-modified and unmodified TSRCs was somewhat different. The difference was the fact that the sealing became more efficient for the MGF-modified samples made by a 30-day long curing. In fact, the wider cracks representing a brittle fracture mode were sealed after 5-day healing, instead of 10-day treatment which was required for 1-day cured samples. The most likely explanation for this reduced healing time was the presence of reactive ionic species as healing promoters and accelerators released by the slow continuous disintegration of MGF under alkaline environment of the composite at 300°C long-term curing. Namely, these ionic reactants released from MGF interacted with counter reactants in the composite to form and precipitate new sealing and plugging solid state phases in crack spacing. Hence, even after longer initial curing, the samples still possessed the sealing capacity in the presence of MGF, thereby confirming MGF's role as a healing aid. Consequently, such a slow disintegration of MGF healing aid was a very important factor for a long-term healing. Additionally, the increase in MGF's disintegration along with prolonged curing time likely leads to the formation of amorphous phases which could help in developing smaller cracks that fill faster because of ductile nature of amorphous phase. In fact, the widths of cracks at 30-day curing ages were relatively smaller than that were imposed by the damage of a 1-day aged samples; for instance, an average cracks size was ~0.15-0.35 mm after 30-day curing vs. 0.2-0.5 mm after the first day. This is one of the reasons why the cracks in aged composites were readily sealed.

The early-forming phases, crystallizing shortly after the cement set at 300^{o}C-1-day age, were for the most part hydration and SMS-reaction products of CAC. They include hydrogrossular, feldspars (dmisteinbergite and anorthite) and boehmite. At longer curing times, garnets (various stoichiometries of hydrogrossular) become predominant. Continuous slow reactions of FAF introduce additional aluminum, silicon, iron and magnesium into the crystalline phases. Garnets with higher silicon content and with aluminum partially substituted by ferric iron replace earlier formed grossular; boehmite and silica contents noticeable increase. Additionally, mica group calcium-magnesium and calcium-magnesium-iron silicates form in the matrix. The slow reactions of FAF contributing such crystals-building ions as aluminum, silicon, iron and magnesium result in the recoveries of compressive strength for damaged samples. MGF become

an additional source of silica, aluminum, calcium, and some magnesium and iron. These ions stabilize analcime for longer time, preventing its conversion into cancrinite and improving cracks sealing. Additional silica from MGF crystalizes in the fractures further filling them. MGF decomposition in alkali cement environments also introduces ions that form magnesium and iron-containing phases increasing strength of the matrix. MGF reacts slowly, and its effect becomes more noticeable after longer curing times in samples exposed to 300^{o}C for 15 or 30 days.

Relating this information to a lower recovery rate of compressive strength at 30-day initial curing than that of unmodified composite at same curing age, such a lack of strength recovery may be due to the formation of these new iron-related reaction products, but independent of excellent crack sealing efficacy.

Regarding the contributors to crack sealing, the most cracks included silica, high-temperature zeolites (analcime and amicite), sodium-iron-silicate (aegirine), aluminum oxide hydroxide (bohmite) and feldspar minerals with varied calcium and alkali metals contents. The phase transition occurring in the fractures along with the curing progress can be described as follows. The major crystalline phases participating in crack sealing from early curing times are zeolite analcime and silica mostly from sodium silicate and calcium aluminate cement early reactions. As the curing continues analcime converts to cancrinite through carbonation, so the content of analcime declines. Another zeolite, sodalite, forms and more silica precipitates because of alkali dissolution of FAF and MGF (for MGF-modified samples) with release of silicon and aluminum ions. Silica remains the main sealing phase throughout the healing, and especially after longer curing times when FAF and MGF dissolution releases more silicon ions. In addition to silicon, alkali dissolution of FAF and MGF contributes more aluminum, some iron and alkalis to the pool of reacting ions after longer curing. They form (sodium, potassium, calcium)-aluminum-silicates from feldspar group of minerals with varied calcium and alkali metal contents replacing originally formed calcium-aluminum silicate feldspars, anorthite and dmisteinbergite. Sodium iron silicate, aegirine, also precipitates in the cracks.

Task 7. Assessing the re-adhering performance of debonded composites to carbon steel (CS) casing and granite rock formation

Composite/CS interfaces

To determine the re-adhering properties of three MGF-modified composites (OPC/SiO_2, TSRC, and CAP-B) debonded from CS casing, the composite-sheathed CS tube samples were prepared in 300°C- 24-hr-palin water. For the unmodified composites, the high unconfined bond strength was ranked in order of TSRC>CAP-B>OPC/SiO_2. This strength for all cements was improved by adding MGF. The most significant effect in strength improvement was observed for TSRC, leading to 196 psi with MGF from 74 psi without one. Thus, MGF conferred the most improved bond strength on TSRC sheath. However, such high bond strength at nearly 200 psi led to the development of radial cracks in the composite sheath during debonding process at composite/CS joints. This fact clearly suggested that a further improvement of interfacial bond toughness to alleviate crack development is required for advanced bond performance. Although there is no experimental evidence in this limited work, if the composites are placed between casing and geological formation under the confined condition, the crack-width and- propagation, and micro-separation between casing and composite may be suppressed and minimized.

Nevertheless, the 300°C- 5-day exposure of debonded sheath/CS joint samples in water triggered the re-adhering activity of debonded sheaths to CS. Without MGF, the re-adhered bond strength of OPC/SiO_2, TSRC, and CAP-B composites, respectively, was 5.2, 36.3, and 13.0 psi, corresponding to 15, 49, and 26% bond recovery rate. Thus, TSRC displayed the best re-adhering performance. With MGF, despite the generation of radial cracks, the sheath bond strength of re-adhered TSRC was 97 psi, corresponding to 49% recovery rate. From this result, both MGF-modified and unmodified TSRC composites met the *material criterion of sheath-shear bond recovery of >40%.* The other composites did not meet this material criterion.

Composite/granite rock interfaces

All the composites made in 300°C-1-day plain water exerted high sheath-shear bond strength of more than 170 psi, particularly, TSRC/MGF developed a very high bond strength of more than 300 psi. This fact clearly demonstrated that granite rock surfaces were highly susceptible to reactions with these composites, compared with CS surface. In fact, the 300, 200, and 177 psi bond strength, respectively, for TSRC/MGF, OPC/SiO_2, and CAP-B/MGF, was tantamount to the increases in 1.5-, 5.9- and 3.5-fold, compared with that of CS joint samples. If the degree of this susceptibility is directly related to the sheath bond strength, TSRC/MGF along with the highest pH resulted in a better adherence to granite than that of the lowest pH of CAP-B. Nevertheless, only 1 day curing of composites at 300°C was enough to establish a great interfacial bonding. Like the composite-sheathed CS tube samples, the excessive sheath bond strength ≥200 psi for TSRC/MGF and OPC/SiO_2 triggered the development of undesirable multi-radial cracks in the sheaths' bodies during the bond testing. Despite the crack's generation, two alkali-based composites, TSRC/MGF and OPC/SiO_2, revealed a good bond recovery of *>41% meeting the material criterion* after 300°C-5-day re-adhering treatment in plain water, while the recovery of CAP-B/MGF was only 25%.

Task 8. Surveying re-adhering properties of 30-day-long autoclaved composites

In this task, we evaluated the re-adhering ability of three composites cured in 300°C-30-day plain water. One was MGF-modified TSR and the other two were unmodified OPC/SiO_2 and TSRC as reference samples. The value of 30-day sheath-steel shear bond strength for these samples were 70 psi for OPC/SiO_2, 82 psi for TSRC, and 245 psi for TSRC/MGF, which is tantamount to 2.1-, 1.1-, and 1.3-fold increase in bond strength, respectively, over the 1-day bond strength. As expected, the excessive sheath shear bond strength of nearly 250 psi for TSRC/MGF caused the generation of undesirable multi-radial cracks in the sheath during the debonding process of composite from CS. Such crack generation directly reflected on a low rate (28%) of bond recovery, strongly suggesting that re-adhering treatment for 5 days may be not enough for an adequate recovery. No visual cracks were found for the two other reference composites. Correspondingly, MGF-free TSRC exhibited the best bond recovering performance of 49% and 57 % for 1-day- and 30-day-autoclaved composites, respectively, meeting the *material criterion of >40% recovery*. On the other hand, the bond recovery of 30-day-autoclaved OPC/SiO_2 reference was 38%.

Task 9. Bond durability in acid and thermal shock environments
Acid (pH 0.6 H_2SO_4/brine) environment

The work focused on the durability of lap-shear bond at CS plate/composite adhesive/CS plate joint for three MGF-free composites, OPC/SiO_2, TSRC, and GBFS/SiO_2, in pH 0.6 H_2SO_4/brine environment at 90°C for up to 30 days. Such a long-term acid exposure caused a dramatical change in bond behavior for two composite adhesives, OPC/SiO_2 and GBFS/SiO_2. The most of OPC/SiO_2 adhesive layers were undermined by acid erosion of composite after exposure of 18 days, engendering a catastrophic interfacial bond failure. The bond failure mode of GBFS/SiO_2 differed from that of OPC/SiO_2; the acid erosion was minor for GBFS/SiO_2. Instead, the bonding structure formed in the critical interfacial boundary region underwent the acidic damage after 20-day exposure, thereby resulting in the interfacial debondement of composite from CS. In contrast, TSRC adhesive remained in effect for 30 days exposure, and still had lap-shear bond strength of 80 psi by the end of the exposure, strongly demonstrating great interfacial bond resistance to a pH 0.6 acid/brine at 90°C. TSRC provided an outstanding bond durability in such a harsh environment.

To obtain a better understanding of acid degradation and stabilization of these three adhesives, the additional studies were accomplished using the combination of analytical tools, including XRD, µEDX, FT-IR, and Raman imaging. As a result, the calcium depletion was the most severe for GBFS/SiO_2, followed by TSRC and OPC/SiO_2. For the TSRC composites, the crystalline (analcime) and amorphous phases in sodium aluminosilicate-based reaction products played a pivotal role in preserving cement/CS bond for 30 days in the acid/brine environment after calcium depletion. The post-test analyses of GBFS/SiO_2 samples suggested that in the absence of sufficient aluminum content, calcium removal from calcium-silicate hydrates leads to the phase transformation of silicon-containing phases into silica gel.

Acid (pH 5.5 $scCO_2$-laden brine) environment

In this specific acid environment at 90°C, all composite adhesives withstood mild acid attack for 30 days without any severe acid erosion and degradation, except for the reduction of lap-shear bond strength as a function of exposure time. The lowest bond strength reduction of 11% at exposure period of 30 days was measured for TSRC. Compared with this, a high bond reduction of 36 and 35%, respectively, was reported for 30-day-exposed OPC/SiO_2 and GBFS/SiO_2. Nonetheless, 30-day-exposed TSRC and GBFS/SiO_2 adhesives exhibited the lap-shear bond strength of 180 and 165 psi, respectively, which is equivalent to 5.0- and 4.5-fold higher than that of OPC/SiO_2 for the same exposure time.

Thermal shock environment

Among the material criteria, the composite sheath was required to withstand 6-cycle of thermal shock stresses (one cycle, 350°C heating and 25°C water cooling by passing water through inner CS casing) for 300°C-1-day-autoclaved composites. The criterion was as follows: The composites' bond strength should remain 30% higher than that of OPC/SiO_2 reference composite after thermal shock testing.

For the composite-sheathed CS tube samples, MGF-addition provided very high bond strength, engendering the generation of multi-radial cracks in composite sheath during interfacial debonding process. So, in this bond durability tests under the 6-cycle thermal shock stresses, three different composites (TSRC, GBFS/SiO_2, and OPC/SiO_2) without MGF were evaluated. After thermal shock, for TSRC, the sheath-shear bond strength was reduced by 51% to 36 psi.

By contrast, the OPC/SiO_2 composite strikingly lost bond strength from 34 psi before to 7 psi after thermal shock, corresponding to nearly 80% reduction. In contrast, GBFS/SiO_2 sheath encountered the catastrophic bond failure in the first thermal shock cycle. Thus, TSRC possessed a great thermal shock durability and met the *material criterion of ≥30% higher sheath-shear bond strength than that of OPC/SiO_2 reference composite after thermal shock testing.*

Task 10. Inspecting the ability of adhered and re-adhered composites to protect CS against brine-caused corrosion for short- and long-term cured composites

One important question that must be asked is how well the composite layers adhering and re-adhering to the CS surfaces protect the CS against brine-caused corrosion. To answer this question, we needed a better understanding of the interfacial bond failure modes at CS plate/composite adhesive/CS plate lap joints. Next, we evaluated the ability of re-adhered composites made under the original curing conditions to further improve the corrosion mitigation of CS.

Interfacial debonding failure modes

For the short-term (1 day) cured samples in 300°C plain water, there are three different bond failure modes, 1) cohesive failure in composite layer, 2) adhesive failure at interfaces between composite and CS, and 3) 1) and 2) mixed failure. For the steel corrosion protection, the most ideal failure is the cohesive failure, meaning that the bond strength of composite to CS is higher than that of the composite itself. All alkali-activated composites including TSRC, FAC/FAF, GBFS/SiO_2 and phosphate-reacted CAP-B composite had the ideal cohesive bond failure, whereas OPC-based composites like OPC/SiO_2 and FlexCem/SiO_2 disclosed the mixed modes of adhesive and cohesive failures. Relating these failure modes to lap-shear bond strength, the average shear bond strength in plain water and carbonate environments was ranked in the following orders; GBFS/SiO_2 (230 psi) > TSRC (210 psi) > FAC/FAF (175 psi) > CAP-B (160 psi) > OPC/SiO_2 (80 psi) > FlexCem (50 psi). Thus, all composites belonging to cohesive failure mode displayed much greater lap-shear bond strength, than that of OPC-based composites attributed to adhesive and cohesive mixed modes. More importantly, the visual corrosion inspection of debonded CS sites for post-lap shear bond test samples revealed that there were three factors affecting corrosion of CS during 300°C-1-day curing: They were 1) poor bond; 2) unsuitable chemistry of composite; and 3) porous microstructure of composite layers adhering to CS. The two composites, TSRC and GBFS/SiO_2, possessed an adequate protection of CS against corrosion. All other composites engendered the CS corrosion; as for the cause of corrosion, that of FAC/FAF and CAP-B was due to No.3 and No.2 factors, respectively, while No. 1 factor was related to OPC/SiO_2 and FlexCem. In the case of CAP-B, a lower pH (8.5-9.5) of the slurry compared with that of alkali-activated composite slurries with pH >13 was the reason for the lack of corrosion protection.

For the long-term (30 days) cured samples, the test results were similar to that obtained from sheath-shear bond test; the very high lap-shear bond strength of about 300 psi was determined from TSRC/MGF. This bond strength value was 1.3- and 3.3-fold higher than that of TSRC and OPC/SiO_2 references, respectively.

Corrosion mitigation of CS by adhered and re-adhered composites

When the micro-separation of composite sheath from CS casing was encountered, there were two important questions regarding the composite layers that remained on CS's surfaces: One was how well the remaining composites protect CS against brine-caused corrosion; the other was related to the CS's corrosion mitigation after re-adhering. For the latter, the study was directed towards the evaluation of the effectiveness of the additional composite layers superimposed on the composites remaining after debonding in further enhancing protection of CS against corrosion. In this work, three composites (OPC/SiO_2, TSRC, and CAP-B) modified and unmodified with MGF were employed. The lap-shear bond samples were cured for a day in 300°C water before testing. Their ability to inhibit corrosion of CS was evaluated, for composite layer adhering to CS surfaces after 1st (before re-adhering) and 2nd (after re-adhering treatment for 5 days in 300°C water) lap-shear bond destructions, by DC electrochemical polarization in brine. The resulting average corrosion rate strongly demonstrated that the combination of three parameters, higher E_{corr}, lower I_{corr}, and thicker debonded composite layer adhering to CS, played a pivotal role in decreasing the corrosion rate of composite-covered CS. Without MGF, the corrosion rate of CS by these composites was in the following order: OPC/SiO_2 (0.68 mm/year) > CAP-B (0.56 mm/year) > TSRC (0.36 mm/year). With MGF, for all composites, the incorporation of MGF led to the reduction of corrosion rate, compared with that of MGF-free composites, strongly verifying that MGF conferred an improved protection of CS against corrosion on composites. Particularly, the lowest corrosion rate of 0.18 mm/year was determined for TSRC/MGF composite. A further reduction (0.16 mm/year) of corrosion rate was observed after the re-adherence of TSRC/MGF composites. This reduction was due to the presence of new re-adhered composite layer superimposed on the pre-existing composite layer, importantly suggesting that the thickness of composite layers covering on CS was increased by re-adhering treatment.

When the curing time of TSRC/MGF composite adhesive was extended to 30 days, it appeared that the coverage of 30-day-cured composites over CS was much greater than those of 1-day-cured ones, corresponding to nearly 2.4-fold increased thickness. This increase coverage provided a better mitigation of corrosion. Furthermore, after the re-adhering treatment, the thickness of re-adhered composite somewhat increased to 0.32 mm from 0.28 mm before re-adhering and brought about a further reduced corrosion rate of 0.13 mm/year, underscoring that although the interfacial debondement for 30-day-aged composites occurred, the remaining composites adhering to CS surfaces conferred an excellent corrosion protection on CS against corrosion. By contrast, OPC/SiO_2 not only showed no change in thickness after re-adhering treatment, but also there was no enhancement of corrosion impediment; rather the corrosion rate was increased from 0.59 to 0.64 mm/year after re-adhering treatment.

The integrated information of all adhesion- and corrosion-related data described above strongly demonstrated that the adequate corrosion protection of CS was essentially governed by the following two principal factors: One was the good wetting and spreading behaviors of composite slurries over CS surfaces, reflecting uniform coverage of composite layer; the other was an outstanding adhesive behavior of composite to CS, leading to the development of high interfacial bond strength between composite and CS. The alkali-activated TSRC/MGF showed the best wetting and adhesive behaviors with CS, while such behaviors of non-activated OPC/SiO_2 were relatively poor.

Task 11. Validating placement technology of optimized cement composite: Set control, self-healing, re-adhering, and corrosion mitigation properties of retarded cements

Commonly, the pumping time between 3 and 6 hrs may be expected for hot geothermal wells. The retarder added to slow down cement hydration and reactions of slurry components must provide controllable, predictable pumping time of the slurry without compromising development of cement mechanical properties after the set. Using D-(-)-tartaric acid (TA) as the best candidate for retarding hydration of TSRC slurries, this task focused on evaluating the pumpability, self-healing, re-adhering, and corrosion mitigation of the optimized TA-retarded TSRC/MGF composite formula.

Maintenance of pumpability

Based upon the combined analytical results of micro-calorimetry with HPHT consistometer studies, TA confirmed its good performance with MGF-modified TSRC slurries. In fact, thickening time of more than 5 hours was achieved at 100^{o}C bottom-hole-circulating temperature with only 1% by weight of blend TA concentration. Furthermore, the slurry sensitivity to temperature variations was lower than normally expected for OPC-based slurries. However, although the maintenance of pumpability for this optimized formula was very promising, an additional study would be required for evaluation of pressure and retarder content effects on thickening time, as well as, to confirm timely compressive strength development in retarded slurries.

Self-healing behaviors

The combination of TA and MGF revealed an excellent strength development of 3250 psi which was equivalent to nearly 44% increase in comparison with the TSRC without TA. This fact may be due to a temporary hindering effect of TA on the alkali dissolution of MGF because of preferential reactions of TA with Ca and Na hydroxides to form tartrate complexes in a short curing period of only 1 day. Hence, a 5-day self-healing treatment resulted in enhanced decomposition of TA tartrate complexes and the dissolution and increased reactivity of MGF. The retarder also slowed cement hydration that resumed at later times increasing the strength of the composite. Correspondingly, the recovery rate of compressive strength for TA-retarded composites at 1- and 10-day ages was more than 110%. In contrast, this recovery rate of TA-free composite at 10-day age was only 82%, suggesting that TA offered the improved strength recovery of TSRC/MGF composites.

The role of TA in self-healing behavior can be described as follows: The lower Ca content-associated crystalline phases including zeolite-type minerals and boehmite were preferentially formed in TA-modified cement. Importantly, the subsurface areas and the matrix were more likely to be assembled by (CaO,Na_2O)-Al_2O_3-SiO_2-H_2O amorphous phases, rather than crystalline ones. This amorphous phase contributed to the strength recovery and fractures sealing. The superior strength recovery and crack sealing in carbonate environment strongly suggested the importance of carbonate compounds in the healing process. Furthermore, TA served in the creation of the crack-plugging reaction products in this environment. Ca and Na

cations removal through binding to TA and carbonates at early hydration times seems to help strength recoveries and cracks sealing possibly through the formation of Na_2O-CaO-Al_2O_3-SiO_2 gel consisting of network structure, crystallization of carbonated compounds and tobermorite in alkali carbonate. Silica also assisted in sealing the cracks.

Sheath-shear bond strength and its recovery

Like TA-free composite, TA-retarded composites displayed very high sheath bond strength of nearly 200 and 250 psi for 300^{o}C-1-and -10-day-cured composite/CS joint samples, thereby resulting in the generation of undesirable multi-radial wide cracks in the composite sheath during bond test procedure. Thus, more work is needed to improve the toughness of interfacial bonding by advanced reinforce composite technology responsible for the creation of re-adherable cement layer that would form a minimum number of thin cracks during debonding.

Corrosion mitigation of CS by composite adhering to CS

Concerning the corrosion protection of CS by these adhesive layers covering CS surfaces, three findings can be described: 1) there was no significant difference in protection between retarded and non-retarded slurries; 2) the re-adhered adhesive layers displayed a better protection of CS than before re-adhering treatment; and, 3) re-adhered 10-day-age adhesives provided the lowest corrosion rate of 0.12 mm/year for both retarded and non-retarded composites, corresponding to 33% reduction of corrosion rate compared with that before re-adhering treatment.

4. Impact of work

The pozzolanic chemistry-based self-healing and re-adhering cement composites technology developed in this project provided the healing composite formulas suitable for three different cement systems, OPC, phosphate-bonded, and alkali-activated. Among them, the thermal shock-resistant cement (TSRC) modified with MGF as an artificial pozzolanic additive led to the establishment of an upgraded geothermal well cementing system possessing eight advanced properties for the completion of conventional downhole reservoir- and Enhanced Geothermal System-related wells. The eight advanced properties were 1) self-healing capability for repeatedly cracked cement composites at short- and long-curing ages, 2) minimum acid erosion without scale depositions as acid reaction products, 3) compressive strength recovery >100% after cyclic thermal shock, 4) considerably improved bond strength to carbon steel (CS) and granite rock, 5) great re-adhering ability of debonded composite to CS and granite, 6) excellent bond durability in acid and thermal shock environments, 7) enhanced corrosion protection of CS by composite adhering and re-adhering to CS, and 8) maintenance of pumpability for > 5 hours at 100^{o}C well temperature. Although a real field application of this composite system is contingent upon its scale-up validation, these advanced properties will bring the following potential benefits: 1) Extension of CS-based casing's lifecycle; 2) reduction of capital cost by replacing corrosion-resistant expensive alloys with inexpensive CS-based materials; 3) considerable reduction of well operation and maintenance costs by eliminating expensive well abandonment, remedy-and repairing-operations including re-drilling and re-cementing for the catastrophically damaged well structure after cement's failure, 4) decrease in cement material cost due to the use of cost-effective industrial by-products as pozzolanic cement, and 5) lowing

of CO_2 footprint by replacing OPC with industrial by-products. Consequently, upgraded well cement composites will contribute to some reduction of the levelized cost of electricity (LCOE) generated from geothermal power stations. Additionally, the fundamental understanding of self-healing and re-adhering cements obtained in this project will provide new science and advanced processing technologies in high temperature cement chemistry and engineering fields.

6. Publications and Awards

1. Pyatina T., Sugama T., Ronne A. "Self-repairing Geothermal Well Cement Composites" *GRC Transactions vol. 40*, 2016.
2. Pyatina T., Sugama T., Zaliznyak T. "Durability of Bond Between High-Temperature Cement Composites and Carbon Steel" *GRC Transaction vol. 41*, 2017
3. Pyatina T. and Sugama T., "Role of tartaric acid in chemical, mechanical and self-healing behaviors of a calcium-aluminate cement blend with fly ash F under steam and alkali carbonate environments at 270°C," *Materials* 10 (2017) 342-362.
4. Pyatina T., Sugama T., Ronne A., Trabits G. "Self-repairing properties of OPC clinker-natural zeolite blend in water and alkali carbonate environments at 270°C" *Adv. Cem. Res*. 2018, http://dx.doi.org/10.1680/jadcr.16.00136
5. Pyatina T., Sugama T., Trabits G., Jordan A. "Calcium- Silicate-Cement Based Blends with Natural Zeolites – Self-Healing Performance under Conditions of High-Temperature Geothermal Wells" *GRC Transaction vol. 42*, 2018.
6. Sugama T., Pyatina T. "Self-healing, re-adhering, and corrosion mitigating properties of fly ash-containing calcium aluminum phosphate cement composite at 300oC hydrothermal temperature", submitted to Cement and Concrete Composites, 2018.
7. Pyatina T., Sugama T. "Cements for high-temperature geothermal wells" in "Cement Based Materials", Saleh H. and Rahman R. (Editors), InTechOpen, London, UK, 2018

Presentations:

1. Pyatina T., Sugama T., Ronne A. "Self-repairing Geothermal Well Cement Composites" *GRC* Oct. 23-26, Sacramento, California, 2016 (**best presentation award)**
2. Pyatina T., Sugama T., Zaliznyak T. "Durability of Bond Between High-Temperature Cement Composites and Carbon Steel" *Transaction vol. 41*, Oct. 1-4, Salt Lake City, Utah, 2017 (**best presentation award**)
3. Pyatina T., Sugama T., Boodhan Y., Nazarov L., High-Temperature Self-Healing and Re-Adhering Geothermal Cement Composites, MR13B-0317 presented at 2017 Fall Meeting, AGU, New Orleans, LA, 11-15 December 2017
4. Pyatina T., Sugama T. "Self-healing calcium-aluminate-cement-based blends for well cementing" presented at Interpore 2018 Meeting, New Orleans, LA.
5. Pyatina T., Sugama T., Trabits G., Jordan A. "Calcium- Silicate-Cement Based Blends with Natural Zeolites – Self-Healing Performance under Conditions of High-Temperature Geothermal Wells" GRC, Oct. 14-17, Reno Nevada.
6. Pyatina T., Sugama T. "BNL cement work", invited by Japanese government (NEDO), Tokyo, Himeji, Japan, November 2017.

7. Pyatina T., Sugama T. “Multifunctional cementitious blends for ultra-high temperature geothermal wells”, invited by GEORG workshop, Nov. 14-15, Reykjavik, Iceland, 2018

7. Acknowledgements

This publication was based on the work supported by the Geothermal Technologies Office in the US Department of Energy (DOE) Office of Energy Efficiency and Renewable Energy (EERE), under the auspices of the US DOE, Washington, DC, under contract No. DE-AC02-98CH 10886. Raman data were acquired in SoMAS’ Nano-Raman Molecular Imaging Laboratory (NARMIL), a community facility dedicated to environmental sciences’ applications and founded with NSF-MRI grant OCE-1336724. Research was carried out in part at the Center for Functional Nanomaterials, Brookhaven National Laboratory, which is supported by the US Department of Energy, Office of Basic Energy Sciences, under Contract No. DE-SC0012704.

8. References

[1] K. Ravi, M. Bosma, O. Gastebled, Improve the Economics of Oil and Gas Wells by Reducing the Risk of Cement Failure, IADC/SPE Drill. Conf. (2002) 13. doi:10.2118/74497-MS.

[2] J. McCulloch, J. Gastineau, D. Bour, K. Ravi, No Title, in: Geotherm. Resour. Counc. Trans., Geothermal Resources Council, 2003: pp. 12–15.

[3] M.N. Amin, J.S. Kim, Y. Lee, J.K. Kim, Simulation of the thermal stress in mass concrete using a thermal stress measuring device, Cem. Concr. Res. 39 (2009) 154–164. doi:10.1016/j.cemconres.2008.12.008.

[4] C. Teodoriu, C. Kosinowski, M. Amani, J. Schubert, A. Shadravan, Wellbore integrity and cement failure at HPHT conditions, Int. J. Eng. Appl. Sci. 2 (2013) 1–13.

[5] T. Zhijun, Z. Yanjun, J. Jianghong, Technology for improving life of thermal recovery well casing., Adv. Pet. Explor. Dev. 5 (2013) 71–76.

[6] C. Edvardsen, Water permeability and autogenous healing of cracks in concrete., Am. Concr. Inst. Mater. J. 96 (1999) 448–454.

[7] H. Huang, G. Ye, D. Damidot, Characterization and quantification of self-healing behaviors of microcracks due to further hydration in cement paste, Cem. Concr. Res. 52 (2013) 71–81. doi:10.1016/j.cemconres.2013.05.003.

[8] M. Şahmaran, S.B. Keskin, G. Ozerkan, I.O. Yaman, Self-healing of mechanically-loaded self consolidating concretes with high volumes of fly ash, Cem. Concr. Compos. 30 (2008) 872–879. doi:10.1016/j.cemconcomp.2008.07.001.

[9] P. Termkhajornkit, T. Nawa, Y. Yamashiro, T. Saito, Self-healing ability of fly ash-cement systems, Cem. Concr. Compos. 31 (2009) 195–203. doi:10.1016/j.cemconcomp.2008.12.009.

[10] M. Sahmaran, G. Yildirim, T.K. Erdem, Self-healing capability of cementitious composites incorporating different supplementary cementitious materials, Cem. Concr. Compos. 35 (2013) 89–101. doi:10.1016/j.cemconcomp.2012.08.013.

[11] H. Huang, G. Ye, D. Damidot, Effect of blast furnace slag on self-healing of microcracks in cementitious materials, Cem. Concr. Res. 60 (2014) 68–82. doi:10.1016/j.cemconres.2014.03.010.

[12] S.Z. Qian, J. Zhou, E. Schlangen, Influence of curing condition and precracking time on the self-healing behavior of Engineered Cementitious Composites, Cem. Concr. Compos. 32 (2010) 686–693. doi:10.1016/j.cemconcomp.2010.07.015.

[13] T.-H. Ahn, T. Kishi, Crack Self-healing Behavior of Cementitious Composites Incorporating Various Mineral Admixtures, J. Adv. Concr. Technol. 8 (2010) 171–186. doi:10.3151/jact.8.171.

[14] G. Mertens, R. Snellings, K. Van Balen, B. Bicer-Simsir, P. Verlooy, J. Elsen, Pozzolanic reactions of common natural zeolites with lime and parameters affecting their reactivity, Cem. Concr. Res. 39 (2009) 233–240. doi:10.1016/j.cemconres.2008.11.008.

[15] R.L. Virta, Zeolites (Natural), US Geol. Surv. (2015). http://minerals.usgs.gov/minerals/pubs/commodity/zeolites/mcs-2015-zeoli.pdf.

[16] C. Karakurt, I.B. Topçu, Effect of blended cements produced with natural zeolite and industrial by-products on alkali-silica reaction and sulfate resistance of concrete, Constr. Build. Mater. 25 (2011) 1789–1795. doi:10.1016/j.conbuildmat.2010.11.087.

[17] B. Uzal, L. Turanli, H. Yücel, M.C. Göncüoğlu, A. Çulfaz, Pozzolanic activity of clinoptilolite: A comparative study with silica fume, fly ash and a non-zeolitic natural pozzolan, Cem. Concr. Res. 40 (2010) 398–404. doi:10.1016/j.cemconres.2009.10.016.

[18] B. Yilmaz, A. Ucar, B. Oteyaka, V. Uz, Properties of zeolite tuff (clinoptilolite) blended Portland cement., Build. Environ. 42 (2007) 3808–3815.

[19] B. Ahmadi, M. Shekarchi, Use of natural zeolite as a supplementary cementitious material, Cem. Concr. Compos. 32 (2010) 134–141. doi:10.1016/j.cemconcomp.2009.10.006.

[20] C. Bilim, Properties of cement mortars containing clinoptilolite as a supplementary cementitious material, Constr. Build. Mater. 25 (2011) 3175–3180. doi:10.1016/j.conbuildmat.2011.02.006.

[21] E.A. Ortega, C. Cheeseman, J. Knight, M. Loizidou, Properties of alkali-activated clinoptilolite., Cem. Concr. Res. 30 (2000) 1641–1646.

[22] B.H. Misaelides P, Godelistas A Link F, Effects of the secondary minerals of the natural pozzolans on their pozzolanic activity, Cem. Concr. Res. 38 (2008) 963–975. doi:10.1016/j.cemconres.2008.02.005.

[23] B.H. Misaelides P, Godelistas A Link F, The effect of zeolite on the properties and

hydration of blended cements, Cem. Concr. Compos. 32 (2010) 128–133. doi:10.1016/j.cemconcomp.2009.10.004.

[24] B.H. Misaelides P, Godelistas A Link F, Stepwise dehydration of heulandite-clinoptilolite from Succor Creek, Oregon, USA: a single-crystal X-ray study at 100K, Am. Mineral. 76 (1991) 1872–1883.

[25] B.H. Misaelides P, Godelistas A Link F, Metal ion exchange by natural and modified zeolites, Water Res. 31 (1997) 1379–1382. doi:10.1016/S0043-1354(96)00411-3.

[26] B.H. Misaelides P, Godelistas A Link F, Evolution of iron states and formation of α-sites upon activation of FeZSM-5 zeolites, J. Catal. 207 (2002) 341–352. doi:10.1006/jcat.2002.3552.

[27] B.H. Misaelides P, Godelistas A Link F, Steam-activated FeMFI zeolites. Evolution of iron species and activity in direct N2O decomposition, J. Catal. 214 (2003) 33–45. doi:10.1016/S0021-9517(02)00021-0.

[28] B.H. Misaelides P, Godelistas A Link F, Active sites in HZSM-5 with low Fe content for the formation of surface oxygen by decomposing N2O: Is every deposited oxygen active?, J. Catal. 219 (2003) 273–285. doi:10.1016/S0021-9517(03)00222-7.

[29] B.H. Misaelides P, Godelistas A Link F, Characterization and pozzolanic activity of thermally treated zeolite, J. Therm. Anal. Calorim. 82 (2005) 109–113. doi:10.1007/s10973-005-0849-5.

[30] B.H. Misaelides P, Godelistas A Link F, Influence of the fineness of pozzolan on the strength of lime natural-pozzolan cement pastes, Cem. Concr. Res. 24 (1994) 1485–1491. doi:10.1016/0008-8846(94)90162-7.

[31] K.M. Alexander, Reactivity of ultrafine powders produced from siliceous rocks, J. Am. Concr. Inst. 57 (1960) 557–569.

[32] B.H. Misaelides P, Godelistas A Link F, Calcining natural zeolites to improve their effect on cementitious mixture workability, Cem. Concr. Res. 85 (2016) 102–110. doi:10.1016/j.cemconres.2016.04.002.

[33] M. Collepardi, A. Marcialis, L. Massidda, U. Sanna, Low pressure steam curing of compacted lime-pozzolana mixtures, Cem. Concr. Compos. 6 (1976) 497–506.

[34] U. Costa, F. Massazza, Influence of thermal treatment on the activity of some natural pozzolans with lime, Cemento. 74 (1977) 105–122.

[35] R. Hemings, E. Berry, B. Cornelius, D. Golden, Evaluation of Acid-Leached Fly Ash as a Pozzolan., MRS Proc. 136 (1988). doi:10.1557/PROC-136-141.

[36] B.H. Misaelides P, Godelistas A Link F, Chemical activation of blended cements made with lime and natural pozzolans, Cem. Concr. Res. 23 (1993) 1389–1396. doi:10.1016/0008-8846(93)90076-L.

[37] P. Misaelides, A. Godelistas, F. Link, H. Bauman, Application of the 27Al(p,7)2aSi nuclear reaction to the characterization of the near-surface layers of acid-treated HEU-type zeolite crystals, Microporous Mater. 6 (1966) 37–42.

[38] W. Zhang, X. Han, X. Liu, H. Lei, X. Liu, X. Bao, Investigation of the microporous structure and non-framework aluminum distribution in dealuminated nanosized HZSM-5 zeolite by129Xe NMR spectroscopy, Microporous Mesoporous Mater. 53 (2002) 145–152. doi:10.1016/S1387-1811(02)00335-9.

[39] F. Cakicioglu-Ozkan, S. Ulku, The effect of HCl treatment on water vapor adsorption characteristics of clinoptilolite rich natural zeolite, Microporous Mesoporous Mater. 77 (2005) 47–53. doi:10.1016/j.micromeso.2004.08.013.

[40] K. Elaiopoulos, T. Perraki, E. Grigoropoulou, Monitoring the effect of hydrothermal treatments on the structure of a natural zeolite through a combined XRD, FTIR, XRF, SEM and N2-porosimetry analysis, Microporous Mesoporous Mater. 134 (2010) 29–43. doi:10.1016/j.micromeso.2010.05.004.

[41] A. Ates, C. Hardacre, The effect of various treatment conditions on natural zeolites: Ion exchange, acidic, thermal and steam treatments, J. Colloid Interface Sci. 372 (2012) 130–140. doi:10.1016/j.jcis.2012.01.017.

[42] C. Shi, R.L. Day, Comparison of different methods for enhancing reactivity of pozzolans, Cem. Concr. Res. 31 (2001) 813–818. doi:10.1016/S0008-8846(01)00481-1.

[43] D.N. Huntzinger, T.D. Eatmon, A life-cycle assessment of Portland cement manufacturing: comparing the traditional process with alternative technologies, J. Clean. Prod. 17 (2009) 668–675. doi:10.1016/j.jclepro.2008.04.007.

[44] C. Li, X. Gong, S. Cui, Z. Wang, Y. Zheng, B. Chi, CO2 Emissions due to Cement Manufacture, Mater. Sci. Forum. 685 (2011) 181–187. doi:10.4028/www.scientific.net/MSF.685.181.

[45] L.K. Turner, F.G. Collins, Carbon dioxide equivalent (CO2-e) emissions: A comparison between geopolymer and OPC cement concrete, Constr. Build. Mater. 43 (2013) 125–130. doi:10.1016/j.conbuildmat.2013.01.023.

[46] S. Gill, T. Pyatina, T. Sugama, Thermal shock-resistant cement, Geotherm. Resour. Counc. Trans. 36 (2012) 445–451.

[47] T. Pyatina, T. Sugama, Set controlling additive for thermal shock-resistant cement, Geotherm. Resour. Counc. Trans. 38 (2014) 251–257.

[48] T. Sugama, L. Brothers, Sodium-silicate-activated slag for acid-resistant geothermal well cements, Adv. Cem. Res. 16 (2004) 77–87.

[49] E. Weber, E. Emerson, K. Harris, L. Brothers, The Application of a New Corrosion Resistant Cement in Geothermal Wells, Geotherm. Resour. Counc. Trans. 22 (1998) 25–30.

[50] T. Sugama, Advanced Cements for Geothermal Wells, Brookhaven Sci. Lab. under Contract No. …. (2006). http://www.bnl.gov/isd/documents/35393.pdf.

[51] H.W. Reinhardt, M. Jooss, Permeability and self-healing of cracked concrete as a function of temperature and crack width, Cem. Concr. Res. 33 (2003) 981–985. doi:10.1016/S0008-8846(02)01099-2.

[52] V.C. Li, E.H. Yang, Self-Healing in Concrete Materials in Self Healing Materials: An Alternative Approach to 20 Centuries of Materials Science., in: R. Hull, R.M.J. Osgood, J. Parisi, H. Warlimont (Eds.), Springer Ser. Mater. Sci., 2007: pp. 161–193.

[53] P.S. Mangat, K. Gurusamy, Permissible crack widths in steel fibre reinforced marine concrete, Mater. Struct. 20 (1987) 338–347. doi:10.1007/BF02472580.

[54] Y. Yang, D.L. Michael, E. Yang, V.C. Li, Autogenous Healing of Engineered Cementitious Composites under Wet-Dry Cycles., Cem. Concr. Res. 39 (2009) 382–390.

[55] Z. Yang, J. Hollar, X. He, X. Shi, A self-healing cementitious composite using oil core/silica gel shell microcapsules., Cem. Concr. Compos. 33 (2011) 506–512.

[56] L. Sui, M. Luo, K. Yu, F. Xing, P. Li, Y. Zhou, C. Chen, Effect of engineered cementitious composite on the bond behavior between fiber-reinforced polymer and concrete, Compos. Struct. 184 (2018) 775–788. doi:10.1016/j.compstruct.2017.10.050.

[57] T. Pyatina, T. Sugama, Toughness improvement of geothermal well cement at up to 300oC: Using carbon microfiber., J. Compos. Mater. 4 (2014) 177–190.

[58] T. Pyatina, T. Sugama, Use of carbon microfibers for reinforcement of calcium aluminate-class F fly ash cement activated with sodium silicate at up to 300oC, Geotherm. Resour. Counc. Trans. 39 (2015) 209–216.

[59] T. Sugama, T. Pyatina, Bond Durability of Carbon-Microfiber-Reinforced Alkali-Activated High-Temperature Cement Adhering to Carbon Steel, Engineering. 09 (2017) 142–170. doi:10.4236/eng.2017.92007.

[60] T. Pyatina, T. Sugama, Durability of bond between high-temperature cement composites and carbon steel, Geotherm. Resour. Counc. Trans. 41 (2017) 461–479.

[61] M.N. Amin, J.-S. Kim, Y. Lee, J.-K. Kim, Simulation of the thermal stress in mass concrete using a thermal stress measuring device, Cem. Concr. Res. 39 (2009) 154–164.

[62] J. Cowie, F.P. Glasser, The reaction between cement and natural waters containing dissolved carbon dioxide, Adv. Cem. Res. 4 (1992) 119–134.

[63] S. Jacobsen, J. Marchand, L. Boisvert, Effect of cracking and healing on chloride transport in OPC concrete, Cem. Concr. Res. 26 (1996) 869–881. doi:10.1016/0008-8846(96)00072-5.

[64] M.C.R. Farage, J. Sercombe, C. Gallé, Rehydration and microstructure of cement paste after heating at temperatures up to 300 °C, Cem. Concr. Res. 33 (2003) 1047–1056.

doi:10.1016/S0008-8846(03)00005-X.

[65] M.H. Ozyurtkan, M. Radonjic, An experimental study of the effect of CO2rich brine on artificially fractured well-cement, Cem. Concr. Compos. 45 (2014) 201–208. doi:10.1016/j.cemconcomp.2013.10.007.

[66] D. Palin, V. Wiktor, H.M. Jonkers, Autogenous healing of marine exposed concrete: Characterization and quantification through visual crack closure, Cem. Concr. Res. 73 (2015) 17–24. doi:10.1016/j.cemconres.2015.02.021.

[67] Z. Jiang, W. Li, Z. Yuan, Influence of mineral additives and environmental conditions on the self-healing capabilities of cementitious materials, Cem. Concr. Compos. 57 (2015) 116–127. doi:10.1016/j.cemconcomp.2014.11.014.

[68] T. Sugama, T. Pyatina, Self-healing, re-adhering, and corrosion mitigating properties of fly ash-containing calcium aluminum phosphate cement composite at 300oC hydrothermal temperature, Cem. Concr. Compos. submitted (2018).

[69] Petersson, P.E., FRACTURE ENERGY OF CONCRETE; METHOD OF DETERMINATION, Cem. Concr. Res. 10 (1980) 78–89.

[70] T. Pyatina, T. Sugama, A. Ronne, Self-repairing geothermal well cement composite, Geotherm. Resour. Counc. Trans. 40 (2016) 235–243.

[71] T. Pyatina, Resistance of fly ash – Portland cement blends to thermal shock, 28 (2016) 121–131. doi:10.1680/adcr.15.00030.

[72] A.G. Xyla, P.G. Koutsoukos, Quantitative Analysis of Calcium Carbonate Polymorphs by Infrared Spectroscopy, 85 (1989) 3165–3172.

[73] S. Gunasekaran, G. Anbalagan, S. Pandi, Raman and infrared spectra of carbonate of calcite structure., J. Raman Spectrosc. 37 (2006) 892–899.

[74] R. Ylmen, U. Jaglid, Carbonation of Portland cement studied by diffuse reflection Fourier transform infrared spectroscopy., Int. J. Concr. Struct. Mater. 7 (2013) 119–125.

[75] B.N. Roy, Spectroscopic analysis of the structure of silicate glasses along the joint of xMAlO2-(1-x)SiO2 (M=Li, Na, K, Rb, Cs)., J. Am. Ceram. Soc. 70 (1987) 183–192.

[76] L. Fernandez-Carrasco, D. Torrens-Martin, S. Morales, L.M., Martinez-Ramirez, Infrared spectroscopy in the analysis of building and construction materials, in: T. Theophile (Ed.), Infrared Spectrosc. Sci. Eng. Technol., Intechopen, 2012: pp. 370–382.

[77] A.B. Kiss, G. Keresztury, L. Farkas, Raman and ir spectra and structure of boehmite (γ-AlOOH). Evidence for the recently discarded D 17 2h space group, Spectrochim. Acta Part A Mol. Spectrosc. 36 (1980) 653–658.

[78] C. Morterra, C. Emanuel, Infrared Study of some Surface Properties of Boehmite (y-AlO2H), J. Chem. Soc. Faraday. 88 (1992) 339–348.

[79] A. Boumaza, L. Favaro, J. Lédion, G. Sattonnay, J.B. Brubach, P. Berthet, A.M. Huntz, P.

Roy, R. Tétot, Transition alumina phases induced by heat treatment of boehmite: An X-ray diffraction and infrared spectroscopy study, J. Solid State Chem. 182 (2009) 1171–1176. doi:10.1016/j.jssc.2009.02.006.

[80] M.T. Palomo, A. Grutzeck, M. W. Blanco, Alkali activated fly ashes: A cement for future, Cem. Concr. Res. 29 (1999) 1323–1329.

[81] A. Fernandez-Jimenez, A. Palomo, Composition and microstructure of alkali activated fly ash binder: Effect of the activator., Cem. Concr. Res. 35 (2005) 1984–1992.

[82] I. Garcia-Lodeiro, A. Palomo, A. Fernández-Jiménez, D.E. MacPhee, Compatibility studies between N-A-S-H and C-A-S-H gels. Study in the ternary diagram Na2O-CaO-Al2O3-SiO2-H2O, Cem. Concr. Res. 41 (2011) 923–931. doi:10.1016/j.cemconres.2011.05.006.

[83] K.L. Low, S.H.S. Zein, S.H. Tan, D.S. McPhail, A.R. Boccaccini, The effect of interfacial bonding of calcium phosphate cements containing bio-mineralized multi-walled carbon nanotube and bovine serum albumin on the mechanical properties of calcium phosphate cements, Ceram. Int. 37 (2011) 2429–2435. doi:10.1016/j.ceramint.2011.05.092.

[84] B. Nasiri-Tabrizi, A. Fahami, Mechanochemical synthesis and structural characterization of nano-sized amorphous tricalcium phosphate, Ceram. Int. 39 (2013) 8657–8666. doi:10.1016/j.ceramint.2013.04.045.

[85] J. Kolmas, A. Kaflak, A. Zima, A. Ślósarczyk, Alpha-tricalcium phosphate synthesized by two different routes: Structural and spectroscopic characterization, Ceram. Int. 41 (2015) 5727–5733. doi:10.1016/j.ceramint.2014.12.159.

[86] E. Wloch, A. Lukaszczyk, Z. Zurek, B. Sulikowski, Synthesis of ferrierite coatings on the FeCrAl substrate, Catal. Today. 114 (2006) 231–236.

[87] A. Bonilla, D. Baudouin, J. Perez-Ramirez, Desilication of ferrierite zeolite for porosity generation and improved effectiveness in polyethylene pyrolysis., J. Catal. 2 (2009) 170–180.

[88] T. Mitsuda, S. Banno, Hydrothermal formation of pseudowollastonite from lime-quartz mixtures at 165°C and 200°C., Cem. Concr. Res. 7 (1977) 457–460.

[89] T. Mitsuda, J. Asami, Y. Matsubara, H. Toraya, Hydrothermal formation of gamma-dicalcium silicate from lime-silica mixtures using a rapid-heating method and its reaction to give kilchoanite or calciochondrodite., Cem. Concr. Res. 15 (1985) 613–621.

[90] G. Kalousek, E. Nelson, Hydrothermal reactions of dicalcium silicate and silica., Cem. Concr. Res. 8 (1978) 283–289.

[91] A. Milodowski, C. Rochelle, A. Lacinska, D. Wagner, A natural analogue study of CO2-cement interaction: Carbonation of calcium silicate hydrate-bearing rocks from Northern Ireland, in: Energy Procedia, 2011: pp. 5235–5242.

[92] J. Bensted, Special cements. In Lea's Chemistry of Cement and Concrete, Elsevier,

Oxford, UK, 1988.

[93] M. Foldvari, Handbook of Thermogravimetric System of Minerals and its Use in Geological Practice, Geological Institute of Hungary, Budapest, Hungary, 2011.

[94] H. Ishida, S. Sasaki, K. Okada, T. Mitsuda, α-Dicalcium silicate hydrate: preparation, decomposition and its hydration, J. Am. Ceram. Soc. 76 (1993) 1707–1712.

[95] L. Stevula, J. Petrovic, Formation of scawtite from mixtures of CaO, magnesite and quartz under hydrothermal conditions, Cem. Concr. Res. 11 (1981) 549–557.

[96] J. McConnell, A chemical, optical and x-ray study of scawtite from Ballycraigy, Larne, N. Ireland, Am. Mineral. 40 (1955) 510–514.

[97] R. Frost, M. Weier, W. Martens, Thermal decomposition of jarosites of potassium, sodium and lead, J. Therm. Anal. Calorim. 82 (2005) 115–118.

[98] R. Ewell, E. Bunting, R. Geller, Thermal decomposition of talc: research paper RP848, J. Res. Natl. Bur. Stand. (1934). 15 (1935) 551–556.

[99] G. Christidis, D. Moraetis, E. Keheyan, E. Al., Chemical and thermal modification of natural HEU-type zeolite materials from Armenia, Georgia and Greece, Appl. Clay Sci. 24 (2003) 79–91.

[100] M. Mollah, W. Yu, R. Schennach, D. Cocke, A Fourier transform infrared spectroscopic investigation of the early hydration of Portland cement and the influence of sodium lignosulfonate, Cem. Concr. Res. 30 (2000) 267–273.

[101] A. Gaki, R. Chrysafi, G. Kakali, Chemical synthesis of hydraulic calcium aluminate compounds using the Pechini technique., J. Eur. Ceram. Soc. 27 (2007) 1781–1784.

[102] P. Taddei, E. Modena, A. Tinti, E. Al., Effect of the fluoride content on the bioactivity of calcium silicate-based endodontic cements, Ceram. Int. 40 (2014) 4095–4107.

[103] R. Ylmén, U. Jäglid, B.M. Steenari, I. Panas, Early hydration and setting of Portland cement monitored by IR, SEM and Vicat techniques, Cem. Concr. Res. 39 (2009) 433–439. doi:10.1016/j.cemconres.2009.01.017.

[104] C. Otero Areán, M. Rodríguez Delgado, K. Frolich, E. Al., Computational and Fourier transform infrared spectroscopic studies on carbon monoxide adsorption on the zeolites Na-ZSM-5 and K-ZSM-5: evidence of dual-cation sites, J. Phys. Chem. C. 112 (2008) 4658–4666.

[105] R. Almecida, C. Pantano, Structural investigation of silica gel films by infrared spectroscopy, J. Appl. Phys. 68 (1990) 4225–4232.

[106] M. Thompson, R. Palmer, In situ Fourier transform infrared diffuse reflectance and photoacoustic spectroscopy characterization of sulfur-oxygen species resulting from the reaction of SO2 with CaCO3, Appl. Spectrosc. 42 (1988) 945–951.

[107] H. Al-Hosney, V. Grassian, Water, sulfate dioxide and nitric acid adsorption on calcium

carbonate: a transmission and ATR-FTIR study, Phys. Chem. Chem. Phys. 7 (2005) 1266–1276.

[108] N. Mostafa, A. Shaltout, H. Omar, S. Abo-El-Enein, Hydrothermal synthesis and characterization of aluminium and sulfate substituted 1.1 nm tobermorites, J. Alloys Compd. 467 (2009) 332–337.

[109] B. Saikia, G. Parthasarathy, N. Sarmah, Fourier transform infrared spectroscopic estimation of crystallinity in SiO2 based rocks, Bull. Mater. Sci. 31 (2008) 775–779.

[110] V. Ramasamy, G. Suresh, Mineral characterization and crystalline nature of quartz in Ponnaiyar river sediments, Tamilnadu, India, Am. J. Sci. Res. 4 (2009) 103–107.

[111] W. Guan, F. Zhuoyao, F. Dexin, D. Fang, Y. Cheng, P. Yan, Q. Chen, Low hydrothermal temperature synthesis of porous calcium silicate hydrate with enhanced reactivity SiO2, Ceram. Int. 40 (2014) 4415–4420.

[112] T. Pyatina, T. Sugama, Acid resistance of calcium aluminate cement-fly ash F blends, Adv. Cem. Res. 28 (2016) 1–25.

[113] T. Pyatina, T. Sugama, J. Moon, S. James, Effect of tartaric acid on hydration of a sodium-metasilicate-activated blend of calcium aluminate cement and fly ash F, Materials (Basel). 9 (2016) 422–441.

[114] F. Winnefeld, A. Leemann, M. Lucuk, P. Svoboda, M. Neuroth, Assessment of phase formation in alkali activated low and high calcium fly ashes in building materials, Constr. Build. Mater. 24 (2010) 1086–1093.

[115] S. Andini, R. Cioffi, F. Colangelo, T. Grieco, F. Montagnaro, L. Santoro, Coal fly ash as raw material for the manufacture of geopolymer-based products, Waste Manag. 28 (2008) 416–423.

[116] K. Harada, K. Tanaka, K. Nagashima, New data on the analcime-wairakite series, Am. Mineral. 57 (1972) 924–931.

[117] C. Gosselin, K.. Scrivener, Microstructure development of calcium aluminate cements accelerated by lithium sulphate, in: C.. Fentiman, R.. Mangabhai, K.. Scrivener (Eds.), Calcium Aluminate Cem. Proceeding Centen. Conf. 2008, IHS BRE Press, 2008: pp. 109–122.

[118] D. Klimesch, A. Ray, DTA-TGA of unstirred autoclaved metakaolin-lime-quartz slurries. Formation of hydrogarnet, Thermochim. Acta. 316 (1998) 149–154.

[119] D. Klimesch, A. Ray, DTA-TGA evaluations of the CaO-Al2O3-SiO2-H2O system treated hydrothermally, Thermochim. Acta. 334 (1999) 115–122.

[120] D. Breck, Zeolite molecular sieves: Structure, Chemistry and Use, Wiley and Sons: New York, NY, USA, 1974.

[121] I. Hassan, The thermal behavior of cancrinite, Can. Mineral. 34 (1996) 893–900.

[122] W. Hannicutt, Characterization of calcium-silicate-hydrate and calcium-alumino-silicate hydrate, University of Illinois, 2013.

[123] R. Husung, R.. Doremus, The infrared transmission spectra of four silicate glasses before and after exposure to water, J. Mater. Res. 5 (1990) 2209–2216.

[124] A. Kline, M.. Mullins, Sol-gel kinetics followed by cylindrical attenuated total reflectance infrared spectroscopy, J. Am. Ceram. Soc. 74 (1991) 2559–2563.

[125] T. Bakharev, Resistance of geopolymer materials to acid attack, Cem. Concr. Res. 35 (2005) 658–670.

[126] S. Gunasekaran, G. Anbalagan, S. Pandi, Raman and infrared spectra of carbonate of calcite structure, Spectroscopy. 37 (2006) 892–899.

[127] A. Fidalgo, L.. Ilharco, The defect structure of sol-gel-derived silica/polytetrahydrofuran hybrid films by FTIR, J. Non. Cryst. Solids. 283 (2001) 144–154.

[128] P.. Tanner, B. Yan, H. Zhang, Preparation and luminescence properties of sol-gel hybrid materials incorporated with europium complexes, J. Mater. Sci. 35 (2000) 4325–4328.

[129] A. Boumaza, L. Favaro, J. Ledion, G. Sattonnay, J.. Brubach, P. Berthet, A.. Huntz, P. Roy, Structural transitions in alumina nanoparticles by heat treatment, J. Solid State Chem. 182 (2009) 1171–1176.

[130] N. Van Garderen, F.. Clemens, C.. Aneziris, T. Graule, Improve γ-alumina support based pseudo-bohmite shaped by micro-extrusion process for oxygen carrier support application, Ceram. Int. 38 (2012) 5481–5492.

[131] I. García-Lodeiro, A. Palomo, D. Fernández-Jimenez, A Macphee, Compatibility studies between N–A–S–H and C–A–S–H gels. Study in the ternary diagram Na2O–CaO–Al2O3–SiO2–H2O, Cem. Concr. Res. 41 (2011) 923–931.

[132] I. Giannopoulou, D. Panias, Hydrolytic stability of sodium silicate gels in the presence of aluminum, J. Mater. Sci. 45 (2010) 5370–5377.

[133] M. Roig-Flores, S. Moscato, P. Serna, L. Ferrara, Self-healing capability of concrete with crystalline admixtures in different environments, Constr. Build. Mater. 86 (2015) 1–11.

[134] M.J.. Qomi, F.. Ulm, R.J.. Pellenq, Evidence on the dual nature of aluminum in the calcium-silicate-hydrates based on atomistic simulations, J. Am. Ceram. Soc. 95 (2012) 1128–1137.

[135] R.. Myers, S.. Bernal, R. San Nicolas, J.. Provis, Generalized structural description of calcium-sodium aluminosilicate hydrate gels: The cross-linked substituted tobermorite model, Langmuir. 29 (2013) 5294–5306.

[136] S. Shaw, S.M. Clark, C.M.. Henderson, Hydrothermal formation of the calcium silicate hydrates, tobermorite (Ca5Si6O16(OH)2·4H2O) and xonotlite (Ca6Si6O17(OH)2): An synchrotron study, Chem. Geol. 167 (2000) 129–140.